



N° ordre : 09/18

Année 2009

ED 072 – UNIV LILLE NORD-DE-FRANCE  
 ECOLE DOCTORALE REGIONALE SCIENCES POUR  
 L'INGENIEUR

---

**TRANSIENT NUMERICAL COMPUTATION  
 OF THE TEMPERATURE  
 OF THE ELECTRONIC EQUIPMENT  
 IN PASSENGER CARS**

---

**THESE DE DOCTORAT**  
 présentée par Florence MICHEL, ingénieur ENSIAME  
 en vue de l'obtention du titre de  
 Docteur de l'Université de Valenciennes et du Hainaut-Cambrésis  
 Spécialité : Mécanique et Energétique

Le travail de thèse a été effectué au sein de Mercedes-Benz (Sindelfingen, Allemagne), en coopération avec l'Université de Valenciennes et du Hainaut-Cambrésis (France) et soutenu le 16 septembre 2009 devant la commission d'examen suivante :

Examineur	Bernard BAUDOIN, Prof. – Ecole des Mines Douai, France
Directeur de thèse	Bernard DESMET, Prof. – LME Valenciennes, France
Rapporteur	Eckart LAURIEN, Prof. Dr.-Ing. – IKE Stuttgart, Allemagne
Examineur	Hassan PEERHOSSAINI, Prof. – Polytech'Nantes, France
Rapporteur	Mourad REBAY, HDR – GRESPI Reims, France
Examineur	Heinrich REISTER, Dr.-Ing. – Mercedes-Benz, Allemagne

---

## Acknowledgments

« A la source de toute connaissance, il y a une idée, une pensée, puis l'expérience vient confirmer l'idée. »

Claude Bernard

The origin of any knowledge is an idea, a notion, and then the experience comes confirming the idea. This quote perfectly reflects the development of my doctoral thesis, with at the beginning the notion of a new numerical strategy, which is then examined, tested and validated by many and various computations in comparison with experiments. This validation work that I completed as busy as a bee is the experience described by Claude Bernard; the whole work during these last three years is my experience of the doctoral thesis.

My first special thanks goes out to my university advisor, Prof. Bernard Desmet, for his assistance, scientifically as well as humanly. Also, I want to express my deep gratitude to my first reviewer Prof. Eckart Laurien for his several fruitful suggestions and for introducing me the fundamental research at the university. I would like to thank my second reviewer Prof. Mourad Rebay, who I first met coincidentally at the 5<sup>th</sup> European Thermal-Sciences Conference and who already provided me his vast knowledge and skills in this same research area.

My second special thanks heads for my advisor and mentor at Daimler AG, Dr.-Ing. Heinrich Reister. It was under his tutelage that I always open my mind for new investigation areas and that I developed goal-oriented and supervision skills. I would also like to thank the whole department energy management for the warm welcome I enjoyed. In particular, I want to thank Dipl.-Math. Walter Bauer for his continuous understanding and kindness. Thanks also goes out to Drs.-Ing. Thomas Binner, Ernst-Peter Weidmann and Klaus Ickert, who provided me with advice at times of critical need. I would like to truly thank my colleagues of the experimental teams for their collaboration and confidence in my proposals for different measurement techniques and other sensor positions. Finally, I would like to acknowledge Prof. Dr.-Ing. Andreas Griesinger and Peter Fink of the Steinbeis institute, whose deepened knowledge in electronic systems added considerably to my thermodynamic and fluid mechanics experience.

Last but not least, I recognize that this research work would not have been possible without the financial support of Daimler AG. Moreover, I would like to thank Prof. Thomas Breitling and Dr.-Ing. Raimund Siegert for taking interest in my work. Also, I would like to thank Prof. Alain Lecocq for favoring the cooperation between the university of Valenciennes and Daimler AG.



---

## Abstract

In order to ensure a reliable operation of the electronic equipment in a passenger car, its thermal situation is successively evaluated during each digital phase of the development process. The operating conditions of the car and electronic device, also the climatic conditions are settled with a so-called use case. Standard use cases consist of a first phase of pre-conditioning with warming-up, followed by a period of thermal load, e.g. uphill driving with load trailers. Of particular interest in the development process is for a specified use case to predict the time period, during which the electronic system embedded in the vehicle works within its optimal operating temperature range, in order to compare it with the requirements of the device and vehicle specifications. If necessary, the positioning of the electronic system can be optimized in the course of the development phases to enlarge the operating time period. In the present work, computational methods and numerical models to predict the temperature of the electronic equipment in a passenger car under time-dependent operating conditions and thermal loads have been developed and validated. It focuses on electronic devices assembled in vehicles with conventional powertrain, characterized by a tight operating temperature range and a significant heat dissipation or a critical position in the car. Moreover, the results of present work are used by now as foundation for the thermal management of the upcoming HEVs (hybrid electric vehicle) and PEVs (pure electric vehicles).

According to the up-to-date state of literature, there is presently no numerical method to compute the temperature of automotive electronic systems dealing with complex geometries and environment boundaries. Moreover, the methods presented in the literature to solve the coupled heat transfer modes – convection, conduction and radiation – are limited to stationary operating conditions.

In the first part of the present work, simulation strategies for the transient computation of the different modes of heat transfer are investigated with a system analysis. In order to determine the geometric limits of the computational system, the time scales relevant for the temperature prediction of the electronic equipment in a passenger car are requested. These time scales are calculated with a non-dimensionalization analysis of the transport equations in the fluid by convection and in the solid by conduction. The corresponding characteristic time is analyzed for the geometric level of an electronic device as well as of the electronic compartment in the vehicle. In order to avoid the computation of heat transfer modes characterized by large discrepancies in the time scales, the computed system is restricted to four geometric levels: the semi-conductor case, the board, the electronic package and its near environment in the vehicle. Nevertheless, different time-steps are requested for the computation of conductive and convective heat transfer modes. Consequently, the different heat transfer modes are solved separately with adapted codes using iterative coupling simulation strategies, which

---

enables also different grade of details in each numerical model. For reasonable computing times in the development process, a steady-state approach is used to solve the conservation equations of the convective flow. Two iterative coupling codes strategies are proposed according to the convection boundary conditions. Experimental techniques are then briefly described for validation measurements under laboratory conditions and real environment conditions.

In a second part, numerical models for the prediction of the convective heat transfer mode are examined with test cases, in particular in view of mesh requirements and turbulence modeling, and validated in comparison with literature. First, the accuracy of the steady-state approach for the prediction of the convection heat transfer mode has been investigated for the computation of buoyancy-driven flows encountered in electronic systems without active cooling. Moreover, numerical models for fan flow simulation and flow computation through thin electronic grills have been validated regarding the fan prescribed volume flow rate and the establishing pressure distribution in the system in comparison with measurements and correlations from the literature.

In the third and last part, the coupling codes strategies are validated by means of two complex electronic systems, on the one hand a lead-acid battery situated in a spare-wheel cavity in the rear of the car, on the other hand a sound amplifier assembled in a cavity located between the engine compartment and under the floor covering of the passenger. First, the critical components, the thermal requirements and the use case applied are specified. In order to build a numerical model of the electronic system from the real device in the vehicle, a parameterization of the model is carried out in a first step, whereby measurement data are used to model the convective heat flux. In a second step, the co-simulation strategies proposed previously are applied on the parameterized numerical model, disposing of flow computations for the prediction of the convective heat transfer. For the validation of the coupling simulations, the temperature of the critical components predicted by the transient computation is compared to experimental results in the vehicle. Finally, the efficiency and the reliability of both co-simulation strategies are discussed for implementation in the digital development process.

**Keywords:** thermal management, electronic devices, transient computation, co-simulation, natural convection, conduction, radiation, fan flow, thin electronic grill, lead-acid battery, sound amplifier.

---

## Résumé

Afin d'assurer la fiabilité des composants électroniques d'un véhicule, leur situation thermique est évaluée successivement à chaque phase du processus de développement. Les conditions d'utilisation du véhicule et du composant électronique, ainsi que les conditions environnantes, sont fixées par un protocole de charge ou d'utilisation. Les protocoles standards de charge sont basés sur une première phase d'échauffement du véhicule, suivie par une phase de charge thermique, par exemple en conduite en côte avec une remorque chargée. Dans le processus de développement, il est particulièrement intéressant de pronostiquer la durée, pendant laquelle le système électronique travaille dans son régime optimal de température de fonctionnement, afin de la comparer avec les exigences du cahier des charges. Pour augmenter la durée de fonctionnement du système électronique, son positionnement dans le véhicule peut être optimisé au cours des différentes phases du processus de développement. Afin de calculer la température des composants électroniques d'une voiture dans des conditions d'utilisation et de charge thermique instationnaires, différents modèles numériques et méthodes de simulation ont été développés et validés dans l'étude présente. L'étude se concentre sur des systèmes électroniques assemblés dans des véhicules de propulsion conventionnelle, et caractérisés par un champ de température étroit ou par un positionnement critique dans le véhicule. En outre, les résultats de la présente étude sont utilisés actuellement pour assurer la protection thermique des prochains véhicules hybrides et électriques.

L'état actuel de la science montre le manque de méthodes numériques pour le calcul de la température des systèmes électroniques automobiles classiques, de géométrie complexe et dont les conditions environnantes présentent une forte variation dans l'espace et le temps. De plus, les méthodes présentées dans la littérature pour résoudre le couplage des modes de transfert de chaleur – convection, conduction et rayonnement – sont limitées à des conditions d'utilisation stationnaires.

Dans une première partie de cette étude, plusieurs stratégies numériques permettant le calcul instationnaire des modes de transfert de chaleur sont étudiées à l'aide d'une analyse de système. Afin de déterminer les limites géométriques du système numérique, il est nécessaire d'évaluer les échelles temporelles pertinentes pour le calcul de la température des composants électroniques dans un véhicule. Ces échelles temporelles sont calculées à partir d'une analyse adimensionnelle des équations de transport dans le fluide par convection et dans le solide par conduction. Le temps caractéristique correspondant est analysé à l'échelle géométrique d'un composant électronique et à l'échelle de son compartiment dans le véhicule. Afin d'éviter le calcul des modes de transferts dont le champ des temps caractéristiques serait trop dispersé, le système numérique se restreint à tous les domaines géométriques situés entre le boîtier d'un semi-conducteur et le proche environnement du système électronique dans le véhicule.

---

Néanmoins, différents pas de temps sont nécessaires pour le calcul numérique des modes de transfert conductif et convectif. Par conséquent, les modes de transfert de chaleur sont calculés séparément avec des codes adaptés s'intégrant dans une stratégie de couplage, ce qui permet également d'adopter différents grades de détails dans chaque modèle numérique. Pour réduire le temps de calcul dans le processus de développement, les équations de conservation de l'écoulement convectif sont calculées avec une approche stationnaire. Deux stratégies itératives de couplage sont proposées selon les conditions limites convectives. En outre, les techniques de mesure utilisées dans cette étude sont brièvement décrites.

Dans la deuxième partie, plusieurs modèles numériques pour le calcul du mode de transfert convectif sont examinés sur des cas test et validés en comparaison avec la littérature, en particulier avec une analyse du maillage et des modèles de turbulence. Tout d'abord, la précision de l'approche stationnaire utilisée pour le calcul du transfert convectif est étudiée sur des écoulements en convection naturelle rencontrés dans des systèmes électroniques démunis de ventilateur ou d'autres sources de refroidissement actif. En outre, différents modèles numériques pour la simulation de l'écoulement généré par un ventilateur et pour le calcul de l'écoulement au travers de fines grilles électroniques sont validés en comparaison avec des résultats expérimentaux et des corrélations de la littérature. Les critères pris en compte pour la validation des modèles numériques sont le débit volumique prescrit par le ventilateur et la distribution de pression statique s'établissant dans le système.

Dans la troisième et dernière partie, les stratégies de couplage de codes sont validées pour deux systèmes électroniques complexes, d'une part une batterie au plomb assemblée dans une cavité de roue de secours, et d'autre part un amplificateur audio monté dans une cavité située entre le compartiment moteur et la cabine sous le passager. Les composants critiques, les exigences thermiques vis-à-vis du cahier des charges et le protocole d'utilisation appliqué, sont tout d'abord spécifiés. Pour construire un modèle numérique du système électronique à partir du composant réel dans le véhicule, un paramétrage du modèle est effectué dans un premier temps à l'aide de données expérimentales pour modéliser le flux de chaleur convectif. Dans un second temps, les stratégies de couplage proposées précédemment sont appliquées au modèle numérique paramétré, ce qui permet le calcul de la convection dans le fluide et fournit le flux de chaleur convectif. Afin de valider la co-simulation, la température des composants critiques donnée par le calcul instationnaire est comparée aux résultats expérimentaux. Finalement, l'efficacité et la fiabilité de chacune des stratégies de co-simulation sont discutées en considérant l'implémentation dans le processus de développement digital.

Mots-clés: protection thermique, composants électroniques, calcul instationnaire, co-simulation, convection naturelle, conduction, rayonnement, écoulement généré par un ventilateur, fine grille électronique, batterie au plomb, amplificateur audio.

---

## Zusammenfassung

Um einen sicheren Betrieb der elektronischen Komponenten in einem Kraftfahrzeug zu gewährleisten, wird deren thermische Situation in jeder digitalen Phase des Entwicklungsprozesses bewertet. Die Betriebsbedingungen eines Fahrzeugs und der Komponenten werden mit einem sogenannten Lastfall definiert. Übliche Lastfälle setzen sich zusammen aus einer Vorkonditionierungsphase mit Warmfahren und einer anschließenden Belastungsphase, z.B. Bergfahrt mit Anhänger. Im Entwicklungsprozess ist es besonders interessant, für einen bestimmten Lastfall den Zeitraum zu prognostizieren, in dem das elektronische System im Fahrzeug innerhalb seines optimalen Temperaturbereichs arbeitet, um einen Vergleich mit den Anforderungen der Lastenhefte von Komponente und Fahrzeug zu bekommen. Wenn nötig kann die Einbausituation des elektronischen Systems im Laufe der Entwicklungsphasen optimiert werden, um den Betriebszeitraum zu vergrößern. In der vorliegenden Arbeit wurden Berechnungsmethoden und numerische Modelle entwickelt und validiert, um die Temperatur der elektronischen Komponenten im Fahrzeug unter zeitabhängigen Betriebsbedingungen und thermischen Lasten zu ermitteln. Dabei richtet sich der Fokus auf die elektronischen Komponenten in Fahrzeugen mit konventionellem Antrieb (Verbrennungsmotor), die in einem engen Temperaturbereich arbeiten und durch eine signifikante Wärmeabgabe oder eine kritische Einbaulage im Fahrzeug charakterisiert sind. Die Ergebnisse der vorliegenden Arbeit werden darüber hinaus inzwischen auch als Grundlage für die thermische Absicherung der kommenden hybridisierten und elektrischen Fahrzeuge verwendet.

Nach dem aktuellen Stand der Literatur gibt es zur Zeit noch kein numerisches Verfahren zur Berechnung der Temperatur elektronischer Komponenten in einem komplexen Fahrzeugumfeld. Außerdem sind die in der Literatur beschriebenen Methoden zur Auflösung der gekoppelten Wärmeübergangsmechanismen – Konvektion, Wärmeleitung und Strahlung – auf stationäre Randbedingungen beschränkt.

Im ersten Teil der vorliegenden Arbeit werden numerische Strategien für die instationäre Berechnung der verschiedenen Wärmeübergangsmechanismen mit einer Systemanalyse untersucht. Für die Auslegung des Berechnungssystems werden die relevanten Zeitskalen für die Temperaturberechnung elektronischer Komponenten im Fahrzeug benötigt. Diese werden über die Analyse der dimensionslosen Transportgleichungen für den Wärmetransport im Fluid (über Konvektion) bzw. im Solid (über Wärmeleitung) ermittelt. Die entsprechende charakteristische Zeit wird sowohl für die geometrische Dimension einer elektronischen Komponente als auch der des Bauraums im Fahrzeug berechnet. Um näherungsweise mit ähnlichen charakteristischen Zeiten zu arbeiten, wird sich das Berechnungssystem in der geometrischen Dimension der elektronischen Komponenten auf die Chip- und Komponentenebene und beim Bauraum auf die nahe Umgebung der elektronischen Komponente beschränkt. Dennoch sind unterschiedlich große Zeitschritte bei der Berechnung der Konvektion und

---

Wärmeleitung notwendig. Somit werden Konvektion und Wärmeleitung mit geeigneten Programmen und mit Hilfe von iterativen Kopplungsstrategien getrennt gelöst. Zusätzlich lässt die Kopplungsstrategie verschiedene Detaillierungsgrade in den einzelnen numerischen Modellen zu. Zur Erreichung akzeptabler Rechenzeiten im Entwicklungsprozess wird das Geschwindigkeitsfeld der Konvektionsströmung stationär behandelt. Abhängig von den konvektiven Randbedingungen werden zwei iterative Kopplungsstrategien vorgeschlagen. Anschließend werden kurz mögliche Versuchsanordnungen für Validierungsmessungen unter Labor- und Real-Bedingungen beschrieben.

Im zweiten Teil werden numerische Modelle zur Berechnung des konvektiven Wärmeübergangs anhand von Testfällen untersucht, insbesondere im Hinblick auf Turbulenzmodellierung und Netzanforderung, und mit Vergleichsfällen aus der Literatur validiert. Zuerst wird die Genauigkeit des stationären Geschwindigkeitsansatzes zur Ermittlung der Wärmeübertragung für den Fall der natürlichen Konvektion in elektronischen Systemen ohne aktive Kühlung überprüft. Danach werden numerische Modelle zur Berechnung der vom Lüfter erzwungenen Konvektionsströmung und der Strömung durch dünne Lochbleche untersucht und mit Messungen sowie Literaturangaben verglichen. Als Kriterien zur Validierung der numerischen Modelle dienen der vom Lüfter erzeugte Volumenstrom sowie die Druckverteilung in der elektronischen Komponente im Einbauzustand.

Im dritten Teil werden die Kopplungsstrategien anhand zweier komplexer elektronischer Systeme validiert, zum einen für eine konventionelle Batterie, eingebaut in die Ersatzradmulde (im Fahrzeugheck), zum zweiten für einen Soundverstärker, eingebaut im Freiraum zwischen Stirnwand (Trennwand zum Motorraum) und Bodenbelag des Beifahrerfußraums. Zuerst werden die kritischen Komponenten, die thermischen Anforderungen und der relevante Lastfall spezifiziert. Im ersten Schritt werden zur Bedatung des numerischen Modells des elektronischen Systems als Randbedingungen direkt Wärme Flüsse aufgebracht, welche aus Messungen ermittelt wurden. Im zweiten Schritt werden die vorgeschlagenen Kopplungsstrategien auf das bedatete Modell des elektronischen Systems angewandt, wobei nun die konvektiven Wärme Flüsse mit Hilfe der Strömungssimulation ermittelt werden. Die Ergebnisse dieser gekoppelten Simulation werden durch Vergleich mit Gesamtfahrzeugmessungen validiert. Schließlich werden die Effizienz und Zuverlässigkeit beider Kopplungsstrategien für eine Implementierung im digitalen Entwicklungsprozess diskutiert.

Stichwörter: thermische Absicherung, elektronische Systeme, instationäre Berechnung, Codekopplungsstrategien, natürliche Konvektion, Wärmeleitung, Strahlung, vom Lüfter erzwungene Konvektion, dünnes elektronisches Lochblech, konventionelle Batterie, Soundverstärker.

---

# Contents

<b>Nomenclature</b>	<b>15</b>
<b>1. Industrial motivation</b>	<b>19</b>
1.1. Digital development process .....	19
1.2. Electronic equipment in a passenger car, heat transfer mechanisms.....	21
1.2.1. Heat sources .....	21
1.2.2. Heat transport by convection .....	21
1.2.3. Heat transport by conduction.....	22
1.2.4. Heat transport by radiation.....	23
1.3. Use cases for the electronics temperature.....	23
1.4. Target electronic devices in the development process .....	25
1.5. Thermal management of electronics in the digital development process.....	26
<b>2. State of literature</b>	<b>27</b>
2.1. Numerical methods for the thermal management of a passenger car.....	28
2.1.1. Development of coupling simulation methods .....	28
2.1.2. Numerical methods used in the DPT process at Daimler AG .....	29
2.2. Heat transfer mechanisms in elementary electronic systems .....	29
2.2.1. Conduction at junction and case levels.....	30
2.2.2. Natural convection in electronic cavities .....	31
2.2.3. Forced convection in electronic channels .....	33
2.2.4. Mixed convection in electronic channels.....	33
2.3. Thermal management of electronic systems .....	35
2.3.1. Conjugate convective and conductive heat transfer modes .....	35
2.3.2. Convective, conductive and radiation heat transfer modes .....	35
2.4. Partial conclusions .....	37
2.5. Aim and challenge of the project.....	38

---

<b>3. Development of a numerical method for the thermal management of electronics in passenger cars</b>	<b>41</b>
3.1. Characteristic time of temperature propagation .....	41
3.1.1. Transport by convection .....	42
3.1.2. Transport by conduction .....	45
3.1.3. Transport by radiation .....	46
3.1.4. Partial conclusions .....	46
3.2. Mathematical model for the prediction of the electronic temperature in the development process.....	47
3.2.1. Governing equations .....	47
3.2.2. Time-dependent coupled heat transfer problem .....	50
3.2.3. Resolution of the coupled problem in the development process .....	51
3.3. Solid solvers .....	52
3.3.1. Mesh generation for RadTherm and PERMAS computations.....	52
3.3.2. Thermal analysis software RadTherm .....	52
3.3.3. Finite element code PERMAS and radiation code POSRAD.....	53
3.4. Flow solver STAR-CD .....	55
3.4.1. Mesh generation.....	55
3.4.2. Turbulence modeling .....	55
3.4.3. Convective heat transfer at the interface.....	56
3.4.4. Discretisation and solution algorithm .....	57
3.5. Modeling of the flow in electronic enclosures .....	58
3.5.1. Buoyancy-driven flows .....	59
3.5.2. Forced convective flows .....	59
3.6. Coupling codes strategies .....	63
3.6.1. Data transfer at the fluid-solid interface .....	63
3.6.2. Mesh mapping for matching boundary conditions .....	64
3.6.3. Transient coupling of heat transfer modes .....	64
3.7. Experimental methods used for numerical validation .....	68
3.7.1. Laboratory conditions .....	68
3.7.2. Real environment in the vehicle .....	71
3.8. Partial conclusions .....	72

---

<b>4. Validation and accuracy of the convective heat transfer prediction</b>	<b>73</b>
4.1. Buoyancy-driven flows.....	73
4.1.1. Structure of the flow, rectangular box .....	75
4.1.2. Heat transfer rate, cubical cavity .....	79
4.1.3. Partial conclusions .....	85
4.2. Forced convective flows.....	86
4.2.1. MRF simulation .....	86
4.2.2. Rotational body force simulation.....	89
4.2.3. Partial conclusions .....	91
4.3. Outlet grills of the TV-tuner.....	92
4.3.1. Grill modeling in the test-rig.....	93
4.3.2. TV-tuner, outlet grills .....	96
4.3.3. TV-tuner, porous resistance elements.....	100
4.3.4. Partial conclusions .....	104
<b>5. Validation of the co-simulation strategies on electronic systems in a vehicle</b>	<b>105</b>
5.1. Battery in the spare-wheel cavity .....	105
5.1.1. Critical parts and thermal requirements .....	105
5.1.2. Use cases and experimental investigations .....	106
5.1.3. Numerical models .....	108
5.1.4. Model validation of the battery in the spare wheel cavity .....	111
5.1.5. Validation of the coupling strategy, case of summer.....	115
5.1.6. Determination of a critical use case of summer.....	118
5.1.7. Partial conclusions .....	119
5.2. Sound amplifier in a cavity under the passenger's feet.....	120
5.2.1. Thermal requirements and heat transfer mechanisms.....	120
5.2.2. Use case and experimental results .....	122
5.2.3. Numerical models .....	123
5.2.4. Model validation of the sound amplifier in the feet compartment, fan switched off.....	127
5.2.5. Validation of the coupling strategy, fan switched off.....	130
5.2.6. Partial conclusions .....	132
<b>6. Discussion and perspectives</b>	<b>133</b>

---

<b>Bibliography</b>	<b>135</b>
<b>Appendix</b>	<b>149</b>
A.1. Characteristic numbers .....	149
A.2. Thermal analysis with the FEM code PERMAS .....	150
A.3. Experimental methods .....	151
A.3.1. Fan test-rig .....	151
A.3.2. Perforated plate performance curve .....	152
A.3.3. K-type thermocouples .....	153
A.4. Buoyancy-driven flows.....	154
A.4.1. Rectangular box .....	154
A.4.2. Horizontal cubical cavity .....	156
A.5. Forced convective flows .....	162
A.5.1. Electronic fans considered .....	162
A.5.2. Turbulence modeling and mesh refinement study .....	162
A.6. Outlet grills, TV-tuner .....	165
A.6.1. Geometric parameters .....	165
A.6.2. Grill modeling .....	166
A.6.3. TV-tuner, outlet grills .....	168
A.6.4. Upper grill of the TV-tuner in the test-rig .....	171
A.6.5. TV-tuner, 2D and 3D porous elements .....	172
A.7. Battery in the spare-wheel cavity .....	174
A.7.1. Experimental set-up and results .....	174
A.7.2. Numerical model.....	176
A.7.3. Validation of the numerical model .....	177
A.7.4. Validation of the coupling strategy.....	178
A.7.5. Critical use case of summer .....	179
A.8. Sound amplifier in a cavity under the passenger's feet.....	180
A.8.1. Measurements of the thermal resistances and capacitances from the power ICs in the main heat path.....	180
A.8.2. Experimental set-up in the vehicle and results .....	182
A.8.3. Numerical model.....	183
A.8.4. Validation of the numerical model .....	185

---

---

# Nomenclature

## N.1. Latin symbols

$A$	[m <sup>2</sup> ]	Surface area
$c$	[J m <sup>-2</sup> K <sup>-1</sup> ]	Heat capacity per unit surface
$c_k$	[-]	Load factor
$C$	[J m <sup>-3</sup> K <sup>-1</sup> ]	Heat capacity per unit volume
$C$	[J K <sup>-1</sup> ]	Thermal capacitance
$c_p, c_v$	[J kg <sup>-1</sup> K <sup>-1</sup> ]	Specific heat capacity at constant pressure, volume
$D_H$	[m]	Hydraulic diameter
$F$	[N]	Force
$F_{ij}$	[-]	View factor from surface i to surface j
$h$	[W m <sup>-2</sup> K <sup>-1</sup> ]	Heat transfer coefficient
$h_t$	[J kg <sup>-1</sup> ]	Specific static enthalpy
$H$	[m]	Generic length, i.e. height
$H_t$	[J kg <sup>-1</sup> ]	Specific total enthalpy
$I$	[A]	Intensity of the electric current
$I_{ij}$	[kg m <sup>-4</sup> ]	Diagonal tensor, inertial contribution to pressure losses
$k$	[W m <sup>-1</sup> K <sup>-1</sup> ]	Thermal conductivity
$k$	[m <sup>2</sup> s <sup>-2</sup> ]	Turbulence kinetic energy
$K$	[W m <sup>-3</sup> K <sup>-1</sup> ]	Surface thermal conductivity
$L$	[m]	(characteristic) Length
$m$	[kg]	Mass
$\dot{m}$	[kg s <sup>-1</sup> ]	Mass flow rate
$\vec{n}$	[-]	Vector normal to a surface
$P$	[N m <sup>-2</sup> ]	Piezometric pressure
$\dot{q}$	[W m <sup>-2</sup> ]	Heat flux
$\dot{Q}$	[W]	Heat rate

$r$	[K m <sup>2</sup> W <sup>-1</sup> ]	Thermal contact resistance
$r, \theta, x$	[m]	Cylindrical coordinates
$R$	[J kg <sup>-1</sup> ]	Rothalpy
$R$	[K W <sup>-1</sup> ]	Thermal resistance
$\dot{S}$	[W m <sup>-3</sup> ]	Heat rate per unit volume
$s_i$	[N m <sup>-3</sup> ]	Momentum source components
$T$	[K]	Absolute temperature
$t$	[s]	Time
$\delta t$	[s]	Time-step
$u$	[m s <sup>-1</sup> ]	Velocity magnitude
$u_i, u_j$	[m s <sup>-1</sup> ]	Velocity components
$\tilde{u}$	[m s <sup>-1</sup> ]	Relative velocity
$U$	[V]	Voltage
$\dot{V}$	[m <sup>3</sup> s <sup>-1</sup> ]	Volume flow rate
$V_{ij}$	[kg m <sup>-3</sup> s <sup>-1</sup> ]	Diagonal tensor, viscous contribution to pressure losses
$W$	[m]	Generic length, i.e. width
$x_i, x_j$	[m]	Cartesian coordinates
$y$	[m]	Normal distance from the wall to the near-wall cell node
$y^+$	[-]	Dimensionless normal distance from the wall

## N.2. Greek symbols

$\alpha$	[m <sup>2</sup> s <sup>-1</sup> ]	Thermal diffusivity, $\alpha = k / (\rho c_p)$
$\alpha$	[-]	Form drag of a porous membrane
$\beta$	[K <sup>-1</sup> ]	Coefficient of volume expansion at constant pressure
$\beta$	[rad]	Plane angle
$\beta$	[m s <sup>-1</sup> ]	Permeability of a porous membrane
$\gamma$	[-]	Ratio of specific heats, $\gamma = c_p / c_v$
$\delta$	[-]	Kronecker delta
$\varepsilon$	[-]	Emissivity (radiation)
$\varepsilon$	[m <sup>2</sup> s <sup>-3</sup> ]	Turbulence dissipation rate
$\kappa$	[W m <sup>-2</sup> K <sup>-1</sup> ]	Conduction
$\mu$	[kg m <sup>-1</sup> s <sup>-1</sup> ]	Dynamic (molecular) viscosity
$\nu$	[m <sup>2</sup> s <sup>-1</sup> ]	Kinematic viscosity
$\rho$	[kg m <sup>-3</sup> ]	Mass density
$\rho$	[-]	Reflectivity (radiation)

---

$\sigma_{ij}$	[kg m <sup>-1</sup> s <sup>-2</sup> ]	Stress tensor components
$\tau_{ij,Re}$	[kg m <sup>-1</sup> s <sup>-2</sup> ]	Reynolds stress tensor components
$\omega$	[min <sup>-1</sup> ]	Angular velocity
$\omega$	[s <sup>-1</sup> ]	Specific dissipation rate

### N.3. Physical constants

$c = 2.99792 \times 10^8$	[m s <sup>-1</sup> ]	Speed of light in vacuum
$g = 9.81$	[m s <sup>-2</sup> ]	Gravitational acceleration
$R = 2.8705 \times 10^2$	[J kg <sup>-1</sup> K <sup>-1</sup> ]	Specific gas constant of air
$\sigma = 5.67051 \times 10^{-8}$	[W m <sup>-2</sup> K <sup>-4</sup> ]	Stefan-Boltzmann's constant

### N.4. Subscripts and superscripts

<i>a</i>	Accuracy of measurement
<i>abs</i>	Absolute
<i>amb</i>	Ambient
BF	Rotational body force
<i>c</i>	Coupling
CAD	Computer aided design
CAE	Computer aided engineering
CD	Central differencing
CFD	Computational fluid dynamics
CG	Conjugate gradient
CPLD	Complex programmable logic device
DPT	Digital prototype
DSP	Digital signal processor
<i>dyn</i>	Dynamic
<i>env</i>	Environment
<i>f</i>	Fluid
FEM	Finite element method
FNM	Flow network modeling
FR-4	Flame retardant 4
FV	Finite volume
<i>in</i>	Inlet
IR	Infrared
IT	Information technology
JEDEC	Joint electron device engineering councils
<i>m</i>	Momentum

## NOMENCLATURE

---

MARS	Monotone advection and reconstruction scheme
MCM	Multi-chip module
min	Minute
MRF	Multiple reference frames
<i>n</i>	Normal
NEDC	New European drive cycle
NMOS	N-channel MOSFET
<i>n1</i>	Node of the near-wall cell
<i>out</i>	Outlet
PBGA	Plastic ball grid array
PCB	Printed circuit board
PISO	Pressure implicit by splitting of operator
PQFP	Plastic quad flat pack
<i>ref</i>	Reference
RANS	Reynolds average Navier-Stokes
Re	Reynolds
rpm	Revolutions per minute
<i>s</i>	Solid
<i>sc</i>	Scale
SGDH	Simple gradient diffusion hypothesis
SIMPLE	Semi-implicit method for pressure linked equations
SOI	Silicon on isolator
SOR	Successive over-relaxation
<i>stat</i>	Static
<i>t</i>	Turbulent
<i>u</i>	Uncertainty of measurement
0	Reference
$\infty$	Free-stream

---

## Chapter 1

# Industrial motivation

With increasing demand on new electronic technologies in passenger cars, the electronic equipment embedded in the vehicle has boomed over the last two decades. Today, innovative power electronics systems are investigated and under current development for the upcoming fuel cells and hybrid vehicles. Responsible for diverse functional and controlling driving applications, the electronic equipment is consequently a vital element of a passenger car.

Before opening a passenger car, the temperature of the seat can be regulated by the control unit of the auxiliary heating system. By driving, the park assistant control unit and the back drive camera help parking out by signaling the distance with other obstacles. The steering control unit makes the handling easier. The engine control unit regulates its operation; the speed limit control unit regulates the speed of the vehicle according to the vehicle ahead. The headlights and wipers switch on depending on if it is dark or raining outside. The list goes on: most of the functions of a vehicle are regulated by electronic control units. What a potential client is expecting of a Mercedes-Benz passenger car is a high level of security, comfort and styling. Therefore, reliability and performance of the electronic equipment must be ensured wherever it is positioned in the vehicle. To increase the robustness of electronic devices, a new method has been reported in [1] based on a more integrative development process between engineering and testing. At Daimler AG, the reliability of the electronic equipment is evaluated during two development phases: a first one involving numerical simulations and a second testing phase. The role of the simulation in the development process is presented in the following.

### 1.1. Digital development process

During the development process of a passenger car, the integration of the electronic equipment in the vehicle results from the intervention of different departments. The functional group checks that the integration of an electronic component meets the requirements towards packaging, performance, architecture in the whole vehicle, buildability and production. In the department Energy Management of Daimler AG, the energy sources and power systems of the whole vehicle are analyzed regarding consumption and emission reduction for several operating conditions. Moreover, the temperature of critical components of the vehicle is examined within a thermal management process. On that score, the thermal management process contributes to the integration of the electronic equipment in the vehicle towards performance and packaging.

During the last 30 years, the development of a passenger car relied mainly on experiments with physical prototypes, while simulations were only required to support measurements. In order to increase the speed and grade of maturity of the development process of a vehicle, digital methods involving numerical simulations are employed today already in the early stages of the development process [2]. The development process is structured in different phases, which follow a determined process control quality plan, as shown in figure 1.1.

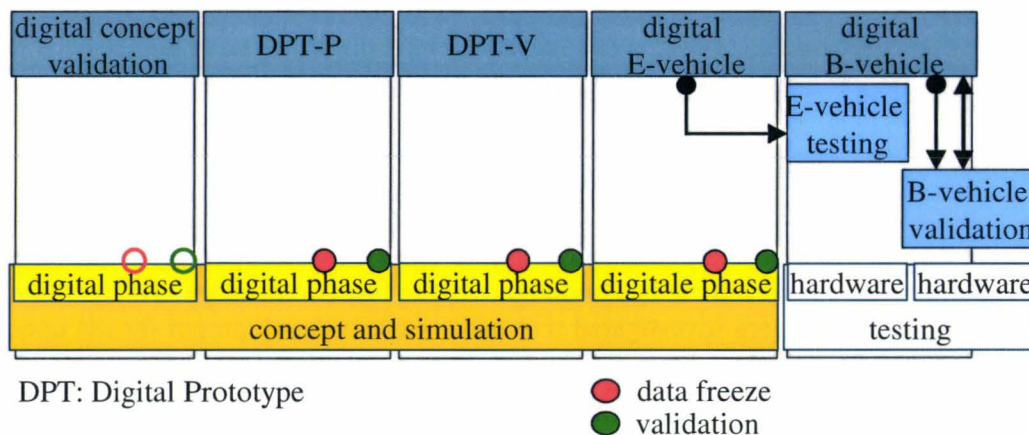


Figure 1.1. Digital prototype phases in the development process.

The development process of a passenger car is composed of a first development phase with digital prototypes (DPT) and a second one with real hardware prototypes. Each function of the vehicle – e.g. crash, pedestrian protection, NVH, stiffness and fatigue strength, ride and handling, underbody dynamic, aerodynamics, energy and thermal management, EMC, refrigerant and cooling cycles – is evaluated successively at each phase of the digital development process yielding to optimization cycles. Therefore, possible development conflicts can be detected in the early stages of the development process. Moreover, a common digital prototype is used by each numerical discipline, increasing the development efficiency. With successive evaluations of the vehicle functions, the digital prototype can reach a high degree of maturity before the first hardware prototype is developed. The DPT process begins with a first concept phase, during which new concepts are analyzed numerically based on the previous vehicle class. Together with the project manager, the simulation can help to define the advantages and drawbacks of a new concept. In the second stage DPT-P, the concepts decided at the previous phase are evaluated in the new digital target prototype. First recommendations for optimization are made during this stage. In the third phase DPT-V, the digital prototype is evaluated considering the serial production maturity and provides a first description of the specifications. Each function of the digital prototype is numerically inspected a last time before the development of the first hardware prototype. If necessary, final corrections of the interior and exterior can be done before the fabrication of the assembly tools. With the following digital E-vehicle phase, the testing departments are now carrying the responsibility in the development process and the simulation intervene for layouts of a vehicle or specific problems. Within this stage, the hardware vehicles are extensively tested and finishing can be provided if necessary. Finally, each property of the definitive hardware prototype is examined a last time; then, the prototype is released for serial production.

## 1.2. Electronic equipment in a passenger car, heat transfer mechanisms

For multiple reasons such as the architecture of electronics, cabin styling and assembly facilities for serial production, the electronic equipment is often located in small enclosures of the vehicle (figure 1.2). There, the electronic device tends to warm up over the time until its temperature operating range, which can lead to a drop in its performance, reliability or life expectancy. Depending on the position of the electronic device in the vehicle, its temperature can be affected by convection, conduction and radiation.

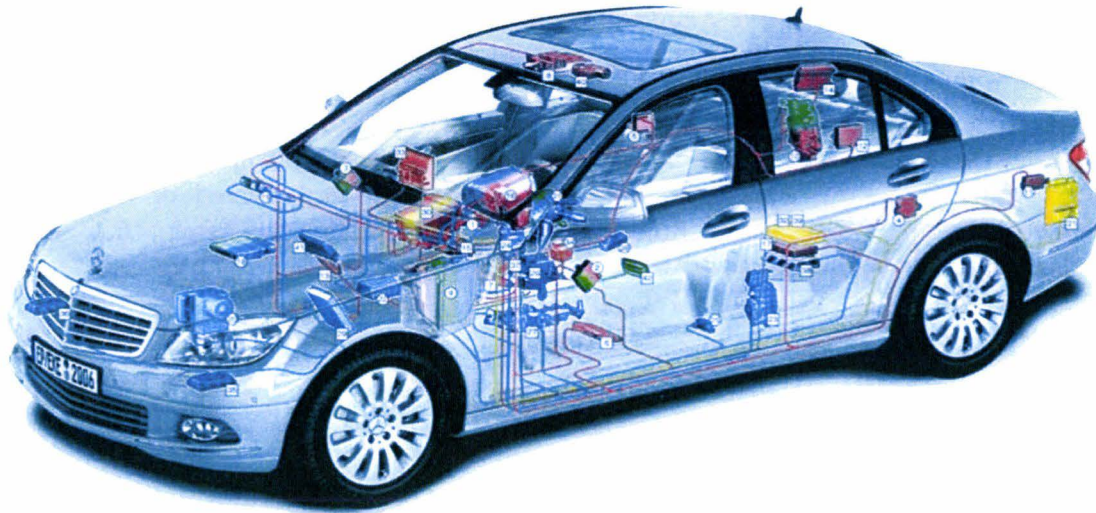


Figure 1.2. Packaging of the electronic equipment in the current Mercedes-Benz C-Class.

### 1.2.1. Heat sources

Two main heat sources in a passenger car are to consider affecting the electronics temperature:

- The underhood by driving, which may affect the temperature of the whole body shell by conduction;
- Local heat sources generated by the operation of electronic devices.

### 1.2.2. Heat transport by convection

To cool some electronic devices like the sound amplifier or the TV-tuner, an internal axial fan switches on at a fixed ambient temperature. In such cases, heat transport may rely on a forced convective flow induced by a pressure gradient. Some enclosures like under the trunk are completely sealed, so that without electronics fan running the heat transport results from the slight differences of air density conjugated with buoyancy forces, i.e. pure natural convection. Because of the complex inner geometry of the vehicle, some enclosures are connected to each other or to the cabin by small openings or leakages. For particular operating conditions, these leakages may let stream a certain air flow rate inside and outside the vehicle. For example, in the aggregate compartment containing the battery next to the engine compartment, leakages can be found at the contact between the engine hood and both fenders and under the battery

for the evacuation of rain water. By driving the vehicle, a complex pressure distribution appears under the engine hood creating a significant flow rate through the leakage. Moreover, leakages are found in the rear-end compartments to the trunk and to the outside through the underbody of the rear bumper. Experiments by idle of the vehicle were carried out in a climatic chamber to determine the effect of the setting of the sliding roofs and air conditioning on the flow rate in the rear-end compartments. With roof and windows closed and air conditioning activated with maximum mass flow rate, overpressure in the cabin creates a slight air flow in the rear end compartment outgoing in the underbody with a volume flow rate of  $3 \times 10^{-4}$  m<sup>3</sup>/s. With a leakage in the cabin, i.e. roof slightly opened, the rear end compartment is streamed with a volume flow rate of  $1.2 \times 10^{-4}$  m<sup>3</sup>/s if the air conditioning delivers a maximum flow rate sufficient to provide an overpressure in the cabin.

In such complex systems, both convective sources, the buoyancy-driven flow and the pressure gradient of the mean flow, have to be considered. The resulting heat transport may result from a mixed convective flow. For each kind of convection (natural, forced or mixed), the convective heat flux from solid to fluid can be defined as follows, whereby  $h$  is highly dependent on the flow conditions:

$$\dot{q}_{convection} = h(T_s - T_{ref}) \quad (1.1)$$

### 1.2.3. Heat transport by conduction

Most of the electronic equipment is mounted on steel or aluminum plates, which are tightly screwed on the body shell (figure 1.3). Both are highly conducting materials, which can easily transport the heat from distant sources.



Figure 1.3. Packaging of the electronics in the right rear-end of the Mercedes-Benz E-Class.

Moreover, the electronic components of systems like the sound amplifier and the TV-tuner are mounted on multi-layers printed wiring boards (PWBs) of isolator substrates FR4 and copper tracks, which permit conduction. In an electronic component, heat is generated at the junction, where conduction lies in the sub-micron regime. For other macroscopic regime conduction, the Fourier law can be used to describe the conductive heat transfer:

$$\vec{q}_{conduction} = -k \overrightarrow{grad}(T_s) \quad (1.2)$$

### 1.2.4. Heat transport by radiation

Between different surfaces of a passenger car, the transmitted radiation can be indirect. Therefore, the heat transfer is based on surface exchange between the electronic components and the case of the electronic device, also between the case and the body shell or other compartment surfaces. For each surface, the incident, absorbed, emitted and reflected heat fluxes must be taken into account in the balance. With  $F_{ji}$  the view factor from the surface  $j$  to  $i$ , the fraction of the heat flux emitted by all surfaces  $j$  incident on surface  $i$  is given by:

$$\dot{q}_{ji} = \sum_j \dot{q}_j F_{ji} = \sum_j (\varepsilon_j \sigma T_j^4 + \rho_j \dot{q}_{ij}) F_{ji} \quad (1.3)$$

The net radiant heat flux at the surface  $i$  (absorbed heat rate) can be written as the difference between the incoming (incident) and leaving (reflecting and emitting) heat fluxes:

$$\dot{q}_{radiation} = \dot{q}_{ji} - \rho_i \dot{q}_{ji} - \varepsilon_i \sigma T_i^4 \quad (1.4)$$

Using equation 1.5 for grey and opaque surfaces with  $\varepsilon$  and  $\rho$  respectively the surface emissivity and reflectivity, the net radiant heat flux is finally provided by:

$$\varepsilon_i + \rho_i = 1 \quad (1.5)$$

$$\dot{q}_{radiation} = \varepsilon_i \dot{q}_{ji} - \varepsilon_i \sigma T_i^4 \quad (1.6)$$

Accordingly, heat transport by radiation may be considered in case of high temperature on surfaces of relatively high areas. Typical examples of radiation surfaces in a passenger car are the exhaust gas system and the engine compartment. Moreover, solar radiation on the car body may affect significantly the temperature of the electronic equipment for particular cases, as the aggregate and rear-end compartments.

### 1.3. Use cases for the electronics temperature

Use cases are defined to evaluate the electronics performance during both digital and hardware phases of the development process. Based on the specifications, it is checked that the electronic equipment runs within its optimal temperature range during a certain operating time. Depending on the location of the electronic device in the vehicle, its temperature may be more or less affected by one or another heat transfer mode (convection, conduction and radiation) and different operating conditions may have an effect on its temperature. Use cases are consequently defined by the following operating conditions:

- Driving mode and setting of air conditioner, windows and sliding roof;
- Operating mode of the electronic equipment and electrical load situation;
- Climatic conditions (weather, environment temperature).

Most of the electronic equipment embedded in a passenger car is damageable at high operating temperature range. But, in case of a common lead-acid battery, its efficiency at lower operating temperature range must also be verified. Consequently, two use cases with

critical climatic conditions are chosen to test the devices in their high or low critical range. The running mode of the electronic equipment is defined by standards in case of most electronic components. Moreover, use cases must be representative of a “mean” driver and correspond to realistic driving conditions.

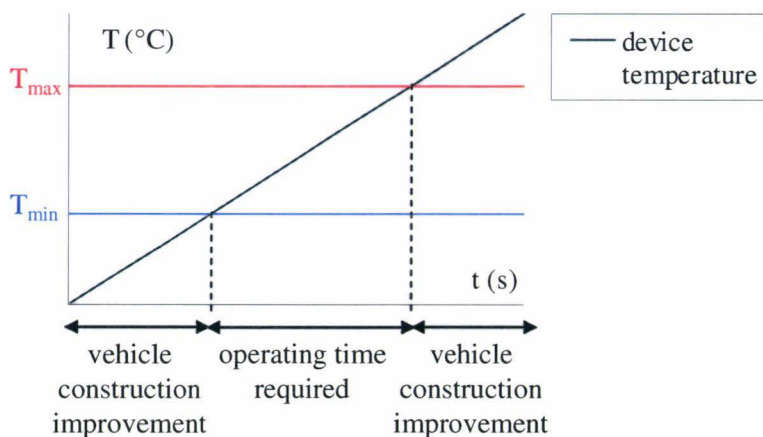


Figure 1.4. Use cases of winter and summer used for the thermal management of electronics; the dependence of the device’s temperature with time is arbitrarily constant.

One use case, typically a case of winter, states an extreme low environment temperature to test the warm-up of the battery at low temperature range. Moreover, due to the extreme warm-up of the running air conditioner at low environment temperatures, the electronic equipment in the cockpit is also tested with the use case of winter. With this use case, the time necessary for the electronic equipment to reach its lower operating temperature range can be determined, as shown in figure 1.4. Correspondingly, the arrangement of the device can be revised to reduce this time period and improve the efficiency of the electronic device at low temperatures. The second use case, a case of summer, is used to check most of the electronic devices at high temperature range. Of particular interest in the development process is the time period of operation until overheating (figure 1.4). If this time period is shorter than the required operating time stipulated by the specifications, additional packaging or another construction of the device in the vehicle must be decided to increase the operating time.

Usual use cases define a period of pre-conditioning of several hours followed by a period of uphill driving with load trailers and finally by idle with engine running. The driving and idle period are highly affecting the solid temperatures of the vehicle with time. Due to their high heat load capacity, the engine compartment and the body shell of the passenger car need a very long time before their temperatures reach a constant value. Therefore, the solid temperatures of the vehicle are transient during the operating time settled by the use case. Moreover, the convective heat transfer is also varying with time, due to the transient solid temperatures and the possible activation of fans. It is consequently important to consider the evolution of the temperature of the electronics under transient operating conditions. More details can be found in [3].

#### 1.4. Target electronic devices in the development process

Among the electronic equipment of the whole vehicle, only target electronic devices are examined in the development process, characterized by:

- a relatively high minimum temperature (case of winter)
- or a relatively low maximum temperature (case of summer);

And:

- a significant heat flux;
- a critical location in the vehicle.

One target electronic device is the battery. Most of the passenger cars have a single battery, situated in the aggregate compartment, to supply electric current to the generator and to the whole electrical system of the vehicle. In this compartment, a slight air flow can circulate near the battery depending on the pressure distribution under the engine hood. In some vehicles, an additional battery positioned in the spare wheel cavity is used for the electronic system, while the battery in the aggregate compartment fulfills the starter functions. Heat is generated by the battery charge and discharge, for example at the start of the engine. Due to the proximity of the engine compartment and exhaust gas system, both enclosures for the battery may be critical, in particular for use cases with uphill and thermal soak, conditioning high temperatures of the engine and exhaust gas system.

A group of target electronics is situated in the cockpit or close to (dashboard, glove box, compartment under the passenger feet). The dashboard is composed of telematics devices such as the head-unit, the tuner audio and the monitor. Other usual devices are also situated in the blackboard, as the instrument panel and the parktronic. Due to the limited possibilities of packaging in this compartment, the electronics is encapsulated with only tiny air slits around, restricting the convective heat transport. In some passenger cars, the sound amplifier is positioned in the compartment under the passenger feet. Most of these devices are characterized by a significant heat production and therefore assembled with an axial fan, as the head-unit and sound amplifier. Moreover, several heat sources are affecting these electronics enclosures: the engine compartment, the transmission system, the underbody and the air conditioning.

The last group of target devices is positioned in the rear of the vehicle, usually the rear-end compartments in the C- or D-pillars and the rear passenger compartment under the seats. High power telematics like the TV-tuner and the sound amplifier are situated in these compartments. The back drive camera and the central relay control unit are also to consider as target devices because of their packaging with the high power devices and their operating range in lower temperatures. These compartments have outlets with the underbody of the car and the cabin, so that depending on the pressure distribution in the cabin, these devices can be cooled by a slight volume flow rate from the cabin. Nevertheless, the rear-end compartments can be affected by the solar radiation on the body of the vehicle and the rear passenger compartment by radiation from the exhaust gas system.

## 1.5. Thermal management of electronics in the digital development process

In order to ensure the good performance of the electronic equipment in a passenger car, its temperature is successively evaluated during each phase of the digital development process. During the first DPT phase, a new electronics generation or a new packaging situation may be computed based on the geometrical data of the previous vehicle class. It is proposed that the environment conditions on the electronics temperature are predicted with simulations and compared with the performance specifications of the electronic device from the supplier. In the second stage DPT-P, only coarse geometrical data of the digital prototype are provided in the common data base, so that the electronics temperature may be computed with a simplified model taking into account heat sources around. To ensure the reliability of the critical components, re-packaging, isolation or innovative ways of cooling are decided considering the distribution of heat sources in the whole vehicle. In the third phase DPT-V, the thermal management of the electronic equipment may be investigated in a detailed model of the full target vehicle and confronted with other functions of the vehicle. With the following digital E-vehicle phase, the numerical results obtained previously can be compared with the experimental results from the hardware prototype. Numerical methods in place to predict the electronic temperature are based on *steady-state* conjugate heat transfer computations of simplified models of electronic enclosure. In these models, the electronic device is represented by its skin surface, while the inner geometry of the device is not taken into account. In case of the operation of an internal fan, an iterative method based on the energy conservation is used to model the volume flow rate created by the fan. This method is applicable to closed enclosures and its accuracy relies highly on the estimation of the convective heat transfer, which is provided as boundary condition.

Depending on the environment of an electronic device in the passenger car and the use case for testing, the electronics temperature may be less or more affected by different heat transfer mechanisms, determining the boundary conditions of the computation. Due to the driving and idle periods settled by use cases, the temperature of electronics must be computed in transient conditions. Therefore, transient boundary conditions defining the enclosure temperature, potential air temperatures and the heat sources must be supplied for the computation. In the early stages of the DPT process, without any hardware prototype, the transient boundary conditions necessary can only be provided by other numerical results with similar use cases. To compute the transient temperature of the target electronic equipment in a passenger car, numerical strategies must be investigated in consideration of:

- the deadlines of the DPT development process;
- the supplied geometric data;
- the complex environment in the passenger car;
- the boundary conditions available.

After the industrial requirements are settled, numerical methods for the thermal management of electronic systems can be explored in the literature.

---

## Chapter 2

# State of literature

With the important development of microelectronics during the last two decades, the thermal management of electronic systems is of practical concern in several industrial sectors. For a better circuit integration in handling systems, new technologies have been developed to reduce the size of semiconductor chips, which are as small as some nanometers today with the current silicon-on-insulator (SOI) transistor. With this miniaturization, circuit densities are always increasing and the heat flux on a usual PWB reaches such a level critical for the junction of the electronic components. Suppliers of usual semiconductors in control units define an ambient operating temperature range under normal power range typically lying between  $-40^{\circ}\text{C}$  and  $85^{\circ}\text{C}$  [4, 5]. They also recommend absolute maximum stress ratings with a maximal temperature in the range  $125^{\circ}\text{C}$ - $150^{\circ}\text{C}$ , beyond which permanent damage may be caused to the device [6, 7]. Moreover, a stannous-lead or lead-free soldering is also sensitive over a long time to temperatures of about  $150^{\circ}\text{C}$  [8]. Furthermore, the performance of an electronic system can be reduced by 50 % if one component is operating permanently  $10^{\circ}\text{C}$  below its upper limit [9]. Temperature loads for electronic control units in passenger cars are usually higher than  $125^{\circ}\text{C}$  due to the rising ambient temperatures and the compact architecture with high integration densities. In 2006, the research department hardware technology electronics of Daimler AG investigated high temperature electronics operating in the temperature range  $130$ - $190^{\circ}\text{C}$  under endurance operating conditions [10]. A field load of electronic control units, so-called mission profile, showed three operating temperature ranges corresponding to shutdown conditions, normal operation and high-load operation of electronic control units (figure 2.1). To ensure the high-load operation of electronics, the damage mechanisms were analyzed for a prognostic of the life expectancy of the electronic equipment in the vehicle.

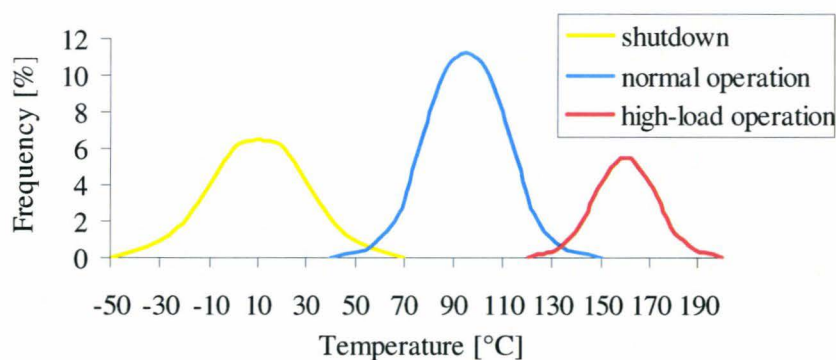


Figure 2.1. Temperature distribution field load [10].

## **2.1. Numerical methods for the thermal management of a passenger car**

As discussed previously, the temperature of an electronic system embedded in a passenger car may be highly dependent on its environment in the vehicle. Therefore, the computational methods for the prediction of the solid temperature in the whole vehicle must be regarded for the thermal management of the electronic equipment in the development process. Several CAE (computer aided engineering) applications of the vehicle interact with each other in many ways [11], like the underhood flow analysis, the brake cooling design, the passenger compartment flow.

### **2.1.1. Development of coupling simulation methods**

One of the first steps in the vehicle thermal management has been done in 1995 with a 3D thermal analysis of the engine compartment, considering heat rejection of the radiator and condenser computed previously with a 1D model [12]. Moreover, the underhood temperature has been of practical concern because of its high temperature range. Steady-state computations were performed with a CFD code to design heat shield for tunnel insulation, solving the conjugate convection, conduction and radiation heat transfer modes for constant driving operation [13]. In 2003, Schuster [14] examined the conjugate heat transfer problem for idle cool down operating conditions after uphill drive with load trailers. A coarse model of the full vehicle is first computed in steady-state; then, the underbody is computed in transient conditions on the basis of experimental data. To represent the interaction between the cooling system, the engine compartment and the underbody with more accuracy and to reduce biased experimental boundary conditions, coupled simulations have been performed. Skea [15] described a thermal analysis of the underhood, based on the exchange of simulation results of a 1D engine compartment model, a 1D cooling system model and 3D conjugate heat transfer model of the underbody. In [16], a simulation strategy is proposed to compute the underhood for long term operating conditions. In a first phase, the conjugate heat transfer modes, including surface-to-surface radiation, are computed with the commercial package CFD-ACE+ [17]. Then, part models of the whole surface mesh and convection boundary conditions are imported from the first phase into the thermal analysis software RadTherm [18] for local optimization of heat shields. In a similar way, Bendell [19] described in 2005 a coupling strategy between the CFD code STAR-CD [20] and the software RadTherm for the computation of the steady-state underhood temperature for trailer towing test operation. The comparison between numerical prediction resulting from the coupled computations and measurements show discrepancies up to 45% in the tunnel heat shield. Some other vehicle cooling applications were also computed with CAE, as the brake discs for heating up followed by a cool down phase operation [21]. Full-detailed steady-state computations were carried out with the CFD code FLUENT [22] for the maximum speed of the vehicle test, to analyze the complex 3D flow over the brake disc and determine the convective heat transfer. Then, a transient thermal analysis is performed with RadTherm using the output of convective heat transfer coefficients, providing a good agreement with measurements. Jones [23] presented in 2007 numerical and experimental methods for the thermal management of a compact electric vehicle. The battery pack temperature and heat rejection were computed under transient conditions, while the cabin temperature was predicted with RadTherm under load thermal soak conditions. In order to estimate the potential of the battery to warm up the cabin, 1D computations were performed for a wide range of scenarios.

### 2.1.2. Numerical methods used in the DPT process at Daimler AG

In order to predict with accuracy the three modes of heat transfer in the case of complex geometrical models of the full outward vehicle within a limited simulation time, coupled simulations were progressively introduced in the development process. In 2003, Reister [24] described a numerical method to compute separately the different heat transfer modes, by exporting the convective data computed with STAR-CD to surface mesh for the thermal analysis with RadTherm and inversely. An iterative coupling between the two codes is provided using the mesh mapping interface MpCCI [25]. First, the flow through the engine compartment and in the underhood is computed in steady-state for uphill drive. The convective data are then exported to RadTherm for the thermal analysis. A similar coupling simulation method based on the CFD code STAR-CD, the FEM (finite element method) code PERMAS [26] and the radiation tool POSRAD [20] has been presented in 2004 for the simulation of a full vehicle [27]. The flow through the engine compartment and the fuselage flow are computed in steady-state for slow uphill with load trailers driving conditions. The resulting convective heat transfer is mapped on the full vehicle model for the coupled steady-state simulation between PERMAS and POSRAD, providing a temperature prediction of the integral and longitudinal bearers within 10% in comparison with measurements. The temperature of the underbody has been computed in steady-state for idle without fan operating conditions using the same numerical strategy [28]. In 2007, Weidmann [29] presented a coupled numerical procedure to compute thermal soak. Firstly, the buoyancy-driven flow of the underhood is computed in steady-state with STAR-CD using the standard  $k-\epsilon$  turbulence model with wall function. The results are coupled with steady-state thermal analysis computations performed by the solid solver PERMAS and POSRAD or RadTherm. Secondly, the resulting convective heat flux data are transferred in the solid solver for transient analysis, used as fixed boundary condition. Due to slight differences between the different meshes, data was exchanged manually after converged runs to correct local errors. The transient temperatures of the integral bearer are found within 6K offset with measurements. The coupling numerical approach using PERMAS, POSRAD and STAR-CD is already implemented in the thermal management process of the underhood for *steady-state* predictions as for uphill driving conditions, while transient coupling simulations for thermal soak are currently under further investigation.

## 2.2. Heat transfer mechanisms in elementary electronic systems

In [30], different strategies have been presented to control and remove the heat generated in electronic systems: with natural convection, with a forced convective flow, with boiling and immersion cooling, with heat pipes, finally with thermal contact resistance or more generally conduction at chip and board levels. In 1964, Metais [31] classified the natural and forced convection regimes in vertical and horizontal tubes, depending on the Rayleigh and Reynolds numbers of the flow. If the horizontal pressure gradient leading the flow in the tube cannot be neglected as compared to the vertical temperature gradient forming thermo-convective structures, the combined effect of both must be considered and the flow regime is called mixed convection. Cooling processes that can be found in the passenger cars of today are based on natural, mixed and forced convection, also on conduction. Therefore, numerical strategies are presented in the following to compute the electronic temperature in these cases. Most of the publications dealing with the thermal management of electronic systems are restricted to the thermal analysis of academic cases. Some of the numerous investigations on

this topic are reviewed in a first part. Few publications are considering a complex electronic system in the whole. These literature sources are presented in a second part.

### 2.2.1. Conduction at junction and case levels

In each IC (integrated circuit), heat is generated in the silicon region of the chip junction [30]. The internal assembly of semiconductors with ball grid array (BGA) or standard packages with pin connectors can be seen in figure 2.2. It involves a chip, which has been bonded to a substrate or to a heat spreader by die attach. The die junction is electrically connected to the substrate with gold wires or to the pins with flying leads. The whole is then encapsulated in mold compound. The IC package is attached to the pin connectors or to the solder balls.

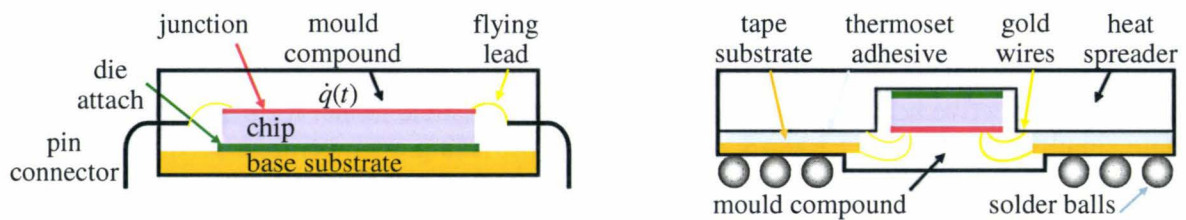


Figure 2.2. Typical package construction of standard semiconductors with pin connectors (left) and ball grid array semiconductors (right).

At the junction scale, which may lie in today's semiconductors between the sub-micron and the nanoscale, heat conduction takes no longer place in a diffusive manner, as the Fourier law states, but the ballistic phonon transport and surface phenomena such as phonon boundary scattering become dominant [32, 33, 34]. In 2008, Lee [35] predicted the peak temperature of the hot spot of a NMOS (n-channel MOSFET) transistor using an electron-phonon interaction model implemented in the Boltzmann transport equations and a transport time-step of 0.2 ns.

At the substrate scale, the contact between two surfaces may occur only at discrete spots, because of imperfect gluing or soldering and impurities at the different surfaces. At the interface, interstices may influence the heat transfer. By applying a contact pressure on the electronic structure, the contact points of the two surfaces may be increased, so as the thermal conductance of the device. To represent the imperfect interface, thermal contact resistances are introduced [36, 37]. With  $\Delta T$  the temperature drop over the interface due to the non-perfect contact and  $\dot{q}$  the normal heat flux from surface 1 to 2 (figure 2.3), the thermal contact resistance  $r$  [ $\text{m}^2 \text{K W}^{-1}$ ] is defined by:

$$r = \frac{T_1 - T_2}{\dot{q}} \quad (2.1)$$

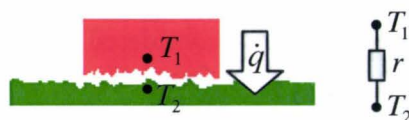


Figure 2.3. Model of an imperfect contact interface using a thermal contact resistance. At the substrate scale, a diffuse heat flux flowing from one material to the other one can be assumed and the Fourier form of the conduction equation is valid. Recently, Vermeersch [38]

calculated numerically the thermal impedance of a silicon layer mounted on an alumina substrate for different values of the thermal contact resistance. Grujicic [39] investigated the role of the thermal contact between a heat source and a heat sink steady-state with a finite element method. The thermal contact resistance is analyzed using the semi-empirical model proposed by Bahrami [40]. The results showed some parameters on the heat transfer from the heat source to the heat sink, such as the surface roughness and the thermal interface material. In 2006, a methodology based on the thermal contact resistance has been presented to compute the chip temperature of a DC-DC converter [41]. A power device pressed screwed on a heat sink with a silicon rubber sheet in between has been investigated as test case. First, the contact pressure profile due to screwing is obtained with an analysis with a FEM code. Then, the thermal contact resistance is estimated depending on the contact pressure. As an application, the power device is assembled in a DC-DC converter with water forced cooling on the lower side. A thermal analysis is carried out in steady-state with the commercial software Icepack [42] applying the contact resistance previously predicted on plate elements corresponding to the upside and downside of the rubber sheet. The chip temperature predicted is found very similar to measurements of the DC-DC converter.

Therefore, considering only the package of the chip as heat source, the problem of the modeling of the ballistic phonon transport can be avoided. The heat path between the silicon junction and the package is unsolved, so that the heat flux boundary condition must be corrected.

### **2.2.2. Natural convection in electronic cavities**

The first numerical investigations for fifty years aimed at determining an optimal electronics cooling with natural convection for the low-power devices. Two-dimensional finite-difference computations were carried out on elementary geometries – a vertical channel – to determine the laminar natural convective heat transfer in air [43, 44, 45]. With the development of CFD codes and computational capabilities, transient simulations were examined in the 1990's. Shyy [46] investigated in 1993 a two-dimensional heated vertical channel in a cold enclosure has been computed for some seconds. The air flow was computed in transient conditions for a Grashof number of  $10^5$  without turbulence model. An oscillating flow was found periodically reversing its direction, due to the shielding effect of a thin layer adjacent to the vertical walls. The previous study has been widened for a larger range of Grashof numbers [47]. The heat transfer at lower Grashof number was found first transient and then reaching a steady-state. The flow obtained at  $Gr = 10^7$  is turbulent, providing an enhancement of the heat transfer.

In order to analyze the class of laminar periodically fully developed natural convective flows encountered in electronics cooling applications (draft cooling), Kelkar [48] investigated a 2D vertical channel with repetitive heated blocks mounted on one of the walls. As the flow in the channel periodically absorbs the heat generated by one block, the air flow temperature increases continuously block by block. In order to compute only one heated block with periodic boundary conditions, a mathematical formulation with a decomposition of the temperature field into a linear and a periodic part had been proposed in this case and implemented into the commercial CFD code FLUENT. Similarly, the natural convective heat transfer of an array of integrated circuits has been examined experimentally and numerically in a 2D channel with protruding heat sources [49]. The system is based on two patterns of heated blocks with periodic boundary conditions. Between the protrusions, recirculation flow patterns are observed, enhancing the heat transfer near the protrusion surfaces. The 2D

numerical model provides a good agreement with the experimental results, except for smaller aspect ratios of the plate where 3D effects cannot be neglected. More recently, Desrayaud [50] carried out a parametric study with a 2D system constituted of parallel vertical channels with a single protruding heat source mounted on a conducting substrate, which showed the significant effect of conduction through the substrate as effective cooling mechanism.

Due to the limit of 2D computations in electronic applications, the classical case of arrays of heat sources is then explored with 3D numerical models. In 1995, 2D and 3D numerical models have been developed for the computation of the laminar natural convection in a vertical cavity with an array of discrete heat sources on one wall [51]. The numerical results were compared with measurements of the heater temperature and visualizations of the fluid flow. A very good agreement was found with the 3D model, while the 2D model over-predicted the heater temperature. Yu [52] investigated the 3D laminar natural convection in a cubical vented enclosure composed of a discrete heat source mounted on a substrate for the simulation of an electronic device. The vent is treated as an opening without grills. Different positions of the vents are examined to provide the largest cooling effect. Moreover, it was found that conduction in the substrate plays an important role on the cooling.

For electronics packaging application, the effect of radiation on the laminar conjugate heat transfer problem has been investigated with finite-volume methods [53, 54, 55]. Sieres [55] analyzed the effect of surface radiation on the convective heat transfer for two different triangular cavities. The 2D results show that the Nusselt number is higher accounting for the interaction between natural convection and radiation than with the sole contribution of convection. Bazylak [54] computed a horizontal cavity with an infinite array of flushed-mounted heat sources to investigate the effect of sinusoidal modulation of heat fluxes. The transient computations were carried out with the CFD code FLUENT. It was found that the Nusselt number decreases when a phase-shift is introduced between alternating heat sources. Ait-taleb [53] studied numerically the interactions between heat transfer modes by convection, conduction and radiation have been studied numerically in 2D horizontal hollow blocks heated from below or above. It was found out that both conductive and radiation heat transfer modes are predominant for the range of considered parameters.

In order to determine the effect of transient heat flux conditions in an electronic enclosure, the laminar natural convective flow in a 2D enclosure containing three discrete heaters has been computed in transient conditions with a finite volume method [56]. A significant effect on the flow and the heater temperature is obtained with a periodic step of the heat flux. In 2005, Oosthuizen [57] studied numerically the development of the 3D air flow in an electronics enclosure partially heated from below. The unsteady momentum and energy flow equations written in terms of vorticity and stream function are solved with an iterative, finite-difference implicit method. The flow is found steady at low Rayleigh numbers, becomes unsteady at intermediate Rayleigh numbers and steady again at higher Rayleigh numbers. For both configurations, the unsteadiness lies in the range of Rayleigh numbers  $10^4$ - $10^6$  and is almost independent of the heater geometry. In [58], the conjugate convection and conduction heat transfer problem has been solved with a finite-volume method in a 2D vertical adiabatic channel with heat sources mounted on a vertical wall. The flow is computed unsteady with the URANS standard k- $\epsilon$  low Reynolds turbulence model. The model has been validated with test cases in comparison with measurements.

### 2.2.3. Forced convection in electronic channels

The forced convection cooling of flush-mounted rectangular sources mounted on a solid substrate has been first investigated in 1985. Conjugate heat transfer computations were performed in a 2D channel partially heated from below and exposed to a fully developed laminar [59] and turbulent [60] inflow conditions. The same electronic configuration with water and coolant has been numerically studied by Xu [61] using a control-volume finite-difference procedure and an eddy-viscosity model with logarithmic wall functions for turbulence closure. The resulting Nusselt numbers were compared with different experimental results, showing discrepancies of about 30% with Incropera [62]. In 1983, Kennedy [63] studied the case of a single heat source, flush-mounted in an adiabatic channel exposed to a forced laminar inflow for different Richardson numbers in the range  $10^{-2}$  -  $10^{-1}$ . The 2D numerical results obtained with the method of false transient were compared with measurements, suggesting that local buoyancy effects may introduce secondary flows, which enhance locally the convective heat transfer.

Laminar forced convection in 2D channel with heated blocks on the lower surface has been investigated for laminar fully developed conditions [64] and for developing flow conditions with conjugate effects of convection and conduction [65]. Schmidt [64] studied the effect of the ratio the channel height with the streamwise length of the protrusion (wall spacing) on the convective heat transfer. It was found out, that the convective heat transfer is enhanced with smaller wall spacing, due to acceleration of the flow at the top of the protrusion. Similar results were found later experimentally [66, 67, 68], revealing the presence of flow separation and strong recirculation zones both upstream and downstream of the protrusion. Moreover, the measurements could also extend the comprehension of the heat transport, which is dominated by two competing phenomena: increased flow velocities due to the contraction of the channel at the protrusion and the three dimensional effects as the flow is forced around the width of the protrusion.

As the heat transport in forced convection cooling electronic systems may be associated to the developing structure of the flow, suitable turbulence models were investigated to capture the flow around a package. About that, different authors [69, 70] recently compared different usual algebraic and RANS eddy-viscosity turbulence models such as LVEL, Wolfshtein, high-Re  $k$ - $\epsilon$ , Wilcox  $k$ - $\omega$ , SST  $k$ - $\omega$ . In [69], the models were implemented in the finite volume code PHYSICA for the computation of the fluid flow around a cube in a channel in comparison with the results of [71]. The velocity profile around the cube and the cube surface temperature were analyzed, demonstrating the poor prediction of the standard  $k$ - $\epsilon$  high Reynolds model, while the two-layer model best fits the experimental data.

### 2.2.4. Mixed convection in electronic channels

In 1990, the group of Incropera [72] performed a detailed analysis of mixed convection heat transfer over a large range of Rayleigh and Reynolds numbers covering the different heat transfer regimes, from natural convection to laminar forced convection and the initiation of transition to turbulence. The flow in a 3D horizontal channel with four rows, in-line array of 12 flush-mounted heat sources on the lower wall has been solved steady-state based on the parabolic calculation method proposed by Patankar and Spalding [73]. The numerical and experimental results were in very good agreement over the whole range of Rayleigh and Reynolds numbers. In order to characterize the strength of the buoyancy-induced secondary

flow for each heater row, scaling parameters are introduced based on the Nusselt, Rayleigh and Peclet numbers. At low Reynolds number, the heat transfer is enhanced due to the buoyancy-induced flow except for the first row. With Reynolds number increasing, a minimum of the Nusselt number is reached, for which the forced convective effects are balanced with the buoyancy-driven flow. With a further increase of the Reynolds number, the Nusselt number increases due to the transport by the mean flow.

To determine an appropriate electronics package inclination for an efficient cooling, the mixed convective flow in an inclined parallel plate channel with a single discrete flush-mounted heat source has been computed steady-state [74, 75] and transient [76]. The onset of instability due to the secondary flow was found delayed for increasing Reynolds number and increasing inclination angle from the horizontal position. In [77], the conjugate heat transfer modes were computed in an air-cooled enclosure with discrete heat sources embedded on a vertical board at the bottom. Steady-state computations were performed using the cubic-spline collocation method, revealing significant parameters of the mean heat transfer coefficient: the position of the heat sources and the board conductivity. Similar investigations were carried out by Leung [78] to determine an efficient cooling of printed circuit board assemblies. Measurements and corresponding numerical simulations were carried out in a horizontal or vertical rectangular duct assembled with a 2D array of heated ribs in fully-developed laminar flow convection. It showed that the heat transfer coefficient at the rib is enhanced with a higher Reynolds number, due to the vortex forming in the cavity between two ribs and becoming more energetic. Moreover, buoyancy-driven flow effects are more significant for a higher ratio of the channel height with the rib height, perturbing the main flow and enhancing the overall heat transfer. In 1985, Braaten [79] computed in steady-state shrouded arrays of rectangular blocks with the finite-volume method described by Patankar in [80]. Due to secondary flow, the enhancement in heat transfer is accompanied by a small increase of the axial pressure drop. Single- and multiple-eddy patterns are found at respectively low and higher Rayleigh numbers. The study has been extended by Madhusudhana Rao [81] considering conjugate convection and conduction heat transfer modes in vertical arrays of protruding heated ribs mounted on substrate plates. The thermal coupling between the solid and fluid regions is solved by the harmonic thermal conductivity method. For the parameters considered, the heat transferred to the fluid via substrate conduction is found to account for 40-50% of the total heat removed from the ribs.

The characteristics of mixed convective internal flows under transient conditions for electronic applications have received little attention. In 1999, Tsay [82] analyzed the conjugate effects of convection and conduction with finite difference method in a 2D vertical channel with one wall suddenly subjected to discrete heat sources. The results showed that discrete heating can cause a heat transfer direction conversely from fluid to the heated wall during the transient period. In order to investigate the flow structure induced by buoyancy effects, Hasnaoui [83] examined a 2D channel periodically flushed heated from below. It was found out that below a critical Reynolds number, the buoyancy-induced eddy patterns remain attached to the heated elements. Above the critical Reynolds number, the flow is periodic and the cells are carried downstream. In order to determine the heat transfer during cross-flow mixed convection in electronic circuit boards, the transient response of four protruding heat sources mounted on a vertical conducting board has been computed with conjugate heat transfer [84]. The heat transfer from both sides of the board was found to be significant during the transient period. About 75% heat dissipation occurred at the heated side, while 25% were conducted through the substrate.

## **2.3. Thermal management of electronic systems**

The studies of complex electronic systems are mainly carried out regarding the heat flux at one level of the electronic system: the chip junction, the chip package, the board or the electronic device. Some studies combine both of them. The computations of the conjugate heat transfer and additionally taking into account radiation are presented in the following.

### **2.3.1. Conjugate convective and conductive heat transfer modes**

In 1989, a general formulation of the flow-solid conjugate heat transfer problem has been proposed in the finite-element model ADINA-F [85]. The equations are transformed using the Galerkin procedure and discretized by finite-element interpolations. In transient analysis, the automatic time-stepping (ATS) method can be used with Newton-Raphson iterations for more efficiency in case of strong nonlinearities. An application to the conjugate heat transfer conduction-convection in cooling of electronic equipment was presented. Madhavan [86] performed a 2D parametric study to determine the effect of the Prandtl and Rayleigh numbers on the laminar natural convective heat transfer in a typical electronics enclosure composed of three heat sources mounted on a cooled substrate. The conjugated convection and conduction heat transfer modes are computed with the commercial CFD code FLUENT. An optimal coolant with a low viscosity has been found for this configuration.

In 1999, Teertstra [87] proposed an analytical model that predicts the average heat transfer rate for forced convection cooling a plate fin heat sink. Considering that the distance between two fins is negligible compared with the fin height, the model is reduced to the 2D conjugate forced convection and conduction problem between isothermal parallel plates. The two limiting cases of this problem, fully developed flow and developing flow, are used as asymptotic solutions. The resulting Nusselt numbers were compared with measurements providing a good agreement. In a similar way, the spacing between heat generating boards in a stack cooled by laminar forced convection has been studied analytically for an optimal cooling [88]. Three cases are examined: fixed pressure drop, fixed mass flow rate and a fixed pumping power. In order to predict the forced convection cooling of a complex data center, where the server racks are installed on a raised floor constituted of perforated tiles, different parameters on the air flow distribution in the data center have been examined in [89], including in the under- and upper-floor plenum. In [90], Agonafer studied the steady-state forced convection in an electronics channel using the software Flotherm [91] to design an active heat sink to cool integrated circuit electronics in high power logic processors. Several ways to optimize the recirculation of the cooled air flow over electronics as a duct, a hub or a shroud have been investigated.

### **2.3.2. Convective, conductive and radiation heat transfer modes**

In order to predict the thermal limits of an electronic package, the thermal parameters of a flip chip on a PCB board in case of natural convection have been investigated to model the coupled heat transfer modes in the PCB [92]. A heat source is assigned on the surface of the junction of the chip. The thermal resistance of the junction to ambient has been compared with experimental data, showing a good agreement. Thermal paths were analyzed considering the thermal resistances junction-to-ambient, junction-to-board and board-to-ambient. For thermal design, the heat flux is examined at two different levels (component and package) and combined with a balance. For thermal design at board-level, the heat transfer characteristics of

a plastic ball grid array package (PBGA) on a PCB in natural convection have been studied in steady-state [93]. Heat conduction in the PBGA assembly was computed with a full detailed 3D finite element model. Correlations were used for the prediction of the two other modes of heat transfer (radiation and convection). The accuracy of the direct FEM computational approach is evaluated with two measurement techniques – infrared thermography and the measurement of the junction temperature – showing a good agreement.

For the design of electronic enclosures, an analytical model has been proposed for natural convection from a circuit board in a sealed enclosure [94]. The model is based on the combination of three asymptotic terms corresponding to the different modes of heat transfer in the fluid region: pure conduction, the laminar boundary layer flow and the transition flow at low Rayleigh number. The analytical Nusselt numbers were compared with numerical results from Flotherm and Icepack, showing some discrepancies for particular package configurations. In 1995, the software Icepack has been validated for steady-state predictions of the temperature and air flow in a three-chip multi-chip module (MCM) cooled by natural convection [95]. Lee [96] computed the natural convective flow in sealed portable handheld electronics products has been computed in steady-state with Flotherm. A conjugate heat transfer computation was performed, taking into account the component power dissipation. In a first case, the temperature of a typical portable product was computed at the system level. Due to the low surface emissivities and absorptivities of the enclosure, radiation was not considered in this study. The maximal temperature in the electronics enclosure was found in good agreement with experimental results. In a second case, a MCM package composed of two dies was investigated at the component level. One or both dies were powered and heat generation was considered as boundary condition. Considering internal and external radiation heat transfer, the computation could predict the dies temperature with a good agreement with the measurements.

For efficient thermal analyses of complex electronic systems in the design process, the solver I-DEAS Electronic System Cooling [97] has been developed using semi-analytical techniques to model the three modes of heat transfer based on the creation of conductance thermal couplings [98]. The solver proposed has been tested with different usual systems cooled by forced convection, providing analysis results within 15% of measured values. Very complex electronic systems have been analyzed in [99, 100]. Kowalski [99] examined a high speed internet subscriber consisting of two axial fans and 13 PCBs with numerous heat generating components. A coupling method between a CFD code and a FNM (flow network modeling) code has been described to predict the flow distribution for further temperature computations. The CFD analysis is used for an accurate characterization of the flow behavior between two PCBs, providing the variation of the pressure loss with the flow rate in the passage. The flow network analysis considers the interaction of the various flow impedances to determine the flow rate and inlet temperature for each passage and provides the boundary conditions for the CFD computations. With this coupled methodology, the predicted flow rates through individual cards passage were found within 10% of the measured values. Zhao [100] investigated a broadband network communication box with two stacked identical partitioned modules with Icepak for the steady-state computation of the three coupled heat transfer modes. A PCB with a surface mounted array of 16 power dissipating TBGA (tape ball grid array) and 4 PBGA (plastic ball grid array) is located in each module. To cool down the package, pin-fin heat sinks are attached to the heating components and two exhaust fans are mounted at the flow exit. The simulation results in the electronic module were found in good agreement with the estimations based on the thermal resistance values obtained from

measurements in a wind tunnel. In order to find a suitable turbulence modeling for complex systems cooled by forced convection [70], several turbulence models have been implemented in Flotherm and Icepack. In comparison with a benchmark case consisting of a PCB incorporating four package types, the component junction temperatures were well predicted with the Spalart-Allmaras, the two-layer and the SST  $k-\omega$  models within  $\pm 6^{\circ}\text{C}$ , while the use of wall functions with the standard  $k-\epsilon$  high Reynolds model provided more than  $\pm 10^{\circ}\text{C}$  of the measurement.

Very few thermal analyses of complex electronic systems were carried out transient. In 2004, Eveloy [101] performed a transient analysis of a PQFP (plastic quad flat pack) mounted on a PCB in still-air and forced convection. Different types of transient operating conditions are examined, considering passive or dynamic component power dissipation and ambient conditions. The numerical analysis was undertaken using Flotherm with a detailed modeling at the component level for the computation of the conductive heat transfer. The standard  $k-\epsilon$  high Reynolds model has been used for forced convective flows and the grids were constructed for time-steps ranging from  $3\text{ ms}$  to  $5\text{ s}$ . The temperature of the electronic system was computed for a total time of  $800\text{ s}$  operating conditions. In comparison to measurements, the component junction temperature was found in good agreement for the different operating conditions. Discrepancies were found in the PCB temperature for dynamic ambient conditions representative of those in a standard convective reflow soldering process.

Due to its apparent robustness, the code Flotherm has been tested in this work for the computation of the temperature of a common lead-acid battery cooled by natural convection in a rectangular enclosure, as the spare wheel cavity of a passenger car. A steady-state analysis provided reasonable results in a relatively short time, while the transient analysis was highly time-consuming to compute 10 min of battery operation and could not be run for two hours operating conditions. On one side, several attractive numerical capabilities were pointed out: fast model building based on a library of elementary electronic geometries, automatic generation of a Cartesian structured grid, steady-state and transient conjugate heat transfer computations. On the other side, the modeling of each heat transfer mode is very restrictive offering few options. Moreover, setting boundary conditions is limited to uniform solid temperature distributions. Furthermore, complex geometries such as a usual vehicle electronic enclosure are difficult to import and solve in Flotherm, while a boundary mesh mapping is not available. For these reasons, the implementation of Flotherm or similar codes in the development process is highly restricted.

## **2.4. Partial conclusions**

For the thermal management of a full passenger car, numerical methods have been developed to predict the temperature of the engine compartment and underbody. Two main numerical problems encountered have been solved using a coupling code strategy: the interaction of the different cooling applications of the vehicle and the conjugate heat transfer problem affected in addition by radiation.

In order to investigate the performance of electronic cooling for design packaging, numerous academic cases have been investigated in the past for various geometric configurations. The conjugate heat transfer problem usual in electronic cooling convection has been solved with finite-difference or finite-volume methods. Overall, the three-dimensional effects in a channel

or an enclosure cannot be neglected. Moreover, the heat transfer is enhanced with turbulence, created by protrusions in the main flow direction, as modules in electronic systems. For an electronic component mounted on a PCB substrate, it has been found that conduction plays an important role in the cooling of the component. In case of natural and mixed convection cooling, transient computations have been performed to investigate the effect of a heat flux step, transitional flows and modeling of turbulence. The limits of the standard  $k$ - $\epsilon$  high Reynolds model for heat transfer predictions have been demonstrated in most cases. Forced and mixed convection cooling have been examined in electronic channels with flushed-mounted or protruding heat sources. Secondary flows introduced by local buoyancy effects are found in both regimes, enhancing locally the heat transfer at low Reynolds number. At higher Reynolds numbers, the transport by the mean flow predominates, increasing the Nusselt number.

Due to the complexity of electronic systems, the heat transfer modes, in particular conduction, have been examined in the literature at one geometric level or time scale. At the junction scale, heat conduction in the chip relies on phonon transport and conductive transfer to the substrate is limited by partial contact at the interface, depending on the contact pressure applied to the surfaces. For the thermal management and design of electronic systems, several numerical tools like Flotherm, Icepak and I-DEAS ESC are widely used by electronics suppliers. Nevertheless, their use is limited to design electronic systems in laboratory ambient conditions.

As a conclusion, no numerical method to predict the temperature of an electronic system embedded in a complex environment has been found in the literature. Furthermore, the computational coupling strategies to compute transient solid temperatures of a passenger car are not focused on the transient temperature of electronic systems but merely on the contribution of electronic systems in the thermal management of the whole vehicle. Therefore, a reliable strategy must still be investigated for the systematic thermal prediction of electronic systems in the automotive development process.

## **2.5. Aim and challenge of the project**

In order to ensure the reliability of the electronic equipment embedded in a conventional vehicle, its temperature must be successively predicted by transient computations at each stage of the digital development process. The state of the literature demonstrates the lack of existing numerical methods for the thermal management and design of electronic systems embedded in complex environment geometries and running under time-dependent operating and driving conditions. Until now, complex electronic systems have been examined at one geometric level, respectively one time scale of heat transfer, and under laboratory conditions. Moreover, few investigations have solved the coupling of the three modes of heat transfer, and these studies were restricted to academic cases of reasonable model size.

Therefore, innovative computational methods must be developed in order to predict the temperature of each target electronic device assembled in its real environment in the vehicle operating under time-dependent conditions and thermal loads. For the implementation in the digital development process, efficient and systematic numerical strategies are required, which may adapt to the deadlines of each stage of the development process. Moreover, numerical models of the target electronic systems in their environment in the vehicle must be investigated to solve the coupled three modes of heat transfer at the different geometry levels

and time scales of heat transfer. Accordingly, the numerical requirements for an accurate prediction of the convective heat transfer, in particular towards mesh refinement and turbulence modeling, must be found out. The originality of this Ph.D. work relies on solving these issues, proposing and verifying computational methods to compute the transient temperature of electronic systems in the automotive development process.

In a first part, numerical strategies for the computation of the heat transfer modes in the vehicle are presented regarding numerical capabilities in the development process. To solve the time dependent coupled heat transfer modes problem, computational methods are discussed with the examination of the transient scales encountered in the automotive electronic equipment, yielding to a coupling code strategy. Assumptions are then proposed for a reasonable computing time, fulfilling the industrial requirements. Moreover, motivations for the employment of experimental methods for thermal management of the electronic equipment are explained and measurements techniques are briefly described for laboratory conditions and real environment conditions as in a passenger car.

In a second part, the accuracy of the prediction of the convective heat transfer is examined in comparison with literature, in order to validate the previous assumptions. Appropriate numerical models for the prediction of convective heat transfer are investigated, in particular analyzing mesh requirements and turbulence modeling. Three test cases are examined: natural convection with a differentially heated cavity, fan forced convection and flow computation through thin electronic grills.

The main objective of the third and last part is to validate the coupling strategies in comparison with measurements using complex electronic systems assembled in the vehicle. For the validation, two electronic devices are chosen representative of the whole automotive electronic equipment: a common lead-acid battery and a sound amplifier. After validation of the numerical models of the electronic system in its near environment in the vehicle, the numerical simulation is used to provide a global comprehension of the physical parameters of the electronic temperature.



---

## **Chapter 3**

# **Development of a numerical method for the thermal management of electronics in passenger cars**

As discussed in the last chapter, no numerical method to predict the temperature of an electronic system embedded in a complex environment has been found in the literature. Therefore, innovative simulation strategies must be developed for the thermal management of electronic systems. In order to determine the geometric and time scales relevant for the temperature prediction of the electronic equipment in a passenger car, the characteristic time of temperature propagation by convection and conduction must be first estimated. This must provide the temporal and geometric limits of the physical system considered for the simulation. The computation of the temperature of the physical system can be next described by a mathematical system composed of governing equations, boundary conditions and initial conditions. Based on this mathematical system, a numerical strategy for the transient computation of the different modes of heat transfer must be developed taking into account the industrial requirements.

### **3.1. Characteristic time of temperature propagation**

In this paragraph, the time scales associated to the heat transfer modes are discussed at two geometric levels: the electronic device and the compartment of the vehicle, in which the device is assembled. The time scales are evaluated with a non-dimensionalization analysis of the transport equations in the fluid by convection and in the solid by conduction, involving characteristic dimensions and adimensionalized characteristic numbers (appendix A.1). The resulting characteristic time is representative of the temperature propagation in the fluid at the level of fluid motion and in the solid at the level of temperature gradients. In order to set up the computational time-step so as to ensure the stability of the numerical solution, the discretization schemes of the governing equations and a base size of the mesh are required. The evaluation of the time-step is consequently not carried out in this section.

### 3.1.1. Transport by convection

#### 3.1.1.1. Characteristic time, natural and mixed convection

Transport by natural convection is considered in cavities, where the flow depends mainly on the vertical temperature gradient. As discussed previously, it also occurs in electronic compartments, in which secondary sources of inertial forces are not strong enough to dominate over buoyancy forces. With a non-dimensionalization analysis of the transport equations [102], the velocity scale  $u_{sc}$  is found dependent on the Grashof number and a characteristic length  $L$  of the buoyancy-driven flow:

$$u_{sc} = \frac{\nu}{L} Gr^{1/2} \quad (3.1)$$

The characteristic time is given by:

$$\delta_{conv} = \frac{L}{u_{sc}} = \frac{L^2}{\nu Gr^{1/2}} \quad (3.2)$$

The transport by mixed convection is described by the combined effect of both a pressure gradient leading the main flow, which may be produced by a rotating fan, and a vertical temperature gradient attributed to buoyancy forces. To estimate the characteristic time of temperature propagation by mixed convection, the regime of mixed convection is first characterized using the Richardson number, which represents the ratio of buoyancy to inertial forces. Another possibility is to examine the Reynolds number on one side, ratio of inertial to viscous forces, and the Grashof number on the other side which is the ratio of buoyancy to viscous forces. The characteristic time of temperature propagation is calculated based on the hydraulic diameter of the system  $D_H$  and the prescribed velocity  $u_\infty$  in the system, as illustrated in figure 3.1:

$$\delta_{conv} = \frac{D_H}{u_\infty} \quad (3.3)$$

### 3.1.1.2. Electronic device

In the following, the characteristic time relative to natural and mixed convection is evaluated in an automotive sound amplifier with fan switched off or on, as shown in figure 3.1.

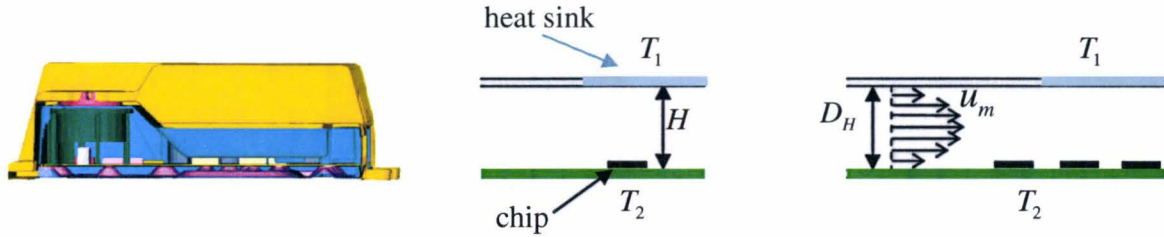


Figure 3.1. Characteristic dimensions for natural convection (middle) and mixed convection (right) in a sound amplifier.

#### i. Characteristic time relative to natural convection

First, the Rayleigh number is estimated in order to characterize the regime of the flow. With a temperature difference of 60 K due to the warm-up of the semiconductors, the Rayleigh number is provided by:

$$Ra = \frac{g\beta\Delta TH^3}{\nu\alpha} = 3.4 \times 10^3 \quad (3.4)$$

According to Kessler and Kirchartz [103,104] who investigated cavities of similar aspect ratio, the flow may be at the onset of the oscillating state in this range of Rayleigh numbers. The characteristic time is given by:

$$\delta t_{conv,device} = \frac{H^2}{\nu Gr^{1/2}} = 7.5 \times 10^{-2} s \quad (3.5)$$

#### ii. Characteristic time relative to mixed convection

A heat source of  $9 \times 10^4$  W/m<sup>2</sup>, a hydraulic diameter of 0.014 m and a mean velocity of 1.5 m/s are considered. The Reynolds and Grashof numbers are provided respectively by:

$$Re_{device} = \frac{u_{\infty} D_H}{\nu} = 1.1 \times 10^3 \quad (3.6)$$

$$Gr^*_{device} = \frac{g\beta\dot{q}D_H^4}{k\nu^2} = 9.6 \times 10^6 \quad (3.7)$$

In this range, the effect of buoyancy forces is small in comparison with the viscous and inertial forces [105]. The characteristic time in the electronic device derives directly from the prescribed velocity:

$$\delta t_{conv,device} = \frac{D_H}{u_{\infty}} = 9.3 \times 10^{-3} s \quad (3.8)$$

### 3.1.1.3. Compartment of a vehicle

In this paragraph, two electronic systems are considered, on the one hand a sound amplifier in a compartment under the passenger's feet, on the other hand a lead-acid battery assembled in a spare-wheel cavity, as shown in figure 3.2.



Figure 3.2. Characteristic dimensions for convection around a sound amplifier (left) and a lead-acid battery (right) assembled in a vehicle.

#### i. Characteristic time in the case of the sound amplifier

In the compartment of the sound amplifier, the fan flow outside the device has a typical mean velocity of  $10^{-1}$  m/s. The Reynolds and Grashof numbers are provided respectively by:

$$Re_{\text{amplifier}} = \frac{u_m L}{\nu} = 4.2 \times 10^2 \quad (3.9)$$

$$Gr_{\text{amplifier}} = \frac{g \beta \Delta T L^3}{\nu^2} = 1.2 \times 10^6 \quad (3.10)$$

Therefore, the strength of buoyancy forces is large enough to reduce the effect of forced convection [72]. Moreover, the Rayleigh number is found of:

$$Ra_{\text{amplifier}} = 3.7 \times 10^5 \quad (3.11)$$

Thus, the flow may be oscillating [106] and the characteristic time is given by:

$$\delta t_{\text{conv,amplifier}} = \frac{L^2}{\nu Gr^{1/2}} = 0.3s \quad (3.12)$$

#### ii. Characteristic time in the case of the battery

In the sealed spare-wheel cavity of the battery, the Rayleigh number is ranging between:

$$9.7 \times 10^5 \leq Ra_{\text{battery}} = \frac{g \beta \Delta T L^3}{\nu \alpha} \leq 4.6 \times 10^7 \quad (3.13)$$

In this range, the flow may be either oscillating or turbulent [104]. The characteristic time is given by:

$$4.4 \times 10^{-3} s \leq \delta t_{\text{conv,battery}} = \frac{L^2}{\nu Gr^{1/2}} \leq 6.4 \times 10^{-1} s \quad (3.14)$$

### 3.1.2. Transport by conduction

#### 3.1.2.1. Characteristic time, conduction

The following dimensionless variables are used:  $\theta_{s,i} = (T_s - T_i) / \Delta T$ ,  $t^* = t / \delta$ ,  $x_i^* = x_i / \delta x_i$ . The energy equation in the solid provides:

$$\frac{1}{\delta} \frac{\partial \theta_{s,i}}{\partial t^*} = \frac{\alpha_s}{\delta x_i^2} \frac{\partial^2 \theta_{s,i}}{\partial x_i^{*2}} \quad (3.15)$$

Therefore, the characteristic time corresponding to transport by diffusion in the device can be written as:

$$\delta t_{cond} = \frac{\delta L^2}{\alpha_s} = \delta L^2 \frac{\rho c_p}{k} \quad (3.16)$$

#### 3.1.2.2. Electronic device

For the comparison with the characteristic time corresponding to the transport by convection, the sound amplifier mentioned previously is considered here. In this case, the heat sink of aluminum alloy is submitted to strong temperature gradients in the heat path between the chips and the cool ambient air. Thus, the mean thickness of the heat sink (10 mm) is attributed as characteristic length, providing a characteristic time of:

$$\boxed{\delta t_{cond, device} = 1.9 s} \quad (3.17)$$

#### 3.1.2.3. Compartment of a vehicle

In this section also, the sound amplifier under the passenger's feet and the lead-acid battery in a spare-wheel cavity are considered.

##### i. Characteristic time in the case of the sound amplifier

At the geometric level of the compartment, temperature gradients in the carpeting of the compartment may occur. The thickness of the walls of the cavity is taken as characteristic length. The characteristic time is found of:

$$\boxed{\delta t_{cond} \leq 425 s} \quad (3.18)$$

##### ii. Characteristic time in the case of the battery

In this case, temperature gradients in the body shell of the spare-wheel cavity may occur. The characteristic time is provided by:

$$\boxed{\delta t_{cond} \leq 3.2 \times 10^{-1} s} \quad (3.19)$$

### **3.1.3. Transport by radiation**

In a passenger car, the dry air separating the surfaces is transparent to thermal radiation; consequently it does not intervene in the radiation transfer. Therefore, the heat transfer is based on surface exchange. Thus, the transport equations describing the radiation heat transfer imply only elements at the fluid-solid interface and are steady-state.

### **3.1.4. Partial conclusions**

The heat transport by convection has been examined for two electronic systems, a sound amplifier and a lead-acid battery, at the scale of the device and at the scale of the embedded cavity, showing different regimes of the flow and multiple characteristic times of heat transfer. For the computation of the three modes of heat transfer, the characteristic times found for convection around the battery are in the range of the characteristic time for conduction in its cavity. However, in the case of the sound amplifier, the characteristic times for convection are estimated much smaller than the characteristic times for conduction.

The characteristic time for diffusive conduction in the package of an electronic system is much higher than the one of the phonon transport in the junction, which lies in the range of nanoseconds. The conduction heat path from the heat generating semiconductors to the electronic package will be consequently regarded at a macroscopic level using the Fourier diffusive approach.

### 3.2. Mathematical model for the prediction of the electronic temperature in the development process

Based on the characteristic time scales for temperature propagation by conduction and convection calculated previously, the temperature of electronic systems embedded in a vehicle operating under time-dependent conditions can be described with a mathematical system of governing equations, boundary conditions and initial conditions. This mathematical system is presented in the following.

#### 3.2.1. Governing equations

##### 3.2.1.1. Solid equations

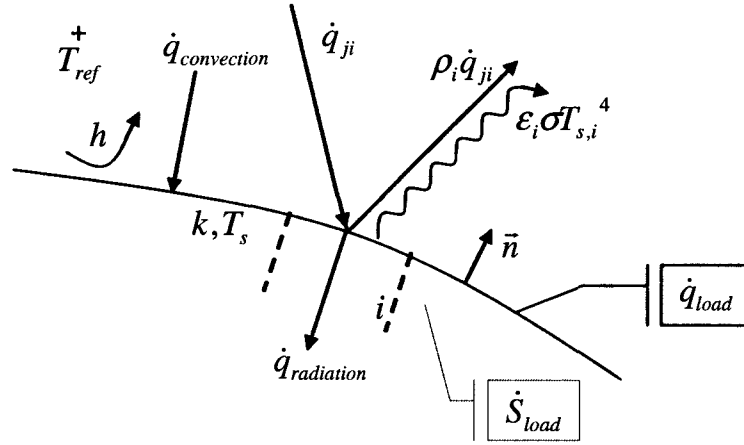


Figure 3.3. Heat fluxes at the fluid-solid interface.

To determine the temperature of the electronic equipment running under transient operating conditions and thermal loads, the energy equation must be solved in the solid region. Due to the negligible phonon transport in the chip junction, diffusive conduction at a macroscopic level only is considered with the extended Fourier equation. With  $\dot{S}_{load}$  the prescribed heat rate per unit volume, it is provided by:

$$\rho(T)c_p(T) \frac{\partial T_s}{\partial t} - \text{div}([k(T)] \overline{\text{grad}}(T_s)) = \dot{S}_{load} \quad (3.20)$$

Moreover, at the interface fluid-solid, the convective and radiation heat fluxes must be given as boundary conditions at each time-step. With  $\vec{n}$  the vector normal to the surface as illustrated in figure 3.3, the Neumann boundary condition at the interface fluid-solid is provided by:

$$[\vec{n}]^T \cdot [k(T)] \overline{\text{grad}}(T_s) - \dot{q}_{convection} = \dot{q}_{radiation} + \dot{q}_{load} \quad (3.21)$$

The radiation heat flux is obtained by solving the system composed of equations 1.3 and 1.6.

Moreover, with  $T_{ref}$  a reference temperature of the fluid, the convective heat flux at the interface is given by:

$$\dot{q}_{convection} = h(T_{ref} - T_s) \quad (3.22)$$

In order to provide a prediction of the convective heat transfer at the fluid-solid interface, the flow must be solved in the electronic system assembled in a vehicle. This is discussed in the following.

### 3.2.1.2. Assumptions done to solve the flow

Depending on the strength of buoyancy and inertial forces in electronic systems and compartments, multiple characteristic times of heat transfer by convection have been found corresponding to different flow regimes. Furthermore, the flow regimes may vary with time as the operating conditions of the device and vehicle may change during the use case. In order to fulfill the industrial requirements, the several time scales of convection and the different flow regimes must be solved within one system, so that assumptions must be done.

In case of oscillating and turbulent natural convection, the unsteadiness of the flow can be captured only with transient computations of the flow and appropriate turbulence models. In regard with the multiple heat transfer time scales, the transient computation of the coupled convective and conductive heat transfer modes would request a time-step in the range of order of  $10^{-3} s$  to describe the turbulent natural convective flow in an electronic enclosure. The computation of the flow only in a typical electronic system for a simulation time of one hour would require a computing time of 42 days using parallel 32 processors AMD2218 Dual Core of a cluster at 2.6 GHz. Consequently, transient computations of the flow to predict the convective heat transfer cannot be *reasonably* implemented in the development process. The flow in electronic enclosures is therefore computed with a steady-state approach.

For high temperature differences in electronic enclosures and devices up to 60 K, the physical properties of the fluid are dependent on temperature. As the Boussinesq approximation considers the linear variation of the fluid density only with temperature in the buoyant term, it is inaccurate in this case to model the buoyancy-driven flow. For higher accuracy, the fluid density is set dependent on temperature and static pressure according to the ideal gases law:

$$\rho = \frac{P_{stat}}{RT} \quad (3.23)$$

Therefore, a continuous flow of a Newtonian expansible gas is assumed in electronic compartments. Moreover, in order to determine the ratio of kinetic energy to enthalpy, the Eckert characteristic number is evaluated in a typical electronic system assembled in a vehicle:

$$3.3 \times 10^{-7} \leq Ec = \frac{u_{\infty}^2}{c_p \Delta T} \leq 2.2 \times 10^{-3} \quad (3.24)$$

Due to the negligible Eckert number compared to unity, the kinetic energy is not taken into account in the enthalpy term of the energy equation. Then, the total enthalpy can be approximated by the static enthalpy.

### 3.2.1.3. Flow conservation equations

For laminar flows, with  $s_i$  the momentum source components, the mass, momentum and energy conservation equations, can be written as, respectively:

$$\frac{\partial(\rho u_j)}{\partial x_j} = 0 \quad (3.25)$$

$$\frac{\partial}{\partial x_j} (\rho u_j u_i) = \frac{\partial \sigma_{ij}}{\partial x_j} + s_i \quad (3.26)$$

$$\frac{\partial}{\partial x_j} (\rho c_p u_j T_f) = \frac{\partial}{\partial x_j} \left( k \frac{\partial T_f}{\partial x_j} \right) + \frac{\partial(\sigma_{ij} u_i)}{\partial x_j} + s_i u_i \quad (3.27)$$

With  $p_{stat}$  the static pressure, the stress tensor for laminar flows is given by:

$$\sigma_{ij} = -p_{stat} \delta_{ij} + \mu \left( \frac{\partial u_i}{\partial x_j} + \frac{\partial u_j}{\partial x_i} \right) - \frac{2}{3} \mu \frac{\partial u_k}{\partial x_k} \delta_{ij} \quad (3.28)$$

The buoyant and rotational forces are provided by, respectively:

$$s_i = \rho g_i \quad (3.29)$$

$$s_i = f(u_k, \omega_k, r_k) \quad (3.30)$$

To model the turbulent flow of an expansible gas, the independent variables  $u_i$  and  $T$  are decomposed into a time average value and time-dependent fluctuations using the Favre averaging [107]:

$$\bar{\Phi} = \frac{1}{\bar{\rho T}} \int_1^{t_2} \rho(t) \Phi(t) dt \quad (3.31)$$

$$\Phi(t) = \bar{\Phi} + \Phi''(t) \quad (3.32)$$

The conservation equations, written with the Reynolds decomposed variables, are time-averaged, providing the RANS (Reynolds averaged Navier-Stokes) equations:

$$\frac{\partial(\bar{\rho} \bar{u}_j)}{\partial x_j} = 0 \quad (3.33)$$

$$\frac{\partial}{\partial x_j} (\bar{\rho} \bar{u}_j u_i) = \frac{\partial}{\partial x_j} (\bar{\sigma}_{ij} - \bar{\rho} \overline{u_i'' u_j''}) + \bar{\rho} g_i \quad (3.34)$$

$$\frac{\partial}{\partial x_j} (\bar{\rho} c_p \overline{u_j T_f}) = \frac{\partial}{\partial x_j} \left( k \frac{\partial \overline{T_f}}{\partial x_j} - \bar{\rho} c_p \overline{u_j T_f''} \right) + \frac{\partial (\overline{\sigma_{ij} u_i})}{\partial x_j} \quad (3.35)$$

For turbulent flows, the total stress tensor  $\overline{\sigma_{ij}} + \tau_{ij,Re}$  is given by:

$$\overline{\sigma_{ij}} = -\bar{p}_{stat} \delta_{ij} + \mu \left( \frac{\partial \overline{u_i}}{\partial x_j} + \frac{\partial \overline{u_j}}{\partial x_i} \right) - \frac{2}{3} \mu \frac{\partial \overline{u_k}}{\partial x_k} \delta_{ij} \quad (3.36)$$

$$\tau_{ij,Re} = -\overline{\rho u_i'' u_j''} \text{ (Reynolds stress tensor)} \quad (3.37)$$

A similar term for the turbulent heat flux  $\overline{\dot{q}_j} + \overline{\dot{q}_{j,Re}}$  is found:

$$\overline{\dot{q}_j} = k \frac{\partial \overline{T_f}}{\partial x_j} \quad (3.38)$$

$$\overline{\dot{q}_{j,Re}} = -\overline{\rho c_p u_j'' T_f''} \quad (3.39)$$

Moreover, at the fluid-solid interface, both solid and fluid share the same temperature. The Dirichlet boundary condition at the interface fluid-solid is provided by:

$$T_f = T_s \quad (3.40)$$

#### 3.2.1.4. Initial conditions

The parabolic energy equation (3.20) requires initial conditions, which may be specified at the fluid-solid interface. As the standard use cases to test the temperature of the electronic equipment in a vehicle are based on a first phase of pre-conditioning of several hours, the solid temperature is assumed initially homogeneous and the fluid isothermal and at rest.

### 3.2.2. Time-dependent coupled heat transfer problem

For the heat flux balance at the fluid-solid interface, heat conduction in the solid needs to be considered along with convection in the adjacent fluid and radiation of both emitting and incident surfaces. Moreover, a proper matching between the different grids must exist at the fluid-solid interface for global flux conservation. This coupled heat transfer problem can be numerically solved either with iterative methods or with fully coupled methods [108, 109]. In the first case (iterative methods), the fluid and solid regions are solved separately with an iterative procedure for matching the interface condition. In the other case (fully coupled methods), numerical methods are proposed using a calculation domain including both fluid and solid regions with matching grids at the interface, as the harmonic mean practice with formulation of the internal diffusivities proposed by Patankar [80]. In the literature, most of numerical methods for the thermal management of electronic are solved in one code, iteratively [82, 85] or fully coupled [53, 86].

### 3.2.3. Resolution of the coupled problem in the development process

In the development process of Daimler AG, coupled methods are used for the computation of the engine compartment and underbody. The flow and the solid are solved successively by respectively CFD and FEM codes to overcome the interaction of the different cooling applications of the vehicle and the prediction of the three coupled modes of heat transfer. For the computation of the electronic equipment, *additional* numerical problems must be solved:

- The long time period until the transient solid temperatures reach a constant value. This corresponds to the thermal response of the system, composed of the electronic enclosure and its environment in the passenger car.
- The interaction of the cabin, the cockpit or the engine compartment by mass transfer through leakages;
- The multiple characteristic times, associated to the geometrical scales (semiconductor case, electronic package, car environment);
- The time-dependent boundary conditions in the fluid (activation of a fan) and in the solid.

In order to take into account the mass transfer through leakages from another enclosure in the electronic cavity, mass flow rate boundary conditions may be given in CFD computations or the flow must be computed with CFD in both enclosures. Such boundary conditions based on numerical or experimental results are not as accurate as a computation of the flow in both enclosures. The coupling code strategy is then particularly attracting, as the flow can be computed in an extended system, while conduction is only computed in the electronic enclosure. Moreover, to model the different geometry scales, the coupling code methodology is again profitable, as the FEM model can be refined without refining the CFD model. This provides more accuracy, offering a higher level of details.

Therefore, the coupled heat transfer problem is solved in this work, for the most part, iteratively with different adapted codes. The regulation of the running codes, the exchange of heat transfer data and the mesh mapping for matching condition are managed by a coupling mesh interface. These codes are presented in the next part, followed by the coupling strategies adopted in this work for the thermal management of electronics.

### 3.3. Solid solvers

Within the coupling codes methodology, the solid solver is used to solve:

- The energy equation in the solid for the prediction of the conductive heat transfer.
- The heat flux balance at the interface between fluid and solid.

In this work, two different solid solvers are investigated; the thermal analysis software RadTherm and the FEM code PERMAS. For the computation of the radiation heat transfer mode, the radiation code POSRAD is used combined with PERMAS, while RadTherm possess its own radiation solver. The different codes are presented in the next parts.

#### 3.3.1. Mesh generation for RadTherm and PERMAS computations

RadTherm thermal analysis is based on a surface mesh, while PERMAS uses surface and volume elements. Both meshes are generated from CAD surfaces with the meshing tool MEDINA [110]. The CAD surfaces are first re-meshed to obtain a regular mesh refined in the regions, where high temperature gradients are expected. As the volume mesh for the PERMAS computations is composed solely of tetrahedral elements, 2D triangle elements are used for the surface mesh in PERMAS. Then, the triangle elements of a closed surface are extruded to form the 3D tetrahedral elements. For practical reasons, the surface meshes for RadTherm computations are also composed solely of triangle elements.

#### 3.3.2. Thermal analysis software RadTherm

The thermal simulation tool RadTherm performs steady-state and transient heat transfer analysis for the temperature prediction of thin walls. Each element of the thin wall shows two surfaces (front and back) separated by a specified thickness. A thermal node is associated with each surface and one half of the volume bounded by the two surfaces, as shown in figure 3.4.

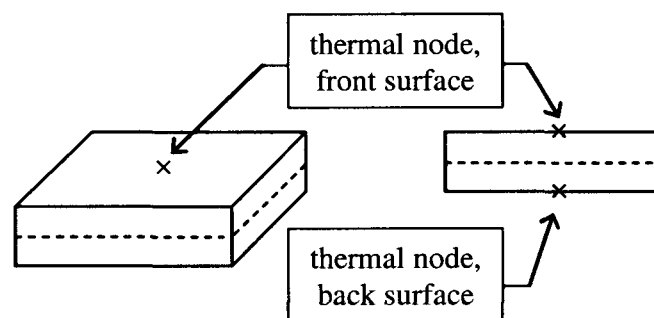


Figure 3.4. Isometric view (left) and section (right) of an element in RadTherm.

The energy balance is calculated at each thermal node, so that a temperature gradient, if existing, can be predicted within the wall thickness. In case of superimposed material layers of different properties, multi-layer elements can be defined, connected together via series conduction through the layers. In order to set environment information of the geometrical

model, a bounding box can be used surrounding the geometry. The geometry and the bounding box are considered as a closed system of uniformly irradiated, diffuse-gray surfaces. At the  $k^{\text{th}}$  node, with heat sources considered in the term “load heat flux”, the transient energy equation in the solid is provided by:

$$\frac{m_k}{A_k} c_{p,k} \frac{\partial T_k}{\partial t} = \sum_{j=1}^{N_{\text{cond}}} \left( -k_{kj} \frac{T_k - T_j}{L_{kj}} \right) + \dot{q}_{\text{convection},k} + \dot{q}_{\text{radiation},k} + \dot{q}_{\text{load},k} \quad (3.41)$$

The convective heat flux is given by equation 3.22. The radiation heat flux on the element surface of the  $k^{\text{th}}$  node is obtained from the net-radiation enclosure equation [111]:

$$\dot{q}_{\text{radiation},k} = \frac{\epsilon_k}{F_{k-k}(1-\epsilon_k)-1} \left[ \sum_{j=1}^N \sigma F_{k-j} (T_k^4 - T_j^4) + \sum_{j=1}^N \dot{q}_{\text{radiation},j} \left( (1-\delta_{kj}) F_{k-j} \frac{1-\epsilon_j}{\epsilon_j} \right) \right] \quad (3.42)$$

The view factors are calculated in RadTherm using a single plane variant of the hemi-cube method [112]. The algorithm repeatedly renders the object geometry as seen with rays cast from viewpoints on the surface associated with each thermal node. The accuracy of the view factor calculation is determined by the number of viewpoints per elements and the number of rays cast from each viewpoint. Radiation patches are created collecting elements assigned with a common view factor to other radiation patches. More details can be found in [113]. The governing equations 3.41 and 3.42 are then discretized using the Crank-Nicholson implicit finite difference scheme, unconditionally stable and second-order accurate in time and space. To solve the discretized governing equations, the iterative SOR (successive over-relaxation) method is used in conjunction with a secondary direct method (Gauss elimination with partial pivoting). For nodes that have a strong interdependence, the direct method is invoked at the beginning of each iteration as pre-conditioner, providing a quick temperature convergence. After the direct solution is completed, the governing equations are solved iteratively with the SOR method until convergence of node temperatures. Then, the solution advances by one time step and repeats the above procedure.

### 3.3.3. Finite element code PERMAS and radiation code POSRAD

The FE code PERMAS affords the computational analysis in several fields of application, in particular it allows the evaluation of temperature and electromagnetic fields. The energy balance is computed by analogy with structural mechanics. The equivalence of variables between structural mechanics and thermodynamics can be seen in appendix A.2. The energy equation 3.20 is solved in 3D shell and solid finite elements. Moreover, the boundary condition at the fluid-solid interface (equation 3.21) is solved in membrane elements, associated with the shell and solid elements. Temperature and heat flux boundary conditions are prescribed with, respectively, constraint displacement and distributed or nodal load. Transient boundary conditions are defined with a transient function based on an initial static load. Due to the strong nonlinearities in the solid field because of the effect of the coupled radiation and convection, the element temperature is calculated in this work with a nonlinear transient analysis.

The governing equations 3.20 and 3.21 are then discretized following the Galerkin procedure and using constitutive matrices by analogy with structural mechanics, providing the system of matrices formed by the following equations:

$$[C] \cdot [\dot{T}_s] + [K] \cdot [T_s] = [\dot{S}] \quad (3.43)$$

$$[c] \cdot [\dot{T}_s] + [\kappa] \cdot [T_s] = [\dot{q}] \quad (3.44)$$

Accordingly, the system is solved with the iterative Newton-Raphson method implemented in PERMAS, particularly effective in case of strong nonlinearities. The computation of the radiation heat transfer is performed by the thermal radiation solver POSRAD, which solves the equations 1.3 and 1.6. For the computation of the view factors, POSRAD works with the discrete beam method. Patches are created automatically so as to resolve adequately the surface geometry and heat fluxes gradients. Beams are emitted from each patch and traced through the fluid until it intercepts an opposing patch. Then, the radiation energy transfer to or from each patch is calculated from the radiation transport equation and boundary conditions. More details can be found in [20].

### 3.4. Flow solver STAR-CD

The commercial finite-volume CFD code STAR-CD is used in this work to solve the flow in electronic enclosures with a steady-state approach and provide a prediction of the convective heat flux.

#### 3.4.1. Mesh generation

First, the surface delimiting the system is cleaned-up with the surface wrapper. Then, a subsurface, delimiting the boundary layer and the core, is generated. A volume mesh is created in the subsurface and extrusion layers are generated based on the exterior surface of the volume mesh to form the boundary layer. In order to mesh the complex geometries with shaped and curved surfaces encountered in electronic enclosures, trimmed meshes are used in this work. They are based on hexahedral cells with trimmed type polyhedral near the subsurface.

#### 3.4.2. Turbulence modeling

The equations to solve the flow proposed previously are written in a conservation form to be solved by STAR-CD. For reasonable computing times in the development process, eddy viscosity models are used to close the system composed of the three RANS equations. Reynolds stress models are not considered in this work because of the time consuming computations due to the direct resolution for the Reynolds stresses. Different turbulence models are investigated in this work, for the computation of natural convection and of fan forced flow convection. Due to tight flow passages in electronic devices and in the compartment near a heat sink for example, boundary layers with 3 to 10 cell layers were created in this work for meshing electronic enclosures. The resulting dimensionless normal distance from the wall is in the range:

$$0 \leq y^+ \leq 30 \quad (3.45)$$

In respect with the dimensionless normal distance from the wall for meshing electronic enclosures, turbulence models are chosen to resolve the near-wall region with transport equations for the turbulent variables. The turbulence models investigated are listed below:

- Standard low-Re number two-equation  $k$ - $\epsilon$  model [114], in which transport equations for the turbulence kinetic energy  $k$  and for the turbulence dissipation rate  $\epsilon$  are solved everywhere, including the near-wall region.
- RNG (Renormalization Group)  $k$ - $\epsilon$  model [115], which is based on the standard  $k$ - $\epsilon$  model and proposes an additional term in the equation of turbulence dissipation rate and other constant values for the coefficients.
- Non-linear quadratic Suga's low-Re number two-equation  $k$ - $\epsilon$  model [116], which uses another transport equation for  $\epsilon$ . Moreover, the turbulent heat flux is given in explicit form and calculated using an algebraic second-moment closure.
- Relaxation V2F model [117, 118], based on the solution of the  $k$ - $\epsilon$  model and solving additionally one more transport equation for the wall-normal turbulence intensity  $\bar{v}_2$  and an elliptic equation for  $f_{22}$ , the redistribution term in the  $\bar{v}_2$  equation. This is

designed to handle near-wall effects in turbulent boundary layers and non-local effects.

- Standard high-Re number  $k$ - $\epsilon$  model with the two-layer approach, in which the near-wall flow is modeled via a one-equation low Reynolds number model, consisting of a transport equation for  $k$  and an algebraic prescription for the turbulence length scale according to the model of Wolfshtein [119]. Elsewhere, the standard high-Re number  $k$ - $\epsilon$  model is applied.
- Spalart-Allmaras model [120], which solves only one transport equation for  $\tilde{\nu}$ , which is equivalent to the turbulent kinematic viscosity far from walls. The transport equation has been developed to reproduce aerodynamic flows of increasing complexity.
- SST (Shear Stress Transport) low-Re (high-Re) number  $k$ - $\omega$  model [121], which activates the standard  $k$ - $\omega$  model in the inner region of the boundary layer and a low-Re (high-Re) number  $k$ - $\epsilon$  model in the near-wall region of the boundary layer with the help of a blending function.

Any type of these eddy viscosity models except Suga's model is based on the eddy conductivity concept, for which the turbulent heat flux follows a similar law as the Fourier law for diffusive conduction. It assumes the simple gradient diffusion hypothesis (SGDH). With  $\sigma_t$ , the turbulent Prandtl number:

$$\overline{\rho c_p u_j' T_f'} = -\frac{\mu_t c_p}{\sigma_t} \frac{\partial \overline{T_f}}{\partial x_j} = -k_t \frac{\partial \overline{T_f}}{\partial x_j} \quad (3.46)$$

### 3.4.3. Convective heat transfer at the interface

With  $T_{ref}$  a reference temperature of the fluid, the usual definition of the convective heat flux at the interface is given by:

$$\dot{q}_{convection} = h(T_s - T_{ref}) \quad (3.47)$$

In STAR-CD, the evaluation of the convective heat transfer is based on the temperature of the first near-wall cell, as illustrated in figure 3.5.

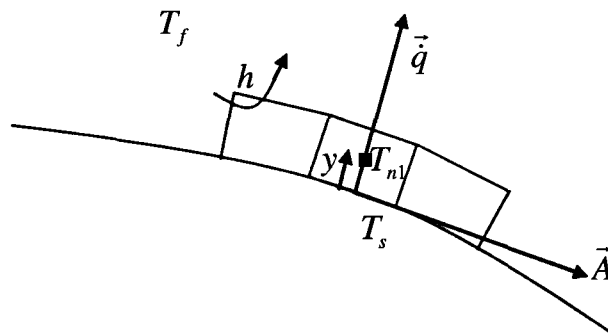


Figure 3.5. Convective heat flux at the fluid-solid interface.

For laminar flows in electronics enclosure, the flow velocity in the boundary layer is moderate. With  $y$  the normal distance from the wall to the near-wall cell node, the convective heat flux at the interface is approximated by STAR-CD by:

$$\dot{q} = k \frac{T_s - T_{n1}}{y} \quad (3.48)$$

Consequently, in STAR-CD, the heat transfer coefficient is set for laminar flows by:

$$h = \frac{k}{y} \quad (3.49)$$

For turbulent flows, small values of  $y^+$  are found (equation 3.45) and the near-wall cell is situated within the laminar sublayer. Therefore, the heat transfer coefficient is also predicted by equation 3.49 for turbulent flows. In this case, that the heat transfer coefficient  $h$  defined by equation 3.49 is only dependent on the mesh and fluid conductivity.

#### 3.4.4. Discretisation and solution algorithm

The governing equations of mass, momentum and energy conservation are discretized by the finite volume (FV) method, which is conservative for connected cell faces [80]. With refinement of the mesh or at the junction between two different mesh types, the cell faces may not be connected together. To ensure the conservation properties of the original differential equations after discretisation, couples are introduced to match the corresponding faces. The conservation equations are first integrated over individual cells into separate contributions due to convection, diffusion and sources. To express the resulting convective and diffusive fluxes in terms of cell-centred nodal values, the average value at the face is interpolated according to differencing schemes. In order to speed-up the convergence of the residuals, the second-order accurate differencing schemes MARS for the convective fluxes and the turbulent quantities and CD (central differencing) for the density are used in this work with a blending factor of 0.5 and 0.01 respectively. MARS (monotone advection and reconstruction scheme) operates in two steps, reconstruction and advection. More details can be found in [20]. The resulting algebraic finite-volume equations are solved iteratively and sequentially with implicit methods involving predictor-corrector stages. The predictor stage produces a provisional velocity field obtained from the momentum equation and a provisional pressure distribution. The provisional fields are then refined with the corrector stage, taking into account corrections of velocity and pressure fields. These corrections are established, under spatial approximations, satisfying the continuity and momentum equations. The coupling between velocity and pressure fields is solved with the sequential resolution of the conservation equations. As the equations are temporarily decoupled to be solved sequentially, the solver is called segregated. In this work, the SIMPLE (semi-implicit method for pressure linked equations) algorithm [73] is used. Large sets of algebraic equations are obtained resulting from the linearization of the equation for each dependent variable, pressure and velocity. They are solved in this work with conjugate-gradient (CG) type solvers with various pre-conditioning methods.

### 3.5. Modeling of the flow in electronic enclosures

In the paragraph 3.1, an academic example with mean boundary conditions has been considered to characterize the flow regime and provide an estimation of time scales. Regarding now a common automotive electronic system composed of a fan, one or several PCBs populated with heated protrusions (electronic components) and outlet grills or vents, the physical mechanisms that affect the convective heat transfer are much more complex.

If the electronic fan is switched off, the buoyancy-driven flow over one heated module is described in [122] as a vertically rising plume in case of a horizontal PCB surface for comparable Rayleigh numbers. As the wake induced by one heated surface interacts with the buoyancy-induced flows at other surfaces, the thermal boundary layer over one module may be affected by the neighbor populating modules. In case of a vertical surface, the main flow is characterized by a wall plume rising along the surface with stronger vicinity than in the horizontal case, resulting in a higher heat transfer coefficient. Depending on the aspect ratio of the module, a secondary eddy motion may form downstream the trailing edge of the module accompanied by locally lower heat transfer coefficients at the vertical wall, due to the separation of the main flow at the trailing edge [50]. In the vehicle compartment, with the closer proximity of conducting sidewalls, eddy patterns may form depending on the temperature distribution of the compartment and the geometrical wall configuration [123].

With the fan drawing the ambient air in the electronic system, in the near downstream region of the fan until the first heated module, the convective heat transfer coefficient strongly decreases according to the boundary layer growth with the developing flow temperature and velocity profiles. With the abrupt change of wall boundary condition at the first heated module, an internal thermal layer develops under the developed outer one, growing faster with higher Rayleigh numbers [124, 125]. Depending on the strength of the shear forces of the main flow on buoyancy forces and on the ratio of the channel height with the protrusion height and width, different structures may develop at the trailing edge of the module. For mixed convective flow, one or two secondary eddy patterns may be found due to the rising warm air from the heated surface replaced by the cooler fluid descending from the channel core. This results in thinner boundary layers on the top and vertical sides of the module and yields to an enhancement of heat transfer, along with a moderate increase in pressure drop [79]. With an increase in the Reynolds number, the strength of shear forces of the main flow inhibits the development of the secondary flow and slows down the enlargement of the internal thermal boundary layer. Due to the channel obstruction with the protrusion, the flow accelerates at the leading edge with a local enhancement of heat transfer due to the boundary layer thinning and separates over the module with a decrease of heat flux from the thickening of the boundary layer. A small recirculation zone is found upstream the module, while the main recirculation zone is located downstream forming an energetic horseshoe structure, characterized by an abrupt pressure drop at the trailing edge, high turbulence fluctuations near the wall and in the shear layer separating the main flow from the recirculation zones and correspondingly a large enhancement of heat transfer [67, 75, 126]. For the computation of the competing effects of buoyancy-driven and shear flows, the modeling of each type of flow is investigated separately in the following.

### 3.5.1. Buoyancy-driven flows

To solve the strong coupling between temperature and flow velocity, the segregated time-marching PISO algorithm [127] is recommended by STAR-CD, as the temperature fields are embedded in the main predictor/correctors sequence. The reliability of the PISO solver has been tested in comparison with the SIMPLE solver for steady-state computations of natural convection in a rectangular cavity heated from below. No significant difference has been noticed in the temperature and velocity fields. As computations with the algorithm PISO are more time-consuming than with the algorithm SIMPLE, the algorithm SIMPLE has been selected for further computations. Furthermore, as the body force terms in the momentum equation may be small in comparison with the other terms, they may be masked by the round-off error of the calculation, resulting in a difficult convergence of the residuals. Therefore, computations in this work are all carried out with double precision.

### 3.5.2. Forced convective flows

In most cases, electronic devices are assembled with internal axial fans, drawing ambient air into the system. The fan induced volume flow rate is then leaving the device through loose outlets or outlet grills in the package. The complex geometry assembly and the outlet grills of the electronic system can be regarded as a total pressure drop of the electronic system for a particular volume flow rate. The pressure drop of the system can be expressed generally by:

$$\Delta p_{stat} = c_1 \rho \dot{V} + c_2 \rho \dot{V}^2 \quad (3.50)$$

The curve representing the system pressure drop as a function of the volume flow rate is called system pressure curve. As the fan can only deliver one flow rate at one pressure in a particular system, this curve is also called load curve. The coefficients  $c_k$  can be regarded as total resistance element of the system and are called load factor. The operating point is defined as the fan pressure rise condition, for which the fan and electronic system are in a stable equilibrium. Therefore, in the graph representing the static pressure difference through the fan as a function of the volume flow rate, the intersection of the system load curve and the fan performance curve provides the system operating point. Moreover, the heat transport by forced convection relies mainly on the geometry assembly, on the prescribed volume flow rate and on the resulting pressure distribution in the electronic system [68, 89]. Consequently, the cooling of critical semiconductor chips is significantly affected by the volume flow rate and pressure rise created by the rotating fan blades and by the geometrical assembly in the electronic system. In particular, outlet grills create a significant pressure drop, which contributes to the total pressure drop of the system. Consequently, it has an indirect effect on the volume flow rate establishing in the electronic system. Therefore, for the thermal management of an electronic system, two important elements must be correctly modeled: the fan generated flow and the outlet grills. The requirements towards the numerical models are to provide an accurate prediction of the pressure distribution, as well as of the induced volume flow rate. In this respect, two steady-state numerical methods for fan flow simulation are investigated with STAR-CD in this work, multiple reference frames (MRF) and rotational body force. The modelling of outlet grills is also examined in the following.

### 3.5.2.1. Fan flow simulation with rotational body force model

As the rotational body force method implemented in STAR-CD is valid only for incompressible flows, the local Mach number is evaluated in the fan region, using the geometric data of the fan of the sound amplifier. It is provided by the ratio of the relative velocity at the blade outlet to the sound velocity with  $A_{BF}$  the surface area swept out by the blades:

$$Ma = \frac{u_{out,relative}}{c} = \frac{\dot{V}}{A_{BF} \cos \beta} \frac{1}{(\gamma RT)^{1/2}} = 1.7 \times 10^{-2} \quad (3.51)$$

According to the velocity vector diagram shown in figure 3.6, the relative velocity can be expressed as a function of the inlet velocity and thus of the volume flow rate. As expected, the flow can be considered incompressible.

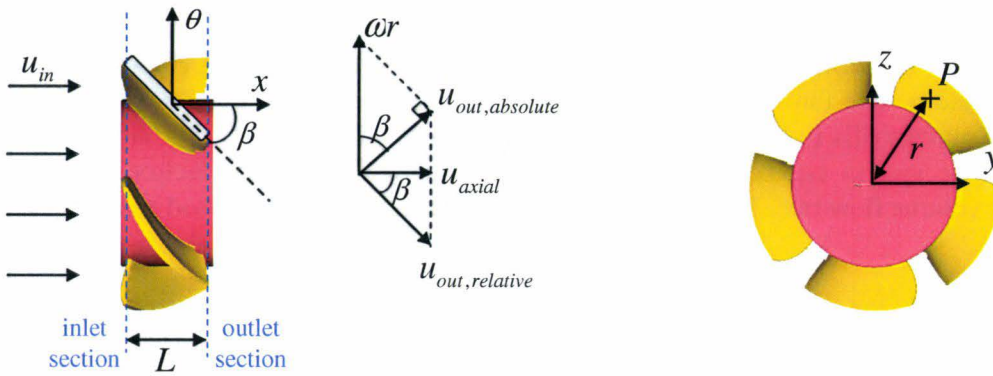


Figure 3.6. Lateral view of an electronic axial fan and velocity vector diagram (left); front view of fan (right).

The rotational body force methodology is based on the actuator disk theory of incompressible flow in axial compressors [128, 129]. To model the rotation of the blades, momentum source terms are set onto the fluid region swept out by the blades. Consequently, the detailed geometry of the blades is not requested. Only the fluid cells swept out by the blades are represented. In addition, one cell layer upstream and downstream, representing the inlet and outlet sections of air through the fan. Air approaches the fan with the velocity  $u_{in}$  assumed axial and uniform. The air velocity leaving the fan  $u_{out,absolute}$  is the vector sum of the rotational and relative velocities. The fan blades are assumed to have no curvature and the outlet relative velocity is assumed to be parallel with the mean blade angle. The outlet absolute velocity is assumed normal to the blade face. The equation of continuity conservation implies  $u_{in} = u_{axial}$ .

Moreover, the projection of the momentum conservation (equation 3.52) on the  $\theta$  and  $x$  axes provides the components of the force acting on the fluid region swept out by the blades, called rotational body force:

$$d\vec{F}_m = \vec{u}_{out,absolute} dm \quad (3.52)$$

The tangential and axial components of the rotational body force are given by, respectively:

$$F_{m,\theta} = (\omega r - u_{axial} \tan \beta) \rho u_{axial} A_{BF} \quad (3.53)$$

$$F_{m,x} = (\omega r - u_{axial} \tan \beta) \rho u_{axial} A_{BF} \tan \beta \quad (3.54)$$

The momentum sources  $s_i$  are given by the volume rotational body force. With  $c_k$  the load factor applied, the momentum source components can be consequently written as:

$$s_i = c_k \frac{F_{m,i}}{A_{BF} L} \quad (3.55)$$

The momentum sources are used in the general momentum and energy conservation equation for the computation of the flow in the electronic system. The system load curve is then calculated with equation 3.50, providing a first estimation of the operating point. The load factor in the momentum sources is adjusted to reach this operating point. The procedure is repeated iteratively until a stable operating point is reached.

### 3.5.2.2. Fan flow simulation with MRF

The MRF simulation consists of regarding the fluid cells swept out by the blades rotating at a constant angular velocity about a fixed axis, relative to the fluid upward and downward. In the fluid region swept out by the blades, a rotating reference frame is defined (relative frame). Upstream and downstream, a stationary inertial reference frame (absolute frame) is used. For more stability, an implicit formulation is used in this work at the interface between the rotating and the stationary reference frames. With the implicit formulation, the velocities on the stationary side of the interface are transformed into the rotating frame of reference and appear in the coefficients of the discretized momentum and pressure correction equations for the rotating side, and conversely. These transformations are done implicitly during each iteration. As a consequence, a matching mesh structure at the interface must exist for the implicit coupling. With  $\vec{r}$  referring to the position vector relative to the axis of rotation, the relative velocity  $\tilde{\vec{u}}$  in the rotating frame is the difference between the absolute velocity  $\vec{u}$  in the static reference frame and the rotational relative velocity:

$$\tilde{\vec{u}} = \vec{u} - \vec{\omega} \times \vec{r} \quad (3.56)$$

In the rotating reference frame, the momentum equations are modified by taking into account the inertial forces, sum of the Coriolis and centrifugal forces:

$$s_i = -\rho \left( 2\vec{\omega} \times \tilde{\vec{u}} + \vec{\omega} \times (\vec{\omega} \times \vec{r}) \right) \quad (3.57)$$

Moreover, the energy conservation equation is based on the rothalpy  $R$  (equation 3.58) instead of the enthalpy. More details about MRF simulation can be found in [20].

$$R = h_i + \frac{|\tilde{\vec{u}}|^2}{2} - \frac{(\vec{\omega} \times \vec{r})^2}{2} \quad (3.58)$$

The boundary conditions are defined as following:

- The spin of the fluid cell region, which is solved by the rotating reference frame, is assigned to the angular fan velocity. The wall boundaries attached to the cells of the rotating region have consequently the same relative velocity.
- The wall boundary of the rotor, which absolute velocity is the angular fan velocity, must have a spin number of zero.
- The wall boundary of the stator attached to the rotating cells, which is not rotating in the stationary frame, must be assigned of the opposite spin.

### 3.5.2.3. Flow through outlet grills with resistance elements

Solving the flow in each orifice of an outlet grill requires a lot of engineering time for the creation of CAD data due to the modeling of each orifice, the preparation of the CFD surface (clean-up) and the reparation of the volume mesh. Moreover, high computing times are expected to solve the flow in each orifice because of mesh requirements. An alternative is to model the outlet grill or perforated plate with a momentum resistance distributed over the plate. The pressure drop through the perforated plate is calculated based on the Forchheimer's law [130], in which  $K_{ij}$  and  $B_{ij}$  are respectively the permeability and Forchheimer tensors:

$$\nabla p_{stat} = - \left( \rho B_{ij} |\bar{u}_k| + \frac{\mu}{K_{ij}} \right) \bar{u}_i \quad (3.59)$$

It is assumed that in the region containing the porous resistance, the pressure and resistance forces are everywhere in balance. Firstly, the perforated plates are considered as an orthotropic porous medium, in which the main flow direction is assumed perpendicular to the outlet grill. With  $L$  the thickness of the perforated plate, the relationship between the plate pressure drop and superficial velocity  $u_i$  in direction  $i$  is given by:

$$\Delta p_{stat} = -L \left( I_{ij} |\bar{u}_k| + V_{ij} \right) \bar{u}_i \quad (3.60)$$

$I_{ij}$  and  $V_{ij}$  are diagonal tensors representing respectively the inertial and viscous contributions to pressure losses. Due to its small thickness, the outlet grill can be also modeled as a 2D planar resistance, called porous baffle. It is consequently assumed that the direction of the flow is unchanged as it passes through the baffle. With  $u_n$  the superficial velocity normal to the baffle surface, the plate pressure drop is provided by:

$$\Delta p_{stat} = -\rho \left( \alpha |\bar{u}_n| + \beta \right) \bar{u}_n \quad (3.61)$$

$\alpha$  and  $\beta$ , in analogy with  $I_{ij}$  and  $V_{ij}$ , describe the form drag and the permeability of the membrane respectively. In the porous region, the governing equations of the flow are solved simultaneously with those governing neighboring regions. The resistance term is treated in the governing equations of the porous region as a momentum source. Due to the discontinuity in pressure gradient at the porous-fluid interface, all gradients in cells adjacent to the interface are based on linear extrapolation of pressure.

### 3.6. Coupling codes strategies

As discussed previously, the different heat transfer modes are calculated separately with adapted codes and the thermal coupling problem is then solved with iterative methods. To ensure a correct time-dependent fluid-solid interaction, two main difficulties must be solved:

- Matching of the thermal boundary conditions at the fluid-solid interface;
- Method and frequency of the heat transfer coupling in transient solid computations, to obtain physical results within a reasonable computing time.

#### 3.6.1. Data transfer at the fluid-solid interface

In both solid solvers, the prescribed load heat flux is user-specified as boundary condition on particular nodes. In RadTherm, the radiation heat flux is solved together with the conductivity equation and must not be taken into account for the coupling. To solve the energy equation in PERMAS, the radiation heat flux is solved separately by POSRAD and must be coupled with PERMAS. The solid solvers, on one hand, and the flow solver, on the other hand, are using two different definitions of the convective heat flux at the interface, given respectively by equations 3.22 and 3.47. For a conservative process, the convective heat flux boundary condition is specified by a couple of two variables other than the solid temperature, i.e. the heat transfer coefficient and the film temperature, or the heat flux and the film temperature.

To provide the boundary conditions necessary for each heat transfer computation, the following data are transferred between the different codes at the interface:

- Sent by PERMAS for computation of convection with STAR-CD and radiation with POSRAD:

$$F_s = \{T_s\} \quad (3.62)$$

- Sent by RadTherm for computation of convection with STAR-CD:

$$F_k = \{T_k\} \quad (3.63)$$

- Sent by STAR-CD for computation of solid conduction with PERMAS or RadTherm:

$$G_f = \{h, T_{n1}\} \quad (3.64)$$

$$\text{or} \quad H_f = \{-\dot{q}, T_{n1}\} \quad (3.65)$$

- Sent by POSRAD for computation of solid conduction with PERMAS:

$$I_r = \{\dot{q}_{radiation}\} \quad (3.66)$$

### 3.6.2. Mesh mapping for matching boundary conditions

The boundary and initial conditions must be given on each surface element of the solid solver and on each volume element of the fluid solver. Typically, the meshes of both solvers differ in element type, element size and node location, which is referred as non-matching grids, as for example shown in figure 3.7.

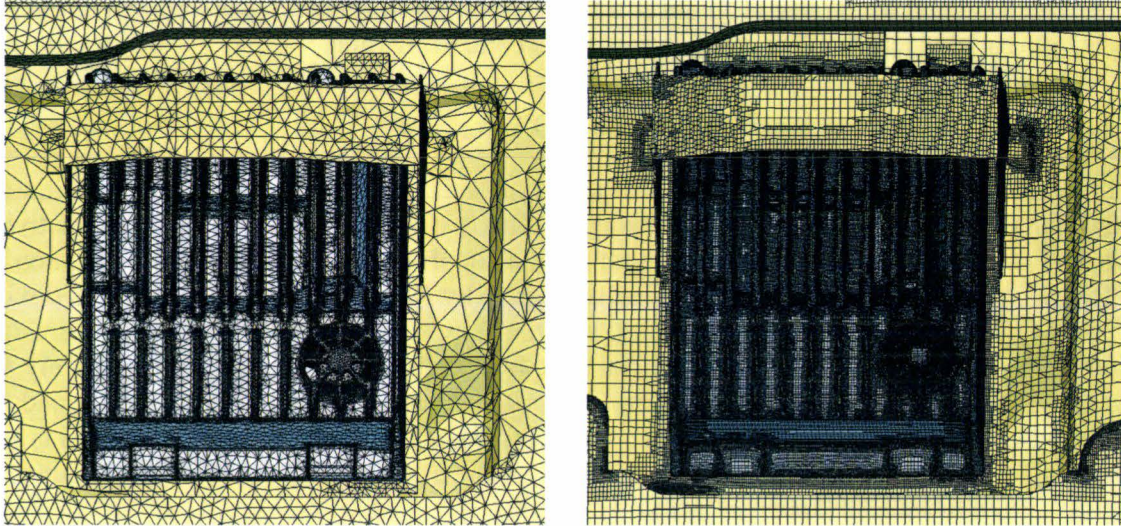


Figure 3.7. Sound amplifier in enclosure, non-matching grids for PERMAS (left) and STAR-CD (right) computations.

For data exchange between the two non-matching grids, the mesh mapping tool MpCCI is used. The exchange procedure is composed of three steps:

1. The pre-contact search, to speed up the next step.
2. The neighborhood search, which consists in searching the partner nodes on each grid with an association algorithm. For grid surfaces that are not completely superimposed, the partner nodes may not be found. These orphaned nodes can neither send nor receive any data from the other mesh. Instead, MpCCI sends user-defined default values or extrapolate values from non-orphaned areas.
3. The data integration through the interface, according to a field interpolation to ensure a conservative transfer.

Therefore, with corresponding nodes between the two non-matching grids, the data exchange allows a conservative transfer. The process of data transfer may not be conservative anymore with orphan nodes, which are assigned of a value different from the original one.

### 3.6.3. Transient coupling of heat transfer modes

For the transient computations of solid conduction, the convective and radiative heat transfer boundary conditions must be given at each time-step. Coupling boundary conditions at each time-step implies two types of time-consuming activities in the development process: firstly, the computation of convection and radiation at this time-step and secondly, the data transfer with mesh mapping. For reasonable computing times in the development process of a passenger car, different approaches are used in this work, a parallel discrete coupling and an

iterative serial coupling. Moreover, the following time scales must be discerned within the coupling process:

- The solid time-step  $t_s$  used for the transient computation of conduction;
- The coupling step size or coupling time-step  $t_c$ , corresponding to the time between two consecutive data exchanges;
- The simulation time, prescribed by the use case for the electronic device considered.

### 3.6.3.1. Convection and radiation heat transfer boundary conditions

The electronic equipment is usually tested according to a first period of pre-conditioning, followed by driving and idle phases (figure 3.8).

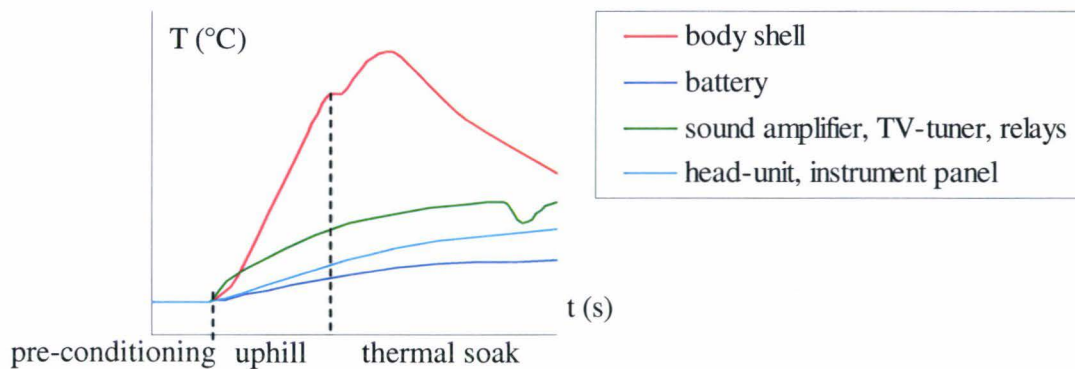


Figure 3.8. Typical temperature profiles in a vehicle for usual use cases.

At the end of the pre-conditioning period, the solid temperatures of the electronic enclosure have reached a permanent state. Due to the relatively small temperature gradient in the solid enclosure at this state, convection in the enclosure approaches the conductivity state with a stratified temperature distribution. The permanent state in the solid and the stratified state in the fluid are representative of the initial conditions of the transient computation. During the driving phase, the electronic ambient temperatures are increasing with a high temperature gradient due to the warm-up of the underhood and body shell. The optional fan may switch on rapidly and the period of natural convection in the electronic device may be consequently relatively short. Due to the activation of the fan, the forced convective flow yields to a local enhancement of the convective heat transfer in the electronic system. During idle, the underhood is first warming-up and then cooling down over the time during thermal soak. But, due to the high heat load capacity of the body shell and the partial isolation of the enclosure, the electronic ambient temperature is always increasing with time with a lower gradient. Furthermore, the thermal interaction between the numerous electronic systems assembled nearby each other in the enclosure leads to transient electronic case temperature. In electronic enclosures without fan, the time-dependent environment temperatures yield to an evolution of the natural convective flow over the simulation time, from oscillating to turbulent regimes. Experiments of the literature show that the time period for the flow to reach a full developed state ranges between several minutes for turbulent flows up to several hours for laminar and oscillating flows [104]. It means that, during the simulation time, the flow may never reach a fully developed regime, but only evolving between different bifurcations. During the simulation time, the temperatures in electronic enclosures may increase from 50°C up to 150°C locally, so that radiation heat flux must be predicted at different time-steps.

### 3.6.3.2. Parallel discrete coupling

A first transient thermal analysis is carried out from the stable initial state of the pre-conditioning period. Then, the convective heat transfer mode is evaluated at selected time-steps  $t^{n_i}$  and coupled back for a transient thermal analysis, as shown in figure 3.9. An estimation of the convective heat transfer between the coupled time-steps is provided by linear interpolation. The thermal analysis is performed by RadTherm and the coupling of boundary conditions is carried out by MpCCI. The convergence criterion for the co-simulation is the equivalence of the solid temperatures between two consecutive iterations. Moreover, as the heat transfer coefficient does not rely on the solution of the flow governing equations, it is not dependent on the temperature boundary conditions and thus constant whatever the time-step computed. To reduce coupling time, the couple  $G_f$  is consequently used as boundary condition for the transient thermal analysis.

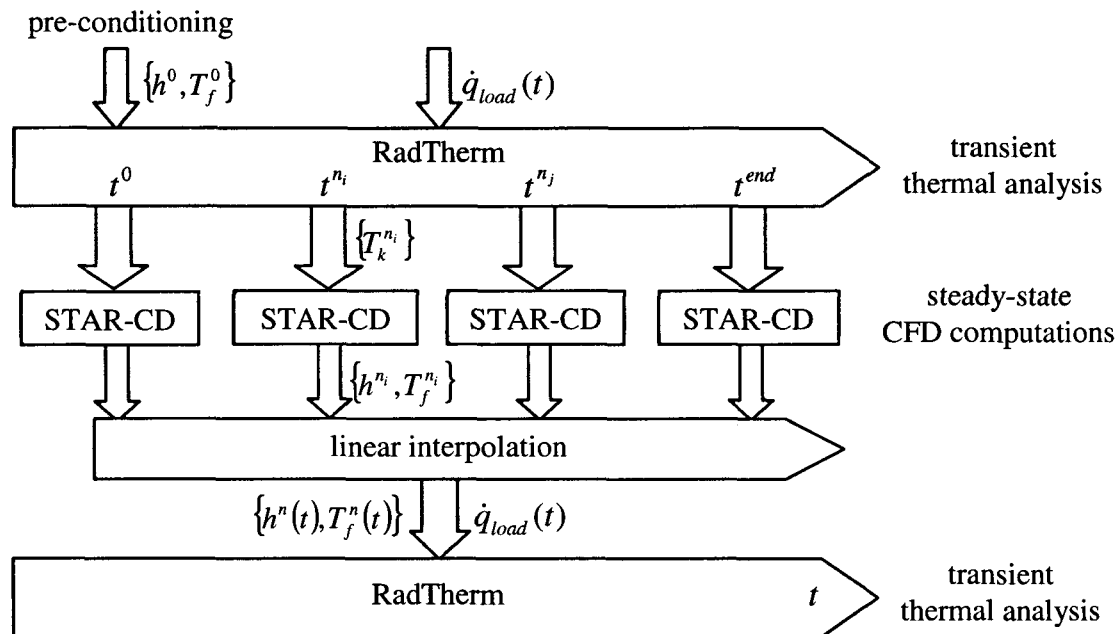


Figure 3.9. Parallel discrete coupling strategy for electronic enclosures without active cooling.

Using linear interpolation of the convective heat transfer assumes that the film temperature gradient is constant between two selected time-steps. Moreover, with steady-state computations of the flow at discrete time-steps, the development of the flow relies only on the prescribed initial and boundary conditions, whereas the natural convective flow in the passenger car highly depends on the flow structure at the previous solid time-step. Therefore, the steady-state numerical modeling of natural convective flows must be investigated in order to reproduce the correct flow structure and provide a reasonable heat flux. This is discussed in chapter 4. Because of the parallel coupling fluid-solid, the heat balance at a certain time-step does not rely on the coupling at a previous time-step and the conjugate heat-transfer problem can be reproduced only partially by this strategy. This co-simulation strategy is adapted to coupled problems, for which the characteristic time for heat transport by convection is strongly dependent on the simulation time. Consequently, the validity of this strategy will be verified on the case of the lead-acid battery in a spare-wheel cavity.

### 3.6.3.3. Serial staggered coupling

For electronic enclosures, in which the convective heat transfer is time-dependent over the simulation time, an iterative coupling of heat transfer data is required. The coupling code MpCCI is used in order to exchange automatically the interface boundary conditions at each coupling time. To compare the performance of both solid solvers for the computation of the conductive heat transfer mode, the iterative methodology has been primary tested with the coupling of PERMAS with POSRAD. Then, the methodology has been extended to the three codes coupling PERMAS, POSRAD and STAR-CD. The pre-conditioning phase is computed with STAR-CD, relying on the electronic environment temperature, which correspond to the permanent state. The resulting convective heat flux provides the initial conditions necessary to solve the solid. The natural approach for the iterative coupling is a sequential process, in which the flow is solved steady-state between two consecutive time-steps of the solid computation (figure 3.10).

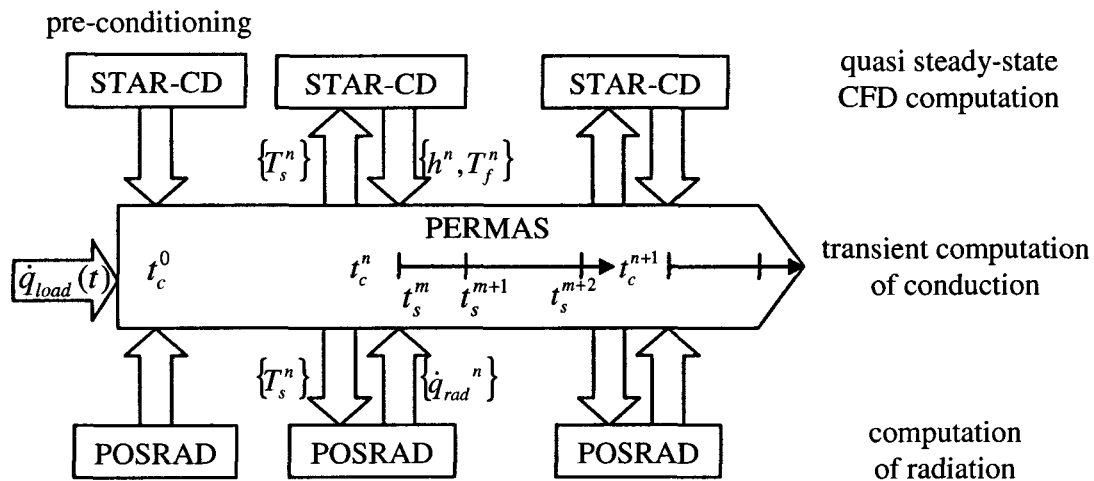


Figure 3.10. Serial staggered coupling strategy for electronic enclosures with active cooling.

This approach can be identified as a serial staggered coupling. The same approach is applicable for the coupling between PERMAS and POSRAD, which synchronization points for data transfer must be the same as for the coupling PERMAS-STAR-CD. The coupling time-steps are user-defined and must be set constant. The solid time-steps are prescribed by PERMAS depending on convergence results and are adjusted to fit the coupling time-steps. In this case also, the co-simulation has converged when the solid temperatures between two consecutive iterations are found equivalent. For small coupling time-steps that are closed to the solid time-steps, it is assumed that the flow state does not change drastically between two consecutive coupling time-steps. It is also assumed that only one computation of the flow is sufficient to reproduce the flow structure existing in electronic enclosures and provide a reasonable prediction of the heat flux. At a certain time-step, this heat flux balance in the solid takes into account the coupling fluid-solid at the previous time-step. The coupling strategy is therefore more accurate for solid temperature predictions than the previous one. It is also more time-consuming due to the numerous CFD computations and mesh mapping operations. As the flow computations provide an iterative evaluation of the convective heat flux, this co-simulation is reasonable in coupled problems, for which the characteristic time for convection is much smaller than the characteristic time for conduction. Therefore, this strategy will be validated on the case of the sound amplifier in a compartment under the passenger's feet.

### 3.7. Experimental methods used for numerical validation

In this work, experimental methods are required: first, to help at the comprehension of the heat transfer mechanisms in the electronic system and its environment in the vehicle; secondly for numerical modeling and finally, to provide experimental results for the validation of numerical models and strategies. The different methods employed are described in the following. Some measurements techniques are not applicable in a complex environment as in a passenger car. These techniques are consequently carried out with laboratory conditions and described in a first section. Experimental methods, for which results require the real environment of the passenger car, are presented in the second section.

#### 3.7.1. Laboratory conditions

In this section, measurements were performed in a laboratory, providing user-defined environment conditions. The measurements were carried out with the sound amplifier, which investigation is presented later in this work (chapter 5).

##### 3.7.1.1. Fan performance curve

As discussed previously, two numerical models for fan flow simulation are investigated in this work, the rotational body force model and the MRF model. The fan performance curve of the fan is required as boundary condition for the rotational body force model. Moreover, for the validation of the MRF model, the pressure rise created by the fan for a certain volume flow rate must be compared with experimental data. For an accurate comparison in a defined environment, the performance curve is used for the validation of the MRF model of the fan. The fan performance curve is measured in the test-rig allocated by the supplier of the fan. The suction type test-rig is in accordance with the standards [131] and satisfies the following requirements:

- Continuous inflow and outflow conditions for the tested fan;
- Uniform distribution with minimal perturbations of the flow in the gauge regions.

The test-rig can be seen in appendix, figure A.3.1.

Two measured performance curves are used in this work, providing a relationship between:

- The pressure rise through the fan  $\Delta p$  with the volume flow rate drawn by the fan  $\dot{V}_1$  ;
- The fan angular velocity  $\omega$  with the volume flow rate  $\dot{V}_1$  .

The fan pressure rise is calculated as the difference between the measured static fan pressure rise and the dynamic pressure at the fan inlet:

$$\Delta p = p_{stat2} - p_{stat1} - p_{dyn1} = \Delta p_{stat} - p_{dyn1} \quad (3.67)$$

$$\text{with: } p_{dyn1} = \frac{1}{2} \rho_1 u_1^2 = \frac{1}{2} \rho_1 \left( \frac{\dot{V}_1}{A_5} \right)^2 \quad (3.68)$$

The volume flow rate drawn by the fan  $\dot{V}_1$  can be expressed as a function of the density at the test-rig inlet  $\rho_0$  and of the static pressure rise through the orifice plate  $\Delta p_0$ . The densities are calculated from the ideal gases law using measured temperatures. The sensors and relating measurement uncertainties are given in appendix, table A.3.1.

### 3.7.1.2. Perforated plate pressure drop

As discussed previously, numerical models to predict the flow and pressure drop through grills or perforated plates are investigated in the following. For the comparison, experimental results are used providing the variation of the pressure drop through different perforated plates with the inlet flow velocity. The pressure drop and flow velocity have been measured according to [132] in the wind tunnel of the Steinbeis institute (appendix, figure A.3.2).

The compressor of the wind tunnel speeds up the air up to 36 m/s, which volume flow rate is controlled with a potentiometer. A diffuser is installed downstream followed by a straightener with honey comb to provide nearly turbulence-free conditions (turbulence grade under 1%) for the measurements. Downstream the diffuser is the measurement section with an inner diameter of  $D = 0.235$  m and a total length of 2.4 m. Finally, the flow is directed to the suction section of the fan. The perforated plate is fixed perpendicularly in the measurement section, clamped and sealed between two flanges.

The velocity of the inlet flow is measured with an Airflow TA5 hot wire anemometer positioned  $2.5D$  upstream of the perforated plate. A static pressure profile of the air flow over the measurement section is obtained with several sets of pressure tappings positioned regularly upstream and downstream the perforated plate. To avoid mutual interference, the tappings on the same side of the perforated plate are offset of  $45^\circ$ . Setra Multi-Sense differential pressure transducers are used to measure the difference between the static pressure of the different tapping probes and the ambient pressure. The wind tunnel test-rig and measurement uncertainties can be seen in appendix, table A.3.2.

### 3.7.1.3. Temperature distribution

In order to better understand the heat transfer mechanisms in the sound amplifier, the time-dependent distribution of its surface temperature has been measured with a thermographic camera. With a photovoltaic detector, the camera detects the infrared (IR) radiation flux received and converts it into an electronic signal proportional to the photon rate received. The IR radiation flux received is composed of the flux emitted and reflected by the sound amplifier then transmitted by the environment. It is also composed of the flux emitted by the environment. Of interest is the emitted radiation, which is dependent on the surface temperature of the sound amplifier and on the surface emissivity. To limit parasitic reflection, the sound amplifier is put in a carton box with high sidewalls. Moreover, black body calibration is performed to set the environment parameters. Due to the low temperature ranges of the sound amplifier, the emissivity of its surface is considered constant. To set the emissivity to a determined value, the surface of the sound amplifier has been painted in black.

The experiments were carried out at the Steinbeis-Transferzentrum institute of Stuttgart using the thermographic camera produced by Infratec. After calibration and in the range of temperature considered, the measurement accuracy is:  $a(T) = \pm 2K$ .

**3.7.1.4. Thermal resistance and capacitance**

As discussed previously, the conduction heat path from the heat generating semiconductors to the package of the electronic system is regarded at a macroscopic level using Fourier thermal transport modeling. A typical semiconductor package construction involves a die attach layer between the chip and the lead frame. With the package assembled on a cooler plate, which can be a heat sink or a PCB, the main heat path is assumed one-dimensional from the chip junction to the cold plate. Accordingly, the heat transfer in the main heat path can be modeled with a 1D network model involving thermal resistances and capacitances, as shown in figure 3.11.

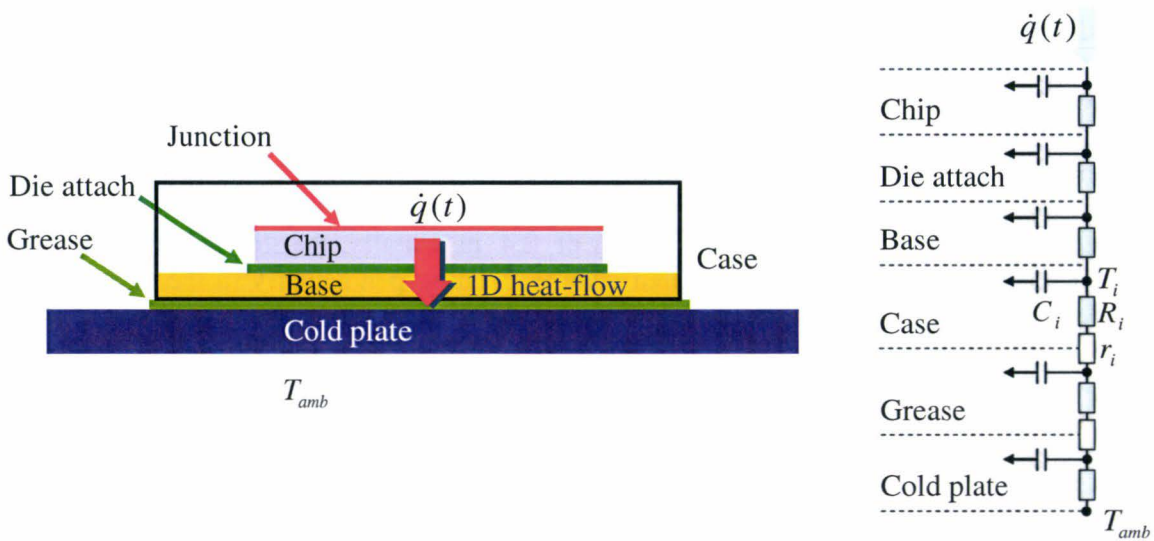


Figure 3.11. Main heat path in a semiconductor on a cold plate (left); network model in Cauer canonic form (right).

Without any contact pressure between the electronic component and the cold plate, the contact interfaces between the case, the grease and the cold plate may be imperfect. It is modeled by thermal contact resistances (equation 2.1). If the component is pressed on the cold plate, the contact at the interfaces with the grease might be almost perfect and the thermal contact resistances negligible. With  $A_i$  and  $H_i$  the cross-sectional area and the element height in the heat flow direction respectively, the conduction and convection thermal resistances of the element  $i$  are provided by, respectively:

$$R_i = \frac{H_i}{k_i A_i} \tag{3.69}$$

$$R_i = \frac{1}{h_i A_i} \tag{3.70}$$

The thermal capacitance is given by:

$$C_i = \rho_i c_{p,i} H_i A_i \tag{3.71}$$

The thermal resistances and capacitances were measured according to the JEDEC standard 51 with T3Ster (Thermal Transient Testing) [133] at the Steinbeis-Transferzentrum institute of

Stuttgart. The system composed of the semiconductor on the cold plate is placed in a still air chamber with a pre-conditioning phase of 400 s for steady-state ambient conditions. After calibration, a step function (Dirac excitation) in input power is used to warm-up the semiconductor. The transient thermal response to the excitation of the chip is continuously measured until reaching steady-state. The temperature variation of the chip is measured on-chip sensing using a TSP (temperature sensitive parameter) – e.g. threshold voltage for MOST semiconductors – as temperature indicator. The resolution of the transient temperature measurement is:  $r(t) = 1\mu s$ ; the accuracy:  $a(T) = \pm 0.01K$ . The repeatability of the measurements is checked for two input power values. Afterwards, the descriptive structure functions are extracted from the transient response function using the NID method [134]. The differential structure function provides the identification of each thermal resistance corresponding to each element constituting the system. The thermal capacitances are identified with the cumulative structure function.

### 3.7.2. Real environment in the vehicle

For the application of the coupling strategy discussed previously, target electronic devices are investigated in the real environment of the passenger car. Relating experimental methods are presented in this part.

#### 3.7.2.1. Local temperature

To validate the numerical results of the coupling code computations, local temperatures of the target electronic device and of its environment in the vehicle are measured with time. K-type thermocouples are used to measure solid temperatures, as well as air temperatures. In the measured range of temperatures, the tolerance range of K-type thermocouple (class 1) is:  $a(T) = \pm 1.5K$  [135]. Thermocouples are based on the Seebeck effect: a thermoelectric electromotive force (EMF) is generated between two conductors of different temperature. By inserting a voltmeter to measure the EMF, the copper connection between the thermocouple and the voltmeter introduce other unknown potentials. To cope with this problem, a reference junction is installed in the circuit with an isothermal conducting bloc, as shown in appendix in figure A.3.3. The reference temperature is measured by the resistance thermometer Pt 100, for which the variation of resistance with temperature is referenced. The use of extension cords is necessary for measurements in the vehicle and does not affect the results.

The resulting temperature measured by the thermocouple is the temperature of the thermocouple. To get a prediction of solid temperatures, thermocouples are mounted on the solid surface with thermal grease. Due to the application of the thermocouple on the solid surface, three types of measurement discrepancies may occur. First, the heat conduction path in the solid may be disturbed due to the application of the thermocouple. Moreover, depending on the quality of the application of the thermocouple, an air gap may exist between the thermocouple and the surface, which highly reduces the grease conductivity and leads to measurement errors. Furthermore, measurement cables near the surface may affect the flow situation and the convective heat transfer. This is a cause of measurement error for measurement of air and solid temperature. Over the experimental time prescribed by the use case, the quality of application of the thermocouple on the solid with the grease may change due to high temperature gradients, which leads to time-dependent errors. Similarly, small displacements of the thermocouple for air temperature measurement may disturb measurements over the time.

### 3.7.2.2. Volume flow rate

A smoke generator is used to determine the direction of the flow in the complex environment of a passenger car, in particular to find out leakages. To provide boundary conditions in electronic enclosures with leakage, the volume flow rate must be known. For the prediction of the volume flow rate in the vehicle, the air velocity is measured with an ultrasonic transit time flow meter. An ultrasonic pulse is sent in the presupposed flow direction and opposite the flow direction. Two transducers are used, one upstream of the other, acting as both transmitter and receiver for the ultrasonic beam. The travel time between both pulses is measured, providing the mean velocity of the fluid in the channel. The measurement accuracy is:  $a(u_{\infty}) = \pm 0.1 \text{ m/s}$ .

## 3.8. Partial conclusions

The characteristic time of temperature propagation by convection and conduction has been estimated for two electronic systems embedded in a vehicle, a sound amplifier and a battery. Multiple characteristic times have been found. Considering first the heat transport by convection, different regimes of the flow have been found depending on the scale of the physical system regarded. For relatively similar time scales of heat transfer, the system considered in this work is restricted to four different geometry levels: the semi-conductor case, the board, the electronic package and its environment in the vehicle. The temperature of an electronic system running under transient operating conditions and thermal loads is described by the Fourier equation. For the prediction of the convective heat transfer at the fluid-solid interface, the flow must be solved in the electronic system assembled in a vehicle. A continuous flow of a Newtonian expansible gas is assumed in electronic compartments. Moreover, for reasonable computing times in the development process, a steady-state approach is requested to solve the flow. Finally, for the transient coupling of conduction, convection and radiation, iterative codes coupling methodologies are proposed, which use different adapted codes for the prediction of each heat transfer mode:

- A discrete parallel coupling strategy to solve coupled problems, for which the characteristic time for heat transport by convection is strongly dependent on the simulation time;
- A serial staggered coupling strategy to solve coupled problems, for which the characteristic time for convection is much smaller than the characteristic time for conduction.

The steady-state approach used to solve the flow yields to approximations in the numerical simulation of buoyancy-driven flows and fan generated flows, because of their inherent time-dependence. The validation of the numerical models proposed to solve these flows is examined in chapter 4. Moreover, both coupling strategies imply certain assumptions, which range of validity is investigated in chapter 5.

---

## Chapter 4

# Validation and accuracy of the convective heat transfer prediction

To solve the coupled heat transfer modes in electronic enclosures, co-simulation strategies, which are based on adapted codes for the prediction of each transfer mode, have been discussed in chapter 3. For reasonable computing time in the development process, the convective heat transfer is computed using a steady-state approach. Moreover, both coupling codes strategies assume that one computation of the flow based on prescribed temperature boundary conditions is sufficient to reproduce the correct flow structure and provide a reasonable heat flux requested at the fluid-solid interface. Therefore, the range of validity of the steady-state approach must be examined in this chapter for the computation of typical flows encountered in electronic systems regarding these requirements. The steady-state numerical methods proposed previously for the treatment of buoyancy-driven flows, fan generated flows and grill flows are investigated in the following. In particular, the requirements towards mesh refinement and turbulence modeling must be determined for an accurate prediction of the convective heat transfer.

### 4.1. Buoyancy-driven flows

As discussed previously, depending on the packaging temperature in the vehicle, the Rayleigh number in electronic enclosures is moderate – in the range  $[10^4; 10^6]$  – and the flow is supposed to evolve between an oscillatory and a turbulent state. Due to the lack of experimental results for similar electronic packaging geometry in a passenger car, the investigation is conducted for the well-documented extended Rayleigh-Bénard convection in an enclosure with conducting sidewalls. This configuration is similar to an electronic package in the vehicle and may provide an estimation of the accuracy of the steady-state approach.

Let us consider the flow in a cavity of finite extent, first isothermal and suddenly subjected to a constant heating on the lower surface. Below a critical temperature difference, the flow can be described by a linear heat conduction profile, characterizing the basic state. At a critical Rayleigh number, a buoyancy-driven cellular convection will occur, proceeding from subcritical motions starting at the lateral walls. The onset of convection results from

instabilities of the vertical temperature stratification and is accompanied by an increase of heat flux in the fluid. As each local perturbation stretches progressively into the whole flow field, the Rayleigh-Bénard problem is an absolutely unstable stability problem. The critical Rayleigh number can be determined with the linear stability theory for horizontal cavities. To solve the initial value problem of the fluid and cope with boundary condition dependency, iterative methods are usually used based on the vorticity and stream functions [136] and on the Galerkin method [137]. Following the onset of convection, a stable steady-state pattern is produced, composed of transverse contra-rotating eddy cells. In a cavity of moderate aspect ratio, the stability of the flow structure is mostly affected by non-linear effects, e.g. the transition in supercritical wavelength. Several experiments showed that the wavelength of the flow motion increases discontinuously as soon as the Rayleigh number is supercritical [138]. Due to the range of non-unique wavelengths, different eddy patterns may form in the cavity of a certain aspect ratio, characterized by discrete bifurcations for flow transition. It was shown, that the preferred convective structure is inhibited by the initial flow field distribution and the thermal boundary conditions [139]. Numerically, the velocity and temperature fields resulting for a given Rayleigh number are often used as initial conditions for the solution at a slightly increased Rayleigh number. Thus, the solutions are successively calculated by increasing quasi steady-state the Rayleigh number [104, 140]. For Rayleigh numbers beyond the supercritical range, time-dependent skewed varicose disturbances yield to an unstable convective flow, causing first a periodic motion of the eddy patterns. The resulting oscillatory convection proceeds from alternatively exchange of mass between the cells, inducing an axial velocity to the cells [103]. Further bifurcations, attributed to strongly non-linear effects, occur for increasing Rayleigh number and the periodic patterns are replaced by quasi-periodic, then non-periodic slow flow motions (weak turbulence) and finally non-periodic stochastic fast flow motions (turbulence). Due to the strong interaction between boundary layers and turbulent core flow, the turbulent heat flux is directed upward in the core, often resulting in strongly anisotropic and counter gradient heat fluxes. For the transient computation of turbulent natural convection, several turbulence models were verified using DNS [141], LES with SGS (subgrid scale) [142] and URANS (unsteady RANS) [143] models. Several attempts at steady-state computations with RANS turbulence models [144, 145, 146] showed some limitations to the prediction of the velocity profile in the near-wall region and of the turbulent heat flux in the whole cavity.

Because of the limitations aforesaid, the accuracy of steady-state RANS computations must be investigated in respect with heat transfer prediction in the co-simulation process. In particular, several aspects of the steady-state model are questioned:

- The capacity of the steady-state approach to determine oscillatory and turbulent flows and the effect of initial conditions on the convective structure;
- The accuracy of the prediction of the velocity profile and convective heat transfer;
- The determination of appropriate turbulence modeling;
- The convergence of steady RANS computations, due to the inherent unsteadiness of buoyancy-driven flows in enclosures with low turbulence level in the core region.

In the following, the results obtained with stationary computations in STAR-CD are compared with experimental and numerical studies from the literature considering two benchmark cases: a rectangular box [104, 147] and a cubical cavity [106, 148]. In the first paper, the investigation focuses on the development of the 3D convection in different rectangular cavities by analyzing the flow structure. The second paper reports the heat transfer

rate in a cubical cavity for a large Rayleigh number range, covering laminar, oscillating and turbulent convection. A brief description of the investigations is given in table 4.1.

Results from the literature	numerical, Kirchartz [104] experimental, Jäger [147]	numerical, Pallares [106] experimental, Leong [148]	
Numerical method	explicit FD (finite-difference)	FV (finite volume) turbulence model: LES, SGS	
Initialization	linear stability analysis: Galerkin method ( $0^\circ$ ) Galerkin/FD (tilted cavity)	velocity and thermal fields obtained for another Rayleigh number [140]	
Cavity aspect ratio (L:W:H)	10:4:1	4:2:1	1:1:1
Cavity inclination	from $0^\circ$ (horizontal) to $60^\circ$	$0^\circ$ (horizontal), $45^\circ$ , $90^\circ$	
Rayleigh number range	$[10^3; 10^4]$	$[10^4; 10^5]$	$[10^4; 10^5]$ $[10^6; 10^8]$
Flow regime	laminar	oscillating-turbulent	laminar-oscillating    turbulent

Table 4.1. Numerical and experimental investigations from the literature for the validation.

#### 4.1.1. Structure of the flow, rectangular box

In this part, the capacity of the steady-state approach to reproduce the structure of the buoyancy-driven flow is investigated in comparison with [104, 147] for  $Pr = 0.71$ .

##### 4.1.1.1. Numerical model

The numerical model for the computation with STAR-CD is based on the experiments of Kirchartz [104]. In the experiment, the sidewalls were made of plate-glass plane, thus not perfectly conducting. In respect with the thermal boundary conditions at the sidewalls, the numerical model consists of a fluid cell enclosed in thin glass plates and differentially heated by copper plates maintained at constant temperature, as illustrated in figure 4.1. In this case, the vertical temperature distribution is nearly linear at the sidewalls. Buoyancy forces are modeled as described in section 3.5.1. For high Rayleigh numbers and differential temperature, the air molecular viscosity and conductivity are defined with polynomials as function of temperature.

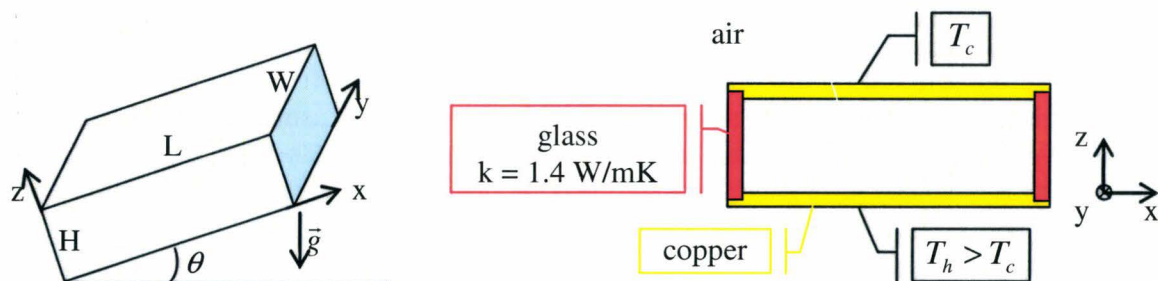


Figure 4.1. Numerical model of the inclined rectangular cavity; fluid layer and coordinate system (left); (x,z) section (right).

#### 4.1.1.2. Initialization

The flow is supposed initially isothermal without motion. Whatever the Rayleigh number computed, steady-state 3D simulations with this initialization provide longitudinal rolls in the horizontal 10:4:1 and 4:2:1 cavities instead of the transversal ones as described by [104]. Several experiments [123, 149] reported the unsteady and dynamic nature of supercritical bifurcations, characterized by a complete reorientation of the flow, corresponding to the change in wavelength. The reproduction of the instabilities leading to the reorientation of the flow is not possible with steady-state computations. However, due to the strong effect of thermal boundary and initial conditions on the instability mechanisms, different types of initialization are investigated in the following to reproduce the correct flow structure described in the literature. Here, the initialization aims at working as the introduction of a perturbation to initiate the motion of the fluid. First, a 2D computation is carried out in the plane perpendicular to the axis of the expected transversal rolls. The resulting flow and thermal fields are used as initialization for the 3D computation. The boundary conditions of the 3D computation are left unchanged (differential temperatures at the top and bottom plates). Two different types of boundary conditions are investigated for the 2D computation:

- with differential temperature boundary conditions at the top and bottom plates, called differential temperature initialization (figure 4.2);
- with a wall movement condition at the top and bottom plates, called moving wall initialization. Velocity vectors  $\vec{u}_x$  of x-component only and constant value are assigned at the middle of the expected convection rolls, as shown in figure 4.2.

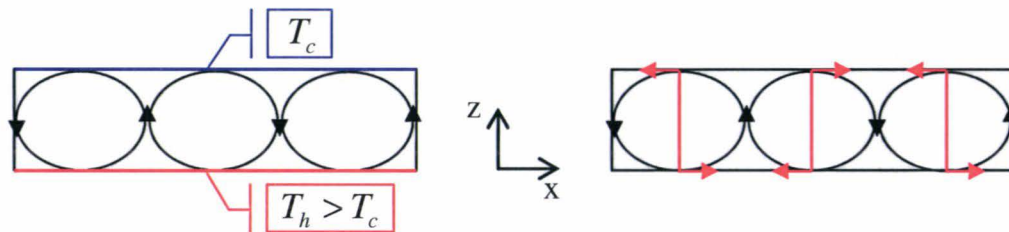


Figure 4.2. Initialization type for the 2D computation, e.g. transverse rolls in the 4:2:1 cavity; differential temperature (left); moving wall (right).

#### 4.1.1.3. Mesh and turbulence model

A mesh refinement study has been carried out in a horizontal cavity with several uniform o-grids, varying the number of cells in the boundary layer [150]. For the computation of the laminar convection in the cavity 10:4:1, a coarse mesh using  $210 \times 84 \times 21$  grid nodes provides an underestimation of 3% of the maximum vertical velocity component computed by [104] and is therefore selected for the validation study. Similar results are found for the computation of the oscillatory convection in the cavity 4:2:1 with a coarse mesh using  $88 \times 44 \times 22$  grid nodes and three cells in the boundary layer. However, a fine mesh using  $300 \times 152 \times 75$  grid nodes and 15 cells in the boundary layer is required for the computation of the turbulent convection in the cavity 4:2:1.

The different k- $\epsilon$  and k- $\omega$  type turbulence models listed in section 3.4.2 have been examined in terms of flow structure and velocity distribution for the computation of turbulent convection occurring for Rayleigh numbers above  $Ra = 7 \times 10^4$  [150]. A very similar velocity

distribution has been obtained with these models, providing a prediction of the maximum vertical velocity component within 3% in comparison with [104]. As the standard low-Re k- $\epsilon$  model provides the best convergence of the turbulent energy and dissipation, it is selected for further computations of turbulent convection. In the range of Rayleigh number  $[3.4 \times 10^4; 5.2 \times 10^4]$ , the flow is oscillating en route to turbulent convection. To determine if a turbulence model is necessary for the computation of this transitional regime, the mean turbulent viscosity computed with the standard low-Re k- $\epsilon$  model is compared with the molecular viscosity. Due to the negligible value of the turbulent viscosity at  $Ra = 4 \times 10^4$ , the oscillating convection is computed laminar in the following.

#### 4.1.1.4. Horizontal cavity

##### i. Steady-state natural convection

Firstly, the steady-state flow is computed in the 10:4:1 cavity with conductive sidewalls for both initialization types at a Rayleigh number of  $Ra = 4 \times 10^3$ . The differential temperature initialization provides a transversal ten-roll structure, instead of the transversal nine-roll structure described by [104]. Therefore, the orientation of the flow can be reproduced with this initialization but the wavenumber of the resulting patterns is not correctly evaluated. With the moving wall initialization, a structure with nine rolls is obtained, as shown in figure 4.3.

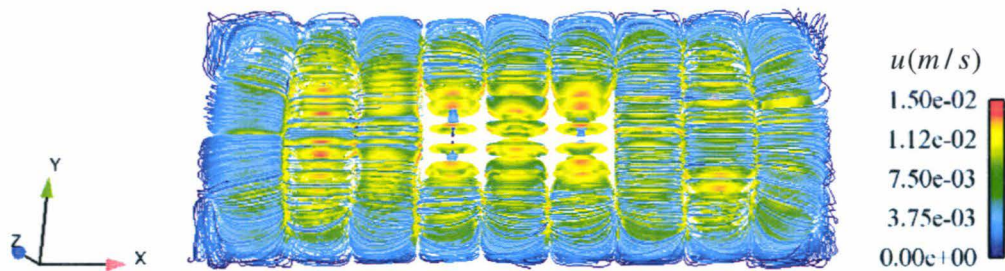


Figure 4.3. Streamlines at  $Ra = 4 \times 10^3$  in the horizontal cavity 10:4:1 with moving wall initialization.

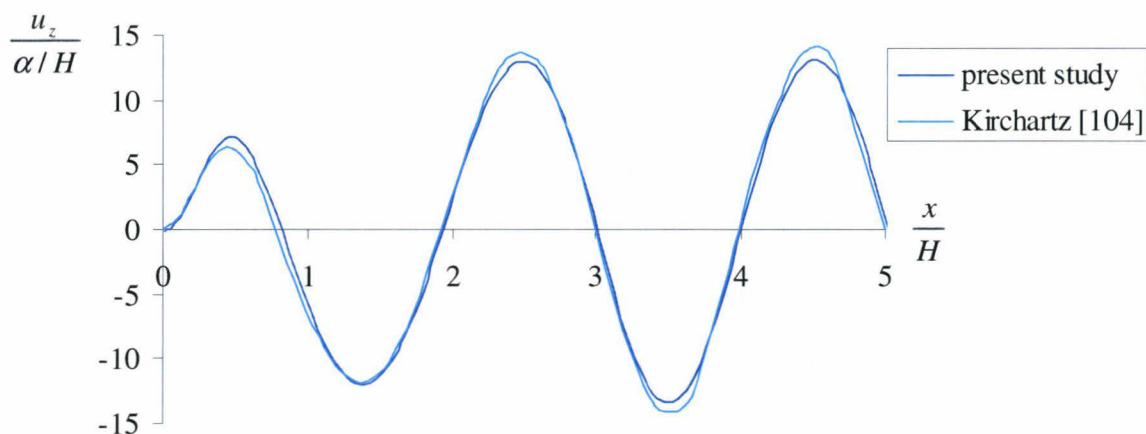


Figure 4.4. Vertical velocity component at  $Ra = 4 \times 10^3$  for  $y/W = 0.5$  and  $z/H = 0.5$  in the horizontal cavity 10:4:1 with moving wall initialization.  
 — Present study; - - numerical results from Kirchartz [104].

The structure of the inner flow is 2D, but in areas where the rotating fluid interacts with the sidewalls, velocity components develop parallel to the rolls' axis showing the effect of inertial forces conjugated with axial pressure gradients. Buoyancy forces close to the wall support this effect. Moreover, corner vortices develop next to the sidewalls resulting from temperature gradients normal the vertical walls, so called thermal-end effect. Both 3D effects are representative of the influence of the conducting lateral walls. The flow amplitude of each roll is evaluated with the vertical velocity component in the horizontal mid-plane (figure 4.4). It is found in very good agreement with the numerical results from the literature. Therefore, the dependency of the flow structure on the type of initialization shows the ability of the numerical model to react to a perturbation introduced in the initial flow and thermal field.

#### ii. Time-dependent natural convection

Secondly, the time-dependent convection is computed for Rayleigh numbers in the range  $[4 \times 10^4; 2.5 \times 10^5]$ . Computing successively the flow by increasing quasi-stationary the Rayleigh number is not possible in the parallel discrete code coupling. Consequently, the flow is not initialized based on the thermal and flow fields solution for a slightly lower Rayleigh number, but using a 2D initialization. Due to the high numerical effort of the moving wall initialization, the differential temperature initialization is used instead.

For Rayleigh numbers in the range  $[7 \times 10^4; 2.5 \times 10^5]$ , the full convergence of mass, turbulent kinetic energy and dissipation residuals could not be reached with steady-state RANS computations. Different flow structures are obtained depending on the Rayleigh number:

- For  $Ra = 4 \times 10^4$ , the steady-state computation provide a four-roll structure, although a three roll structure is experimentally found in the literature. The structure is characterized by strong inertial and thermal-end effects. The thermal-end effects yield to larger outer rolls at the sidewalls, which rotate slower than the inner ones. This is a characteristic of the oscillating convection.
- For  $Ra = 7 \times 10^4$ , a full 3D structure is obtained, composed of two transverse rolls at the sidewalls and two half counter-rotating toroidal rolls in the middle. The structure obtained is not stable during the RANS computation; it evolves progressively with the increasing numbers of iterations into a two longitudinal rolls structure.
- For  $Ra = 1.5 \times 10^5$  and  $Ra = 2.5 \times 10^5$ , a complex structure is found based on two lateral rolls, which is in agreement with the results from the literature [104]. Due to high temperature gradients at lateral walls, secondary superimposed longitudinal rolls are forming along the longest sidewalls at  $Ra = 1.5 \times 10^5$ . These secondary rolls of significant amplitude cover the whole flow field at  $Ra = 2.5 \times 10^5$ . Because of the secondary flow, the mass transfer between both lateral rolls occurs mainly in the middle of the box, accompanied by higher velocities.

The flow structures can be seen in appendix, in figures A.4.1 to A.4.4. Moreover, the maximum vertical velocity component in the mid-plane  $z/H = 0.5$  is compared with the literature [104, 147] in figure 4.5. It shows a good agreement over the whole range of Rayleigh numbers.

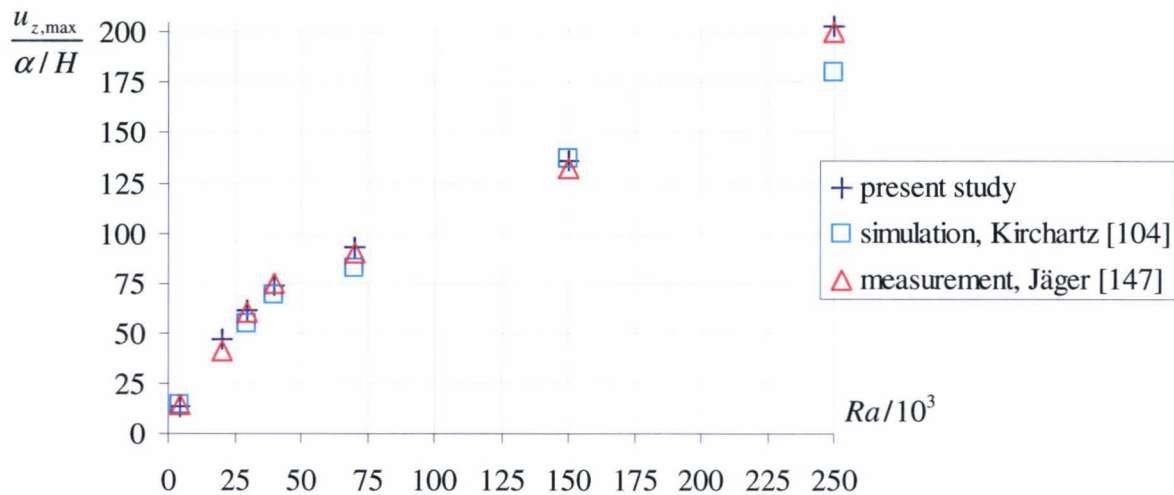


Figure 4.5. Maximum vertical velocity in the mid-plane  $z/H = 0.5$  of the cavity 4:2:1.  
 + Present study;  $\square$  numerical results of Kirchartz [104];  $\triangle$  experimental results of Jäger [147].

#### 4.1.1.5. Tilted cavity

Different electronics packages in a passenger car are inclined, e.g. under the passenger feet, where the package is inclined with an angle of  $50^\circ$  and in the rear-end compartment, where it is vertical. Thus, it is important to consider the effects of inclination on the buoyancy-driven flow. In order to compare with the results from Kirchartz [104], the flow is computed for  $Pr = 7$  in the tilted 10:4:1 cavity for a constant vertical component of the Rayleigh number:  $Ra_z = 3 \times 10^3$ . The actual Rayleigh number is expressed by:  $Ra = Ra_z / \cos \theta$ . Due to the effect of shear forces at sidewalls, the onset of convection in an inclined cavity is fully 3D. Therefore, the flow is not initialized from 2D flow and thermal fields as previously, but it is assumed to be initially at rest and isothermal. Two angles of inclination are investigated:  $\theta = 30^\circ$  and  $\theta = 50^\circ$ . In the corresponding range of Rayleigh numbers, the flow is found in the literature steady-state in the supercritical regime. The structures obtained for both inclinations are marked by the superposition of a single transverse roll formed by the upward motion at the warm lower wall, which characterizes the basic flow, and four longitudinal rolls of cellular convection, as shown in appendix in figure A.4.5. For an inclination of  $\theta = 50^\circ$ , the intensity of the basic flow increases while the cellular convection declines, which is in agreement with the numerical results from the literature. The amplitude of the basic and cellular flows in terms of normalized vertical velocities is compared with the literature (figure A.4.6 in appendix). Slight discrepancies are noticeable for the secondary flow at each inclination – basic flow at  $\theta = 30^\circ$  and cellular convection at  $\theta = 50^\circ$ .

#### 4.1.2. Heat transfer rate, cubical cavity

A cubical cavity with conductive sidewalls of a height of 0.13 m is differentially heated from below with constant temperature boundary conditions, as shown in figure 4.6. To ensure a linear vertical temperature distribution on the sidewalls as in the associated experiment [148], the conductivity of the glass sidewalls is increased. The buoyancy forces are modelled as for the rectangular box. In the following, results are presented for a horizontal cubical cavity. Numerical results obtained for an inclined cavity are shown in a companion paper [150].

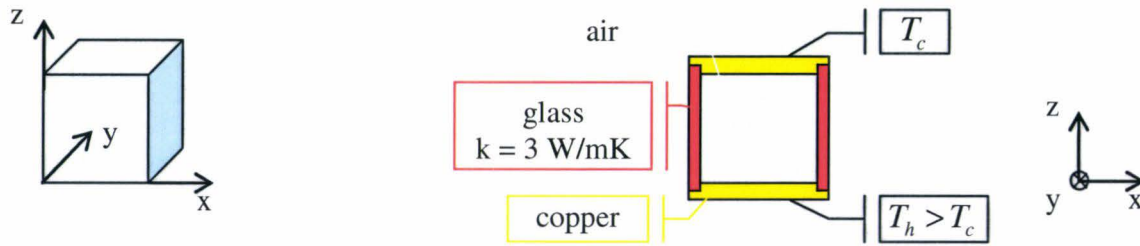


Figure 4.6. Numerical model of the cubical cavity; fluid layer (left); (x,z) section (right).

#### 4.1.2.1. Initialization

The flow is supposed first isothermal and at rest. The lower and upper copper plates are submitted to the desired temperature gradient and the lateral walls to a stratified temperature distribution by conduction. This type of initialization provides for the cubical cavity a good agreement compared to the literature over the range of Rayleigh number considered. Contrary to the stationary computations in horizontal rectangular cavities, for which a 2D initialization is necessary, a 2D initialization is not required for the prediction of the flow field in a cubical cavity. This proves that the instability mechanism is strongly modulated by the proximity of lateral walls, as also demonstrated in the literature [104, 123]. In this particular case, there is no preferred horizontal direction for the development of the pattern, so that more stable patterns may occur than in a rectangular box.

#### 4.1.2.2. Turbulence modeling

The different turbulence models listed previously are investigated in terms of heat transfer prediction for Rayleigh numbers of  $Ra = 10^6$  and above. The mean Nusselt number computed with a fine mesh using  $109^3$  grid nodes is examined for each turbulence model. The results are shown in figure A.4.7 in appendix. The standard low-Re k- $\epsilon$  model provides the best agreement with the results from the literature; thus, it is chosen for further computations. At  $Ra = 10^5$ , an oscillating structure is found in the literature. A computation with the standard low-Re k- $\epsilon$  turbulence model at  $Ra = 10^5$  shows again that the turbulent viscosity is negligible compared to the molecular viscosity. Moreover, the Nusselt number shows a better agreement with the literature using the laminar approach. Consequently, the flow is considered laminar at  $Ra = 10^5$  in the following.

#### 4.1.2.3. Horizontal cavity, flow structure

For a given mesh and Rayleigh number, the structure obtained with the steady-state computation is found to evolve with the number of computed iterations. After a first apparent convergence of the residuals, a first structure is obtained. With further iterations, the residuals decrease suddenly and stabilize again, yielding to another structure. The first structure predicted by the stationary computation, independent of the Rayleigh number, is a nearly toroidal vortex ring (bimodal flow). This pattern has been found stable elsewhere [140, 151] in a cavity with adiabatic sidewalls, occurring in the range of Rayleigh numbers  $[8 \times 10^3; 10^4]$ . The prediction of this structure in the present study may result from the initial boundary conditions at the sidewalls. Indeed, the temperature distribution at the fluid lateral walls cannot be initially linear, as conduction in the sidewalls has not been computed yet. About 50 iterations are necessary for the fluid lateral walls to reach a perfectly conducting state (pre-conditioning).

A summary of the structures obtained in the present study in comparison with Pallares [106] can be found in Table 4.2 and in appendix, figures A.4.8 to A.4.10. The structures obtained after transition are in good agreement with the literature over the range of Rayleigh number considered  $[10^4; 10^7]$ .

$Ra$	Literature, Pallares [106]	Structure, present study	
		primary	after transition
$10^4$	S1: single roll, which axis is parallel to the horizontal edges	S4: nearly toroidal roll	S1
$4 \times 10^4$	S1 S5: four-roll structure	S4	S1
$10^5$	S5	S4	S3: Single main roll with double inner rolls system
$10^6$	Two main counter rotating vortex rings and four small vortex tubes along the y-edges of the cavity	S4	Two counter rotating vortex rings (VR) with impingement in the middle of the cavity
$10^7$	/	S4	Structure similar to VR composed of two main vortex rings of variable diameter

Table 4.2. Flow structure obtained in a horizontal cubical cavity in comparison with literature.

#### 4.1.2.4. Heat flux distribution

The local distribution of heat flux is compared with the literature over the range of Rayleigh numbers considered, as shown in appendix, figures A.4.11 to A.4.15. For comparable structure at a given Rayleigh number, the distribution of heat flux on the lower and upper walls, independent of the mesh computed, is in very good agreement with the numerical results of Pallares [106] for Rayleigh numbers in the range  $[10^4; 10^5]$ . However, for higher Rayleigh numbers ( $Ra = 10^6$  and  $Ra = 10^7$ ), the distributions computed in the present study show more irregularities than described in [106]. These irregularities may be representative of a higher rate of turbulence or smaller scale structures in the present computations than in the literature. In respect with the stationary state computed, the local heat flux integrated over the surface composed of the six walls of the cavity is:

$$\bar{q}|_{z=0} + \bar{q}|_{z=H} + \bar{q}|_{x=0} + \bar{q}|_{x=H} + \bar{q}|_{y=0} + \bar{q}|_{y=H} = 0 \quad (4.1)$$

At low Rayleigh numbers ( $Ra = 10^4$  and  $Ra = 4 \times 10^4$ ), the mean heat flux on the lateral walls is found equal to zero. However, the mean heat flux on the lower wall is different from the mean heat flux at the upper wall for  $Ra = 10^5$  and above. In the corresponding literature, the structure S3 is found to generate different averaged heat transfer rates at the horizontal walls, which confirms the difference between lower and upper walls found at  $Ra = 10^5$  in the present study. For higher Rayleigh numbers, for which the flow is computed turbulent, a full

convergence of the residuals could not be reached in the present study independently of the mesh used. Hence, the averaged heat flux on the upper or lower wall varies of maximum 8% at  $Ra = 10^6$  and 12% at  $Ra = 10^7$  within 50 consecutive iterations after stabilization of the residuals. The large variation of the heat flux over the iterations shows the limit of the computation for turbulent state of the flow and can be interpreted here as a numerical error. To improve the residuals convergence, an URANS computation has been performed using a time-step of  $10^{-3}$  s with 500 inner iterations over a running time of  $10^{-1}$  s. The resulting mean Courant number is of  $4 \times 10^{-2}$ , showing that the Von Neumann stability conditions are fulfilled and that the round-off error is not amplified. With these conditions, the results of the URANS computation show a good convergence of the residuals, but the strong variations of the averaged heat flux on the lower and upper walls is still noticed over the inner iterations. Therefore, the divergence of heat flux over the iterations does not result from the steady-state approach, but may merely rely on turbulence modelling. This will be examined in the following.

#### 4.1.2.5. Mesh independency for heat flux prediction

Different structured and uniform grids using solely hexahedral cells have been generated to investigate the mesh independency for heat flux prediction, as shown in table 4.3. The different grids can be seen in appendix, figure A.4.16. The range of  $y^+$  values found after computation is also shown, indicating that the thermal and velocity fields may be resolved properly in the boundary layer by the standard low-Re  $k-\epsilon$  turbulence model.

Grid	Number of nodes $N_x \times N_y \times N_z = N^3$	Boundary layer		
		Number of cell layers	Growth rate	Range of $y^+$ values
BL9	$72 \times 72 \times 72$	9	1.5	$[10^{-2}; 2.4]$
BL10	$79 \times 79 \times 79$	10	1.5	$[10^{-2}; 1.3]$
BL12	$85 \times 85 \times 85$	12	1.5	$[10^{-2}; 1.2]$
BL15	$94 \times 94 \times 94$	15	1.5	$[10^{-2}; 1.2]$
BL20	$109 \times 109 \times 109$	20	1.5	$[10^{-2}; 0.8]$

Table 4.3. Grids generated for the investigation of mesh independency in the cubical cavity.

In order to verify the validity of the steady-state approach for heat flux prediction of buoyancy-driven flows, the averaged Nusselt number on the lower and upper walls is compared with the literature [106, 148] for reasonable local distribution of heat flux, i.e. after transition. The averaged Nusselt numbers on the lower or upper wall are provided by, respectively:

$$\overline{Nu}|_{z=0} = \frac{H}{k(T_h - T_c)} \bar{q}|_{z=0} \quad (4.2)$$

$$\overline{Nu}|_{z=H} = -\frac{H}{k(T_h - T_c)} \bar{q}|_{z=H} \quad (4.3)$$

For an estimation of the averaged Nusselt number independently of the grid used for the computation, an extrapolation is performed in the Richardson chart, providing a theoretical value of the averaged Nusselt number for a grid using an infinite number of nodes, as illustrated e.g. in figure 4.7. The extrapolation of the Nusselt number in the Richardson chart at other Rayleigh numbers can be found in appendix, figures A.4.17 to A.4.20.

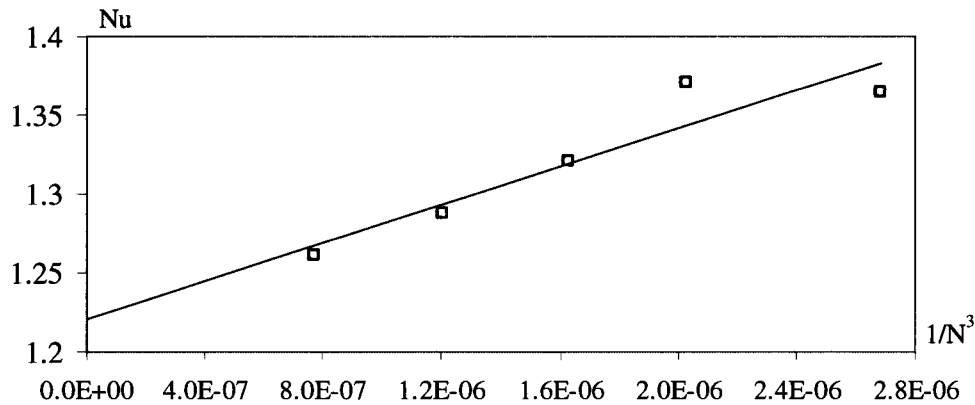


Figure 4.7. Extrapolation of the averaged Nusselt number on a horizontal wall in the Richardson chart,  $Ra = 10^4$ , structure S1.

The comparison with the literature of the averaged Nusselt number independent of the grid is shown in table 4.4. The error resulting from the large variations in heat flux at  $Ra = 10^6$  and  $Ra = 10^7$  is indicated. Moreover, the fluid mean temperature  $T_m$  of the present computations is also specified in table 4.4.

$Ra$	$Nu$ , Leong [148]	$Nu$ , Pallares [106]	$\overline{Nu}$ , present study	
	upper plate		lower plate	upper plate
$10^4$	$1.24 \pm 0.013$	1.18	1.22	
$4 \times 10^4$	$2.02 \pm 0.017$	2.03	2.19	
$10^5$	$3.51 \pm 0.035$ ( $T_m = 298K$ ) $3.92 \pm 0.042$ ( $T_m = 308K$ )	3.38	4.13 ( $T_m = 305K$ )	3.78 ( $T_m = 305K$ )
$10^6$	$7.88 \pm 0.091$	$7.50 \pm 0.05$	$7.43 \pm 0.59$	$7.54 \pm 0.60$
$10^7$	$15.4 \pm 0.19$	/	$13.5 \pm 1.62$	$14.2 \pm 1.70$

Table 4.4. Averaged Nusselt number on the horizontal walls in comparison with literature.

A good agreement is found for Rayleigh numbers in the range  $[10^4, 10^5]$ ; in particular, the difference between the values of Nusselt number measured by Leong [148] and the present predictions are of 2% for  $Ra = 10^4$ , 8.5% for  $Ra = 4 \times 10^4$  and 3.5% for  $Ra = 10^5$ . For Rayleigh numbers in the range  $[10^6, 10^7]$ , the range of error in the present computations is too large for a reasonable comparison with the results found in the literature.

#### 4.1.2.6. Nusselt number and temperature profile of turbulent flows

In Rayleigh-Bénard cells, different studies reported the scaling of thermal and kinetic boundary layers of turbulent flows [152, 153]. Experiments showed that both advection by the large-scale circulation and vertical plumes contributes to heat transport. The thickness of the thermal boundary layer is defined as the distance at which the extrapolation of the gradient at wall of the mean temperature profile is equal to the mean bulk temperature. With  $H$  the height of the convection cell, the thickness of the thermal boundary layer  $\lambda_\theta$  can be expressed as a function of the mean Nusselt number:

$$\lambda_\theta = \frac{H}{2Nu} \quad (4.4)$$

In order to verify the prediction of the thermal boundary layer of turbulent flows in the current study, the mean temperature profile is examined for the developed turbulent regime at  $Ra = 10^7$ , as shown in figure 4.8. The mean temperature profile is calculated based on the juxtaposition of temperature averaging for a thin horizontal layer.

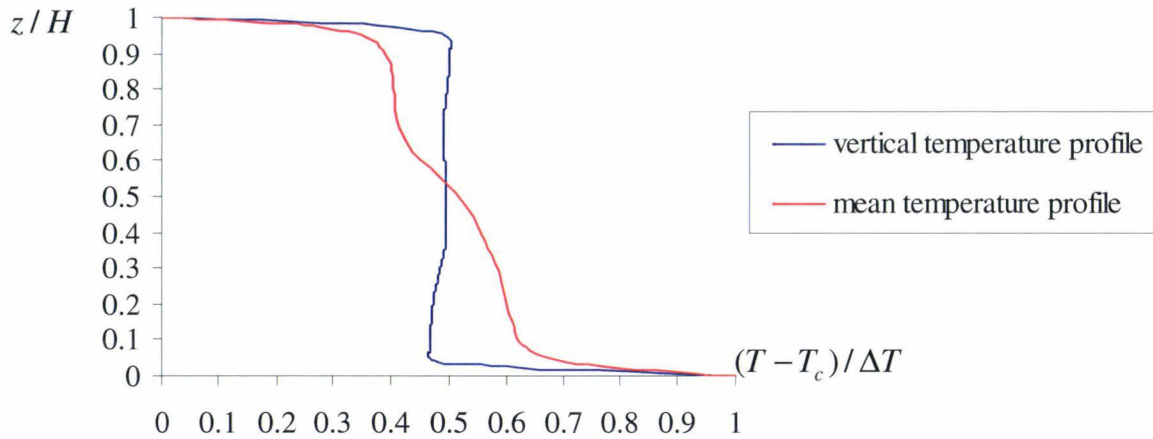


Figure 4.8. Normalized temperature profile,  $Ra = 10^7$ , standard low-Re k- $\epsilon$  turbulence model. — Vertical temperature profile at the middle of the cavity; — mean temperature profile.

The calculated mean temperature in the bulk is not constant, but varying notably with the height of the cavity, while the mean temperature gradient in the vertical direction is found very small or even zero in the literature for cubical and rectangular cavities [152, 154].

It is first supposed that this difference is due to the proximity of the conducting sidewalls in the cubical cavity. But, the vertical temperature profile at the middle of the cavity shows also irregularities of the bulk temperature (figure 4.8), although the bulk temperature gradient at the middle of the cavity is found equal to zero for turbulent flows in 2D square cavities [155]. Therefore, the difference between the mean temperature gradients found with the present computations and in the literature is attributed to the simple gradient diffusion hypothesis (SGDH) used in this study. Indeed, SGDH assumes that the vertical turbulent heat flux is proportional to the mean temperature gradient in the vertical direction. Consequently, the vertical turbulent heat flux is estimated in the present study to about zero in the bulk and very large near the walls, while DNS results from the literature [146] report large values in the middle of the cavity and very small ones near the walls.

#### 4.1.2.7. Improvement of turbulence modeling

For a better prediction of the turbulent heat flux and thus of the vertical distribution of mean temperature in cavities heated from below, other turbulent heat flux models, which account for the anisotropy of the heat flux, are discussed in [146]. These models are examined in the present study for an implementation in the CFD code STAR-CD. First, second order models are not adapted to steady-state computations in the development process. Secondly, anisotropic first order turbulent heat flux models are still based on a temperature gradient assumption and fail partly to predict the turbulent heat flux in the bulk. However, algebraic heat flux models consider additional production terms, balancing the temperature gradient term. The four-equation algebraic flux model proposed by Hanjalic [155, 156] has been retained in this study for an implementation in STAR-CD as an extension of the standard low-Re k- $\epsilon$  turbulence model. In this model, the expression for the turbulent heat flux is given by:

$$\overline{u'_i T'_f} = -C_\theta \frac{k}{\epsilon} \left( \overline{u'_i u'_j} \frac{\partial \overline{T}_f}{\partial x_j} + \xi \overline{u'_j T'_f} \frac{\partial \overline{u}_i}{\partial x_j} + \eta \beta g_i \overline{T'_f}^2 + \epsilon_\alpha \right) \quad (4.5)$$

The additional production terms are accounting for the mechanical deformations with the gradient of mean velocity and the amplification or attenuation of turbulence fluctuations due to buoyancy forces. The last term represents the molecular dissipation of the turbulent heat flux. The implementation of this model by CD-adapco is currently under investigation and will be verified in the future for the rectangular and cubical cavities investigated previously.

#### 4.1.3. Partial conclusions

The range of validity of the steady-state approach for the computation of buoyancy-driven flows in electronic enclosures has been investigated in this section in comparison with literature for a large range of Rayleigh numbers covering the laminar, oscillating and turbulent regimes. Different initial conditions for the computation were necessary for the prediction of the flow structure in the different cavity configurations, showing that the instability mechanism is strongly affected by the aspect ratio of the cavity and on its inclination. Different RANS turbulent models have been investigated for structure and heat transfer prediction and the standard low-Re k- $\epsilon$  turbulence model has been selected for providing the best agreement with literature. Moreover, the local distribution of heat flux and its averaged value on the horizontal walls of the cubical cavity are in good agreement with the literature, within 8.5%, for laminar and oscillating flows.

## 4.2. Forced convective flows

As discussed previously, the heat transport by forced convection in electronic systems is mainly dependent on the establishing volume flow rate and the pressure distribution in the system and of its environment. In this section, the validity of the numerical methods proposed previously for fan flow computation, rotational body force and MRF, are examined in comparison with experimental results, regarding induced volume flow rate and pressure distribution upstream and downstream the fan.

In the literature, most of the thermal analyses of complex electronic systems cooled by forced convection are using the rotational body force method together with the fan performance curve to simulate the fan operating conditions [90, 100, 157]. Nevertheless, no study could be found, in which the rotational body force method has been validated for electronic axial fan flows. The rotational body force and MRF methods have been also examined with STAR-CD for the computation of the flow through an engine driven fan [158, 159]. Numerical results obtained with a transient moving mesh model and experimental results providing the fan performance curve and velocity distributions upstream and downstream the fan have been used for the comparison. The flow velocities computed with MRF were found in very good agreement with the transient model, while the body force results show some deviations especially in the radial and axial components. The MRF numerical model could predict the measured performance curve within 10%. The geometry of a typical electronic axial fan with relatively small blades in comparison with the hub highly differs from engine axial fans. Therefore, it is necessary to validate the steady-state numerical methods for electronic fans.

### 4.2.1. MRF simulation

In this section, typical electronic fans are considered, for which the performance curve has been measured in the fan test-rig. The performance curve is used for the validation of the steady-state approaches MRF and rotational body force. To reduce the time and effort of the investigation, only one state of the performance curve for the volume flow rate and fan pressure rise is considered. Experiments have been carried out in the fan test-rig to determine the operating point of the system composed of the fan assembled in the electronic system at ambient temperature. This operating point may differ from the one considering the electronic system in its real environment in a passenger car with realistic ambient temperature. Nevertheless, it provides a sensitive situation for the validation of the MRF method. Two electronic fans, situated in the sound-amplifier and TV-tuner of the telematic generation integrated in actual Mercedes-Benz cars, are considered for the validation. The characteristic and the back view of both fans can be found in appendix, table and figure A.5.1. As the real operating point of the TV-tuner could not be measured in the test-rig, one measured point of the performance curve in its stable range is arbitrary chosen for the validation in this case.

#### 4.2.1.1. Numerical model

The numerical model for the steady-state computation with MRF is based on the fan test-rig of the supplier (figure A.3.1.) accounting only for the measurement chamber after the straightener and for the free outlet chamber, as shown in figure 4.9. The tested fan is positioned perpendicularly at the downstream section of the measurement chamber and subjected to a homogeneous inlet flow. The free outlet chamber is modeled by a cylindrical chamber including the measurement chamber. It is constructed with a downstream length of

ten times the length of the measurement chamber and a diameter of three times the diameter of the measurement chamber to ensure the stabilization of the downstream flow avoiding unreasonable recirculation of the flow.

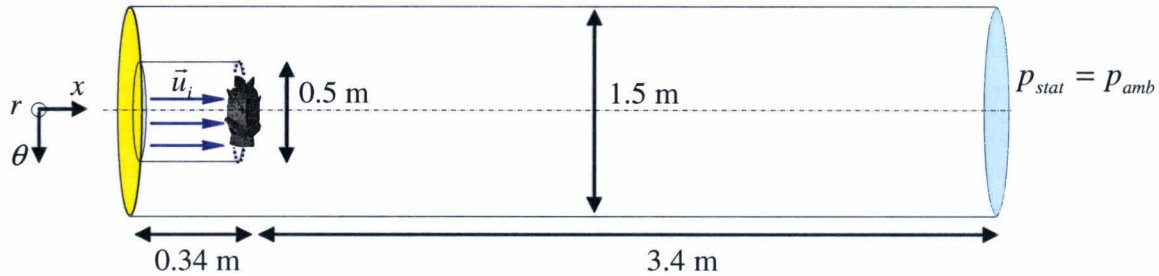


Figure 4.9. Schema of the numerical model for the computation of the fan flow in the test-rig.

A constant axial velocity distribution is imposed at the inlet of the measurement chamber with a given mass flow rate, reproducing the effect of the straightener. A pressure outlet boundary condition is imposed at the far end of the free outlet chamber. The walls of the measurement and free outlet chambers are assigned of no-slip condition. The flow is initialized with the ambient pressure and temperature measured in the fan test-rig.

#### 4.2.1.2. Fan of the sound amplifier

In the following, the accuracy of the MRF method is evaluated considering the fan of the sound amplifier for an operating voltage of 13.6 V. The operating point of the fan installed in the sound amplifier is found in the test-rig for a volume flow rate of  $2.71 \times 10^{-3} \text{ m}^3/\text{s}$ , corresponding to a fan pressure rise of 14.2 Pa and a rotational speed of 7116 rpm.

In a previous study considering the fan of the sound amplifier embedded in the test-rig [160], different turbulence models have been investigated using a MRF method to model the rotation of the fan. As discussed previously, forced convective flows over electronic boards can be classified as low-Re number flows, on account of the relatively low velocities and small length scales encountered. Moreover, spots of turbulence are expected in the strong energetic recirculation zones, located upstream and downstream an electronic component. Due to the high friction rate at the wall in this case, the standard low-Re  $k-\varepsilon$  model is not adapted. According to the relatively large values of  $y^+$  up to 30 in such electronic systems, the following turbulence models are chosen for the investigation: the Spalart-Allmaras model, the standard high-Re  $k-\varepsilon$  model with the two-layer approach, the RNG  $k-\varepsilon$  model and the SST  $k-\omega$  model. A relatively fine trimmed mesh (T2) generated with STAR-CD with two and four million cells respectively in the fan region and elsewhere is used for the study (appendix, table A.5.2). The fan volume flow rate is found within 0.5% in comparison with the experimental results independently of the turbulence model used. Moreover, the Spalart-Allmaras model and the SST  $k-\omega$  provide the best agreement for the fan pressure rise within respectively 5.6% and 5.9%, while a larger discrepancy of 14% is found with the RNG  $k-\varepsilon$  model and the two-layer approach (appendix, figure A.5.3.). Used in electronic systems of complex geometry, the Spalart-Allmaras and SST  $k-\omega$  models diverge rapidly. On the contrary, the two-layer approach with the model of Wolfshtein is adapted to this type of shear-driven flow and geometry. Consequently, it is selected as turbulence model for the computation of forced convection in electronic systems.

In order to improve the prediction of the two-layer approach, a mesh refinement study is performed. Several grids using polyhedral cells were generated with STAR-CCM<sup>+</sup>, which allows a better matching with the rotor and stator geometries. For comparable results, only the fan region has been refined. The different grids can be seen in appendix, table A.5.2 and figure A.5.2. The results of the mesh refinement study using the two-layer approach are shown in appendix, figure A.5.4. The  $y^+$  values are found in the range  $[10^{-3};23]$  and only 0.5% of the total cells are lying in the range  $[5;23]$ , so that the velocity profile may be accurately solved in the near-wall region of the fan. A good agreement with the experimental results is achieved using the grid with minimum six cell layers in the near-wall region. As shown in table 4.5, the difference between the experimental results and the numerical results obtained with the MRF method is of 9.5% with the grid using six cell layers in the near-wall region and 9% with the grid using nine cell layers in the near-wall region.

	Sound amplifier fan		TV-tuner fan	
	Experiment	MRF simulation	Experiment	MRF simulation
Operating voltage (DC)	13.6		5	
Rotational speed (rpm)	7116 ± 36		5908 ± 30	
Volume flow rate (m <sup>3</sup> /s)	2.71 × 10 <sup>-3</sup> ± 5.42 × 10 <sup>-5</sup>	2.71 × 10 <sup>-3</sup>	1.20 × 10 <sup>-3</sup> ± 2.40 × 10 <sup>-5</sup>	1.20 × 10 <sup>-3</sup>
Fan pressure rise (Pa)	14.2 ± 0.14	12.9 (NW6) 15.5 (NW9)	8.78 ± 0.09	9.30

Table 4.5. Comparison of the numerical results obtained with the MRF method with the performance curve for electronic fans in the test-rig.

#### 4.2.1.3. Fan of the TV-tuner

Based on the detailed mesh refinement study and turbulence modeling investigation carried out in the previous paragraph, the validity of the MRF method is again examined for the fan situated in the actual TV-tuner generation for an operating voltage of 5 V. For the validation, the measurement point with a volume flow rate of  $1.20 \times 10^{-3} \text{ m}^3/\text{s}$  is chosen in the stability range of the performance curve, corresponding to a fan pressure rise of 8.87 Pa and a rotational speed of 5908 rpm. A comparable mesh is generated using 6 cell layers in the fan near-wall region and composed of  $1.31 \times 10^6$  cells in the fan region and  $1.38 \times 10^6$  cells elsewhere. The  $y^+$  values are found in the range  $[10^{-3};65]$  with only 1% of the cells lying in the range  $[5;65]$  in the interface region with the fan. According to the previous discussion, the standard high-Re  $k-\epsilon$  turbulence model with the two-layer approach is used in the computation. The results are also provided in table 4.5. The volume flow rate and the fan pressure rise are found respectively within 0.5% and 6% in comparison with the experimental results. The investigated state of the performance curve providing volume flow rate and fan pressure rise is a measured point in case of the TV-tuner, while it is the result of an interpolation in case of the sound amplifier. This may explain why a better agreement is obtained with the fan of the TV-tuner in comparison with the fan of the sound amplifier.

## 4.2.2. Rotational body force simulation

In the following, the study focuses on the fan of the sound amplifier for which the operating point installed in the sound amplifier is known. For the comparison of both methods for fan flow simulation, the same fan operating voltage is used as in the previous study, providing the same operating conditions.

### 4.2.2.1. Numerical model, turbulence modeling

The rotational body force model utilizes the same geometry and grid as the MRF model, except for the fan region, in which the fan blades are not represented. The same boundary conditions (inlet axial velocity and a pressure outlet boundary condition) and initial conditions as for the MRF computation are adopted in the present computation. For fan flow simulation with the rotational body force method, three additional boundary conditions must be provided: the fan performance curve, the fan operating speed and the blade angle. While the fan performance curve and operating speed are known from the experimental results, the blade angle is not a priori known due to the 3D geometry of a blade and investigated as parameter for the rotational body force computation:

- As the blades are supposed to have no curvature, the mean blade angle ( $\beta = 53^\circ$ ) with respect to the straight virtual blade connecting the leading and trailing edges is first assumed for the computation;
- Reckoning that the outlet relative velocity is mainly affected by the trailing edge, the trailing blade angle ( $\beta = 25^\circ$ ) with respect to the middle of the chord is secondly given as boundary condition.

In order to compare the results obtained with the rotational body force and MRF methods, the standard high-Re k- $\epsilon$  model with the two-layer approach is used for the investigation.

### 4.2.2.2. Comparison of the results obtained with the rotational body force and MRF methods

During the computation, the load factor is scaled so that the operating point of the fan lies on the provided performance curve and reach a stable state. For both conditions of the blade angle, the operating point of the installed fan in the sound amplifier is reached within 0.5% of the static pressure rise and 1.5% of the volume flow rate. In order to determine which of the blade angles is the most realistic, the static pressure distribution is evaluated in the fan region in comparison with the results provided by the MRF method, as shown in figure 4.10. Compared to the MRF reference solution, the local under pressure and overpressure created respectively upstream and downstream the blades are better predicted accounting the trailing blade angle ( $\beta = 25^\circ$ ) in the body force simulation. Besides, both body force methods predict a slight mean pressure rise between the measurement and free outlet chambers, while the MRF simulation creates a much larger pressure rise by drawing the flow. This limitation of the body force method may be enhanced with conjugate heat transfer computations in electronic systems, for which no pressure boundary condition is given but only wall temperature boundary conditions.

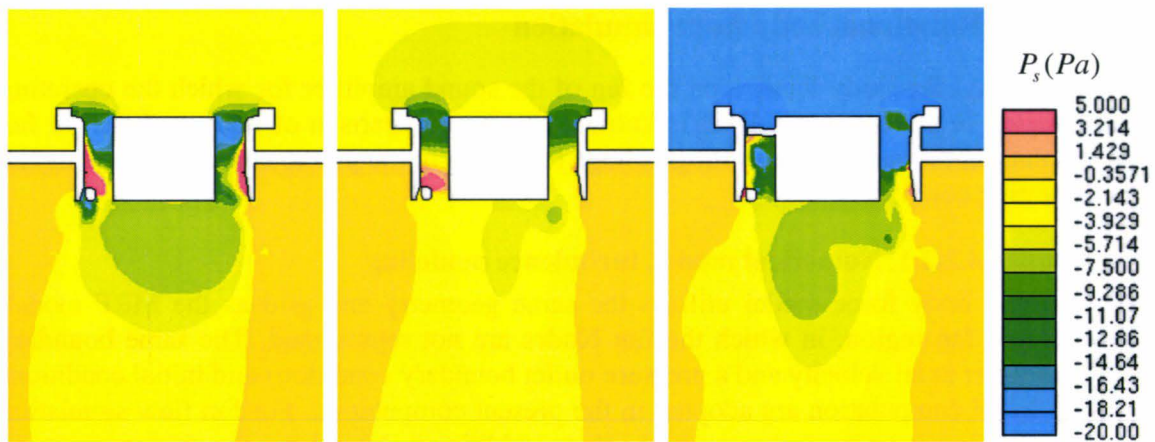


Figure 4.10. Fan pressure rise (Pa) at the operating point in the fan middle section plane ( $r; x$ ); Body force computation with  $\beta = 25^\circ$  (left) and  $\beta = 53^\circ$  (middle); MRF computation (right).

Figure 4.11 shows the mean circumferential velocity components with the normalized radial position in the rotating region of the fan for the MRF and rotational body force computations. The results provided by the MRF computation shows the dominance of the axial and tangential components, in particular around the rotor. The distribution of the circumferential radial velocity component is quite homogeneous and the radial component can be neglected in comparison with the other components. The low mean circumferential axial velocity component obtained at the tip clearance results from the balance with positive velocity magnitude in the region of the strut. In comparison with the results of the MRF computation, the body force method using the trailing blade angle provides overall reasonable results, in particular for the axial velocity. The discrepancy found for the tangential velocity component at the tip clearance is attributed to the lack of geometry of the blades in the rotational body force method.

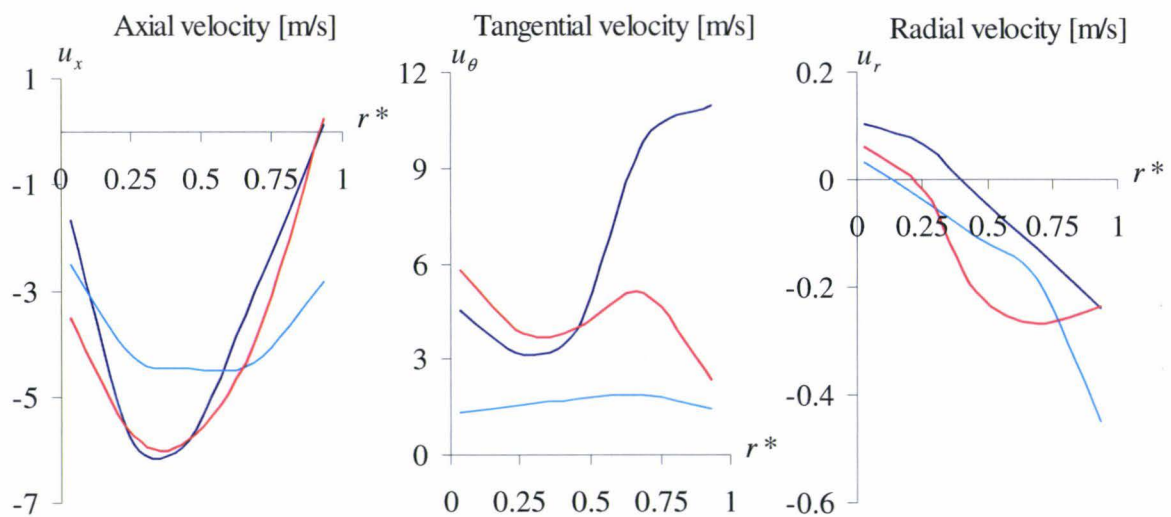


Figure 4.11. Mean circumferential velocity components in the fan rotating region with the normalized radial position  $r^* = (r - r_{in}) / (r_{out} - r_{in})$  at the operating point; Body force computation,  $\beta = 25^\circ$ ,  $\beta = 53^\circ$ ; — MRF computation.

### 4.2.3. Partial conclusions

The validity of the numerical methods rotational body force and MRF for fan flow simulation has been examined in comparison with the performance curve measured in the fan test-rig for electronic fans. The operating point measured for the fan installed in the electronic system running under its usual operating voltage, if provided, has been used for the comparison. In order to model the spots of turbulence expected over electronic boards, the standard high-Re  $k$ - $\epsilon$  model with the two-layer approach has been chosen for the investigation. A mesh refinement study is performed, showing that an accurate prediction of the fan pressure rise with the MRF method is achieved with a grid using minimum six cell layers in the fan near-wall region, within 9.5% for the fan of a sound amplifier and 6% for the fan of a TV-tuner in comparison with the experimental results. Moreover, as the fan static pressure rise at the operating point is always reached by the iterative scaling procedure, the validation of the rotational body force method is based on the comparison of the fan volume flow rate, the static pressure distribution and the velocity components with the results of the MRF method. The comparison shows discrepancies in the tangential velocity component at the tip clearance, which is attributed to the lack of geometry of the blades in the rotational body force method.

### 4.3. Outlet grills of the TV-tuner

Numerical models for flow simulation through outlet grills are investigated in a representative electronic device constituted of different outlet grills: the TV-tuner of the actual telematic generation. The TV-tuner is a car hybrid receiver system, which completes the integration of analog as well as digital signals for audio and video. Two populated PCBs are superimposed in the TV-tuner mounted with different ICs (integrated circuit), which dissipate in the whole 12.3 W. For electromagnetic compatibility, grill housing is used as shield to prevent from continuous interferences with audio frequencies emitted from several power supply units mounted on the lower PCB. An axial fan is mounted on the TV-tuner package, drawing the ambient air into the system. The rotational speed of the fan is regulated according two operation levels – with an operating voltage of 4 V or 5 V – depending on the ambient temperature of the most critical component. The operating rotational speed of the fan installed in the TV-tuner measured with a photoelectric tachometer for both operation levels is given in appendix, table A.6.2. The Reynolds number based on the mean volume flow rate prescribed by the fan and accounting for both operating levels is found in the range [6000;8300]. For flow outlet, the TV-tuner package is constituted of four grill areas of different hole geometries located on the lower, upper and side-walls, as shown in figure 4.12. The geometrical parameters of the different outlet grills of the TV-tuner are provided in table A.6.1.

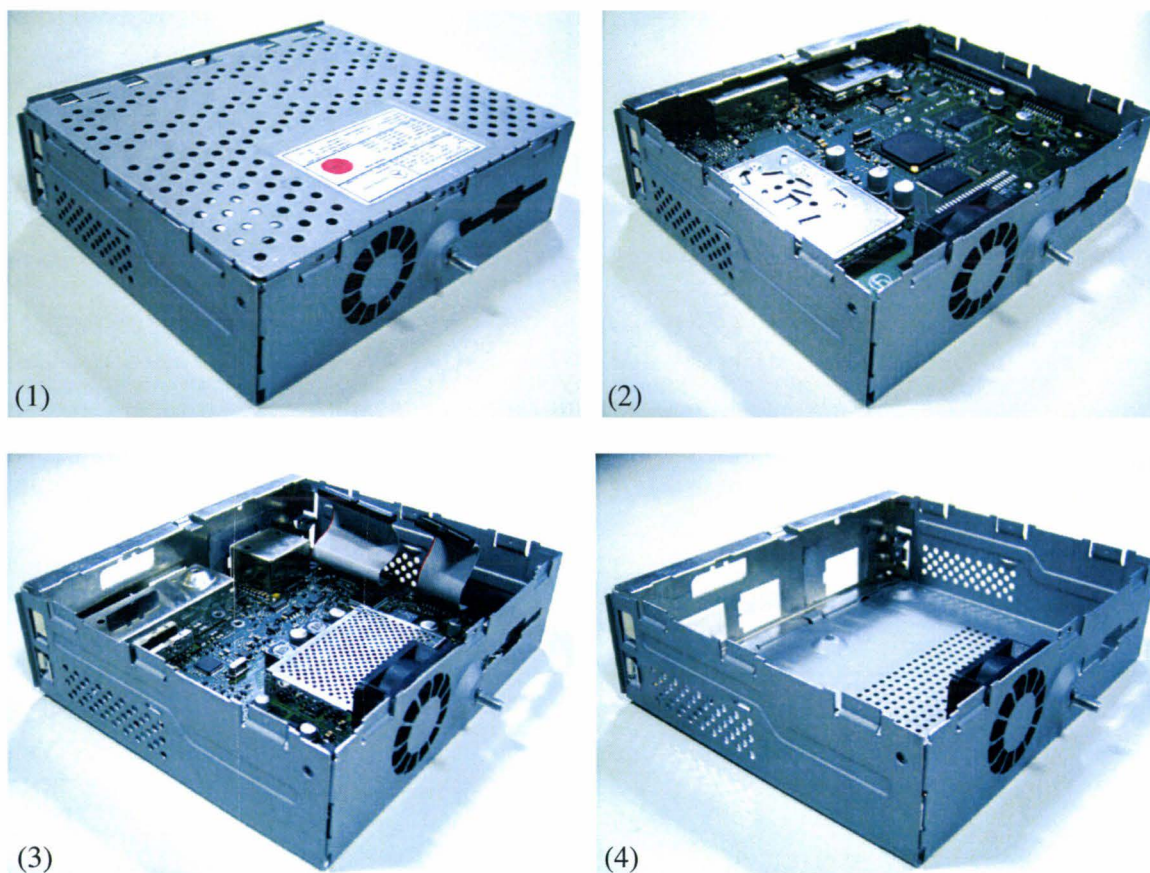


Figure 4.12. TV-tuner, upper wall (1), upper PCB (2), lower PCB (3), lower wall (4).

The aim of the current investigation is to determine numerical methods that can be implemented in the development process, in order to reproduce the volume flow rate distribution in the TV-tuner and the pressure drop created by the outlet grills. In this respect, different numerical models for the outlet grills are generated:

- a complete model of the TV-tuner grills, in which each orifice is solved with several grid cells;
- a model using 2D planar resistance elements (porous baffle) for the outlet grills;
- and a model using 3D resistance elements (porous region) for the outlet grills.

The results provided by the porous models are compared with the detailed computation, once validated, which solves each orifice separately. Moreover, in order to ensure the accuracy of the detailed computation, the modeling of the grill is first investigated in comparison with literature. Due to the complexity of the geometry, the study is performed with STAR-CCM+.

#### 4.3.1. Grill modeling in the test-rig

For the characterization and design of perforated plates, its pressure drop and discharge coefficients have been investigated analytically and experimentally very early in the past for a perforated plate installed perpendicularly in a duct and submitted to a homogeneous inlet flow [161, 162, 163]. For small plate thickness to hole diameter ratio as for the TV-tuner, the plate pressure drop contribution due to friction losses in the orifice can be respectively neglected. Considering the only contributions due to the flow constriction before the orifice and section enlargement after the orifice, the pressure drop through the perforated plate has only an inertial loss contribution. We define:  $\rho$  and  $\bar{u}$  the density and mean velocity of the duct flow respectively,  $u_o$  the velocity in the orifices and  $k$  the pressure loss coefficient.  $A_o$  and  $A_g$  are the surface areas of respectively the orifice and grill;  $L$  and  $d_o$  the grill plate thickness and the orifice diameter respectively. The static pressure drop of the perforated plate can be expressed as a function of the inflow mean velocity:

$$\Delta p_{stat} = k \frac{\rho u_o^2}{2} = k \left( \frac{A_g}{A_o} \right)^2 \frac{\rho \bar{u}^2}{2} \quad (4.6)$$

Mühle [162] provides a correlation between the pressure loss coefficient and the geometrical parameters of the perforated plate (equation 4.7) available for similar inflow conditions and plate geometrical parameters as in the TV-tuner. The Reynolds number  $Re_o$  is based on the mean orifice velocity and on the orifice diameter.

$$k = 1.75 \left( 1 - \frac{A_o}{A_g} \right) + \frac{64}{Re_o} \frac{L}{d_o} \quad (4.7)$$

Experiments have been carried out in a wind tunnel with similar thin plates, providing the variation of the pressure drop with the inlet flow velocity (section 3.7.1.2). Two additional parameters on the static pressure drop of the perforated plate have been highlighted: firstly, the direction of perforation with different orientations of the perforated plate; secondly, the position and diameter of the orifice for the same free area ratio of the perforated plate [164].

However, the pressure losses due to friction are theoretically negligible for plates of small plate thickness to hole diameter ratio, so that the direction of perforation should have no effect on the plate pressure drop. Therefore, the dependence of the experimental results on the direction of perforation may show a problem of measurement repeatability or a slight contribution of friction on pressure losses.

In the following, the modeling of perforated plates is investigated for an accurate prediction of plate pressure drop. For the validation of the numerical method, the correlation 4.7 and the experimental results in a wind tunnel [164] are used for the comparison.

#### 4.3.1.1. Numerical model

For a direct comparison with the experiments, the numerical model is based on the wind tunnel test-rig (figure A.3.2) accounting only the measurement section after the straightener. The perforated plate is positioned perpendicularly in the duct and submitted to a homogeneous inlet flow, as illustrated in figure 4.13.

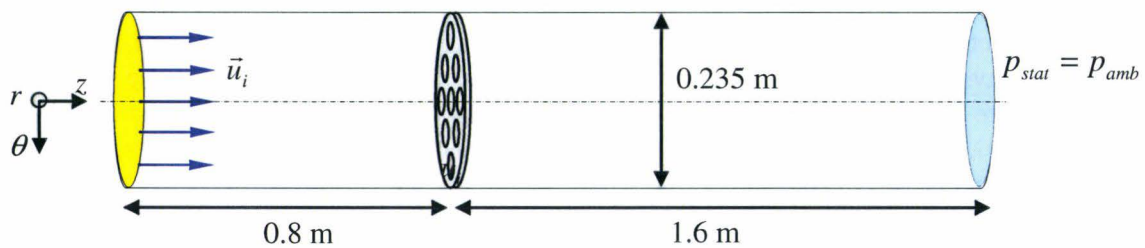


Figure 4.13. Schema of the numerical model for the computation of the perforated plate in the test-rig.

Among the perforated plates measured in the wind tunnel, one of similar free area ratio as of the TV-tuner is chosen for the computation. The geometrical characteristics of the computed perforated plate are provided in appendix, table A.6.3. Based on the numerical results of Gan [165], the measured perforated plate with circular orifice is modeled with hexagonal orifices of same free area ratio. A constant axial velocity distribution is imposed at the inlet of the measurement section with a given mass flow rate. A pressure outlet boundary condition is imposed at the far end of the measurement section. The walls of the measurement section are assigned of no-slip condition. The flow is initialized with the ambient pressure and temperature measured in the test-rig. As explained previously, the standard high-Re  $k$ - $\epsilon$  model with the two-layer approach is adapted to the computation of forced convection in electronic systems. It is therefore used in this investigation.

#### 4.3.1.2. Mesh refinement study

In this section, the inlet velocity is set constant to  $u_i = 1$  m/s for a mesh refinement study. Three different grids have been generated using mainly hexahedral cells and some trimmed cells. For comparable results, only the region of the perforated plate has been refined. The different grids can be seen in appendix, figure A.6.1 and table A.6.4. The  $y^+$  values are found in the range  $[10^{-2}; 48]$  with 3% of the total cells are lying in the range  $[5; 48]$ , so that the velocity profile may be quite accurately solved in the near-wall region of the perforated plate. Downstream of the perforated plate, the static pressure is constant equal to the ambient pressure ( $p_{amb} = 101325$  Pa) set as boundary condition. Upstream of the plate, a constant and

homogeneous static pressure distribution is found in section planes parallel to the plate until a normal distance of  $9 \times 10^{-2}$  m upstream of the plate. Therefore, the static pressure drop is evaluated as the difference between the static pressure in a parallel section plane located at  $1 \times 10^{-1}$  m upstream of the plate and the ambient pressure. The results of the refinement study can be seen in appendix, figure A.6.2 and table A.6.5. The numerical results obtained in the present study using the finest mesh (NW5) show a good agreement with the correlation 4.7 within 8%. This proves that such a mesh refinement is required in the region of the perforated plate to accurately solve the pressure losses due to flow constriction and section enlargement.

#### 4.3.1.3. Variation of the inlet velocity

For the validation of the present numerical model, the pressure loss coefficients are further examined in comparison with literature for different inlet velocities in the range of volume flow rate of interest. Computations in the test-rig are carried out for inlet velocities of  $u_i = 0.25$  m/s and  $u_i = 0.5$  m/s, according to the range of Reynolds number based on the mean volume flow rate prescribed by the fan in the TV-tuner. Moreover, to obtain a general trend of the pressure loss coefficient, an additional computation is performed with an inlet velocity of  $u_i = 3$  m/s. The comparison of the pressure loss coefficients between the numerical results, the correlation 4.7 and the experimental results over the Reynolds number based on the inlet velocity is provided in figure 4.14. Moreover, the pressure drop and pressure loss coefficient of the perforated plate can be seen in appendix, table A.6.6.

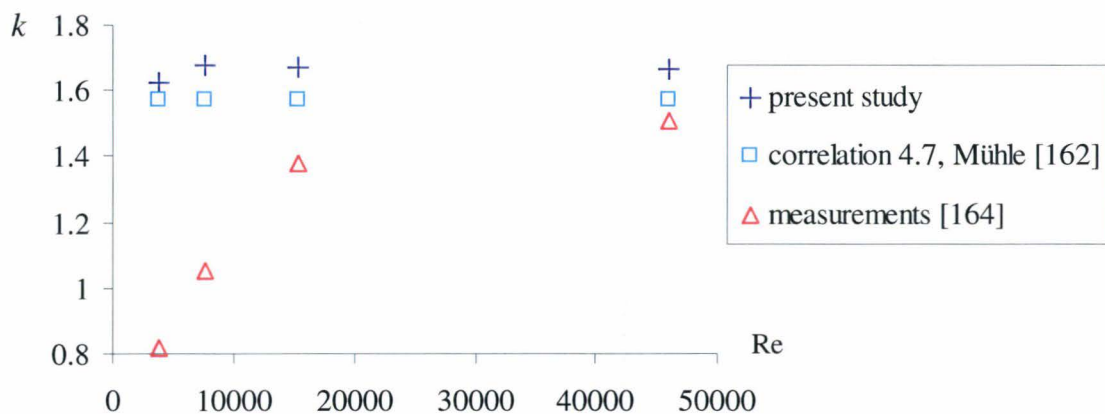


Figure 4.14. Variation of the pressure loss coefficient of the perforated plate in the test-rig with the Reynolds number; + present study, □ correlation 4.7 [162], △ measurements [164].

Firstly, the pressure loss coefficient predicted by the correlation 4.7 and the present computations is about constant over the range of Reynolds numbers considered, showing the square dependence of the plate pressure drop on the inlet velocity and confirming the main contribution of inertial losses. A much stronger decrease is predicted by the experiments, leading to strong deviations with the correlation 4.7 and the numerical results. This is attributed to a problem of measurement repeatability. The plate pressure drop and loss coefficient is in very good agreement with the correlation 4.7 within 6%. Therefore, the mesh parameters employed for the generation of the present numerical model can be used in the following study to solve the outlet grills of the TV-tuner.

### 4.3.2. TV-tuner, outlet grills

Based on the numerical models for fan flow and grill pressure drop which have been validated in the previous sections, a detailed numerical model is generated to solve the flow in the TV-tuner ideally situated in a free environment. The flow is examined regarding volume flow rate and pressure distributions. Thus, heat transport by forced convection only is considered in this section. The inlet conditions are regulated by the two operation levels for 4 and 5 V.

#### 4.3.2.1. Numerical model

The geometric surface of the TV-tuner, including the fan blades and the fan housing, the lower and upper populated PCBs and the flat ribbon cable connecting it and the case with its four outlet grills, is extracted for mesh generation using polyhedral cells. Only the largest ICs, which may alter the boundary layer growth developing downstream the fan, are accounted in the numerical model. According to the previous results (section 4.2), the MRF method is employed for fan flow simulation. To save CAD modeling and computing time, the orifices of the different outlet grills are represented with hexagons, as in the last section. The mesh parameters for reasonable MRF and perforated plate computation investigated previously (with respectively six and five cell layers in the near-wall region) are adopted in the fan and grill regions of the present model. The resulting mesh is composed of a total of  $1.07 \times 10^7$  cells, as shown in appendix in table A.6.7 and figure A.6.3. The numerical model can be seen in figure 4.15. The fan angular velocity is given as boundary condition to the rotating region. The walls of the environment box are assigned of a constant pressure outlet boundary condition and of no-slip condition. The flow is considered initially at rest and at ambient pressure. The turbulent flow is computed with the standard high-Re k- $\epsilon$  model using the two-layer approach.

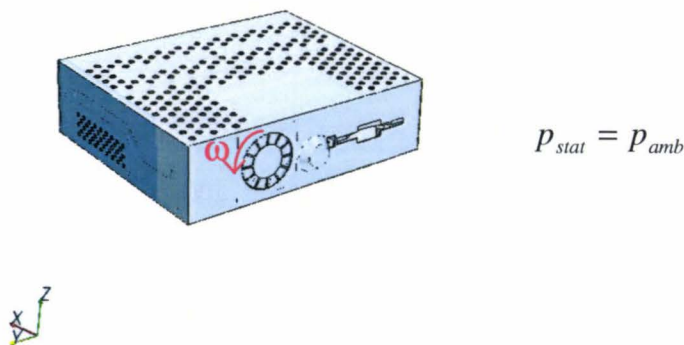


Figure 4.15. Numerical model for the computation of the outlet grills of the TV-tuner.

#### 4.3.2.2. Velocity and volume flow rate distributions

The flow velocity distribution in the TV-tuner is analyzed using different section planes, as illustrated in appendix, figures A.6.4 and A.6.5. As very similar velocity distributions are found for both rotational speeds, only the results for  $\omega = 5065$  rpm are presented. The flow drawn by the fan, characterized at the fan outlet by high velocities with a main axial component, is distributed among both lower and upper PCBs. On the lower PCB, the

interference shield grill housing is mainly bypassed by the fan induced flow and streamed through with backflow. Therefore, porous resistance cannot be used to model the interference shield. As expected, boundary layers are developing in the near-downstream region of the fan on the lower and upper sides of the PCBs, growing over the ICs. Six outlets in the TV-tuner package let the fan induced flow leaving the TV-tuner: four grills, one leakage between the card reader and the package on the front side and the last outlet is a small single hole on the back side. The mass flux through each outlet, based on the grill or outlet area, and the distribution of the fan induced mass flow rate among the six outlets can be seen in table 4.6.

	3860 rpm		5065 rpm	
	Mass flux ( $kg / m^2 s$ )	Ratio of mass flow rate (%)	Mass flux ( $kg / m^2 s$ )	Ratio of mass flow rate (%)
Fan	3.11	100	4.14	100
Grill, upper wall	$3.44 \times 10^{-1}$	43.5	$4.59 \times 10^{-1}$	43.6
Grill, lower wall	$3.13 \times 10^{-1}$	16.9	$4.34 \times 10^{-1}$	17.6
Grill, sidewall 1	$7.85 \times 10^{-1}$	13.1	1.03	12.9
Grill, sidewall 2	$5.72 \times 10^{-1}$	9.56	$7.44 \times 10^{-1}$	9.35
Leakage, front wall	$7.37 \times 10^{-1}$	16.5	$9.56 \times 10^{-1}$	16.1
Single hole, back wall	$5.33 \times 10^{-1}$	0.368	$7.32 \times 10^{-1}$	0.380

Table 4.6. Distribution of the fan induced volume flow rate over the different outlets of the TV-tuner for both operating rotational speeds.

The sidewall grill called one is the one located on the nearest sidewall from the fan. Again, similar volume flow rate distributions are obtained for both rotational speeds. The volume flow rate over the lower PCB is distributed among the sidewall grills, the lower grill and the leakage, while the volume flow rate over the upper PCB is mainly distributed among the upper grill and the leakage. The mass flux through the leakage on the front wall is relatively high in comparison with the other grills, as the volume flow rate over both PCBs participates. Moreover, the mass flux through the upper and lower grill is relatively low due to the high surface areas of both grills, whereas the sidewall grill one is characterized by a large mass flux due to its proximity to the fan. Streamlines over each PCB can be seen in figure 4.16. The velocity vectors in sections coincident with each outlet grill for  $\omega = 5065$  rpm can be seen in appendix, figures A.6.6 and A.6.7.

The flow is leaving the TV-tuner through each grill without backflow direction. Strong inhomogeneities of the velocity magnitude are found at the upper wall and sidewall one. On the contrary, a quite homogeneous velocity field is obtained at the lower wall and sidewall two, due to the absence of ICs in the vicinity and the regularity of the geometry nearby. Moreover, the velocity vectors in the grill sections show different directions not necessary normal to the grill wall. Only the sidewall grill one, which benefits from a large part of the fan induced flow, is streamed perpendicularly to the package sidewall.

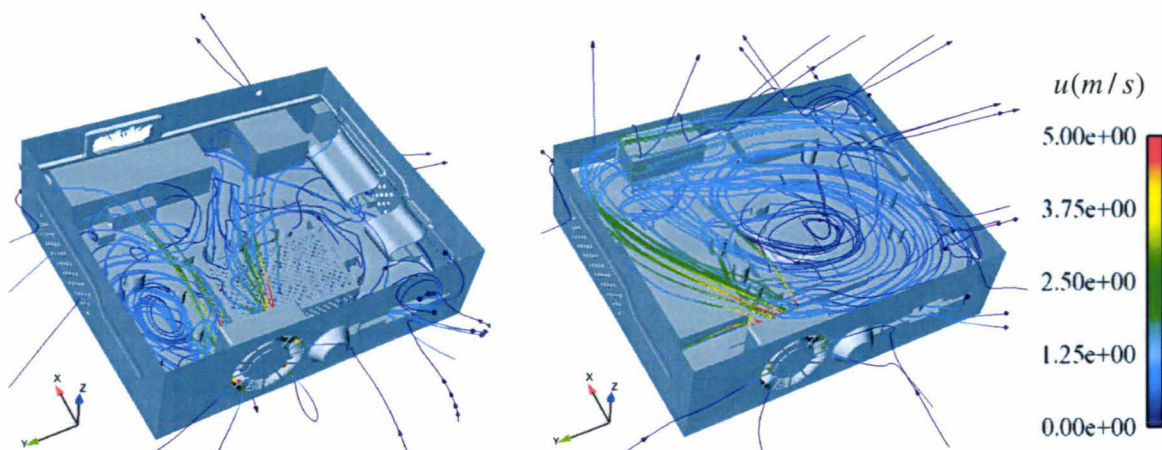


Figure 4.16. Velocity streamlines for  $\omega = 5065$  rpm; lower PCB (left) and upper PCB (right).

#### 4.3.2.3. Static pressure distributions

Outside the TV-tuner, the static pressure is constant equal to the ambient pressure ( $p_{amb} = 101325$  Pa) set as boundary condition. Inside the TV-tuner, the static pressure distribution in section planes parallel with the grills is strongly affected by the ICs geometry. In order to evaluate the static pressure drop of the outlet grills, section planes are set parallel to the outlet grill, so that the pressure distribution upstream the grill recovers. The static pressure recovery occurs from one half up to one and half orifice diameters, as shown in table 4.7. The distribution of the static pressure in these section planes upstream of the outlet grills can be seen in figure 4.17 for  $\omega = 5065$  rpm and in figure A.6.8 in appendix for  $\omega = 3860$  rpm.

Outlet grill	Section plane	Normal distance to the grill inner wall	
		[m]	Number of orifice diameter
Upper wall	$P_1(x; y)$	$6 \times 10^{-3}$	1.5
Lower wall	$P_2(x; y)$	$2.5 \times 10^{-3}$	1
Sidewall, grill 1	$P_3(x; z)$	$3 \times 10^{-3}$	1
Sidewall, grill 2	$P_4(x; z)$	$1.5 \times 10^{-3}$	0.5

Table 4.7. Section plane for the evaluation of the static pressure drop of the outlet grills.

The pressure distribution shows strong inhomogeneities in the sections parallel to the upper wall and sidewall one, for which strong variations of the velocity magnitude have been also found. Therefore, the geometry of the populated PCBs has a considerable effect on the static pressure distribution in the TV-tuner, yielding to an inhomogeneous pressure field just upstream of the outlet grills. In order to account for the standard deviations of the static pressure with the mean value in the section planes considered, the grill static pressure drop is evaluated as the difference between the RMS (root mean square) of the static pressure field over the whole grill in these section planes and the ambient pressure.

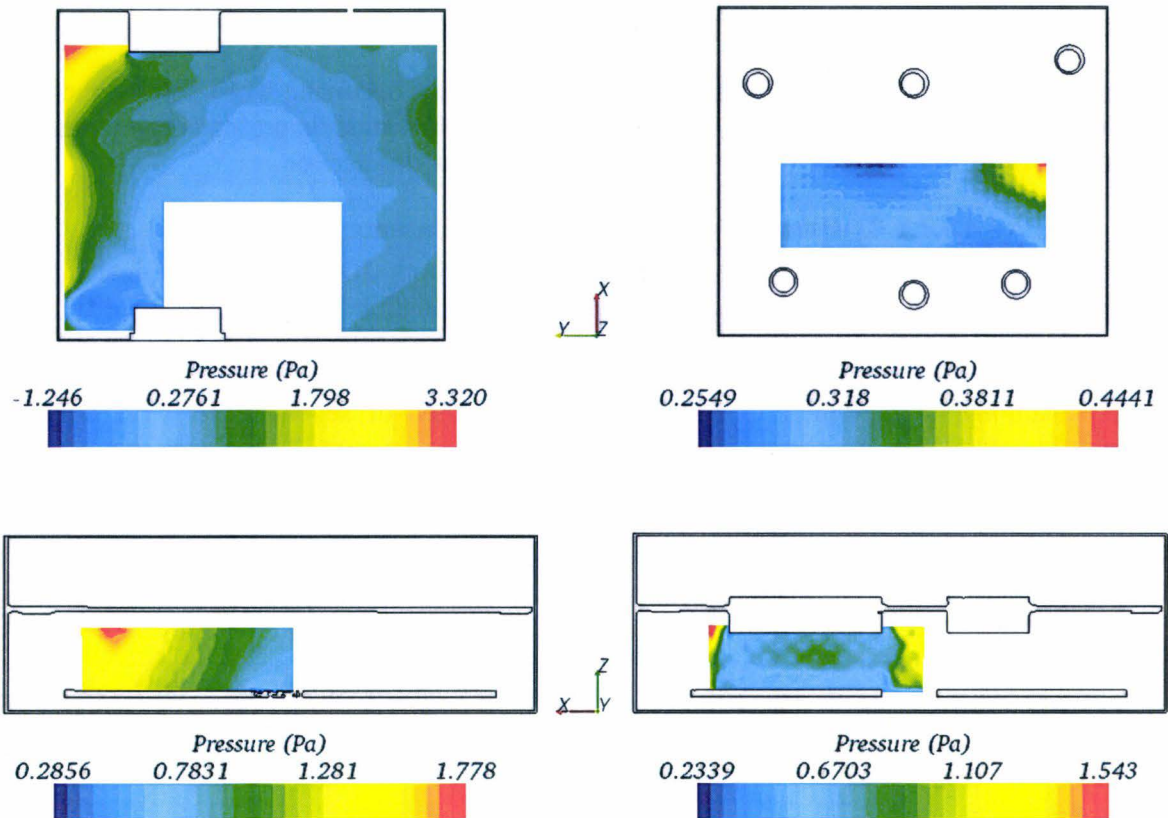


Figure 4.17. Static pressure distribution in the section planes  $P_1$  (top left),  $P_2$  (top right),  $P_3$  (bottom left) and  $P_4$  (bottom right); results of the detailed model for  $\omega = 5065$  rpm.

	3860 rpm		5065 rpm	
	$\Delta p_{stat,RMS}$ (Pa)	$\sigma_p$ (Pa)	$\Delta p_{stat,RMS}$ (Pa)	$\sigma_p$ (Pa)
Grill, upper wall	0.2916	0.3277	0.5053	0.5771
Grill, lower wall	0.1677	0.02026	0.3061	0.02392
Grill, sidewall 1	0.6958	0.1544	1.180	0.2614
Grill, sidewall 2	0.4590	0.1157	0.7665	0.1997

Table 4.8. RMS of the static pressure drop through the different outlet grills of the TV-tuner and corresponding standard deviation values for both operating rotational speeds.

The RMS of the static pressure drop and the corresponding standard deviation are shown for both fan rotational speeds in table 4.8. Relatively high values of the standard deviations are obtained for the grill of the upper wall as a result of the strong inhomogeneities of the static pressure. Moreover, due to the high surface area of the upper grill, a small static pressure drop is found. As most of the fan flow between the lower and upper PCBs is directed to the left of the fan, the highest pressure drop is found through the sidewall grill one.

### 4.3.3. TV-tuner, porous resistance elements

In order to reduce the engineering time and computing time occurring when solving the flow in each orifice of the outlet grills, the 2D and 3D numerical models presented previously to reproduce the grill resistance to the flow are investigated in this section.

#### 4.3.3.1. Determination of the porous coefficients

Inertial and viscous porous coefficients are required in both 2D and 3D numerical models (equations 3.61 and 3.60 respectively). For the determination of the porous coefficients, measurements or computations of the grill in the test-rig should be carried out in order to provide the variation of the grill pressure drop with the inlet flow velocity. This is particularly time-consuming, in particular if the system is constituted of several grills with different geometric parameters. An alternative is to assume the viscous contribution to pressure losses negligible for thin plates, so that the grill pressure drop can be expressed as in equation 4.6. With this assumption, the inertial coefficient for 2D model and tensor for 3D model, are respectively provided by:

$$\alpha = \frac{k}{2} \left( \frac{A_g}{A_o} \right)^2 \quad (4.8)$$

$$I_{ij} \bar{u}_i = \frac{\rho}{L} \frac{k}{2} \left( \frac{A_g}{A_o} \right)^2 \bar{u}_i \quad (4.9)$$

The reasonability of this assumption is considered in the following for the case of the TV-tuner. Moreover, the correlation 4.7 has been validated previously with numerical computations for grills of regular geometric parameters and may help at the determination of the pressure loss coefficient.

#### 4.3.3.2. Analysis of the outlet grills of the TV-tuner in terms of porosity

In order to verify the assumption made in the last paragraph, the range of order of the porosity coefficients is calculated for each grill of the TV-tuner, based on the grill mass flux and static pressure drop. Considering the grill as a planar porous resistance of thickness  $L$ , the grill static pressure drop can be expressed with the grill mass flux  $\dot{M}$  as the sum of an inertial term  $I$  and a viscous term  $V$  :

$$\Delta p_{stat} = I \frac{\dot{M}^2}{\rho} + V \dot{M} \quad (4.10)$$

The computed fan operating states for rotational speeds of  $\omega = 3860$  and  $\omega = 5065$  provide the variation of the grill pressure drop with the mass flux. The range of order of the inertial and viscous terms is calculated assuming a linear variation and shown in table 4.9. Different inertial terms are obtained for the sidewall grill one and two, although the grills have the same geometric parameters. Therefore, the difference of inertial resistance as contribution to grill pressure drop results only on the geometry of the populated PCBs in the vicinity of the grill. Moreover, the estimated values of the viscous term are within 3% of the inertial term values. Consequently, the viscous contributions to pressure losses of thin grills can be neglected in comparison with the inertial contribution and it is reasonable to calculate the inertial coefficient and tensor using equations 4.8 and 4.9.

	Inertial term $I$ (-)	Viscous term $V$ ( $m/s$ )
Grill, upper wall	$1.94 \times 10^2$	$3.46 \times 10^{-1}$
Grill, lower wall	$4.80 \times 10^1$	$7.34 \times 10^{-1}$
Grill, sidewall 1	$1.95 \times 10^1$	$5.87 \times 10^{-1}$
Grill, sidewall 2	$2.49 \times 10^1$	$5.35 \times 10^{-1}$

Table 4.9. Estimation of the inertial and viscous contributions to grill pressure losses, based on the computation of the flow in the TV-tuner solving the flow in the grill orifices.

For the calculation of the inertial coefficients to model the resistance of the lower and sidewall grills, the correlation 4.7 is used. Nevertheless, this correlation is not valid for the upper grill, due to its complex orifice distribution. The inertial coefficient is calculated in this case from computations of the grill in the test-rig.

#### 4.3.3.3. Porous coefficients of the upper grill of the TV-tuner

For the determination of its porous coefficients, the characterization of the upper grill of the TV-tuner is carried out numerically in a similar way as experimentally in a wind tunnel. Several computations are carried out for different inlet velocities, providing the variation of the grill pressure drop with the mass flux and, consequently, the porous coefficients. A similar grid as the grid NW5 used previously in the test-rig is generated with the upper grill positioned perpendicularly in a channel of rectangular section. The numerical model is illustrated in figure 4.18 and the grid parameters can be found in table A.6.8 in appendix. An axial velocity inlet and a pressure outlet are imposed as boundary condition and the flow is initialized with ambient pressure and temperature. The standard high-Re  $k$ - $\epsilon$  model with the two-layer approach is used.

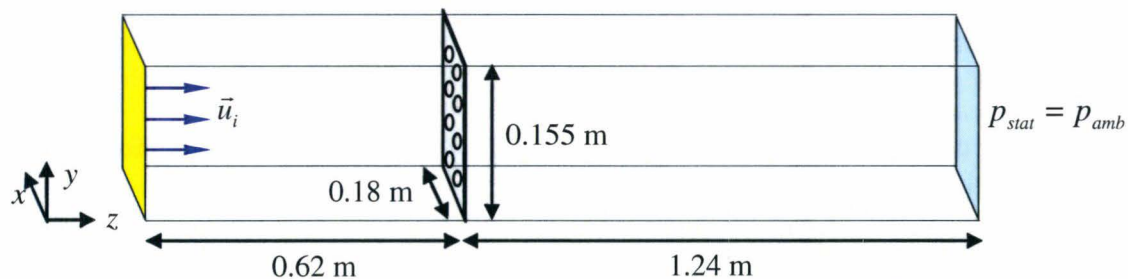


Figure 4.18. Schema of the numerical model for the computation of the upper grill of the TV-tuner in the test-rig.

The static pressure distribution is examined in a comparable section plane as previously in the TV-tuner, situated at  $10^{-2}$  m upstream the grill. It can be seen in figure A.6.9 in appendix. It is only dependent on the grill geometry, as over pressure areas are found in front of obstruction region and under pressure areas in front of orifices. Due to the very small spatial range of static pressure in this section, the corresponding standard deviation is negligible and the RMS values of the static pressure are about equal to their mean (table A.6.9). The inertial and viscous porous coefficients for the 2D and 3D resistance models are calculated using equations 3.61 and 3.60 respectively (table A.6.10). Again, the viscous contribution to

pressure losses is very small in comparison with the inertial one. Moreover, the static pressure drop and thus the inertial coefficient  $\alpha$  of the upper plate computed in the test-rig are highly different from the results found for the upper plate installed in the TV-tuner, although the upper plate is submitted to the same mass flow rate in both cases. This difference is attributed to the geometric environment, which affects the inflow direction and the pressure distribution.

#### 4.3.3.4. Computation of the grill flow with 2D and 3D porous elements

The outlet grills of the existing geometric surface of the TV-tuner are replaced by fluid regions. The mesh parameters for the perforated plate computation used previously are adopted in the present model; they can be seen in table A.6.11 in appendix. The resulting grid illustrated in figure 4.19 is composed of a total of  $8.25 \times 10^6$  cells, i.e.  $2.45 \times 10^6$  less cells than solving the flow in the orifices of the outlet grills.

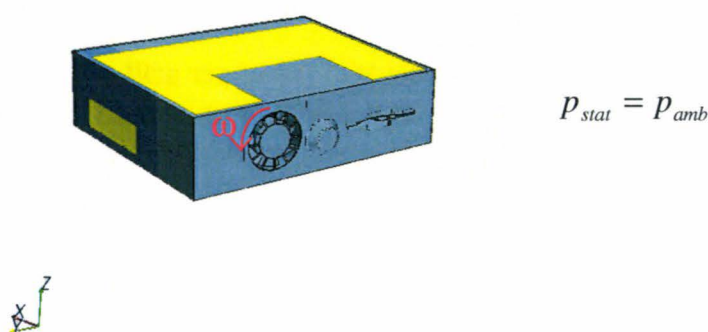


Figure 4.19. Numerical model for the computation of the grill flow with porous elements.

Two numerical models are computed:

- A first one with 2D porous elements, created at the limit between the TV-tuner flow region and the fluid regions in place of the outlet grills, where planar interfaces are laid instead of the grill walls.
- Another one with 3D porous elements, created in the whole fluid regions in place of the outlet grills.

The porous coefficients of the lower and sidewall grills are calculated based on the correlation 4.7, while the previous results in the test-rig are used for the upper grill. The porous coefficients of the 2D and 3D porous models can be found in table A.6.12 in appendix. The flow is considered initially at rest and at ambient pressure. The turbulent flow is computed with the standard high-Re  $k$ - $\epsilon$  model using the two-layer approach. A computation is carried out for a fan rotational speed of 5065 rpm.

The mass flux through each outlet computed by the 2D and 3D porous resistance models can be seen in tables A.6.13 and A.6.14 in appendix. The mass flow rate distribution predicted by the different numerical models is shown in figure 4.20. Compared to the results of the detailed computation, a similar distribution of mass flow rate in the TV-tuner is obtained with the 2D porous model, while discrepancies in the mass flow rate up to 25% for the sidewall 1 have been found with the 3D porous resistance model.

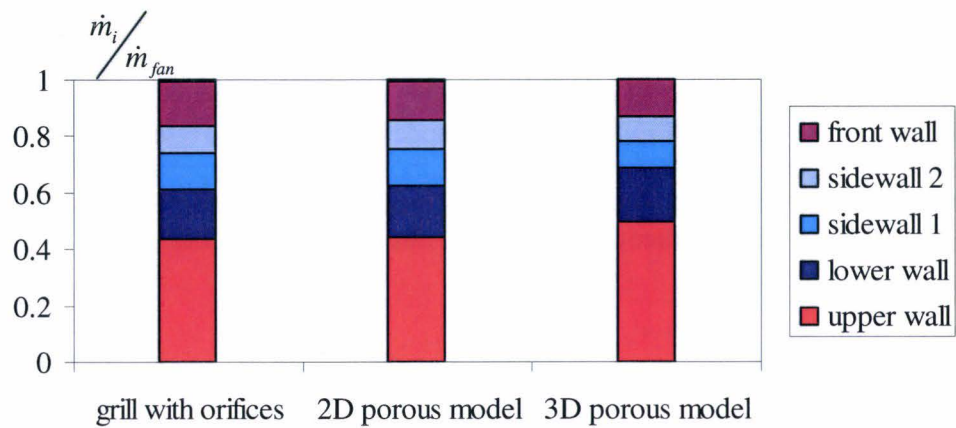


Figure 4.20. Mass flow rate distributions predicted by the different numerical models.

The static pressure drop is evaluated as previously considering the RMS of the static pressure field in the same section planes. The distribution of the static pressure in these section planes upstream of the porous element regions computed by the 2D model can be seen in figures 4.21. The results of the 3D porous resistance model can be found in figure A.6.10 in appendix. In these section planes, the spatial distributions of the static pressure predicted by the 2D and 3D porous resistance models are similar to the detailed computation solving the grill orifices. The RMS of the static pressure drop through the different outlets of the TV-tuner modeled with the 2D and 3D porous models can be found in appendix, tables A.6.13 and A.6.14.

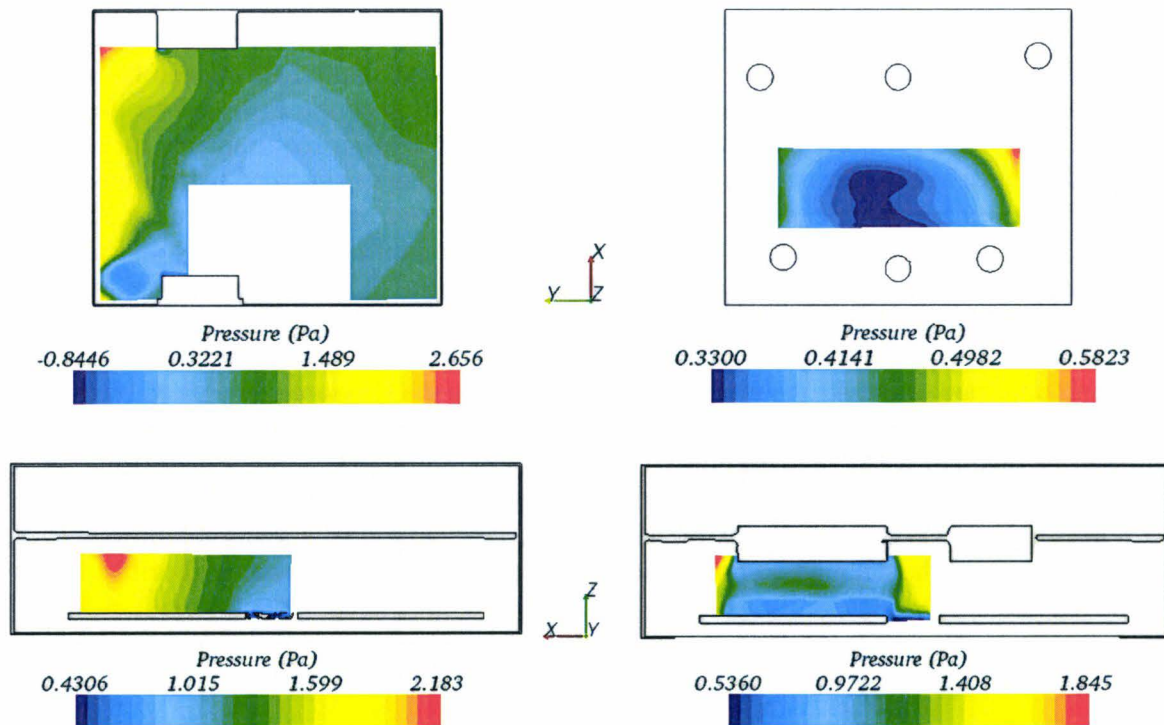


Figure 4.21. Static pressure distribution in the section planes  $P_1$  (top left),  $P_2$  (top right),  $P_3$  (bottom left) and  $P_4$  (bottom right); results of the 2D porous model for  $\omega = 5065$  rpm.

Again, a relatively high value of the standard deviation is found for the grill of the upper wall. Correspondingly, a strong discrepancy in the pressure drop is found at the upper grill. The comparison between the static pressure drop of the outlet grills provided by the detailed simulation and the 2D and 3D porous resistance models is shown in figure 4.22. Overall, the static pressure drop of the outlets predicted by the 2D and 3D porous elements is not consistent with the detailed computation. Strong discrepancies are found up to 46% for the upper outlet between the prediction of the porous resistance models and the detailed computation.

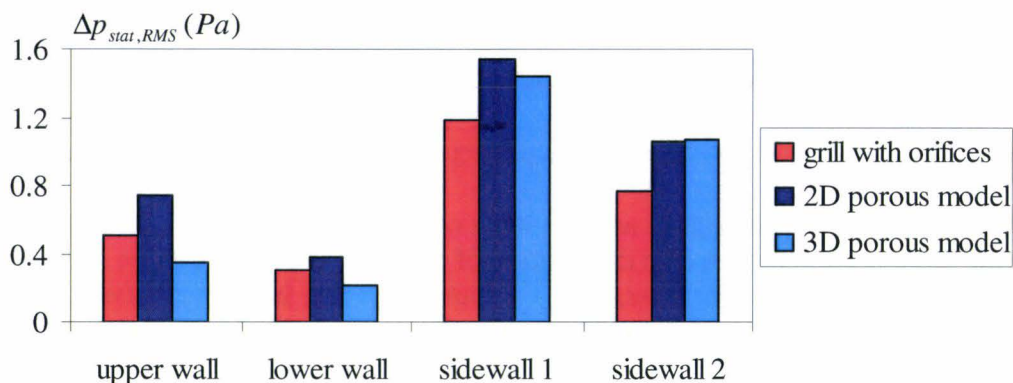


Figure 4.22. RMS of the static pressure drop through the outlets of the TV-tuner predicted by the different numerical models.

#### 4.3.4. Partial conclusions

For flow computation through thin electronic grills, different numerical models have been investigated, on the one hand solving the flow in each orifice of the grill and on the other hand using 2D and 3D porous resistance elements. First, the mesh requirements for solving each orifice have been examined on a perforated plate in comparison with correlations from the literature and measurements in a wind tunnel. A very good agreement has been obtained with the correlation 4.7 [162] using a grid with 5 cell layers in the near-wall region. Based on this grid to solve the thin grills, a detailed numerical model of the TV-tuner located in a free environment of constant pressure is then computed. Due to the complex geometry of the populated PCBs in the vicinity of the grill, strong inhomogeneities of the static pressure field are found upstream of the different outlet grills. Relative to the pressure rise created by the fan of  $6.8 Pa$  for a rotational speed of 5065 rpm, the RMS of the static pressure drop through the outlet grills is small with a maximum of  $1.17 Pa$ . Using porous elements to model the grills of the TV-tuner, strong discrepancies of the RMS pressure drop through the grills up to 46% have been found between the porous models and the detailed model solving the flow in each orifice. Therefore, the detailed computation solving the flow through each grill orifice has to be carried out.

---

## Chapter 5

# Validation of the co-simulation strategies on electronic systems in a vehicle

In the last chapter, the steady-state numerical methods for the treatment of electronic flows have been validated in elementary systems and can be applied in the coupling codes strategies for the prediction of the convective heat transfer. For an implementation in the development process, the co-simulation strategies must be validated in comparison with experimental results and appraised towards efficiency and reliability. In this respect, two complex electronic systems embedded in a vehicle are investigated in the following: a lead-acid battery and a sound amplifier. First, a numerical model of the electronic system in the vehicle must be validated to ensure that sufficient parameters are taken into account in the model to represent the thermal behavior of the real system. Once validated, the numerical models of the lead-acid battery and sound amplifier can be used for the validation of the co-simulation strategies, disposing of flow computations for the prediction of the convective heat transfer.

### 5.1. Battery in the spare-wheel cavity

The following investigation focuses on an AGM (absorbent glass mat) VLRA (valve regulated lead-acid) battery positioned in the sealed spare wheel cavity under the trunk.

#### 5.1.1. Critical parts and thermal requirements

The battery considered is composed of six serial mounted cells, separated by polypropylene walls. Each charged cell contains plates of lead metal (anode) and lead dioxide (cathode) with an insulating material in between (separator) to prevent from short circuit. The plates are submersed in an electrolyte composed of sulfuric acid and water and absorbed into a mat of glass fibers. The difference of charge between the plates leads to the origin of an electric current, consequently of an electrical power. During discharge, the electrodes react with the electrolyte to create lead sulfate, water and electric current. By charging, the cycle is reversed: the lead sulfate and water are electrochemically converted to lead, lead oxide and sulfuric acid with the help of an external charging source. According to the Arrhenius's equation, the rate of charge or discharge increases exponentially as cell temperature rises. Regarding critical operating conditions, below 0°C, the rate of chemical reaction is highly reduced and the performance of the battery may be impaired.

Moreover, temperatures lying in the range or exceeding  $55^{\circ}\text{C}$  -  $60^{\circ}\text{C}$  may initiate the vaporization of the electrolyte resulting in a complete failure of the battery. Therefore, the temperature of the battery cells should reach as soon as possible  $0^{\circ}\text{C}$  for a satisfying performance and must not exceed  $60^{\circ}\text{C}$ .

In order to predict the transient temperature of the battery cells in the future, a thermal model of the inner battery and surroundings in the vehicle must be investigated. For the validation of the model and to provide initial boundary conditions for the computation, experiments are carried out and described in the following.

## 5.1.2. Use cases and experimental investigations

### 5.1.2.1. Parameters of the temperature of the battery assembled in vehicle

During the operation of the battery, whether charging or discharging, heat is generated as current flows through the internal resistance of the battery, called Joule heating. According to the electric circuit of the battery illustrated in figure 5.1, the Joule heating is given by:

$$P_{Joule} = R_{i,B} I_B^2 \quad (5.1)$$

$$\text{or: } P_{Joule} = (U_B - U_0) I_B \quad (5.2)$$

with  $U_0$  the open-circuit voltage (OCV) of the battery,  $R_{i,B}$  its internal resistance,  $I_B$  and  $U_B$  the instantaneous current and the voltage measured at the electrical connectors respectively.

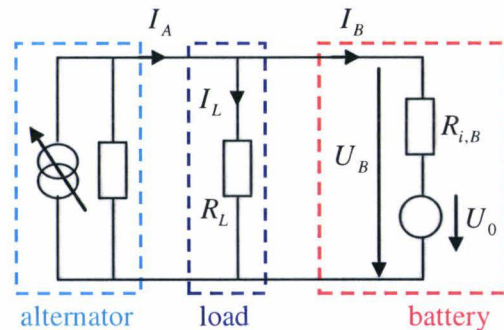


Figure 5.1. Battery charge and discharge electric circuit diagram.

Moreover, heat generation may result from the exothermic chemical reaction during battery charging. This fraction of heat generation is neglected in comparison with the Joule heating in the following. For a constant charge or discharge rate, the open-circuit voltage of the battery depends on the state of charge (SOC) of the battery and on the ambient temperature. The total internal resistance of the battery, which is the sum of each cell internal resistance, accounts for the resistances of the metallic and electrochemical paths and the contact resistance between the electrodes and the electrolyte of each cell. The internal resistance of a cell is temperature dependent, decreasing as temperature rises, so that the efficiency of the battery is improved at higher temperatures. Moreover, the internal resistance increases significantly with lower SOC of the battery. Typical characteristics of internal resistance and OCV with ambient temperature and SOC can be seen in figure 5.2.

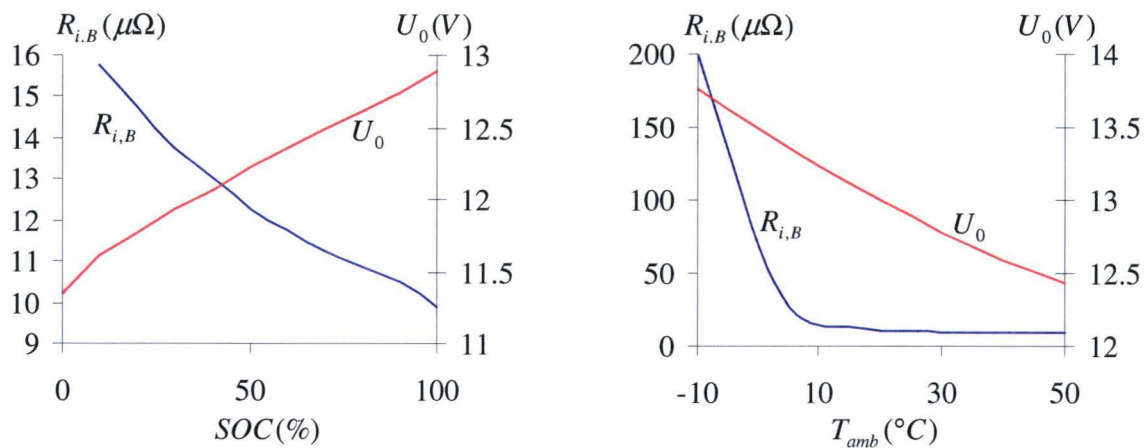


Figure 5.2. Typical variation of the internal resistance and OCV with SOC for  $T_{amb} = 25^\circ\text{C}$  (left) and with temperature for  $\text{SOC} = 100\%$  (right).

The operating current and voltage of the battery depend on the energy distribution in the vehicle according to the use case. Before the alternator is running, the battery alone provides the electrical power necessary for engine cranking. The short phase of discharge corresponding to engine cranking is characterized by strong heat losses due to the high current ranges required by the engine. After engine cranking, the alternator restores charge of the battery and may power other electrical systems, such as the engine fan, the compressor or the auxiliary heater. Such electrical loads yields to a current drop of the alternator and variations of the battery charging voltage.



Figure 5.3. Battery in the spare-wheel cavity; experimental set-up.

Moreover, in the present study, the battery is assembled in the spare-wheel cavity, laid on the bottom wall. Due to fluted surface of the bottom wall, the contact area between the battery case and the wall is limited. Two silencers joined with exhaust pipes are situated laterally to the spare-wheel cavity with shield plates in between to limit radiation. Depending on the engine and vehicle speeds, the surface temperature of the exhaust gas system is ranging between  $100^\circ\text{C}$  and  $400^\circ\text{C}$ , heating the lower surface of the spare-wheel cavity.

### 5.1.2.2. Use cases of winter and summer

The use case defined initially to test the performance of the battery in the spare-wheel cavity consists of engine cranking followed by idle with battery charge during two hours, without electrical load manually prescribed. From the thermal requirements of the battery mentioned previously, ambient temperatures of  $-10^{\circ}\text{C}$  and  $25^{\circ}\text{C}$  are prescribed to simulate use cases of winter and summer respectively. In the case of winter, the vehicle is situated in a climatic chamber maintained at constant ambient temperature, while it is located outdoors with sun radiation exposure in the case of summer. In both cases, the vehicle has been pre-conditioned during several hours with the same experimental conditions. The state of charge of the battery at the beginning of the experiment is of 70% in case of winter and 50% in case of summer. The effects on the internal resistance of the battery of the higher ambient temperature and of the lower SOC in case of summer are balancing each other, so that the internal resistances in both experimental cases should be equivalent. The experimental set-up can be seen in figure 5.3. The position of the thermocouples in the spare-wheel cavity is shown in appendix, figure A.7.1.

### 5.1.2.3. Experimental results

The experimental results can be seen in appendix, figures A.7.2 and A.7.3. Due to the heat generated by battery and the warm-up of the whole body shell with idle, the temperature of the whole spare-wheel cavity is increasing with time for the cases of winter and summer. Moreover, the temporal temperature gradient is about constant for each battery cell with an overall warm-up of about 5.3 K in case of winter and about 10.8 K in case of summer. This difference between the cases of winter and summer may come from a larger convective heat transfer between the battery and the ambient air in summer. The inhomogeneous temperature distribution at the beginning of the experiments in case of summer is attributed to a too short pre-conditioning phase. In both cases of winter and summer, the ambient air temperature obtained is warmer than the temperature of the battery case, indicating the direction of convective heat transfer. The heat generated by the battery is calculated from the experimental instantaneous current flowing through the battery and voltage measured at the electrical connectors using equation 5.2. The variation of the heat generated by battery charge with time can be seen in appendix, figure A.7.4. Large values of heat losses are obtained during the first seconds of engine cranking. Due to the higher SOC of the battery in case of winter than in summer, the battery charge does not require as much current from the alternator as in summer. Moreover, the abrupt drop of the heat generated by the battery at the beginning of the experiments in case of summer comes from a similar drop of the current flowing in the battery. This may be explained by the activation of a user external electrical load, such as the engine fan.

## 5.1.3. Numerical models

The models for the prediction of the transient temperature of the battery cells are described in the following.

### 5.1.3.1. Model of the inner battery

A model of the inner battery has been validated previously [28] in comparison with measurements performed by the supplier in laboratory conditions. The use case measured by the supplier consisted of a first phase of warm-up of the battery case by convection with a fan, followed by a phase of cooling with fan off. The battery, non-operating, was laid on a steel plate in a climatic chamber, so that the only heat transfer mechanisms are convection between

the battery case and the ambient air and conduction with the steel plate. The model of the battery cells, illustrated in figure 5.4, is constituted of a main part of lead sulfate considered as a solid of homogeneous temperature in contact with sulfuric acid. The chemical cell is isolated on the upper part with an air layer. The thermodynamical properties of the polypropylene walls, lead sulfate and sulfuric acid are provided by the supplier. The transient temperature of the battery cells has been found in very good agreement with the measurements.

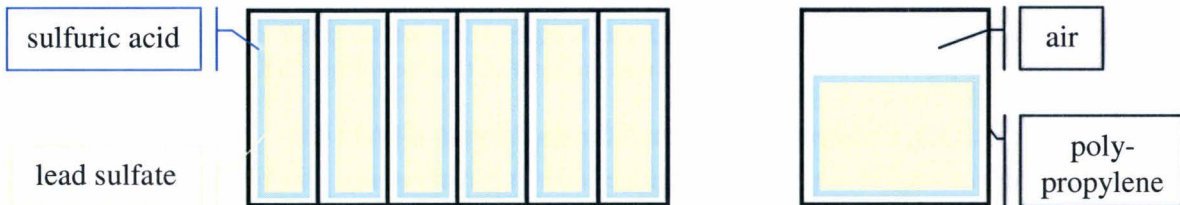


Figure 5.4. Model of the inner battery; view from above (left) and lateral view (right).

### 5.1.3.2. Thermal analysis with RadTherm

The model for the thermal analysis with RadTherm is constituted of the battery in the spare-wheel cavity surrounded by the exhaust-gas system, as illustrated in figure 5.5.

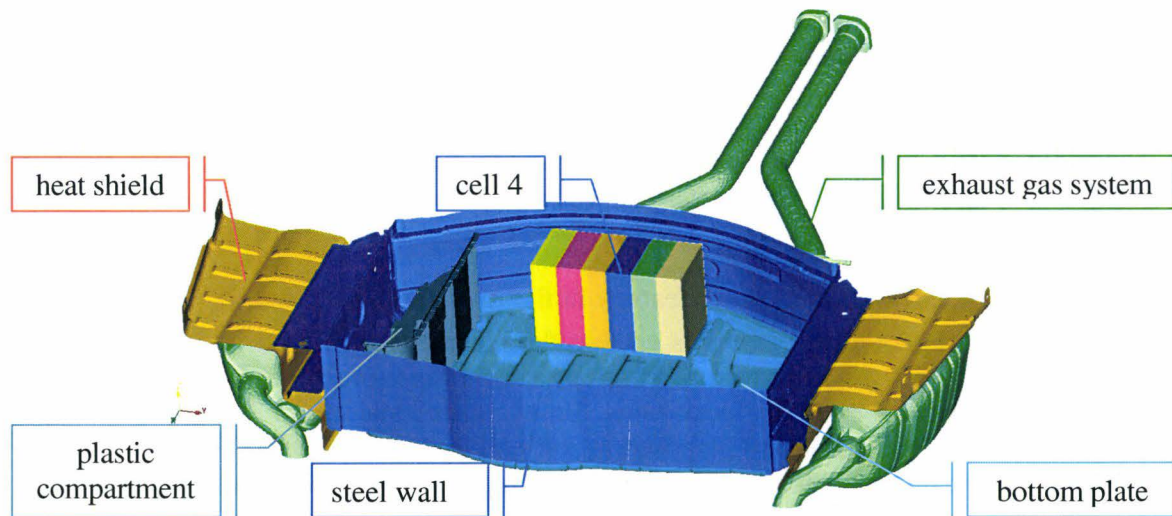


Figure 5.5. Numerical model for the thermal analysis with RadTherm.

The final surface mesh consists of 160,000 elements. The model of the inner battery validated previously is adopted in the present model, considering in addition the heat generated by the battery. To model the conductive and radiative heat transfer modes, the usual material properties are used for the steel exhaust gas system, cavity walls and battery bracket and for the felt cover of the cavity. Convection with the air flow of the underhood is modeled with a constant heat transfer coefficient and a time-dependent film temperature based on the experimental results. Because of the inhomogeneities in the temperature field at the beginning of the measurements, constant initial conditions equal to the ambient temperature would not provide comparable results with the experiments.

Therefore, the measured initial temperatures are used as initial conditions. Moreover, the following boundary conditions are assigned:

- The time-dependent electrical heat generated by the battery is imposed on the fluid part of lead sulfate of each battery cell;
- The time-dependent temperature of the exhaust-gas system is imposed on the silencers and exhaust pipes surface.

Moreover, the time-step is set to 60s and the temperature convergence criterion to 0.01 K. The sensitivity of these solver parameters is examined in the paragraph 5.1.4.2.

### 5.1.3.3. Convective heat transfer mode with STAR-CD

To predict the convective heat transfer mode with more accuracy, the buoyancy-driven air flow in the spare-wheel cavity is computed with STAR-CD. In order to characterize the natural convection regime, the Rayleigh number is determined from the experimental results. As the temperature distribution in the spare-wheel cavity is not known yet, the product of the Rayleigh and Nusselt numbers is calculated based on the measured temperature difference between the battery case and the surrounding air, as shown in appendix, figure A.7.5. The Rayleigh number in the spare-wheel cavity is estimated using the Nusselt numbers obtained previously in the cubical cavity (4.1.2), ranging between  $Ra = 6.7 \times 10^4$  and  $Ra = 2.1 \times 10^6$  in case of winter and between  $Ra = 8.4 \times 10^5$  and  $Ra = 1.5 \times 10^6$  in case of summer. The numerical method investigated and validated in the last chapter for the computation of buoyancy-driven flows is adopted in the present model. As the mesh computed in the cubical cavity did not play a major role on the Nusselt number for turbulent flows, a grid with 12 cell layers in the boundary layer is used in the present computation. The thickness of the boundary layer is calculated using equation 4.4. The grid characteristics can be seen in table A.7.1 in appendix. More details about the numerical model can be found in [166]. In the range of Rayleigh numbers considered, the standard low-Re k- $\epsilon$  model is used in the present study.

### 5.1.3.4. Coupling code strategy in the present study

The parallel discrete coupling process is used in the present study. In this coupling process, the wall temperatures resulting from a selected time-step of the RadTherm transient simulation are given as boundary conditions. Based on the successful initialization in the cubical cavity, the flow is initially supposed at rest and isothermal. As the flow may change between two consecutive time-steps of the discrete coupling simulation, flow computations at later time-steps are not initialized using the flow and temperature fields resulting from the computation at the previous time-step. Instead, the flow is initialized isothermal and at rest for each computation, as proceeded previously with the study of buoyancy-driven flows.

The model of the battery in the spare-wheel cavity proposed previously for the prediction of the transient temperature of the battery cells must be validated independently from the coupling strategy. This is investigated in the next section with a transient thermal analysis for both cases of winter and summer.

### 5.1.4. Model validation of the battery in the spare wheel cavity

A transient analysis is carried out with RadTherm using the numerical model described in paragraph 5.1.3.2 for the computation of two hours of warm-up of the battery. The error range of the measurement of  $\pm 1.5K$  is not represented in the figures.

#### 5.1.4.1. Modeling of the convective heat transfer

In order to ensure a reasonable modeling of the convective heat transfer mode for the model validation without co-simulation, the time-dependent punctual distribution of film temperature measured previously is used. Moreover, an average value for the heat transfer coefficient ( $3 \text{ W/m}^2\text{K}$ ) is prescribed in the spare-wheel cavity, based on the numerical results from the computation of natural convection in the rectangular box of aspect ratio 4:2:1 for  $Ra = 2.5 \times 10^5$ .

#### 5.1.4.2. Sensitivity of the solver parameters, case of winter

First, the sensitivity of the time-step and temperature convergence criterion on the numerical results is studied for the case of winter. Several transient analyses are carried out with time-steps of  $120s$ ,  $60s$ ,  $30s$  and convergence criteria of  $0.05 \text{ K}$ ,  $0.01 \text{ K}$  and  $0.002 \text{ K}$ . In comparison with the measurements, the temperature of the cell 4 predicted by the different computations is shown in figure 5.6.

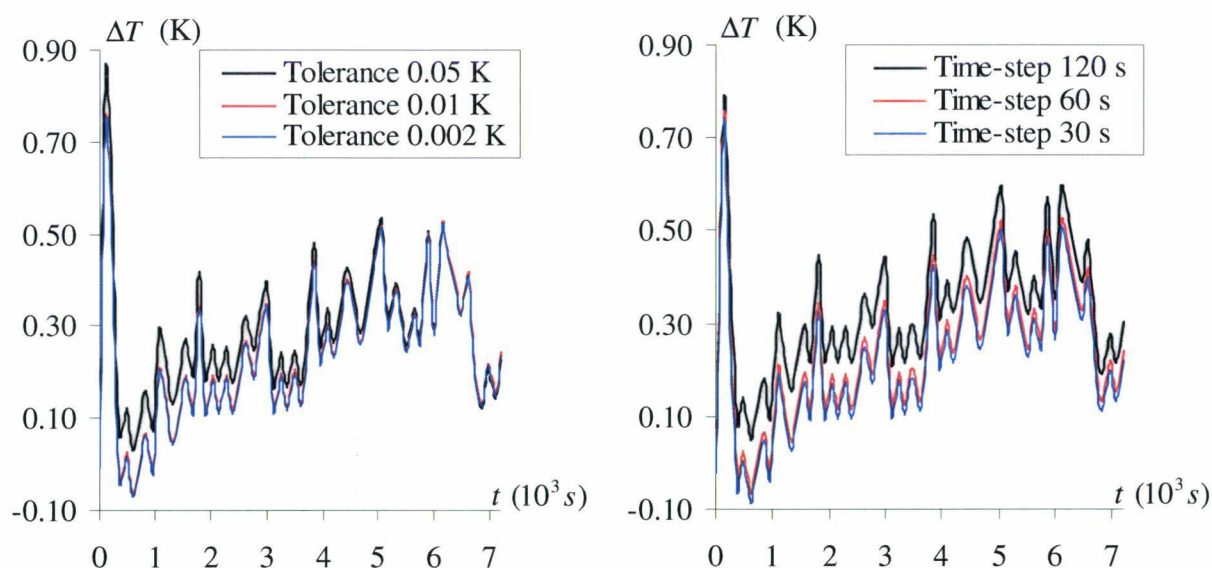


Figure 5.6. Sensitivity of the convergence criterion (left) and time-step (right). Difference between the numerical and experimental predictions for the temperature of the battery cell 4 in case of winter. The blue and red curves are almost superimposed.

The cell temperature predicted with convergence criteria of  $0.01 \text{ K}$  and  $0.002 \text{ K}$  are identical, while the numerical prediction with a convergence criterion of  $0.05 \text{ K}$  shows more discrepancy with the measurements. Similarly, the numerical predictions using time-steps of  $60s$  and  $30s$  are almost identical within  $0.02 \text{ K}$ , while the computation using a time-step of  $120s$  predicts the cell temperature with  $0.1 \text{ K}$  more than measured. Consequently, a convergence criterion and time-step of  $0.01 \text{ K}$  and  $60s$  are used for further computations with RadTherm.

### 5.1.4.3. Numerical results, case of winter

Experimental and numerical results for the temperature of the battery cell four and battery case are presented in figure 5.7. The comparison shows a very good agreement within 0.5 K. Consequently, the current approach used to model the convective heat transfer mode is reasonable in this case.

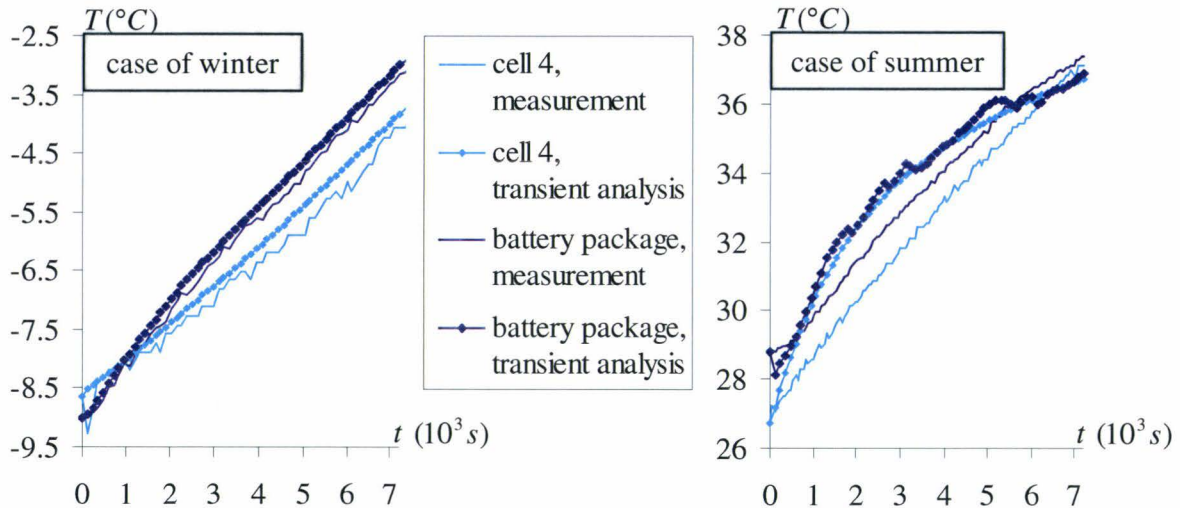


Figure 5.7. Transient temperature of the battery package (blue) and cell 4 (turquoise) for the case of winter (left) and summer (right). Measurements (jagged line) and transient analysis (dotted line).

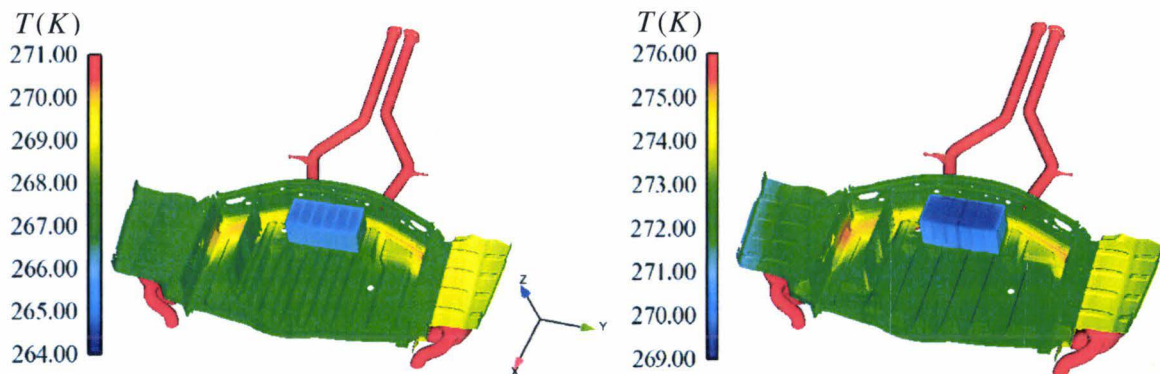


Figure 5.8. Temperature distribution of the battery in the spare-wheel cavity after 1800s (left) and 7200s (right) of simulation time; case of winter.

The temperature distribution in the spare-wheel cavity after half hour and two hours of simulation time is shown in figure 5.8. The local warm-up of the bottom plate above the exhaust pipes and silencers shows the effect of radiation due to the higher temperature of exhaust gas system. Due to the partial contact of the battery case with the bottom plate, the warm-up of the battery by conduction is limited. The distribution of convective net heat rate after half hour and two hours of simulation time can be seen in appendix, figure A.7.6. The convective heat rate is increasing with time with local higher heat rates after two hours. Moreover, the battery is the coolest element of the spare-wheel cavity, as the battery package is affected only slightly by convection and conduction.

**5.1.4.4. Numerical results, case of summer**

The computed temperatures of the battery cell four and battery case are shown in figure 5.8. A relatively good agreement is obtained within 2.5K. In particular, the computed initial and final temperatures are consistent with the measured ones. Nevertheless, the temperature gradient of both temperatures is not correctly predicted contrary to the case of winter. The temperature distribution in the spare-wheel cavity is shown in figure 5.9. The distribution of convective net heat rate in the spare-wheel cavity is shown in appendix, figure A.7.7. The effect of radiation from the exhaust pipes and silencers increases with time, due to the high heat load capacity of the shield plates near the spare-wheel cavity. Moreover, the temperature gradient within the spare-wheel cavity is found higher after two hours (10 K) than after half an hour (8 K), although the convective net heat rate is almost constant over the simulation time.

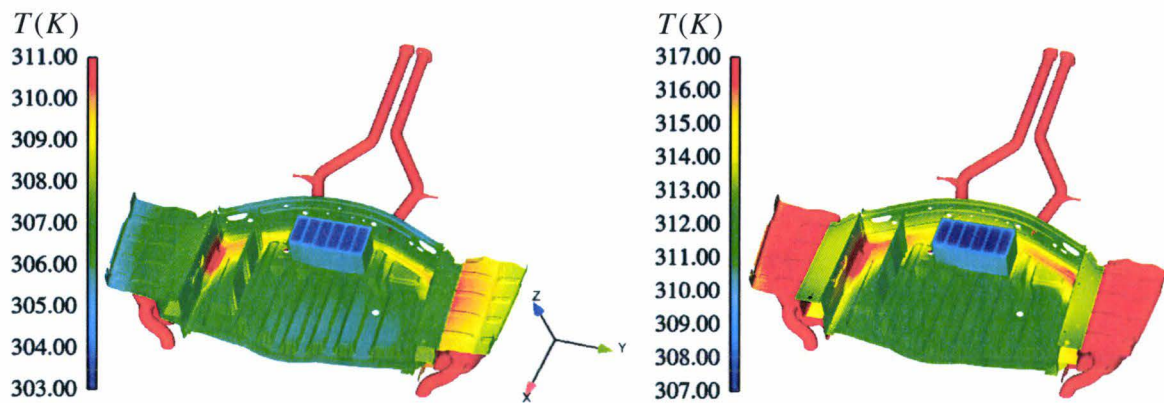


Figure 5.9. Temperature distribution of the battery in the spare-wheel cavity after 1800 s (left) and 7200 s (right) of simulation time; case of summer.

For a better comprehension of the transient heat transfer mechanisms on the temperature of the battery, the net heat transfer rates on the battery back case are compared over the simulation time. The radiation net heat rate is found within 25% of the convection and conduction net heat rates for both uses cases, thus negligible in comparison with the other heat rates. Moreover, the ratio of the convective to the conductive net heat rate is shown in figure 5.10.

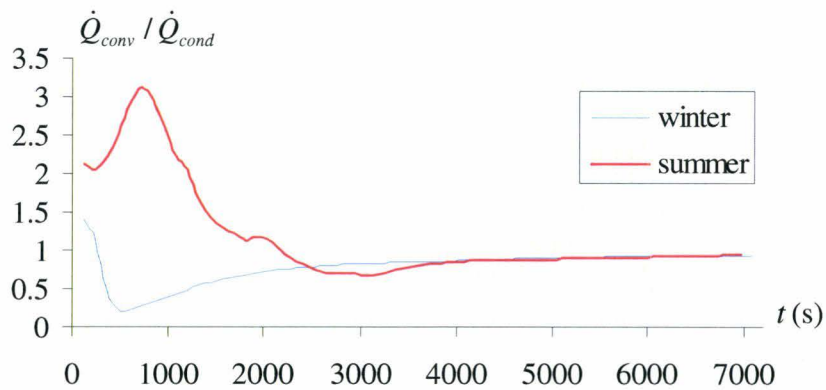


Figure 5.10. Ratio of the convective net heat rate to the conductive net heat rate at the battery package back for both cases of winter and summer.

During the first half hour, the battery case temperature is mainly affected by convection in the case of summer, while conduction dominates in the case of winter. Indeed, the temperature difference between the surrounding air and the battery case is higher in the case of summer than in the case of winter. After this period, the two heat fluxes tend to balance each other. This may explain why the current approach for the modeling of the convective heat transfer mode is sufficient for an accurate prediction of the battery temperature in case of winter, as convection never dominates. On the contrary, an accurate distribution of heat flux may improve the battery case temperature in case of summer.

#### 5.1.4.5. Examination of the heat generated by the battery, case of summer

In comparison with the measurements, the computed temperature gradient of the battery cell is found higher during the first half an hour and lower during the last hour, following the transient variation of the electrical heat generated by the battery cell assigned as boundary condition in the numerical model. In order to evaluate the validity of the measured current flowing through the battery, the heat generated is calculated with an energy balance for the battery cells, in order to provide the measured cells temperature. The cell part, which is the heat source, is treated as a fluid of homogeneous temperature as in the current model. In a first approach, the lead sulfate is considered solely as the heat source. The heat generated is given by:

$$P(t) = \left[ (mc_p)_{PbSO_4} \right] \frac{dT_{cell}}{dt} - \dot{Q}_{conduction} \quad (5.3)$$

In a second approach, the kinetics of the reactions of charge and discharge are considered based on the use case to determine the variation of the molar heat capacity of each chemical component  $i$  with time:

$$P(t) = \left[ \sum_i m_i(t) c_{p,i} \right] \frac{dT_{cell}}{dt} - \dot{Q}_{conduction} \quad (5.4)$$

The calculation of the mass of each substance during the first phase of discharge, followed by charging can be seen in table A.7.2 and figure A.7.8 in appendix. The comparison between the measured value for the heat generated by the battery and the analytical ones provided by equation 5.3 and 5.4 can be seen in figure 5.11.

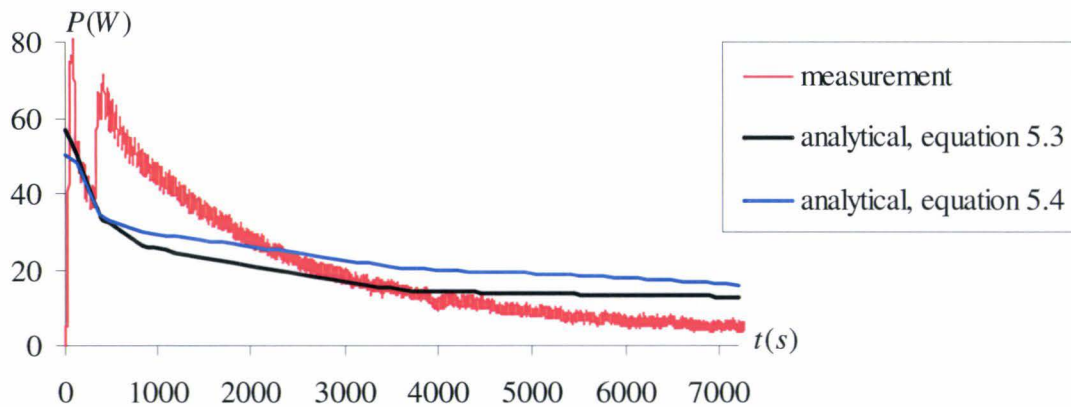


Figure 5.11. Transient heat generated by the battery; measured value (red) and analytical value using equation 5.3 (black) or equation 5.4 (blue).

Very similar analytical predictions of the heat generated by the battery are obtained considering the kinetics of the chemical reactions in the energy balance or a constant reacting mass of heat source. Large discrepancies over the whole simulation time can be seen between the analytical and measured values of the heat generated. Moreover, both analytical estimations of the battery heat generated are coincident with the measured value on a short phase characterized by an abrupt drop, which can also be found in the current flowing in the battery. Therefore, the fidelity of the measurement of the current intensity in the battery is questionable. Overall, the numerical model of the battery installed in the spare-wheel cavity provides consistent transient predictions of the battery temperature in comparison with the measurements for both use cases of winter and summer. An improvement of the prediction in case of summer is expected with the computation of the heat flux distribution with STAR-CD and realistic heat source boundary condition. This is examined in the next section.

### 5.1.5. Validation of the coupling strategy, case of summer

As the battery temperature is most affected by convection in case of summer, the validity of the parallel discrete coupling process is investigated for this use case based on the numerical models presented previously (5.1.3).

#### 5.1.5.1. Initial thermal analysis with RadTherm

Initially, a transient thermal analysis is carried out with RadTherm, computing two hours of simulation time. The time-dependent electrical heat generated by the battery provided by equation 5.3 is imposed on the lead sulfate part of the battery cells. The convective heat transfer in the spare-wheel cavity is modeled, in a first approach, using a fluid part of homogeneous temperature and a constant heat transfer coefficient of 3 W/m<sup>2</sup>K. For the computation of the convective heat flux distribution with STAR-CD, several time-steps are selected at which the wall temperature distribution computed by RadTherm is sent to STAR-CD. These time-steps must be representative of the time-dependent and spatial variation of the convective heat flux in the spare-wheel cavity. The distribution of the convective heat flux for different time-steps is shown in figure A.7.9 in appendix. Moreover, the evolution with time of the convective heat rate on the back of the battery package can be seen in figure 5.12. The results show a strong variation of the distribution of convective heat rate in the first quarter of an hour, while after one hour the convective heat rate is found almost constant. From the transient evolution of the convective heat rate, four relevant time steps are identified for flow computation: 0s; 780s; 3600s and 7200s. The results of the flow computation are presented in the next section.

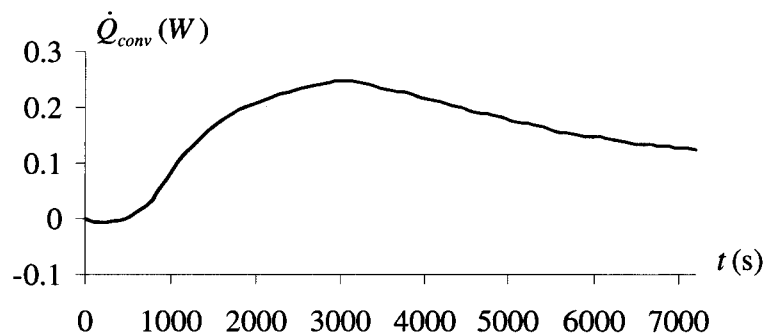


Figure 5.12. Variation with time of the convective net heat rate at the back of the battery package resulting from the initial transient analysis with RadTherm.

### 5.1.5.2. Steady-state flow computations with STAR-CD

The temperature distribution and streamlines in the spare-wheel cavity resulting from steady-state flow computations with STAR-CD are shown in figure 5.13.

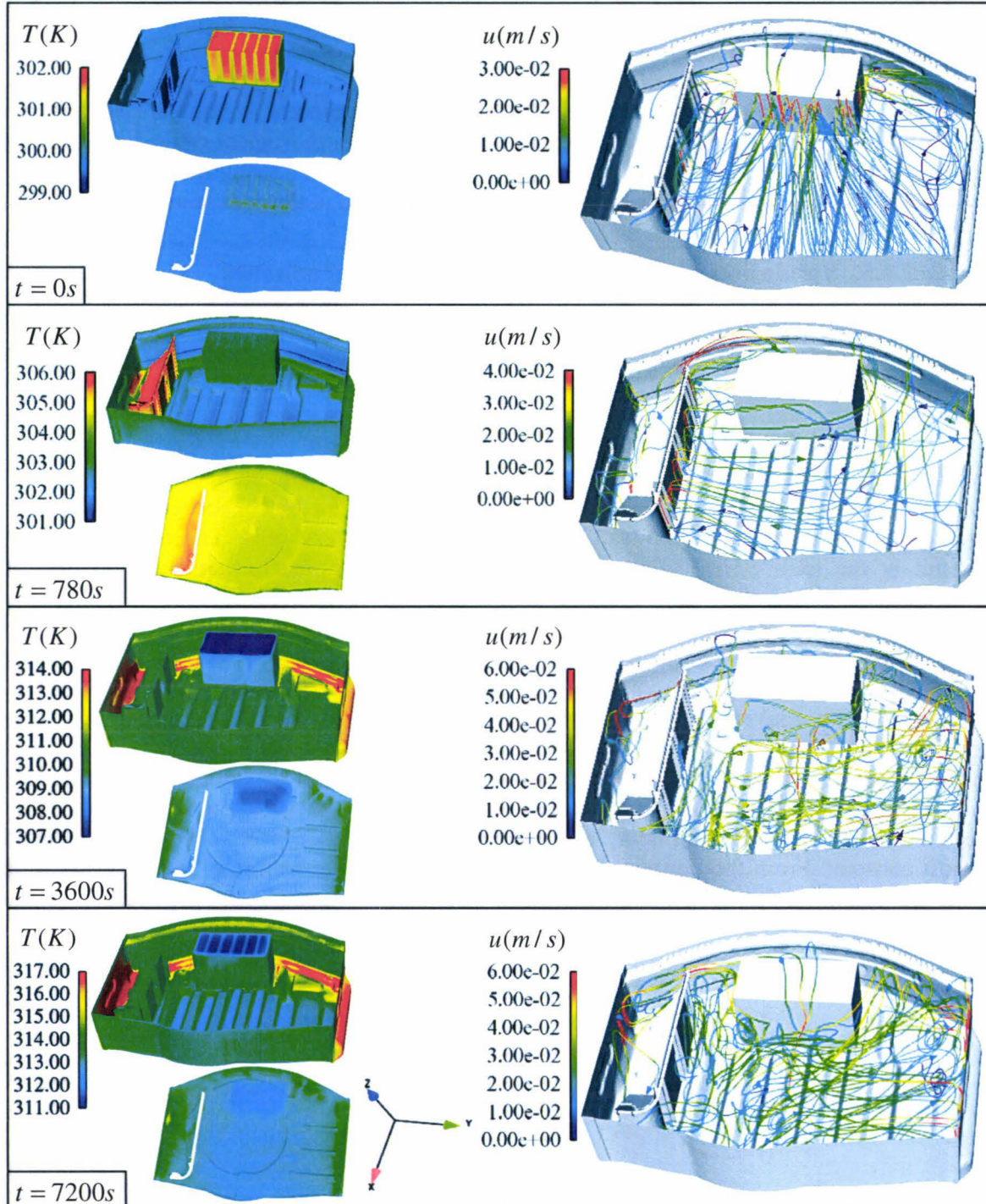


Figure 5.13. Temperature distribution (left) and streamlines (right) in the spare-wheel cavity at different time-steps resulting from a steady-state computation with STAR-CD.

At  $t = 0s$  the only significant wall temperature gradient in the spare-wheel cavity is found between the battery case and the cavity walls, yielding to eddy-viscosity rolls forming between the walls of differential temperature. At  $t = 780s$  rolls are developing longitudinally in the spare-wheel cavity, as the highest temperature gradient is found between the plastic compartment and the cavity walls. At  $t = 3600s$  and  $t = 7200s$  the cavity is heated from below with local hot spots in the vicinity of the exhaust pipes. Due to the complex temperature distribution and the large temperature gradient of the cavity lower and upper walls, the rolls orient themselves in different directions, increasing the apparent rate of turbulence of the flow. According to the rolls orientation, different convective heat flux distributions are obtained with the computed time-step, as shown in figure A.7.10 in appendix. Due to the similar wall temperatures and flow structures at  $t = 3600s$  and  $t = 7200s$ , similar heat flux distributions are found also. The convective heat flux at the walls of the spare-wheel cavity predicted by STAR-CD and RadTherm are lying in the same range of order, but different distributions are found at  $t = 0s$  and  $t = 780s$ .

### 5.1.5.3. Solid temperatures after coupling

The heat transfer coefficient and film temperature computed by STAR-CD are sent to RadTherm for a second transient thermal analysis. To obtain a time-dependent function of the convection boundary conditions, a linear interpolation is used between two consecutive time-steps computed by STAR-CD. The battery temperature computed by the co-simulation is compared with the experimental results and the predictions of the initial thermal analysis based on a constant convective heat transfer coefficient, as shown in figure 5.14.

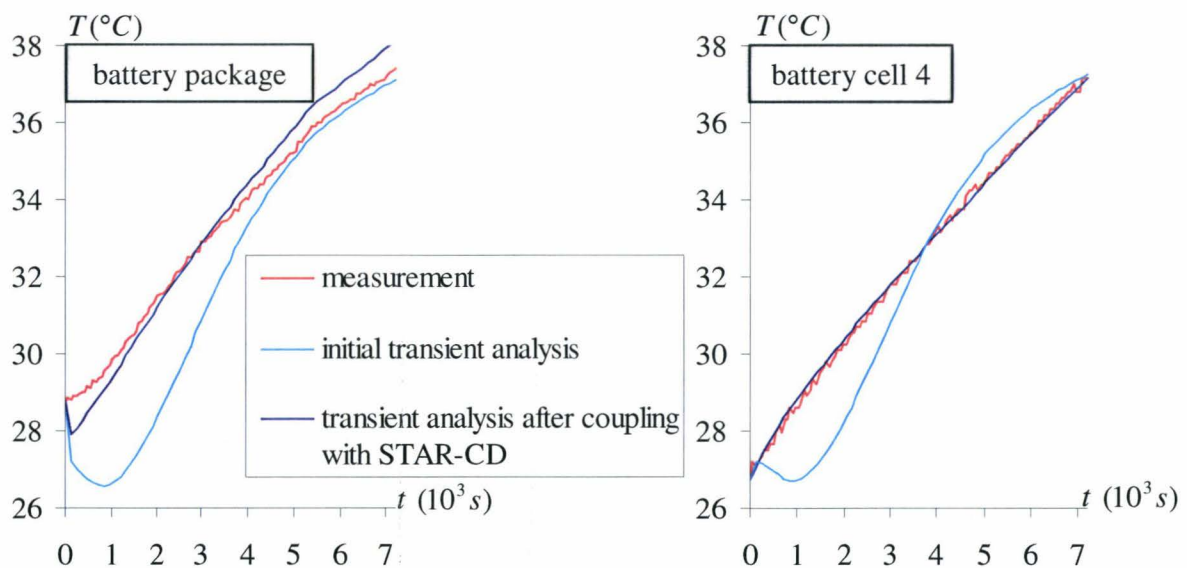


Figure 5.14. Transient temperatures of the battery case (left) and of the battery cell 4 (right). Measurements (jagged line), initial transient analysis (dotted line) and transient analysis after coupling with STAR-CD (cross line).

The battery cell temperature predicted by the co-simulation is lying superimposed with the experimental result. Because of the initial inhomogeneous temperature field initially, the fluid part used to model the convective heat transfer in the spare-wheel cavity for the initial thermal analysis is cooling down during the first ten minutes, which yields to a similar cooling of the battery case and cell. With the flow computations at  $t = 0s$  and  $t = 780s$  with STAR-CD, the

fluid temperature in the spare-wheel cavity is corrected, providing a reasonable prediction for the temperature of the battery case after coupling. Accordingly, the temperature of the battery cells is found in very good agreement with the measurements within 1 K. Therefore, with flow computations at adapted time-steps, the parallel discrete coupling strategy is accurate enough to provide reasonable transient temperature predictions in case of buoyancy-driven flows.

### **5.1.6. Determination of a critical use case of summer**

After two hours, the battery cell temperature is reaching 37°C. Of particular interest is the time for which the upper critical temperature of the battery cells (60°C) is reached and thus the battery is not working in its operating range anymore. This is examined in the following.

#### **5.1.6.1. Operating time period by idle**

For the determination of the operating time period, a transient analysis is performed using the results of the coupling strategy validated in the previous paragraph. The use case computed is the same as previously with engine idle and battery further charging. The convection boundary conditions, film temperature and heat transfer coefficient, are linear extrapolated to obtain a time-dependent distribution over 45000s. As the spatial distribution of convective net heat flux has been found very similar at  $t = 3600s$  and  $t = 7200s$ , it is used for the extrapolation. Similarly, the temperature of the exhaust-gas system and the heat generated by the battery are also extrapolated, assuming an almost constant profile between 7200s and 45000s. This assumption is reasonable, as the temperature loads and electrical loads conditioned by the use case are constant. The moderate increase in the SOC of the battery is considered for the extrapolation of the heat generated by the battery. The battery operating time period predicted by the transient analysis is shown in figure A.7.11 in appendix. The critical temperature of the battery is reached after 11.7 hours. Consequently, the current use case is not representative of realistic driving conditions to test the battery in its higher operating range. Other operating conditions for a new use case are investigated in the following.

#### **5.1.6.2. Critical use case**

A previous study [167] showed that the temperature of the exhaust-gas system and the ambient temperature have a significant effect on the cell temperature. Typical driving conditions yielding to a relatively high temperature range of the exhaust-gas system over a long time are a typical highway drive at high speed over several hours. Such driving conditions preceded by engine cranking with an ambient temperature of 35°C are investigated in the case of battery warm-up. Convection of the underhood with the ambient air is modeled with a constant heat transfer coefficient of 20 W/m<sup>2</sup>K and using a fluid part of homogeneous temperature assigned of a constant volume flow rate and temperature. Similarly, convection in the spare-wheel cavity is modeled with a constant heat transfer coefficient of 3 W/m<sup>2</sup>K and a fluid part of homogeneous temperature, as in paragraph 4.1.5.1. Moreover, the time-dependent electrical heat generated by the battery provided by equation 5.3 is imposed on the fluid part of lead sulfate of each battery cell. The temperature of the exhaust-gas system is defined as a step function with an initial temperature of 35°C and a constant temperature of 400°C reached after 20 minutes. A transient analysis is carried out with RadTherm, computing 3 hours of simulation time. The results of the computation are provided in figure 5.15.

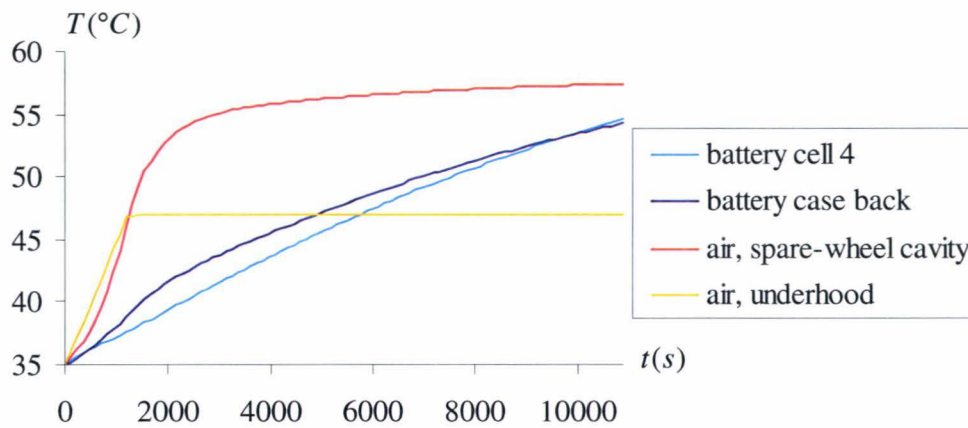


Figure 5.15. Prediction of the temperature of the battery case (blue) and cell 4 (green) with computed film air temperature in the spare-wheel cavity (red) and underhood (orange) for the case of summer with highway driving operating conditions.

With an initial homogeneous temperature field, the prediction for the battery temperature does not show any cooling phase during the first minutes as previously using a fluid part to model the convective heat transfer. Moreover, the battery warm-up is of about 20°C after 3 hours of warm-up, reaching the range of critical temperatures, for which the electrolyte may vaporize. Therefore, the use case with highway drive over several hours is relevant to check the battery temperature in its upper critical range.

### 5.1.7. Partial conclusions

A numerical model in RadTherm of the battery in the spare-wheel cavity has been proposed including the chemical composition of the battery and the heat generation by Joule heating. Numerical results are compared with experimental ones for the validation of the numerical model, providing a very good agreement in case of winter. In case of summer, the electrical heat generated must have been re-evaluated for better predictions of the temperature of the battery cells. As the battery temperature is mostly affected by convection in case of summer, a parallel discrete coupling process between RadTherm and STAR-CD has been carried out for this use case. With flow computations at adapted time-steps, the battery temperature could be reasonably predicted within 1 K; consequently, the parallel discrete coupling strategy is validated.

## 5.2. Sound amplifier in a cavity under the passenger's feet

In the following, thermal models and computational methods are investigated to predict the temperature of a sound amplifier situated in a cavity between the engine compartment and under the floor covering of the passenger under the cockpit.

### 5.2.1. Thermal requirements and heat transfer mechanisms

#### 5.2.1.1. Critical component

The sound amplifier is constituted of one populated PCB, which is screwed between a heat sink of aluminum alloy and a steel bottom plate, as shown in figure 5.16. Among the different electronic modules mounted on the PCB, the FOT (Fiber Optical Transceiver) is the most thermal sensitive and critical component. For the transmission of audio and video data between the telematics devices, a MOST (Media Oriented Systems Transport) infotainment bus system is used. The MOST network transceiver is the FOT, which transforms the light signal in an electrical one for admission in the interface controller and inversely. If the ambient operating temperature of the FOT reaches its critical value, the FOT is switched off and the output volume is mute, resulting in a failure of the MOST ring.

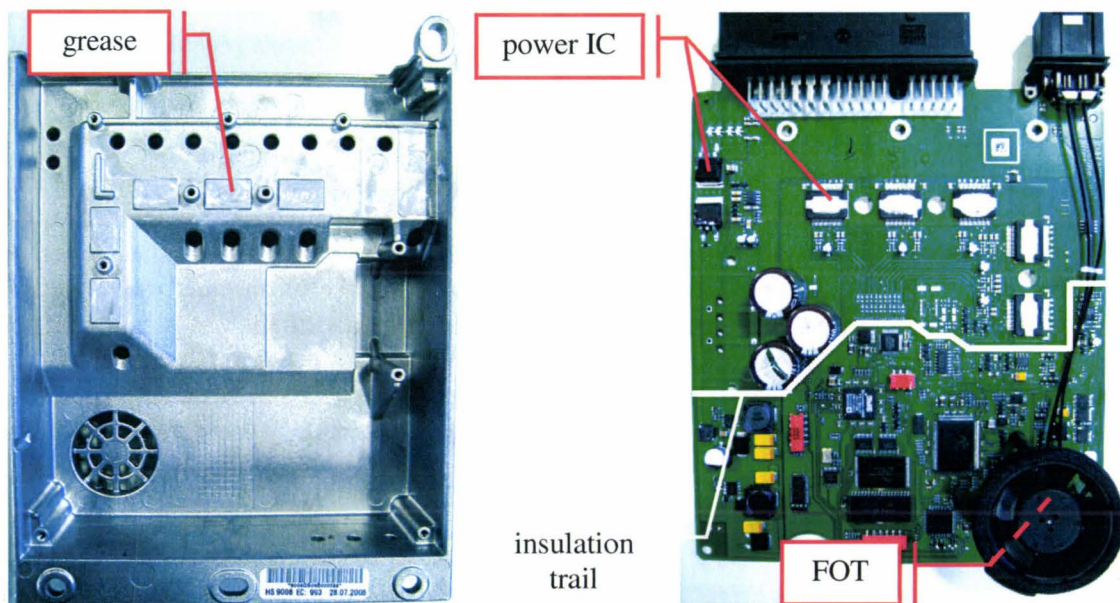


Figure 5.16. Sound amplifier assembly; heat sink viewed from below (left) and PCB viewed from above (right). The FOT is mounted on the PCB under the fan.

#### 5.2.1.2. Heat transfer mechanisms in the sound amplifier

To amplify the low-power signals to a level suitable for driving loudspeakers, seven MOSFET (Metal–Oxide–Semiconductor Field-Effect Transistor) power ICs contribute to 95% of the heat generation in the sound amplifier. The remaining 5% is due to the operation of a group of semiconductors. As the power ICs are pressed on the heat sink, it is assumed that most of the heat is directed by conduction from the junction to the heat sink. This

assumption is verified in the next paragraph. Moreover, a multilayer insulation trail separates the board into two parts, limiting heat conduction between the power ICs and the FOT. To cool down the FOT and the semiconductors during warm-up, a fan is assembled on the PCB above the FOT. The fan operating voltage is regulated according to the ambient operating temperature of the FOT measured in its vicinity. Additionally, in order to ensure that the FOT works in its operating range, the sound level of the radio is reduced automatically before the critical temperature is reached, yielding to a decrease of the heat generated by the power ICs. Accordingly, the ambient operating temperature of the FOT decreases until a certain threshold, for which the sound level is slowly increased.

### 5.2.1.3. Measurements of the thermal resistances and capacitances in the power ICs and its environment

For a better understanding of the heat transfer mechanisms dissipating the heat generated by the power ICs, transient measurements of the thermal response to a step function of a power IC are carried out, providing the thermal resistances and capacitances in the 1D main heat path. The methodology of the measurements is given in section 3.7.1.4. For a better identification of the thermal resistances and capacitances constituting the system, several measurements are performed:

- First, the power IC alone is placed in a still air chamber under natural convection conditions, referenced as system 1. As the package has no contact with any other surface, heat transport is limited to convection.
- Then, the power IC, still placed in the still air chamber, is mounted with grease on a small aluminum plate, referenced as system 2.
- Finally, the power IC is assembled in the sound amplifier as original, i.e. mounted on the lower surface of the heat sink with thermal grease between and pressed between the PCB and the heat sink. The full original contact surface between the chip and the PCB could not be reproduced, as the pins connectors have been cut for the measurements. The fan is off, reproducing natural convection conditions. This is referenced as system 3.

The experimental set-up and results can be seen in appendix, figures A.8.1 to A.8.4. The comparison of the differential structure functions of the different systems shows a common motif in the thermal resistance range [0;2.5] corresponding to the heat transfer by conduction in the power IC.

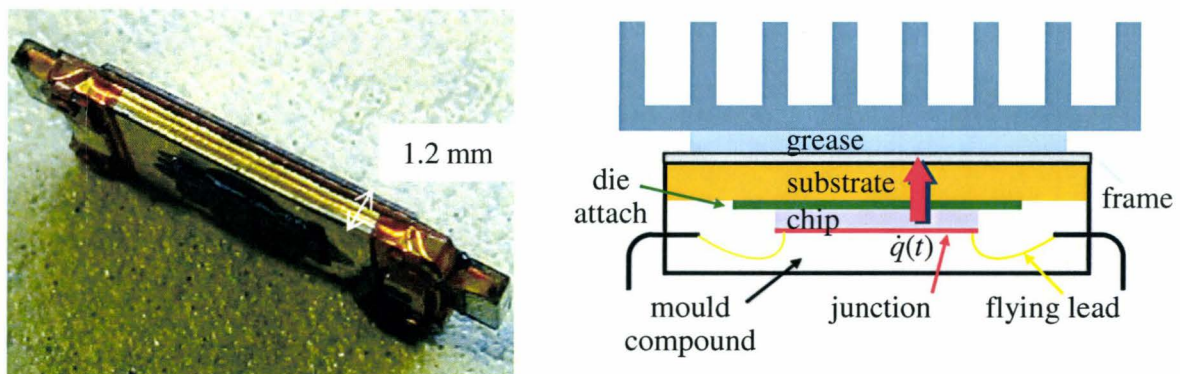


Figure 5.17. Constitutional layers of the upper part of a power IC (left); schematical representation of the main heat path in a power IC (right).

The thermal resistances in this range have been clearly identified in the three systems, showing that the same heat path from the junction to the copper alloy frame, as shown in figure 5.17. Therefore, the heat generated by the junction of the power ICs assembled in the sound amplifier is essentially directed to the copper alloy frame and dissipated by conduction in the heat sink under natural convection conditions. Moreover, the temperature rise after Dirac excitation of the chip assembled in the system 3 is measured, showing that a steady-state is reached after 2 seconds.

## 5.2.2. Use case and experimental results

### 5.2.2.1. Parameters of the heat generated by the power ICs

In most of passenger cars, the radio system has ten channels to drive the different loudspeakers in the front, rear and in the trunk of the vehicle. Depending on the type of the loudspeakers, the current flowing through the front and rear channels may be different. The instantaneous heat generated by the power transistors is the difference between the power drained from the supply and the output power required by the loudspeakers. The supply power depends on the input music signal. For a suitable representation of a real music signal, the signal amplitude must be described by a probability density function (pdf) of the amplitude [168]. Moreover, during the playing of a music program, the parts of low-level output volume are reproduced undistorted, while the loudest parts are suffering from an annoying clipping harmonic distortion. The heat generation increases with the time during which clipping distortion occurs and is also a parameter of the heat generated by the power ICs to consider.

### 5.2.2.2. Heat transfer mechanisms in the cavity of the sound amplifier

In the actual Mercedes-Benz SLK-Class, the sound amplifier is located in a cavity surrounded by the engine compartment on the front side in the driving direction, by the underbody on the lower side and the cabin on the back side, as shown in figure 5.18. On the upper side, the cavity is connected to the cockpit with a small opening surface. The cavity is separated from the engine compartment and underhood by a steel cowl as part of the body shell covered by thick foam. The isolation with the cabin is achieved with a thin steel plate and multilayer carpeting. For high thermal loads of the engine compartment, the cavity of the sound amplifier is considerably heated from below.



Figure 5.18. Sound amplifier in a compartment under the passenger's feet; experimental set-up.

### 5.2.2.3. Use case

To reach high thermal loads of the underhood, the use case consists of a drive period uphill followed by engine idle. The vehicle is situated in a climatic chamber warmed up at a constant environment temperature and radiation exposure with several hours pre-conditioning (figure 5.17). The pre-conditioning and measurement phases are carried out with roof and windows opened, to provide critical thermal conditions in the cabin, in particular for the carpeting and cockpit. The radio is turned on at  $t = 300$  s. after the measurements started, corresponding to the beginning of the operation of the sound amplifier. The sound amplifier operates under critical conditions with maximum sound level, maximum bass and treble and IEC noise according to the standards [169]. Within these conditions, a high THD (total harmonic distortion) rate is expected between 1% and 10%. The position of the thermocouples in the spare-wheel cavity is shown in appendix, figures A.8.5 and A.8.6.

### 5.2.2.4. Experimental results in the vehicle

The experimental results can be seen in appendix, figures A.8.7 and A.8.8. During the first 300s, the temperature field in the sound amplifier and cavity is almost homogeneous as a result of the pre-conditioning. Due to the thermal load from the engine compartment, the temperature of the cowl is increasing during the uphill drive, followed by a slow decrease during idle. The group of semiconductors, to which the SHARC processor belongs, is warming up with a high temperature gradient as soon as the sound amplifier operates, i.e. at  $t = 300$ s. The FOT starts warming up at  $t = 360$ s, followed by the tip of a fin of the heat sink at  $t = 420$ s and by the steel bottom plate after  $t = 480$ s. The temperature of the SHARC component clearly shows the activation of the fan on the first operating level after  $t = 540$ s and on the second one after  $t = 1200$ s. The forced convective volume flow rate created by the fan yields to a slight decrease in the temperature gradient of the components mounted on the PCB. The overall temperature decrease after  $t = 4020$ s comes from the reduction of the sound level of the radio. Due to the proximity of the probe positioned on the feet plate with the outlets of the sound amplifier, a similar temperature decrease is also found for the feet plate. As the FOT is directly situated under the fan, its temperature is very similar to the temperature of the air drawn by the fan. Due to the heat exchange between the electronic components in the sound amplifier and the air by convection, the air temperature at the outlets of the sound amplifier is higher than at the fan inlet. The temperature gradient between inlet and outlets is increasing with time, as the convective heat flux evolves with time.

## 5.2.3. Numerical models

With the present pre-conditioning stated by the use case, the threshold temperature for which the fan switches on is reached in a very short time after operation of the sound amplifier. The goal of the numerical simulation is to predict the time for which the performance of the sound amplifier is impaired, i.e. the time for which the sound level is first reduced.

### 5.2.3.1. Numerical strategy, fan on

When the fan is activated, the heat transport by convection in the sound amplifier depends on the establishing volume flow rate and pressure distribution in the system and in the cavity. Moreover, to predict with accuracy the distribution of convective heat flux and the growth of the temperature and velocity boundary layers in the sound amplifier, the flow must be solved considering the geometrical assembly and the position of the heat sources.

Therefore, the numerical models to solve the flow and the solid must account for:

- the fan environment for the establishment of the volume flow rate depending on the pressure distribution upstream and downstream;
- the power ICs and the group of semiconductors as heat source;
- the wiring board with the protruding ICs and the internal surface of the sound amplifier for the prediction of the boundary layers growth.

### 5.2.3.2. Numerical strategy, fan off

The goal of the computation during the first phase of warm-up without fan running is to predict the temperature distribution at time  $t = 540s$ , which is required for further computations with fan on. When the fan is off, it is first assumed that the heat dissipated by the group of semiconductors is negligible in comparison with the heat generated by the power ICs and does not much affect the temperature distribution in the vicinity. Moreover, the measurements of the thermal resistances and capacitances in the power ICs under natural convection conditions have shown that the heat generated by the junction is mainly directed to the heat sink by conduction because of the assembly of the power ICs. Therefore, it is also assumed that conduction in the board can be neglected in comparison with conduction in the heat sink. Furthermore, good predictions for the battery temperature have been obtained using a fluid part of homogeneous temperature and a constant heat transfer coefficient to model the natural convective heat transfer in the spare-wheel cavity (5.1.7). With these assumptions, a complex numerical model of the internal layout of the sound amplifier is not required when the fan is off, so that considerable computing time can be saved.

### 5.2.3.3. Computation of conduction with PERMAS

The numerical model for the computation of the conductive heat transfer is restricted to the cavity of the sound amplifier encompassed by the steel cowl on one side and the feet plate and carpeting on the other side, as illustrated in figure 5.19. Conduction with the cockpit is not considered and the numerical model is completely sealed in place of the vent with the cockpit. As discussed previously, only the case of the sound amplifier is represented in the model for the computation with fan off, while the board with different components mentioned before are taken into account for the computation with fan on.

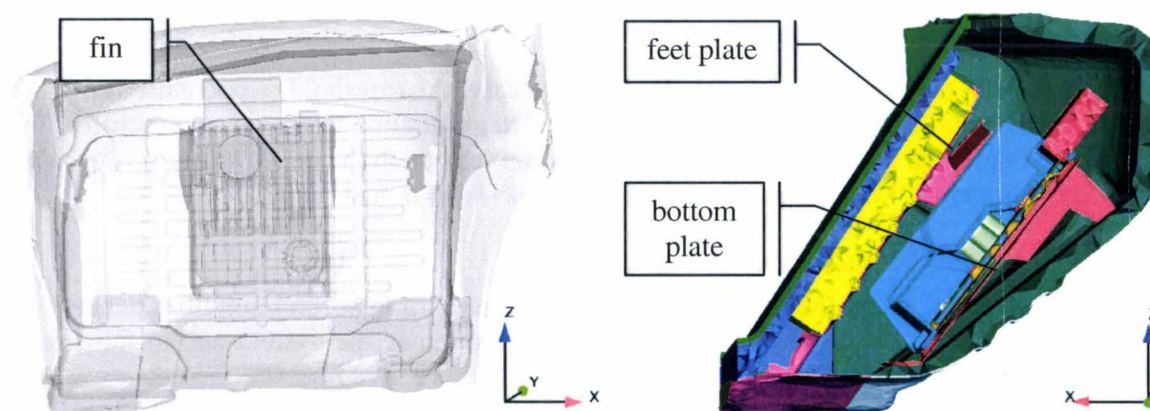


Figure 5.19. PERMAS numerical model for the computation of conduction in the cavity of the sound amplifier with fan off (left) and fan switched on (right).

With fan off, the conductive heat transfer from the junction of the power ICs to the heat sink is modeled using a resistor model, which consists of a copper solid layer and which conductivity is calculated using the thermal resistances measured in paragraph 5.2.1.3. The dimensions of the solid layer are equivalent as the upper part of the power IC, from the junction to the frame.

With fan on, the semiconductors and power ICs are modeled as blocks of real dimension mounted on the board. The conductive heat transfer in the wiring board is modeled as an orthotropic single layer solid assigned of in-plane and through-plane thermal conductivities provided by the supplier. This approach is consistent with the investigations of Hwang [92] and Zhao [100]. Based on the illustrations 2.2 and 5.17, the conductive heat transfer from the junction of the semiconductors and power ICs is modeled with a two-resistor thermal model using junction-to-board and junction-to-top thermal resistances, according to [100]. The lower and upper resistors are assigned of the material thermal properties of the mould compound and copper respectively.

The temperature field resulting from the pre-conditioning phase is given as initial condition. The thermal loads from the engine compartment are considered with temperature boundary conditions. Moreover, the surface temperature of the upper carpeting layer is given as boundary condition using the ambient temperature in the cabin. The heat generated by the junction of the power ICs and semiconductors is imposed on the surfaces between both resistors, given as a step function different from zero for  $t = 300s$ . The final mesh consists of  $1.37 \times 10^6$  solid elements in case of fan off and  $2.4 \times 10^6$  in case of fan on.

#### 5.2.3.4. Computation of radiation with POSRAD

Based on the numerical models for the computation of conduction, models are created for the computation of radiation in the cavity of the sound amplifier using 2D triangular membrane elements laid on the surface of the solid models and superimposed with the tetrahedral elements. The resulting membrane surfaces are constituted of  $3 \times 10^5$  solid elements in case of fan off and  $4.5 \times 10^5$  in case of fan on.

#### 5.2.3.5. Computation of convection with STAR-CD

With fan off, eddy-viscosity rolls may form between the tip of a fin and the upper wall [170], due to the small thickness of the air layer between the fins and the cooler upper wall in comparison with the width of the fins (table A.8.1 in appendix). The Rayleigh number is calculated based on the measured temperature difference between the fins and the upper feet plate. With the warm-up of the heat sink with time, the Rayleigh number increases up to  $Ra = 2 \times 10^5$  at  $t = 540$  s. A boundary layer of variable thickness is generated, which adapts to the complex geometry of the heat sink and to the possible development of the flow. Details of the mesh parameters can be seen in table A.8.2 in appendix. In the range of Rayleigh numbers considered, the standard low-Re  $k$ - $\epsilon$  model is adopted according to the previous results.

With fan on, the Reynolds number based on the inlet velocity of the group of semiconductors and the hydraulic diameter of the channel is estimated of  $Re = 2 \times 10^2$ . The modified Grashof number based on the hydraulic diameter and the heat dissipated by the semiconductor SHARC is  $Gr^* = 6 \times 10^4$ . In this range of Reynolds and Rayleigh numbers, the strength of shear forces is large enough to slow down the enlargement of the thermal boundary layer and inhibit the development of plumes over the group of semiconductors. Both numerical methods

for fan flow computation, MRF and rotational body force, are used in this study and the standard high-Re  $k-\varepsilon$  model with the two-layer approach is chosen for the investigation. Outside the sound amplifier, the fins of the heat sink are much warmer than the feet plate or the cowl. As the walls of the cockpit are cooler than the fins of the heat sink, a plenum cavity representing the cockpit, illustrated in figure 5.20, is connected to the cavity of the sound amplifier and computed for the prediction of a potential mass transfer between both cavities. The corresponding mesh parameters can be seen in table A.8.3 in appendix.

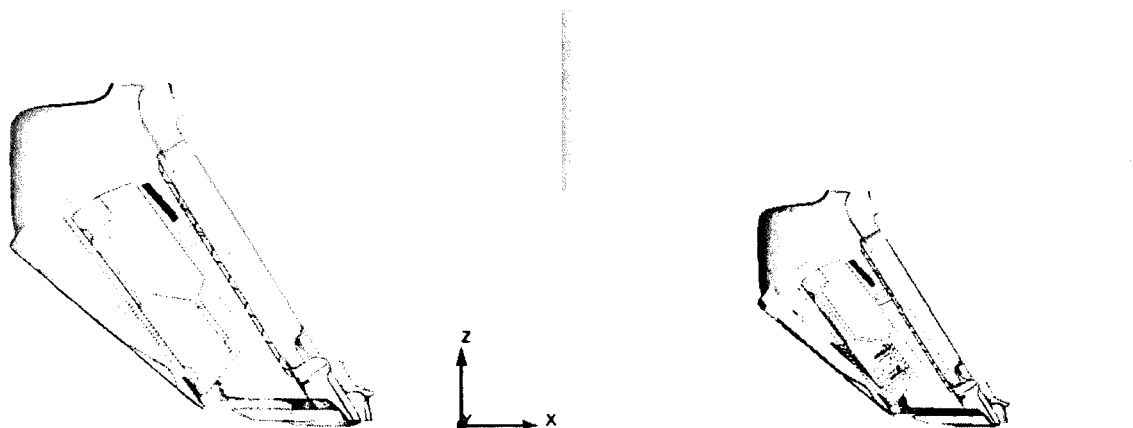


Figure 5.20. STAR-CD numerical model for the computation of convection in the cavity of the sound amplifier with fan switched off (left) and fan on (right); fan mid-section.

For the first computation of the pre-conditioning phase, the flow is initially supposed at rest and isothermal. Moreover, the temperature field resulting from the pre-conditioning phase is given as boundary condition. The slight inhomogeneities in the temperature field at the beginning of the experiments are taken into account. In the serial staggered coupling process, the wall temperature distribution resulting from a solid computation with PERMAS is given as boundary conditions for further flow computations with STAR-CD.

#### 5.2.3.6. Coupling code strategy in the present study and solver parameters

As strong variations of the convective heat flux are expected with fan running, the serial staggered coupling process is used in the present study. The heat transfer coefficient and film temperature are chosen as variables to be sent by STAR-CD to provide the convective heat flux boundary condition in the energy balance computed in PERMAS. The coupling time-steps between PERMAS and POSRAD or PERMAS and STAR-CD are set to  $30s$ . The first solid time-step in PERMAS is set to  $15s$ . The other solid time-steps prescribed by PERMAS depending on the convergence results can be seen in table A.8.4 in appendix. The first computation with STAR-CD predicting the flow at the end of the pre-conditioning phase is fully converged after 1000 iterations. The computation of natural convection in a cubical cavity has shown that a structure consistent with the literature could be obtained after few iterations, if the initial flow field has been computed with a linear temperature distribution at the fluid lateral walls (4.1.2.3). Consequently, the flow computation at one time-step is initialized using the flow and temperature fields of the last flow computation at the previous time-step. Moreover, for reasonable computing times, flow computations with STAR-CD are performed over 100 iterations, assuming that this is sufficient to reach a stable and reasonable flow structure. The sensitivity of the solver parameters is examined afterwards considering the convergence of the flow solution and the plausibility of the results.

### 5.2.4. Model validation of the sound amplifier in the feet compartment, fan switched off

For the model validation, a transient solid simulation is carried out with PERMAS over the simulation time  $t = 540s$  and coupled with POSRAD for the prediction of radiation in the cavity of the sound amplifier. The error range of the measurement of  $\pm 1.5K$  is not represented in the figures.

#### 5.2.4.1. Modeling of the convective heat transfer

For a reasonable modeling of the convective heat transfer mode in the sound amplifier and in the cavity for the model validation, the time-dependent punctual distribution of the outlet temperature measured previously is used. Moreover, an average value for the heat transfer coefficient ( $2 \text{ W/m}^2\text{K}$ ) is prescribed, based on the numerical results from the computation of natural convection in the rectangular box of aspect ratio 4:2:1 (section 4.1.1).

#### 5.2.4.2. Numerical results of the co-simulation PERMAS/POSRAD

The FOT is mounted on the PCB close to a point where the PCB is press-screwed to the heat sink. According to the supplier, the temperature difference between the FOT and the heat sink at the contact is within 1 K. The FOT temperature is approximated with the temperature of the nearest element of the heat sink. The comparison between experimental and numerical results for the temperature of the FOT, of the fin and bottom plate can be seen on figure 5.21. The temperatures are shown as the difference between the transient temperature and the initial temperature for an element corresponding with the position of the probe.

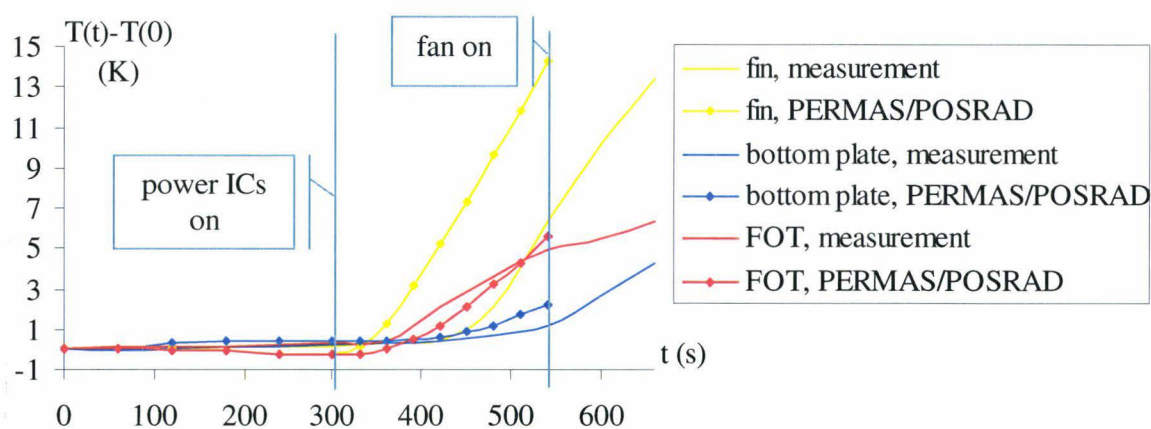


Figure 5.21. Relative temperature of the FOT (red), fin (orange), bottom plate (blue) of the sound amplifier. Measurements (jagged line), computation with PERMAS/POSRAD (dotted line).

A good agreement is obtained for the temperature of the bottom plate and the prediction of the FOT temperature. However, the numerical results show that the FOT is slightly cooling ( $0.2 \text{ K}$ ) before the sound amplifier is operating. This is attributed to the film temperature prescribed to model the convective heat transfer mode in the sound amplifier and in the cavity, which is cooler than the heat sink during this period. Moreover, the co-simulation predicts the beginning of the fin warm-up after  $t = 330s$ , while the experimental results show that the fin starts warming-up after  $t = 420s$ . In order to ensure that this difference doesn't result from the modeling of the conductive heat transfer from the junction of the power ICs to the heat sink, a sensitivity analysis is carried out using RadTherm.

### 5.2.4.3. Sensitivity analysis with RadTherm

The following study aims at investigating more detailed models of the power ICs for a better prediction of the conductive heat transfer mode between the junction heat source and the heat sink. As RadTherm uses a surface mesh, the fins of the heat sink are modeled with a constant thickness. Because of this simplification, the numerical model with RadTherm must be first validated in comparison with the results of the previous co-simulation, using the same model for the convective heat transfer and boundary conditions as in the previous paragraph. Moreover, the conductive heat transfer from the junction of the power ICs to the heat sink is modeled using a resistor thermal model, as previously. The transient analysis with RadTherm and the coupling simulation PERMAS/POSRAD provide very similar results, as shown in figures 5.22 and A.8.10 in appendix. As expected, the fin temperature shows some spatial discrepancies, the co-simulation providing the best agreement with the experimental results. The fin temperature predicted by RadTherm starts increasing at  $t = 330s$ , as predicted by the co-simulation.

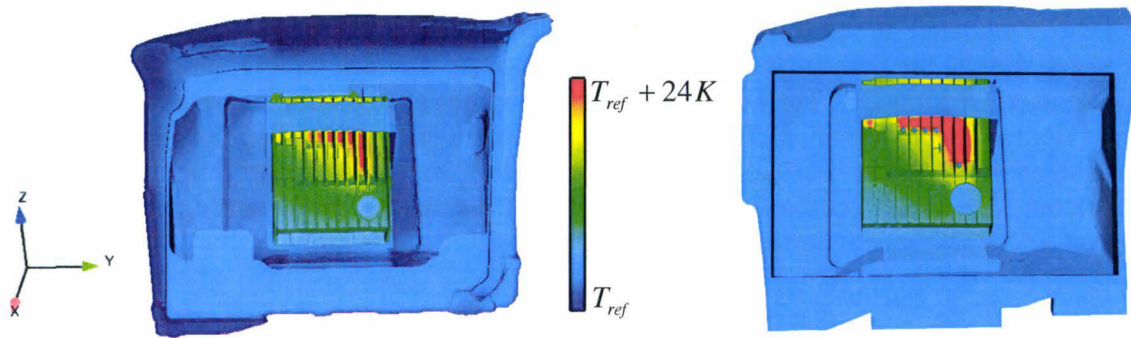


Figure 5.22. Temperature distribution in the cavity of the sound amplifier at  $t = 540s$ ; computation with PERMAS/POSRAD (left) and with RadTherm (right).

A sensitivity study is then performed using a multi-layer model of the power ICs, as suggested by the supplier of the sound amplifier. The multi-layer model consists of one layer of silicon substrate encompassed between two plastic layers to model the IC package. The effect of the thickness and material properties of the different layers on the conductive heat transfer is investigated, showing no noticeable effect on the heat sink temperature. More details can be found in [171]. Consequently, the computed fin temperature is not dependent on the modeling of the conductive heat transfer in the power ICs and the proposed model for the co-simulation PERMAS/POSRAD is reasonable.

### 5.2.4.4. Validation with additional experimental results

For a better understanding of the transient heat transfer mechanisms in the heat sink of the sound amplifier, the distribution of the surface temperature of the heat sink has been measured with a thermographic camera. Measurement probes have been picked on the surface of the heat sink for data storage. In particular, one probe has been placed at the tip of the same fin as measured in the vehicle for the comparison. Moreover, another probe has been picked on the heat sink above the power IC at the base of the same fin. The heat dissipated by the power ICs is set as a step function different from zero for  $t = 5s$ . The distribution of the surface temperature of the heat sink at  $t = 240s$  can be seen in figure 5.23. It is found very similar to the computed distribution, showing the warm-up of the heat sink in the region of the power ICs.

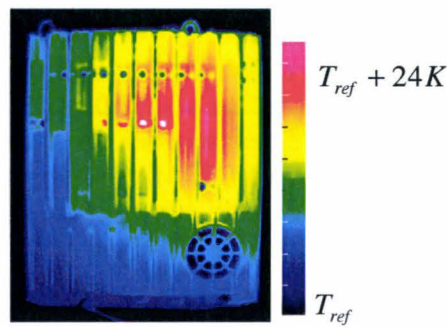


Figure 5.23. Distribution at  $t = 540s$  of the surface temperature of the heat sink measured with a thermographic camera.

Moreover, the temperatures of the fin and of the heat sink above a power IC over the first 60s of measurement can be seen in Appendix A.8.4. The warm-up of the heat sink starts two seconds after Dirac excitation in the power ICs. These two seconds correspond to the time for temperature propagation by conduction from the junction of the power IC to the upper surface of the heat sink. The fin tip starts warming-up 15s after Dirac excitation in the power ICs, while the thermal response has been measured in the vehicle 120s after Dirac excitation of heat generation in the power ICs. The incorrect response time of the fin tip measured in the vehicle is attributed to an insufficient contact between the K-type thermocouple and the surface of the fin.

In order to validate the numerical model of the sound amplifier in the cavity, the fin temperature measured in the vehicle is translated so that the warm-up of the fin tip starts at  $t = 315s$ . The comparison between experimental and numerical results for the fin tip temperature is shown in figure 5.24. The fin temperature measured with thermographic camera under laboratory conditions is also shown. The computed fin temperature is in good agreement with the corrected fin temperature measured in the vehicle. The discrepancies found are attributed to the coarse modeling of the convective heat transfer mode. Moreover, the temperature gradients of both measured temperatures are similar showing that the temperature of the fin tip is mainly affected by conduction.

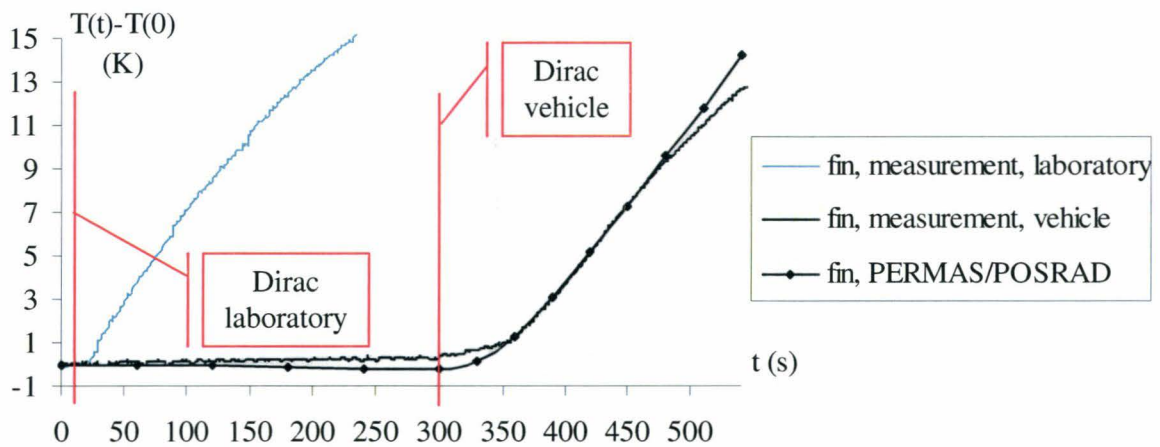


Figure 5.24. Experimental (jagged line) and numerical (dotted line) relative temperature of the fin. Laboratory conditions (grey) and operating conditions in the vehicle (black).

#### 5.2.4.5. Effect of the radiation heat transfer mode

In order to evaluate the effect of the radiative heat transfer on the sound amplifier, a numerical simulation is carried out without coupling with POSRAD. In this case, PERMAS performs the energy balance without radiative heat transfer. The heat sink temperature computed with PERMAS/POSRAD in comparison with PERMAS differs only by 0.5 K [171]. Therefore, the radiative heat transfer has no considerable effect on the sound amplifier temperature during this first phase of warm-up. This can be explained with the moderate temperatures in the enclosure.

#### 5.2.5. Validation of the coupling strategy, fan switched off

As the radiation heat transfer mode has no significant effect on the temperature of the sound amplifier during the first phase of warm-up without fan running, it is not computed in the following. Therefore, a transient solid simulation is carried out with PERMAS coupled with STAR-CD for the prediction of the convective heat transfer mode in the cavity outside the sound amplifier.

##### 5.2.5.1. Sensitivity of the solver parameters

The sensitivity of the following solver parameters is studied for the first phase of warm-up with fan switched off:

- The convective data exchanged;
- The coupling time-step;
- The number of computed iterations to solve the flow.

Several coupled simulations are carried out with coupling time-steps of 15s and 30s, for which the flow is computed using 20 or 100 iterations, using the heat transfer coefficient and film temperature as convective data for the exchange. The first flow initialization, which uses the temperature and velocity fields solution of the pre-conditioning phase, yields to a strong increase of the residuals. For the convergence of the residuals in the flow computation, 100 iterations are required. Moreover, the temperature distributions of the heat sink in the cavity predicted by the computations with coupling time-steps of 15s and 30s are identical. The temperatures of the fin predicted by the both computations are very similar within 0.04 K. Consequently, coupling time-steps of 30s are used in further co-simulations. Finally, a co-simulation is performed using, this time, the heat flux and film temperature distributions as convection boundary conditions. In comparison with the previous computation using the heat transfer coefficient and film temperature as convective data, the temperature distributions of the sound amplifier in the cavity predicted by both computations are identical. Therefore, the choice of the variables exchanged as convection boundary conditions does not affect the thermal solution.

##### 5.2.5.2. Results of the flow computation

The streamlines in the cavity of the sound amplifier computed with STAR-CD at different time-steps can be seen in figure 5.25. The wall temperatures computed with PERMAS are also shown for the comparison. The streamlines at time  $t = 0$ s are provided by the computation of the pre-conditioning phase with STAR-CD. Due to the temperature difference between steel feet plate and the cowl, eddy-viscosity rolls are forming on each side of the sound amplifier, ascending the lower cold wall. At  $t = 420$ s and  $t = 540$ s, the cavity is heated from below with a higher temperature gradient between the base of the fins in the region of

the power ICs and the upper feet plate. It yields to eddy structures of small scale, which develop in the fluid layer between the fins and the feet plate. Due to the additional temperature gradient between the sound amplifier and the cowl, a complex two-roll structure of larger scale is seen on each side of the sound amplifier.

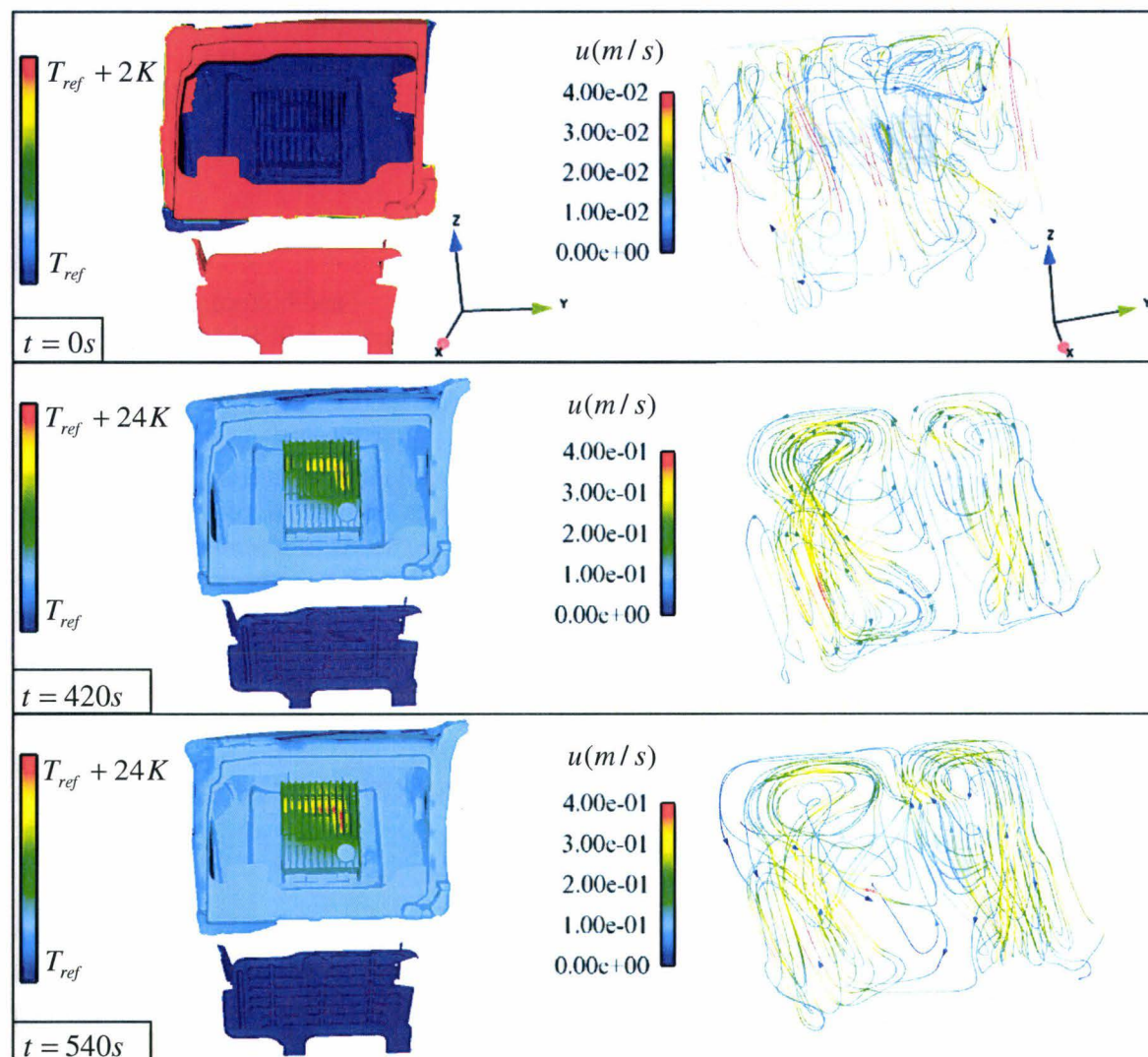


Figure 5.25. Temperature distribution predicted by the co-simulation PERMAS/STAR-CD (left) and streamlines computed by STAR-CD (right) in the cavity of the sound amplifier at different time-steps.

### 5.2.5.3. Solid temperatures after co-simulation

The time-dependent variation of the temperatures of the FOT, of the fin tip and bottom plate is seen in figure 5.26 in comparison with the experimental results. The measured fin temperature shown above is the corrected time-dependent variation discussed in paragraph 5.2.4.4. The results are given as the difference between the transient temperature and the initial temperature for an element corresponding with the position of the probe.

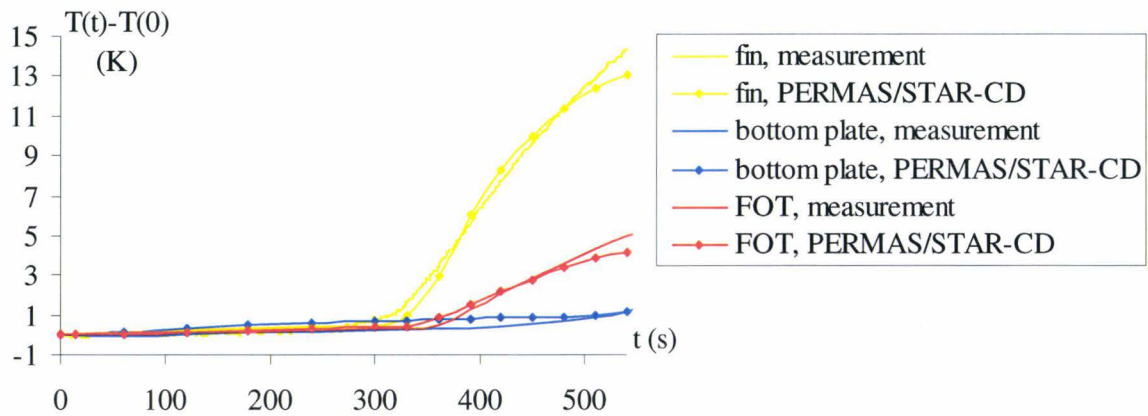


Figure 5.26. Relative temperature of the FOT (red), fin (orange) and bottom plate (blue) of the sound amplifier. Measurements (jagged line), computation with PERMAS/STAR-CD (dotted line).

The slight increase of the overall temperature of the sound amplifier before the sound amplifier is operating is well predicted by the co-simulation between PERMAS and STAR-CD. The flow computation with STAR-CD accounts for the air recirculation in the cavity, which warms up at the contact with the feet plate and leads to a temperature increase of the sound amplifier. After Dirac excitation in the power ICs, the temperature gradients of the FOT and fin tip computed with the co-simulation are in good agreement with the measurements. However, the temperature gradient before the fan switches on is not predicted correctly, yielding to an underestimation of the FOT and fin temperatures at  $t = 540s$ . This is probably due to an overestimation of the convection heat flux at the surface of the feet plate, which is cooler than the rest of the cavity. Overall, the temperature of the sound amplifier is predicted by the co-simulation between PERMAS and STAR-CD within 1.3 K.

### 5.2.6. Partial conclusions

The numerical model proposed for the computation of the first phase of warm-up without fan running has been validated in comparison with experimental results. Moreover, a serial staggered coupling simulation between PERMAS and STAR-CD is carried out, providing a good agreement between numerical and experimental results, except for a short time period before the fan switches on due to the inaccurate temperature of the carpeting given as boundary condition. Nevertheless, due to its high numerical effort, the transient co-simulation can not be presently implemented in the development process for several hours of simulation time.

---

## Chapter 6

# Discussion and perspectives

The objective of the present work has been to develop and verify computational methods that can be implemented in the digital development process for the prediction of the temperature of the electronic equipment in a passenger car under time-dependent operating conditions. To solve the multi-scale coupled heat transfer problem, iterative co-simulation methods are proposed, which use adapted codes for the prediction of each heat transfer mode. Moreover, a steady-state approach is used to solve the flow.

The range of validity of the steady-state approach has been investigated for the computation of buoyancy-driven flows in rectangular and cubical cavities for a large range of Rayleigh number covering laminar, oscillating and turbulent regimes. Flow structures consistent with the literature have been obtained with adapted initial conditions. Moreover, the mean convective heat flux and its local distribution could be predicted within 8.5% for laminar and oscillating flows. RANS turbulence models have been used to solve turbulent flows and the standard low-Re  $k$ - $\epsilon$  model has been selected for providing the best agreement with the literature. However, the full convergence of the solution using the simple gradient diffusion hypothesis could not be reached. For a better prediction of the turbulent heat flux, the implementation of an algebraic model is currently under investigation, which will be followed by model validation in comparison with benchmark cases.

As the heat transport by forced convection depends mainly on the system assembly, the fan prescribed volume flow rate and on the establishing pressure distribution in the system assembled in the vehicle, numerical methods for fan flow simulation have been examined in comparison with the performance curve measured in the fan test-rig. As the MRF simulation accounts for the geometry of the blades, it showed a better agreement with the measurements than the rotational body force method. Moreover, different numerical models have been investigated for flow computation through thin electronic grills in the TV-tuner, solving the flow through each grill orifice and using porous resistance models. Due to the populated PCBs in the vicinity of the grills, strong inhomogeneities of the static pressure field are found upstream the grill, yielding to different flow directions through the grills. Moreover, strong discrepancies of the RMS pressure drop through the grills have been obtained with the porous models. Therefore, the detailed computation solving the flow through each grill orifice has to be carried out.

Finally, numerical models of the battery and sound amplifier in their real environment in the vehicle have been validated using measurement data to provide the convective heat flux boundary conditions. Using the numerical models of the electronic systems with flow computations for the prediction of the convective heat transfer, the co-simulation strategies have been validated in comparison with experimental results. The efficiency and the reliability of both co-simulation strategies have been appraised for implementation in the digital development process. The parallel discrete coupling strategy requires manual mesh mapping, which is relatively time consuming if numerous data exchanges must be performed. Moreover, the prediction of the convective heat flux over time relies highly on the time-steps selected for the coupling. With adapted coupling time-steps, the transient thermal analysis with RadTherm after coupling provided consistent temperature predictions of the battery temperature. As the convective heat flux doesn't vary significantly with time in case of natural convection, the warm-up of the electronic system can be computed for a long simulation time of several hours as in the case of the battery within a reasonable total computing time. However, thermal analyses with RadTherm are limited to partial numerical models, such as an electronic system assembled in a cavity. As for the discrete staggered coupling strategy, the small coupling time-steps required for a quasi steady-state computation of the flow imply numerous mesh mapping processes, which are carried out automatically. These processes yield to unaffordable computing times in the development process for heavy models of several million elements or several hours of simulation time. However, to predict the warm-up of the an electronic system over several minutes as computed in this work with the sound amplifier, the discrete staggered co-simulation provides an efficient model generation using 3D elements and thus accurate temperature predictions within 1K.

Moreover, the investigation of the sound amplifier mounted in the cavity surrounded by the engine compartment, the cabin and the cockpit has shown that the computational results and thus the prediction of the cooling mechanisms in the sound amplifier are completely affected by the flow and temperature boundary conditions assigned. To improve the accuracy of the temperature predictions, it is therefore essential to extend the geometrical limits of the computed system as far as possible up to the vehicle scale. Considering the freeze deadlines of the development process which tend to shorten in the next years and the available computational resources of today, new computational methods must be developed for coupled heat transfer computations in a full vehicle tomorrow. First, to solve the more pronounced multi-scale heat transfer problem and the resulting characteristic times in the fluid and solid, the flow and the solid must be solved separately in the future as before, and the time-consuming mesh mapping processes used in this work must be improved. For more efficient mesh mapping processes, identical surfaces for solid conduction and fluid convection must be used so that the process is reduced to heat flux exchanges at wall. Furthermore, to predict the temperature of the electronic system at a chip level, which is affected at the vehicle level by convection, conduction and radiation, the whole system could be decoupled into multiple quasi-closed systems with common boundary conditions to close them properly. An efficient computational method would require a parallel computation of these systems. This method will be investigated in the next future to predict the temperature of the rear-end compartments full packaged with diverse electronic systems and flowed through by the air from the cabin prescribed by air conditioner, leaving at the underbody.

## Bibliography

- [1] SCHNEIDER K., GIRGSDIES U., Methods to increase the robustness of electronic components, *VDI Berichte Nr. 2000*, 2007, pp. 619-629
- [2] BREITLING T., DRAGON L., GROSSMAN T., Digital prototypes: another milestone for the improvement of processes and cooperation in vehicle development, *VDI Fahrzeug- und Verkehrstechnik*, 2007, Jahrbuch 2007, ISBN 978-3-18-401657-9, pp. 18-30
- [3] MICHEL F., REISTER H., DESMET B., Numerical computation of the transient temperature of the electronic equipment enclosed in a passenger car, *Paper No. F2008-12-089, FISITA World Automotive Congress*, 2008, Munich, Germany
- [4] SAMSUNG ELECTRONICS: K6R4016C1D CMOS SRAM, *Product specification*, 2003, [www.samsung.com](http://www.samsung.com)
- [5] SPANSION, S29GL016A, *Product specification*, 2006, [www.spansion.com](http://www.spansion.com)
- [6] ANALOG DEVICES, SHARC Processor ADSP-21362, *Product specification*, 2006, [www.analog.com](http://www.analog.com)
- [7] XILINX, XC9536XL High Performance CPLD, *Product specification*, 2006, [www.xilinx.com](http://www.xilinx.com)
- [8] EHRHARDT H., BECKER R., RUPP Th., WOLFF J., Mission profile and reliability of lead free control units, *VDI Berichte*, 2007, Nr. 2000, pp. 549-561
- [9] NELSON L.A., SEKHON K.S., FRITZ J.E., Direct heat pipes cooling of semiconductor devices, *3<sup>rd</sup> Proc. Int. Heat Pipe Conf.*, 1978, pp. 373-376
- [10] RITTNER M., Challenge high temperature electronics – from the BMBF funded joint project to the ZVEW working group. *VDI Berichte Nr. 2000*, 2007, pp. 643-652
- [11] WÄSCHLE A., Numerical methods: 3-dimensional, *In: J. Wiedemann, W-H. Hucho, Progress in Vehicle Aerodynamics II, Thermo-Management*, 2002, Expert-Verlag, ISBN 3-8169-2109-4
- [12] BAUER W., EHRENREICH H., REISTER H., Design of cooling systems with computer simulation and underhood flow analysis using CFD, *In: VTMS 2, C496/042, IMechE*, 1995, London

- 
- [13] KARLSSON R., VAN BENTHEM P., Vehicle Underbody Thermal Simulation Using Computational Fluid Dynamics, *In: SAE 1999-01-0579*, 1999
- [14] SCHUSTER M., Application of CFD as an efficient analysis tool supporting the experimental investigation of underhood vehicle flows, *In: Paper No. C599/056/2003, VTMS 6 Conference, SAE*, 2003
- [15] SKEA A., JOLIFFE A., HARRISON R., JONES M., CARDANI P., SMITH I., Using CFD for underbonnet thermal management, *EACC*, 2003, Frankfurt
- [16] SRINIVASAN K., WORONOWYCZ G., ZABAT M., TRIPP J., An efficient procedure for vehicle thermal protection development, *In: Paper No. 2005-01-1904, SAE*, 2005, Detroit
- [17] CFDRC Group: CFD-ACE+, 2006
- [18] THERMOANALYTICS INC.: RadTherm Technical Documentation, 2001, Calumet
- [19] BENDELL E., Investigation of a coupled CFD and thermal modelling methodology for prediction of vehicle underbody temperatures, *Paper No. 2005-01-2044 In: SAE Papers VTMS 7*, 2005, Toronto
- [20] CD-Adapco Group, Methodology and User Guide, Computational Dynamics STAR-CD, Version 3.20, 2004, London
- [21] JANSEN W., Vehicle disc brake cooling factor analysis, *In: 1<sup>st</sup> European User Group Meeting for Automotive Applications with RadTherm*, 2004
- [22] ANSYS, Inc.: Fluent Inc., *Documentation*, 2008, Version 6.3, [www.fluent.com](http://www.fluent.com)
- [23] JONES M., BRIDGE D., BAXENDALE A., An integrated approach to compact electric vehicle thermal management, *In: J. Wiedemann, Progress in Vehicle Aerodynamics and Thermal Management V*, 2007, Expert-Verlag, ISBN 978-3-8169-2771-6
- [24] REISTER H., MAIHÖFER M., Underhood component temperature analysis for passenger cars, *Paper No. C599/028/2003, In: VTMS 6 SAE Conference*, 2003, pp. 859-866
- [25] SCAI FRAUNHOFER: MpCCI 3.0 – Dokumentation, 2006
- [26] INTES GMBH: Permas User Manual, 2004, Version 12, Stuttgart
- [27] MAIHÖFER M., BAUER W., Numerische Simulation der Bauteiltemperaturen eines Gesamtfahrzeugs, *VDI Berechnung und Simulation im Fahrzeugbau*, 2004, Würzburg

- [28] BINNER T., REISTER H., WEIDMANN E.P., WIEDEMANN J., Aspects of underhood thermal analysis, In: WIEDEMANN J., HUCHO W-H., *Progress in Vehicle Aerodynamics IV*, 2006, Numerical Methods, Expert-Verlag, ISBN-10 3-8169-2623-1
- [29] WEIDMANN E.P., WIEDEMANN J., BINNER T., REISTER H., Experimental and numerical investigations of thermal soak, In: J. Wiedemann, *Progress in Vehicle Aerodynamics and Thermal Management V*, 2007, Expert-Verlag, ISBN 978-3-8169-2771-6
- [30] PETERSON G.P., ORTEGA A., Thermal control of electronic equipment and devices, *Advances in Heat Transfer*, 1990, Vol. 20, pp. 181-314
- [31] METAIS B., ECKERT E.R.G., Forced, mixed and free convection regimes, *Journal of Heat Transfer*, 1964, pp. 295-296
- [32] ASHEGHI M., TOUZELBAEV M.N., GOODSSEN K.E., LEUNG Y.K., WONG S.S., Temperature-dependent thermal conductivity of single-crystal silicon layers in SOI substrates, *ASME J. Heat Transfer*, 1998, Vol. 120, No. 1, pp. 30-36
- [33] ESCOBAR R.A., AMON C.H., Lattice-Boltzmann modeling of sub-continuum energy transport in silicon-on-insulator microelectronics including phonon dispersion effects, In: *Inter Society Conference on Thermal Phenomena (ITherm 2004), IEEE Conference Proceedings*, 2004, pp.584-591
- [34] JU Y.S., GOODSSEN K.E., Phonon scattering in silicon films with thickness of order 100 nm, *Appl. Phys. Lett.*, 1999, Vol. 74, No. 20, pp. 3005-3007
- [35] LEE J.S., JIN J.S., Thermal transport modeling for the simulation of heat transfer in micro/nanoscale devices: BTE based approach, In: *ICHMT, Proceedings of CHT-08, CHT-08-006*, 2008, Morocco
- [36] ANTONETTI V.W., YOVANOVICH M.M., Thermal contact resistance in microelectronic equipment, *Int. J. Hybrid. Microelectronic* 7, 1984, pp. 44-50
- [37] LE MEUR G., BOUROUGA B., BARDON J.P., Microscopic analysis of interfacial electrothermal phenomena – definition of a heat generation factor, *Int. J. Heat Mass Transfer*, 2006, Vol. 49, pp. 387-401
- [38] VERMEERSCH B., DE MEY G., Influence of thermal contact resistance on thermal impedance of microelectronic structures, *Microelectronics Reliability*, 2007, Vol. 47, pp. 1233-1238
- [39] GRUJICIC M., ZHAO C.L., DUSEL E.C., The effect of thermal contact resistance on heat management in the electronic packaging, *App. Surf. Science*, 2005, Vol. 246, pp. 290-302

- 
- [40] BAHRAMI M., CULHAM J.R., YOVANOVICH M.M., Thermal resistances of gaseous gap for conforming rough contacts, *Proceedings of the 42<sup>nd</sup> AIAA Aerospace Meeting and Exhibition*, 2004, AIAA Paper No. 2004-0821, January 5-8, Reno, NV
- [41] KABETANI M., MIWA M., Thermal simulation of power devices in the power supply for automobiles, *In: SAE papers, F2006D140*, 2006, FISITA World Congress
- [42] ANSYS, Inc.: Icepack, *Documentation*, 2003, Version 4.0, [www.fluent.com](http://www.fluent.com)
- [43] AUNG W., Heat transfer in electronic systems with emphasis on asymmetric heating, *Bell Syst. Tech. J.* 52, 1973, pp. 907-925
- [44] BODOIA J.R., OSTERLE J.F., The development of free convection between heated vertical plates, *J. Heat Transfer* 84, 1962, pp.40-44
- [45] CHU H.H., CHURCHILL W.S., The development and testing of a numerical method for computation of laminar natural convection in enclosures, *Computers and Chemical Eng.*, 1977, Vol. 1, pp.101-102
- [46] SHYY W., RAO M. M., Simulation of Transient Natural Convection Around an Enclosed Vertical Channel, *In: ASME Journal of Heat Transfer*, 1993, Vol. 115, pp. 946-954
- [47] BAROZZI G.S., CORTICELLI M. A., NOBILE E., Numerical simulation of time-dependent buoyant flows in an enclosed vertical channel, *In Heat and Mass Transfer*, 1999, Vol. 35, pp. 89-99
- [48] KELKAR K. M., CHOUDHURY D., Numerical prediction of periodically fully developed natural convection in a vertical channel with surface mounted heat generating blocks, *Int. J. Heat Mass Transfer*, 1993, Vol. 36, No. 5, pp.1133-1145
- [49] FUJII M., GIMA S., TOMIMURA T., ZHANG X., Natural convection to air from an array of vertical parallel plates with discrete and protruding heat sources. *Int. J. Heat and Fluid Flow*, 1996, Vol. 17, pp.483-490
- [50] DESRAYAUD G., FICHERA A., LAURIAT G., Natural convection air cooling of a substrate-mounted protruding heat source in a stack of parallel boards, *Int. J. Heat and Fluid Flow*, 2007, Vol. 28, pp. 469-482
- [51] HEINDEL T.J., RAMADHYANI S., INCROPERA F.P., Conjugate natural convection from an array of discrete heat sources: part 1 - two- and three-dimensional model validation, *Int. J. Heat and Fluid Flow*, 1995, Vol. 16, pp. 501-510
- [52] YU E., JOSHI Y., A numerical study of three-dimensional laminar natural convection in a vented enclosure, *Int. J. Heat and Fluid Flow*, 1997, Vol. 18, pp. 600-612
- [53] AIT-TALEB T., ABDELBAKI A., ZRIKEM Z., Numerical simulation of coupled heat transfers by conduction, natural convection and radiation in hollow structures heated from below or above, *Int. J. Thermal Sciences*, 2008, Vol. 47, pp 378-387
-

- [54] BAZYLAK A., DJILALI N., SINTON D., Natural convection with distributed heat source modulation, *Int. J. Heat mass Transfer*, 2007, Vol. 50, pp. 1649-1655
- [55] SIERES J., CAMPO A., RIDOUANE E.H., FERNANDEZ-SEARA J., Effect of surface radiation on buoyant convection in vertical triangular cavities with variable aperture angles, *Int. J. Heat Mass Transfer*, 2007, Vol. 50, pp. 5139-5149
- [56] BAE J.H., HYUN J.M., Time-dependent convection in an enclosure with discrete heat sources, *Int. J. Thermal Sciences*, 2004, Vol. 43, pp. 3-11
- [57] OOSTHUIZEN P.A., PAUL J.T., Natural convection in a rectangular enclosure with two heated sections on the lower surface, *Int. J. Heat and Fluid Flow*, 2005, Vol. 26, pp. 587-596
- [58] BESSAIH R., KADJA M., Turbulent natural convection cooling of electronic components mounted on a vertical channel, *Applied Thermal Engrg.*, 2000, Vol. 20, pp. 141-154
- [59] RAMADHYANI S., MOFFAT D.F., INCROPERA F.P., Conjugate heat transfer from small isothermal heat sources embedded in a large substrate, *Int. J. Heat Mass Transfer* 28, 1985, pp. 1945-1952
- [60] MOFFAT D.F., RAMADHYANI S., INCROPERA F.P., Conjugate heat transfer from wall embedded sources in turbulent channel flow, *ASME HDT-57*, 1986, pp. 177-182
- [61] XU G.P., TOU K.W., TSO C.P., Numerical modelling of turbulent heat transfer from discrete heat sources in a liquid-cooled channel, *Int. J. Heat Mass Transfer*, 1998, Vol. 41, No. 10, pp.1157-1166
- [62] INCROPERA F.P., KERBY J.S., MOFFAT D.F., RAMADHYANI S., Convection heat transfer from discrete heat sources in a rectangular channel, *Int. J. Heat Mass Transfer*, 1986, pp. 1051-1058
- [63] KENNEDY K.J., ZEBIB A., Combined free and forced convection between horizontal parallel planes: some case studies, *Int. J. Heat Mass transfer*, 1983, Technical Note, Vol. 26, pp-471-474
- [64] SCHMIDT R.C., PATANKAR S.V., A numerical study of laminar forced convection across heated rectangular blocks in two-dimensional ducts, *In: Paper No. 86WA/HT88, ASME*, 1986
- [65] DAVALATH J., BAYAZITOGU Y., Forced convection cooling across rectangular blocks, *J. Heat Transfer*, 1987, Vol. 109, pp. 321-328
- [66] MC ENTIRE A.B., WEBB B.W., Local forced convective heat transfer from protruding and flush-mounted two-dimensional discrete heat sources, *Int. J. Heat Mass Transfer*, 1990, Vol. 33, No. 7, pp. 1521-1533

- 
- [67] ROELLER P.T., STEVENS J., WEBB B.W., Heat transfer and turbulent flow characteristics of isolated protrusions in channels, *J. Heat Transfer*, 1991, Vol. 113, pp. 597-603
- [68] WANG Y., VAFAI K., Heat transfer and pressure loss characterization in a channel with discrete flush-mounted and protruding heat sources, *Experimental Heat Transfer*, 1999, Vol. 12, pp. 1-16
- [69] DHINSA K., BAILEY C., PERICLEOUS K., Turbulence Modelling and its Impact on CFD Predictions for Cooling of Electronic Components, *In: 2004 Inter Society Conference on Thermal Phenomena, IEEE*, 2004, pp. 487-494
- [70] RODGERS P., EVELOY V., Application of Low-Reynolds Number Turbulent Flow Models to the Prediction of Electronic Component Heat Transfer, *In: 2004 Inter Society Conference on Thermal Phenomena, IEEE*, 2004, pp. 495-503
- [71] MEINDERS E.R., Experimental study of heat transfer in turbulent flows over wall-mounted cubes, *PhD Thesis*, 1988, Faculty of applied Science, Delft University of Technology, Netherlands
- [72] MAHANEY H.V., INCROPERA F.P., RAMADHYANI S., Comparison of predicted and measured mixed convection heat transfer from an array of discrete sources in a horizontal rectangular channel, *Int. J. Heat Mass Transfer*, 1990, Vol. 33, No. 6, pp. 1233-1245
- [73] PATANKAR S.V., SPALDING D.B., A calculation procedure for heat, mass and momentum transfer in three-dimensional parabolic flows, *Int. J. Heat Mass Transfer*, 1972, Vol. 15, pp. 1787-1806
- [74] CHOI C.Y., ORTEGA A., Mixed convection in an inclined channel with a discrete heat source, *Int. J. Heat Mass Transfer*, 1993, Vol. 36, No. 12, pp. 3119-3134
- [75] OZSUNAR A., BASKAYA S., SIVRIOGLU M., Numerical analysis of Grashof number, Reynolds number and inclination effects on mixed convection heat transfer in rectangular channels, *Int. Comm. Heat Mass Transfer*, 2001, Vol. 28, No. 7, pp. 985-994
- [76] GUIMARAES P.M., MENON G.J., Mixed convection in an inclined channel with a discrete heat source, *Mecanica Computacional*, 2003, Vol. 12, pp. 1667-1681
- [77] HSU T.H., WANG S.G., Mixed convection in a rectangular enclosure with discrete heat sources, *Numerical Heat Transfer*, 2000, Part A, Vol. 38, pp. 627-652
- [78] LEUNG C.W., KANG H.J., Convective heat transfer from simulated air-cooled printed-circuit board assembly on horizontal or vertical orientation, *Int. Comm. Heat Mass Transfer*, 1998, Vol. 25, No. 1, pp. 67-80
-

- [79] BRAATEN M.E., PATANKAR S.V., Analysis of laminar mixed convection in shrouded arrays of heated rectangular blocks, *Int. J. Heat Mass Transfer*, 1985, Vol. 28, No. 9, pp. 1699-1709
- [80] PATANKAR S.V., Numerical heat transfer and fluid flow, *In: Series in Computational Methods in Mechanics and Thermal Sciences*, 1980, Ed: W.J. Minkowycz, E.M. Sparrow, Hemisphere Publishing Corporation, New York
- [81] MADHUSUDHANA RAO G., NARASIMHAM G.S.V.L., Laminar conjugate mixed convection in a vertical channel with heat generating components, *Int. J. Heat Mass Transfer*, 2007, Vol. 50, pp. 3561-3574
- [82] TSAY Y.L., Transient conjugated mixed-convective heat transfer in a vertical plate channel with one wall heated discretely, *Heat and Mass Transfer*, 1999, Vol. 35, pp. 391-400
- [83] HASNAOUI M., BILGEN E., VASSEUR P., ROBILLARD L., Mixed convective heat transfer in a horizontal channel heated periodically from below, *Numerical Heat Transfer*, 1991, Part A, Vol. 20, pp. 297-315
- [84] RAHMAN M.M., RAGHAVAN J., Transient response of protruding electronic modules exposed to horizontal cross-flow, *Int. J. Heat Fluid Flow*, 1999, Vol. 20, pp. 48-59
- [85] BATHE K.J., DONG J., Studies of finite-element procedures- the use of ADINA-F in fluid flow analysis, *Computers and Structures*, 1989, Vol. 32, pp. 499-516
- [86] MADHAVAN P.N., SASTRI V.M.K., Conjugate natural convection cooling of protruding heat sources mounted on a substrate placed inside an enclosure, *Comput. Methods Appl. Mech. Engrg.*, 2000, Vol. 188, pp. 187-202
- [87] TEERTSTRA P., YOVANOVICH M.M., CULHAM J.R., Analytical forced convection modeling of plate fin heat sinks, *In: 15<sup>th</sup> IEEE SEMI-THERM<sup>TM</sup> Symposium*, 1999
- [88] MEREU S., SCIUBBA E., BEJAN A., The optimal cooling of a stack of heat generating boards with fixed pressure drop, flowrate or pumping power, *Int. J. Heat mass Transfer*, 1993, Vol. 36, No. 15, pp. 3677-3686
- [89] PATANKAR S.V., CFD simulation of airflow and cooling in a data center, *In: ICHMT, Proceedings of CHT-08, CHT-08-009*, 2008, Morocco
- [90] AGONAFER D., Numerical Investigation of Enclosure Effects on Spot Cooling Devices, *In: 2004 Inter Society Conference on Thermal Phenomena, IEEE*, 2004, pp. 339-343
- [91] FLOMERICS, Flotherm Version 6.1, *Reference and User Manuals*, 2006, Flomerics Limited

- 
- [92] HWANG C.B., Thermal Design for Flip Chip on Board in Natural Convection, *In 15<sup>th</sup> IEEE SEMI-THERM Symposium*, 1999, pp. 125-132
- [93] CHENG H.C., CHEN W.H., CHENG H.F., Theoretical and experimental characterization of heat dissipation in a board-level microelectronic component, *Applied Thermal Engrg.* 28, 2008, pp. 575-588
- [94] TEERTSTRA P., YOVANOVICH M.M., CULHAM J.R., Modeling of natural convection in electronic enclosures, *In: Inter Society Conference on Thermal Phenomena*, 2004, pp. 140-149
- [95] SRIDHAR S., Evaluation of a thermal design tool for electronics – A three chip MCM as a case study, *IEEE*, 1995, pp. 876-878
- [96] LEE T., CHAMBERS B. and MAHALINGAM M., Application of CFD Technology to Electronic Thermal Management, *In: Proceedings of 44<sup>th</sup> Electronic Components & Technology Conference*, 1994, pp. 411-420
- [97] I-DEAS Electronic System Cooling is trademarks of Structural Dynamics Research Corporation: I-DEAS, Ohio
- [98] FREE A., Recent Advances in Thermal/Flow Simulation: Integrating Thermal Analysis into the Mechanical Design Process, *In: 11<sup>th</sup> IEEE SEMI-THERM Symposium*, 1995, pp. 136-145
- [99] KOWALSKI T., RADMEHR A., Thermal analysis of an electronics enclosure: Coupling flow network modeling (FNM) and computational fluid dynamics (CFD), *In: Sixteenth IEEE SEMI-THERM<sup>TM</sup> Symposium*, *IEEE*, 2000, pp. 60-67
- [100] ZHAO Z., Thermal design of a broadband communication system with detailed modeling of TBGA packages, *Microelectronics Reliability*, 2003, Vol. 43, pp. 785-793
- [101] EVELOY V., RODGERS P., HASHMI M.S.J., Application of numerical analysis to the optimisation of electronic component reliability screening and assembly processes, *J. Materials Processing Technology*, 2004, Vol. 155-156, pp. 1788-1796
- [102] DE VAHL DAVIS G., Mostly natural convection, *In: Keynote Paper No. 1, 5<sup>th</sup> European Thermal-Sciences Conference*, 2008, The Netherlands
- [103] KESSLER R., Nonlinear transition in three-dimensional convection, *J. Fluid Mech.*, 1987, Vol. 174, pp. 357-379
- [104] KIRCHARTZ K.R., OERTEL H., Three-dimensional thermal cellular convection in rectangular boxes, *J. Fluid Mech.*, 1988, Vol. 192, pp. 249-286
- [105] MAUGHAN J.R., INCROPERA F.P., Experiments on mixed convection heat transfer for airflow in a horizontal and inclined channel, *Int. J. Heat Mass Transfer*, 1987, Vol. 30, No. 7, pp. 1307-1318

- [106] PALLARES J., CUESTA I., GRAU F.X., Laminar and turbulent Rayleigh-Bénard convection in a perfectly conducting cubical cavity, *Int. J. Heat Fluid Flow*, 2002, Vol. 23, pp.346-358
- [107] OERTEL H. Jr., LAURIEN E., *Numerische Strömungsmechanik*, Berlin: Springer Verlag, 1995, p. 48
- [108] FERZIGER J.H., PERIC M., Computational methods for fluid dynamics, 3<sup>rd</sup> Edition, 2002, ISBN 3-540-42074-6, Springer-Verlag, pp.370-373
- [109] ZIENKIEWICZ O.C., Coupled problems and their numerical solution, *In: Numerical Methods in Coupled Systems*, 1984, Ed. R.W. Lewis, P. Bettess, E. Hinton, John Wiley & Sons Ltd., pp.35-58
- [110] T-SYSTEMS ENTERPRISE SERVICES GMBH: MEDINA, 2008, <https://servicenet.t-systems.com>
- [111] SIEGEL R., HOWELL J., Thermal radiation heat transfer, 1991, Springer-Verlag, Berlin
- [112] COHEN M.F., WALLACE J.R., Radiosity and realistic image synthesis, *Academic Press Professional*, 1993, ISBN 0-12-178270-0, Cambridge, MA
- [113] CURRAN A.R., JOHNSON K.R., MARTTILA E.A., DUDLEY S.P., Automated radiation modeling for vehicle thermal management, *In: SAE Paper No. 950615, SAE International Congress and Exposition*, 1995, Detroit MI
- [114] LIEN F.S., CHEN W.L., LESCHZINER M.A., Low-Reynolds-number eddy-viscosity modeling based on non-linear stress-strain/vorticity relations, *In: Proc. 3<sup>rd</sup> Symposium On Engineering Turbulence Modelling and Measurements*, 1996, Crete, Greece
- [115] YAKHOT V., ORSZAG S.A., THANGAM S., GATSKI T.B., SPEZIALE C.G., Development of turbulence models for shear flows by a double expansion technique, *Phys. Fluids*, 1992, A4(7), pp. 1510-1520
- [116] CRAFT T.J., LAUNDER B.E., SUGA K., Extending the applicability of eddy viscosity models through the use of deformation invariants and non-linear elements, *In: Proc. 5<sup>th</sup> Int. Symp. On Refined Flow Modelling and Turbulence Measurements*, 1993, pp. 125-132
- [117] DURBIN P.A., Separated flow computations with the  $k-\varepsilon-\nu^2$  model, *AIAA Journal*, 1995, 33(4), pp. 659-664
- [118] IACARRINO G., Predictions of turbulent separated flow using commercial CFD codes, *J. Fluids Eng.*, 2001, 123(4), pp. 819-828
- [119] WOLFSHTEIN M., The velocity and temperature distribution in one-dimensional flow with turbulence augmentation and pressure gradient, *Int. J. Heat Mass Transfer*, 1969, Vol. 12, pp. 301-318

- 
- [120] SPALART P.R., ALLMARAS S.R., A one-equation turbulence model for aerodynamic flows, *In: Paper No. AIAA 92-0439, Proc. 30<sup>th</sup> Aerospace Sciences Meeting and Exhibition*, 1992, Reno, Nevada, USA
- [121] WILCOX D.C., Turbulence modelling for CFD, *DCW Industries, Inc.*, 1998, 2<sup>nd</sup> Edition
- [122] KANG B.H., JALURIA Y., Natural convection heat transfer characteristics of a protruding thermal source located on horizontal and vertical surfaces, *Int. J. Heat Mass Transfer*, 1990, Vol. 33, No. 6, pp. 1347-1357
- [123] MAVEETY J.G., LEITH J.R., Heat transfer in Rayleigh-Bénard convection with air in moderate size container, *Int. J. Heat Mass Transfer*, 1998, Vol. 41, Nos. 4-5, pp. 785-796
- [124] ANDREOPOULOS J., The response of a turbulent boundary layer to a double step-change in a wall heat flux, *Journal of Heat Transfer*, 1983, Vol. 105, pp. 841-845
- [125] HACOEN J., CHIU T.W., WRAGG A.A., Forced and free convective heat transfer coefficients for a model printed circuit board channel geometry, *Experimental Thermal and Fluid Science* 10, 1995, pp. 327-334
- [126] HUSSEIN H.J., MARTINUZZI R.J., Energy balance for turbulent flow around a surface mounted cube placed in a channel, *Phys. Fluids* 8 (3), 1996, pp. 764-780
- [127] ISSA R.I., Solution of the implicitly discretised fluid flow equations by operator-splitting, *J. Comp. Phys.*, 1986, Vol. 62, pp. 40-65
- [128] HAWTHORNE W.R., HORLOCK J.H., Actuator disc theory of the incompressible flow in axial compressors, *Proc. Inst. Mech. Engrs.*, 1962, Vol. 176 (30), pp.789-814
- [129] HORLOCK J.H., Actuator disc theory. Discontinuities in thermo-fluid dynamics, 1978, McGraw-Hill, New York
- [130] NAKAYAMA A., Theory of porous media and its numerical applications to engineering problems, *In: ICHMT, Proceedings of CHT-08, CHT-08-008*, 2008, Morocco
- [131] DEUTSCHES INSTITUT FÜR NORMUNG, Ventilatoren, Leistungsmessung an Kleinventilatoren, Normprüfstände, *DIN 24163, Teil 3*, 1985, Beuth Verlag Berlin
- [132] DEUTSCHES INSTITUT FÜR NORMUNG, Measurement of fluid flow by means of pressure differential devices inserted in circular cross-section conduits running full, *DIN EN ISO 5167, Parts 1 and 2*, 2004, Beuth Verlag Berlin
- [133] MicReD (Microelectronics Research and Development) Ltd.: T3Ster, <http://www.micred.com/t3ster>
-

- [134] SZÉKELY V., Identification of RC Networks by Deconvolution: Chances and Limits, *IEEE Transactions on Circuits and Systems-I. Theory and applications*, 1998, Vol. 45, No. 3, pp. 244-258
- [135] DEUTSCHES INSTITUT FÜR NORMUNG, Thermocouples, Part 2: Tolerances, *DIN EN ISO 60584*, 1989, Beuth Verlag Berlin
- [136] DE VAHL DAVIS G., Laminar natural convection in an enclosed rectangular cavity, *Int. J. Heat Mass Transfer*, 1968, Vol. 11, pp.1675-1693
- [137] CATTON I., The effect of insulating vertical walls on the onset of motion in a fluid heated from below, *Int. J. Heat Mass Transfer*, 1972, Vol. 15, pp.665-672
- [138] KOSCHMIEDER E.L. et al., Bénard cells and Taylor vortices, 1993, Cambridge University Press
- [139] TIAN Y.S., KARAYIANNIS T.G., Low turbulence natural convection in an air filled square cavity. Part I: the thermal and fluid flow fields, *Int. J. Heat Mass Transfer*, 2000, Vol. 43, pp. 849-866
- [140] PALLARES J., GRAU F.X., GIRALT F., Flow transitions in laminar Rayleigh-Bénard convection in a cubical cavity at moderate Rayleigh numbers, *Int. J. Heat Mass Transfer*, 1999, Vol. 42, pp. 753-769
- [141] VERZICCO, R., CAMUSSI R., Numerical experiments on strongly turbulent thermal convection in a slender cylindrical cell, *J. Fluid Mech.*, 2003, 477, pp. 19
- [142] PENG S.H., DAVIDSON L., Large eddy simulation for turbulent buoyant flow in a confined cavity, *Int. J. Heat Fluid Flow*, 2001, Vol. 22, pp. 323-331
- [143] HSIEH K.J., LIEN F.S., Numerical modeling of buoyancy-driven turbulent flows in enclosures, *Int. J. Heat Fluid Flow*, 2004, Vol. 25, pp. 659-670
- [144] ADDAD Y., MAHMOODILARI M., LAURENCE D., LES and RANS computations of natural convection in a nearly-horizontal shallow cavity, *In: Paper No. CHT-08-343, ICHMT, Proceedings of CHT-08*, 2008, Morocco
- [145] CHANDRA L., GRÖTZBACH G., Analysis and modeling of the turbulent diffusion of turbulent kinetic energy in natural convection, *In: Flow, turbulence and convection 79*, 2007, pp. 133-154
- [146] GRÖTZBACH G., Anisotropy and buoyancy in nuclear turbulent heat transfer – critical assessment and needs for modelling, *Wissenschaftliche Berichte FZKA 7363*, 2007, Forschungszentrum Karlsruhe.
- [147] JÄGER W., Oszillatorische und turbulente Konvektion, *Dissertation*, 1982, University Karlsruhe, Germany

- 
- [148] LEONG W.H., HOLLANDS K.G.T., BRUNGER A.P., Experimental Nusselt numbers for a cubical-cavity benchmark problem in natural convection, *Int. J. Heat Mass Transfer*, 1999, Vol. 42, pp. 1979-1989
- [149] LIR J.T., LIN T.F., Visualization of roll patterns in Rayleigh-Bénard convection of air in a rectangular cavity, *Int. J. Heat Mass Transfer* 44, 2001, pp. 2889-2902
- [150] MICHEL F., REISTER H., DESMET B., Numerical simulation of the natural convective flow for electronics packaging application, *CHT-08-213, Advances in Computational Heat Transfer 08, ICHMT*, 2008, Begell House Inc.
- [151] YANG H.Q., YANG K.T., Three-dimensional bimodal buoyant flow transitions in tilted enclosures, *Int. J. Heat and Fluid Flow*, 1988, Vol. 9, No. 2, pp. 90-97
- [152] BELMONTE A., TILGNER A., LIBCHABER A., Temperature and velocity boundary layers in turbulent convection, *Phys Review E*, 1994, Vol. 50, Nr. 1, pp. 269-279
- [153] GROSSMANN S., LOHSE D., Scaling in thermal convection: a unifying theory, *J. Fluid Mech.*, 2000, Vol. 407, pp. 27-56
- [154] KENJERES S., HANJALIC K., Transient analysis of Rayleigh-Bénard convection with a RANS model, *Int. J. Heat Fluid Flow*, 1999, Vol. 20, pp. 329-340
- [155] HANJALIC K., VASIC S., Computation of turbulent natural convection in rectangular enclosures with an algebraic flux model, *Int. J. Heat Mass Transfer*, 1993, Vol. 36, No. 14, pp. 3603-3624
- [156] KENJERES S., HANJALIC K., Convective rolls and heat transfer in finite-length Rayleigh-Bénard convection: A two-dimensional numerical study, *Physical Review E*, 2000, Vol. 62, No. 6, pp. 7987-7998
- [157] HOTCHKISS P.J., MEYER C.J., BACKSTRÖM T.W., Numerical investigation into the effect of cross-flow on the performance of axial flow fans in forced draught air-cooled heat exchangers, *Applied Thermal Engineering*, 2006, Vol. 26, pp. 200-208
- [158] REISTER H., ROSS F., Numerical simulation of an axial cooling fan, *Paper No. C971777, VTMS 3, IMechE*, 1997, pp.55-59
- [159] SPINDLER T., Numerische und experimentelle Untersuchung der Durchströmung von Kraftfahrzeuglüftern, *PhD thesis*, 2005, University of Stuttgart
- [160] DIAZ NUNEZ J., Numerical simulation of an axial fan-flow to cool a telematic component, *Final year diploma report*, 2007, University of Valenciennes
- [161] MC ALLISTER R.A., GINNIS M.C., Perforated-plate performance, *Chem. Eng. Sci.*, 1958, Vol.9, p.25
- [162] MÜHLE J., Berechnung des trockenen Druckverlustes von Lochböden, *Chemie-Ing.-Techn.*, 1972, Vol. 44, pp.72-79
-

- [163] SMITH JR. P.L., VAN WINKLE M., Discharge coefficients through perforated plates at Reynolds numbers of 400 to 3,000, *A.I.Ch.E. Journal*, 1958, Vol. 4, No. 3, pp.266-268
- [164] MÜLLER M., HUTH M., KLEINHEMPEL S., Messung des Druckabfalls an Lochblechen und Vergleich mit Literaturangaben, 2006, Berufsakademie Stuttgart
- [165] GAN G., RIFFAT S.B., Pressure loss characteristics of orifice and perforated plates, *Experimental Thermal and Fluid Science*, 1997, Vol. 14, pp. 160-165
- [166] MICHEL F., REISTER H., DESMET B., Transient computation of a battery's temperature in an enclosure, Paper No. C640/010/2007, *In: IMechE, SAE, VTMS 8*, 2007, Nottingham, pp. 479-489
- [167] MICHEL F., Determination of heat transfer mechanisms responsible for the batteries warming up, *Diploma thesis*, 2005, University of Valenciennes, France
- [168] BRAMBILLA D., BRASCA G., FASSINA A., Dissipation and efficiency in audio power amplifiers: an analytical approach, *In: SAE Papers, Paper No. 920387*, 1992, Detroit
- [169] INTERNATIONAL ELECTROTECHNICAL COMMISSION IEC 60268, Sound system equipment, Part 1: General, Bureau Central de la Commission Electrotechnique Internationale, 1985
- [170] ARQUIS E., RADY M., Study of natural convection heat transfer in a finned horizontal fluid layer, *Int. J. Thermal Sciences*, 2005, Vol. 44, pp. 43-52
- [171] MICHEL F., REISTER H., DESMET B., Numerical computation of the transient temperature of a sound amplifier enclosed in a passenger car, *THP04, 5<sup>th</sup> European Thermal Sciences Conference*, 2008, Eindhoven, The Netherlands



## Appendix

### A.1. Characteristic numbers

Eckert number	$Ec = \frac{1}{\Pi_{cp}} = \frac{u_{\infty}^2}{c_p \Delta T}$	Ratio of the flow kinetic energy to enthalpy
Fourier number	$Fo = \frac{\Pi_{\delta}}{Pe} = \frac{\alpha \delta t}{H^2}$	Ratio of heat conduction in the solid to thermal energy storage
Grashof number	$Gr = \frac{\Pi_g \Pi_{\beta}}{\Pi_v^2} = \frac{g \beta \Delta T H^3}{\nu^2}$	Ratio of buoyancy to viscous forces
Modified Grashof number	$Gr^* = \frac{\Pi_g \Pi_{\beta} \Pi_q}{\Pi_v^2 \Pi_k} = \frac{g \beta \dot{q} H^4}{k \nu^2}$	Ratio of buoyancy to viscous forces
Nusselt number	$Nu = \frac{\Pi_q}{\Pi_k} = \frac{\dot{q} H}{k_f \Delta T} = \frac{\Pi_h}{\Pi_k} = \frac{h H}{k_f}$	Ratio of convective heat transfer to fluid conductive heat transfer
Peclet number	$Pe = \frac{\Pi_{cp}}{\Pi_k} = \frac{H u_{\infty}}{\alpha} = Pr \times Re$	Ratio of advection of the flow to thermal diffusion
Prandtl number	$Pr = \frac{\Pi_{cp} \Pi_v}{\Pi_k} = \frac{c_p \mu}{k} = \frac{\nu}{\alpha}$	Ratio of viscous diffusivity to thermal diffusivity
Rayleigh number	$Ra = \frac{\Pi_g \Pi_{\beta} \Pi_{cp}}{\Pi_v \Pi_k} = \frac{g \beta \Delta T H^3}{\nu \alpha} = Gr \times Pr$	Ratio of buoyancy forces to thermal diffusion
Reynolds number	$Re = \frac{1}{\Pi_v} = \frac{u_{\infty} H}{\nu}$	Ratio of inertial forces to viscous forces
Richardson number	$Ri = \Pi_g \Pi_{\beta} = \frac{g \beta \Delta T H}{u_{\infty}^2} = \frac{Gr}{Re^2}$	Ratio of buoyancy to inertial forces

Table A.1.1. Characteristic numbers resulting from a similitude analysis carried out in a representative automotive electronic system.

## A.2. Thermal analysis with the FEM code PERMAS

Quantity	Structural mechanics	Thermodynamics
Basis variables	Displacement $[r]$ , rotation $[\theta]$ Force $[R]$ , torque $[P]$	Temperature $[T]$ Volume heat rate $[\dot{S}]$ , heat flux $[\dot{q}]$
Discretisation	Stiffness $[K]$ , $[k]$ Mass $[M]$ , $[m]$	Conduction $[K]$ , $[\kappa]$ Density of heat capacity $[C]$ , $[c]$
Governing equations	$[M][\ddot{r}] + [K][r] = [R]$ $[m][\ddot{\theta}] + [k][\theta] = [P]$	$[C][\dot{T}] + [K][T] = [\dot{S}]$ $[c][\dot{T}] + [\kappa][T] = [\dot{q}]$
Material properties	Modulus of elasticity $E$ Hook matrix $[E]$ Spring rate $f$	Thermal conductivity $k$ Conductivity matrix $[\kappa]$ Heat transfer coefficient $h$
Boundary conditions	Prescribed displacement Load (distributed, nodal) Elastic foundation Unloaded edge	Prescribed temperature Heat flux Heat transfer Adiabatic, isolation

Table A.2.1. Analogy between conduction heat transfer and structural mechanics.

### A.3. Experimental methods

#### A.3.1. Fan test-rig

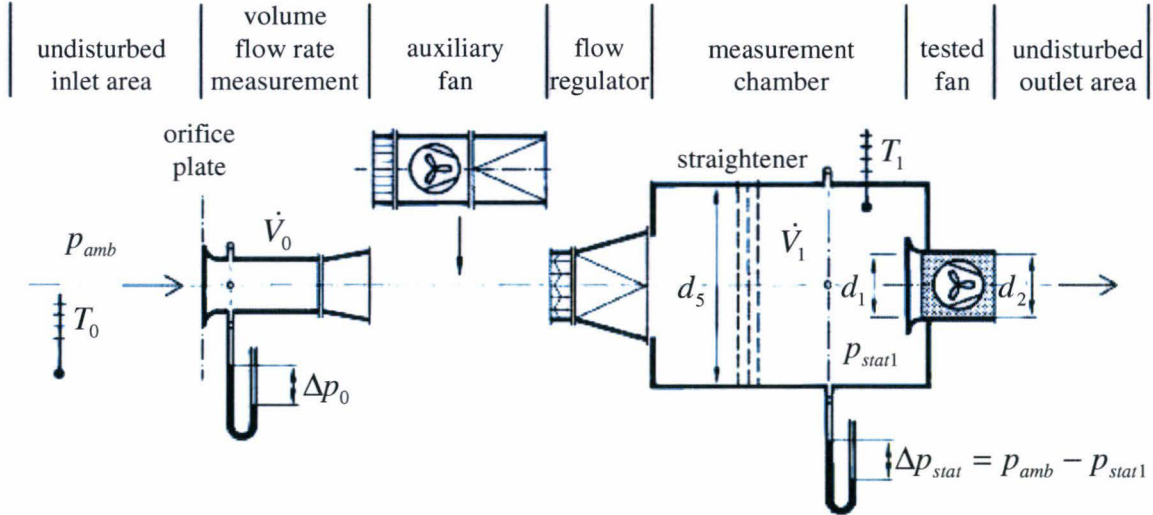


Figure A.3.1. Test-rig for the measurement of the fan performance curve.

The test-rig for the measurement of performance curves is shown in figure A.3.1. It corresponds to the suction type assembly with a drawn in flow and undisturbed outlet flow described by DIN 24163 [131]. The fan is positioned at the downstream section of the measurement chamber. A straightener with honey comb in the measurement chamber allows a uniform distribution and straightened direction of the flow drawn by the fan. With  $\alpha_0$  and  $\varepsilon_0$  the flow rate number and the expansion number of the orifice plate respectively, the relationship providing the volume flow rate drawn by the fan, at the fan inlet, is given by:

$$\dot{V}_1 = \frac{\rho_0}{\rho_1} \dot{V}_0 = \frac{\rho_0}{\rho_1} \alpha_0 \varepsilon_0 \frac{d_0^2 \pi}{4} \left( \frac{2\Delta p_0}{\rho_0} \right)^{1/2} \quad (\text{A.3.1})$$

Moreover, the densities at the test-rig inlet and at the fan inlet  $\rho_1$  are provided by respectively:

$$\rho_0 = \frac{p_{amb}}{RT_0} \quad (\text{A.3.2})$$

$$\rho_1 = \frac{p_{amb} - \Delta p_{stat}}{RT_1} \quad (\text{A.3.3})$$

The dynamic pressure at the fan inlet is calculated by:

$$p_{dyn1} = \frac{\rho_1}{2A_c^2} \dot{V}_1^2 \quad (\text{A.3.4})$$

Measured variable		Sensor	Measurement uncertainty
Volume flow rate	$\dot{V}_0, \dot{V}_1$	-	$u(\dot{V}) = \pm 2\%$
Fan pressure rise	$\Delta p$	-	$u(\Delta p) = \pm 1\%$
Static pressure rise	$\Delta p_0, \Delta p_{stat}$	Micro manometer	$u(\Delta p) = \pm 1\%$
Ambient pressure	$p_{amb}$	Barometer	$u(p_{amb}) = \pm 0.5\%$
Fan rotational speed	$\omega$	Tachometer	$u(\omega) = \pm 0.5\%$

Table A.3.1. Sensors used and measurement uncertainty for the evaluation of the fan performance curve.

### A.3.2. Perforated plate performance curve

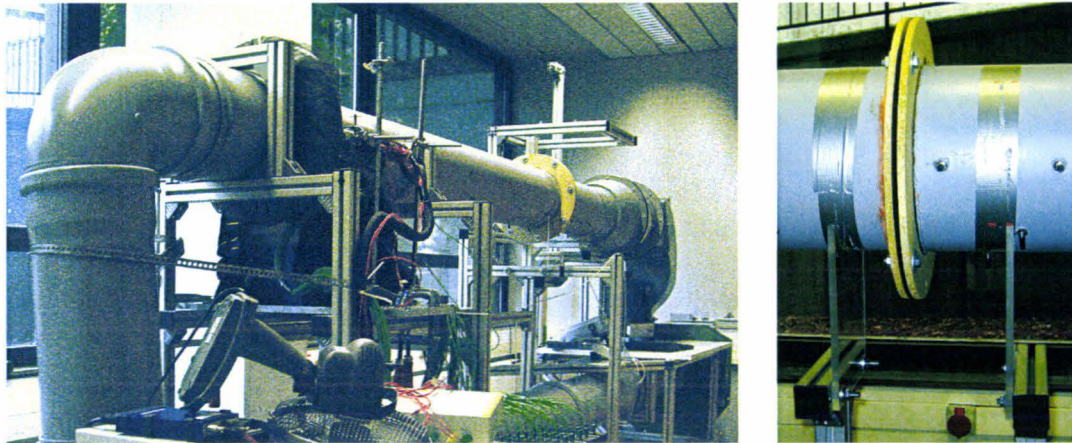


Figure A.3.2. Wind tunnel (left) and clamping of the perforated plate (right); Steinbeis institute.

Measured variable		Sensor	Measurement uncertainty
Flow velocity	$\bar{u}$	Hot-wire anemometer	$u(\bar{u}) = \pm 2\%$
Flow absolute temperature	$T$	Hot-wire anemometer	$u(T) = \pm 3\%$
Flow static pressure	$\Delta p_{stat}$	Differential pressure transducers	$u(\Delta p_{stat}) = \pm 1\%$

Table A.3.2. Sensors used for the evaluation of the perforated plate performance curve.

### A.3.3. K-type thermocouples

The conductors of the K-type thermocouple are composed of nickel chrome alloy and nickel aluminum alloy. A representation of the K-type thermocouple with reference junction is provided in figure A.3.3.

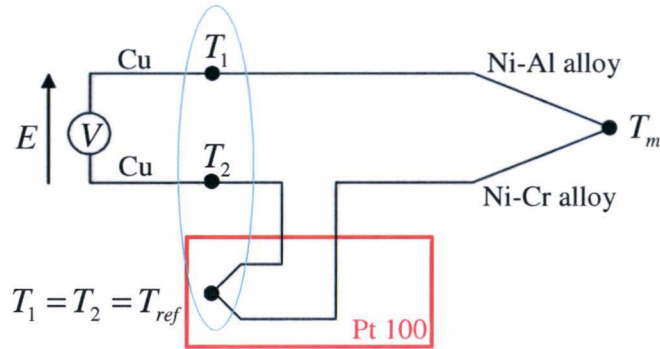


Figure A.3.3. K-type thermocouple with reference junction.

$T_m$  is the temperature to determine, measured by thermocouple.  $T_{ref}$  is measured by the resistance thermometer Pt 100. In this circuit, the electromotive force  $E$  is given by the difference of potential between the junctions  $T_m$  and  $T_{ref}$  :

$$E = [Ni - Al / Ni - Cr]_{T_m} - [Ni - Al / Ni - Cr]_{T_{ref}} \quad (A.3.5)$$

With  $S_i$  the Seebeck coefficient of the conductor  $i$ , the EMF can be expressed dependent on the temperature to determine:

$$E = \int_{T_{ref}}^{T_m} (S_{Ni-Al}(T) - S_{Ni-Cr}(T)) dT \quad (A.3.6)$$

---

## A.4. Buoyancy-driven flows

### A.4.1. Rectangular box

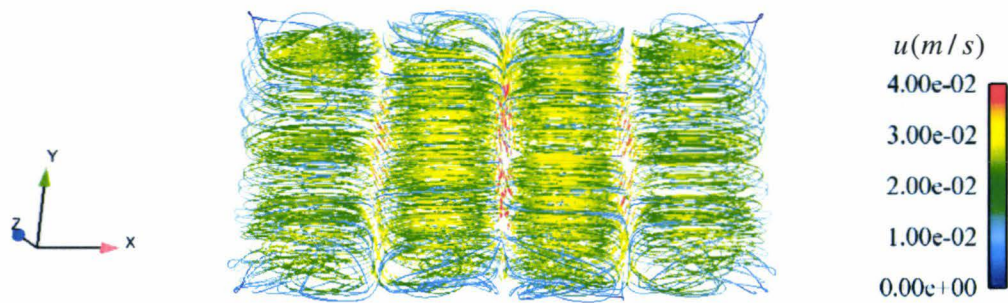


Figure A.4.1. Streamlines at  $Ra = 4 \times 10^4$  in the horizontal cavity 4:2:1 with differential temperature initialization.

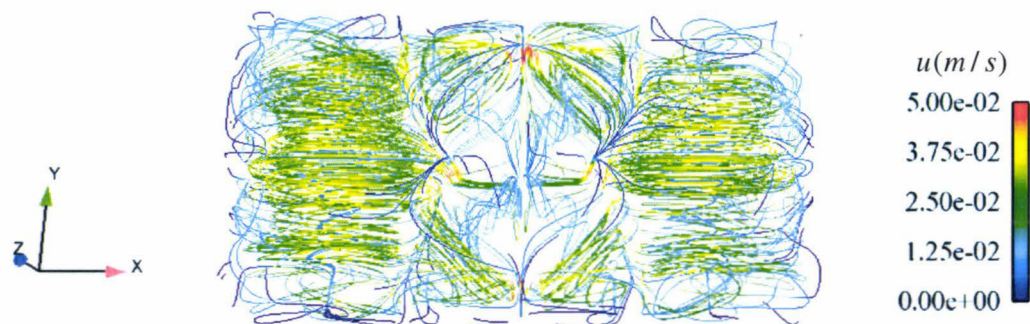


Figure A.4.2. Streamlines at  $Ra = 7 \times 10^4$  in the horizontal cavity 4:2:1 with differential temperature initialization.

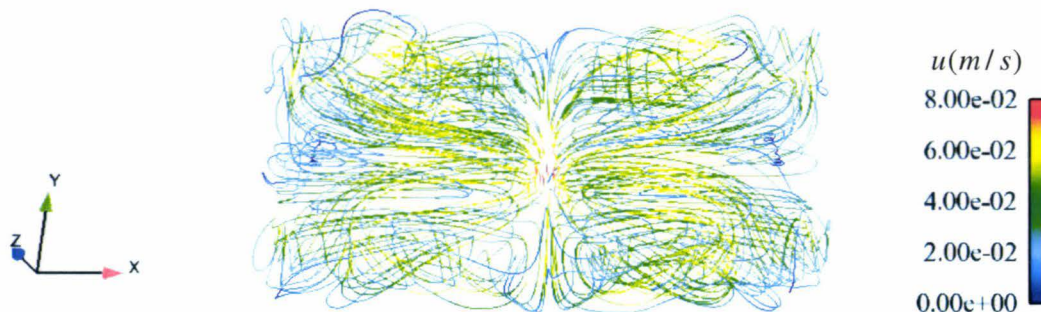


Figure A.4.3. Streamlines at  $Ra = 1.5 \times 10^5$  in the horizontal cavity 4:2:1 with differential temperature initialization.

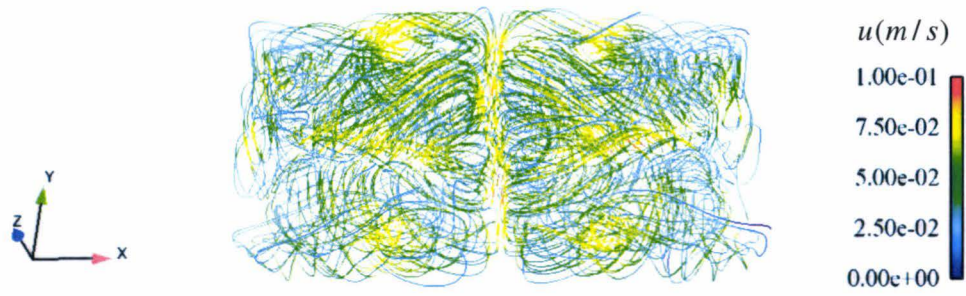


Figure A.4.4. Streamlines at  $Ra = 2.5 \times 10^5$  in the horizontal cavity 4:2:1 with differential temperature initialization.

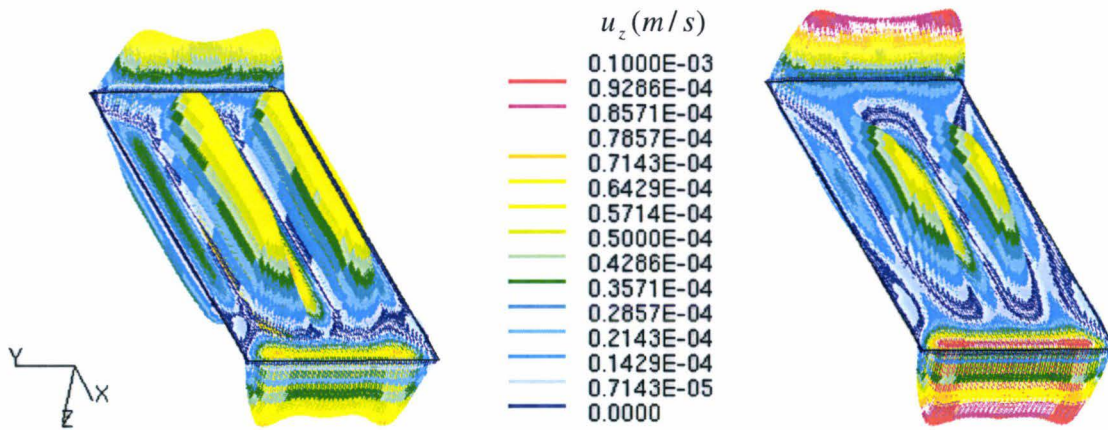


Figure A.4.5. Distribution of the vertical velocity component in the mid-plane  $z/H = 0.5$  of the cavity 10:4:1,  $Pr = 7$ . (Left)  $\theta = 30^\circ$ ,  $Ra = 3464$ ; (Right)  $\theta = 50^\circ$ ,  $Ra = 4670$ .

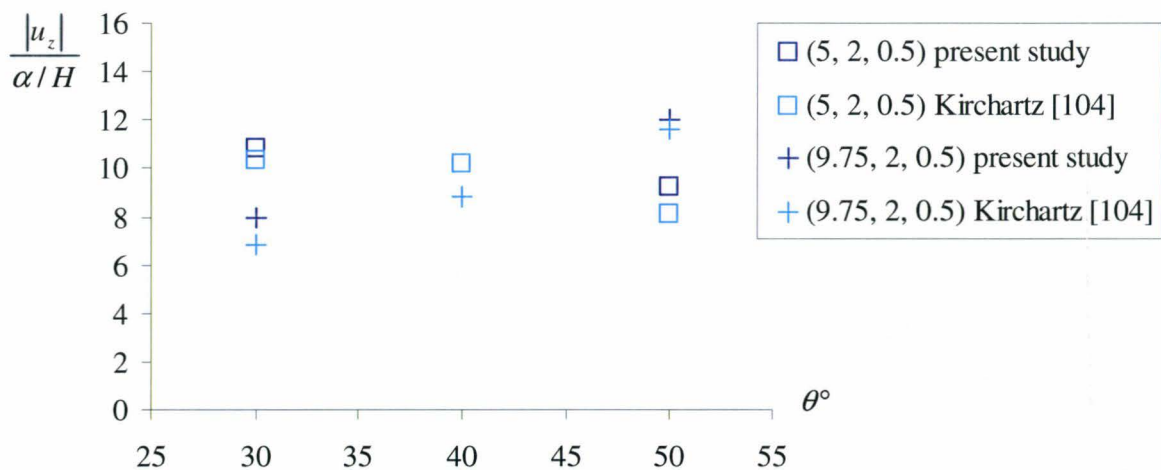


Figure A.4.6. Amplitude of basic and cellular flows in the cavity 10:4:1,  $Pr = 7$ ,  $Ra_z = 3000$

$\square u_z(x = 5, y = 2, z = 0.5)$  present study;  $\square u_z(x = 5, y = 2, z = 0.5)$  [104].  
 $+ u_z(x = 9.75, y = 2, z = 0.5)$  present study;  $+ u_z(x = 9.75, y = 2, z = 0.5)$  [104].

### A.4.2. Horizontal cubical cavity

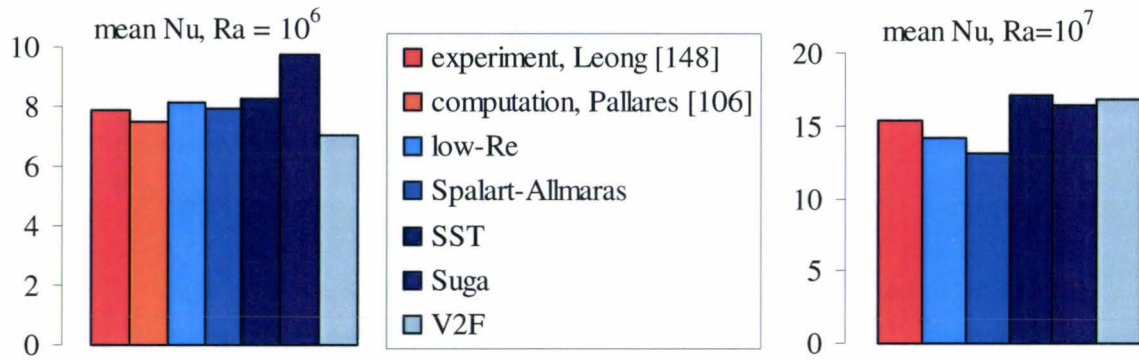


Figure A.4.7. Mean Nusselt number calculated at  $Ra = 10^6$  (left) and  $Ra = 10^7$  (right) with a  $109^3$  nodes grid for different turbulence models in comparison with literature.

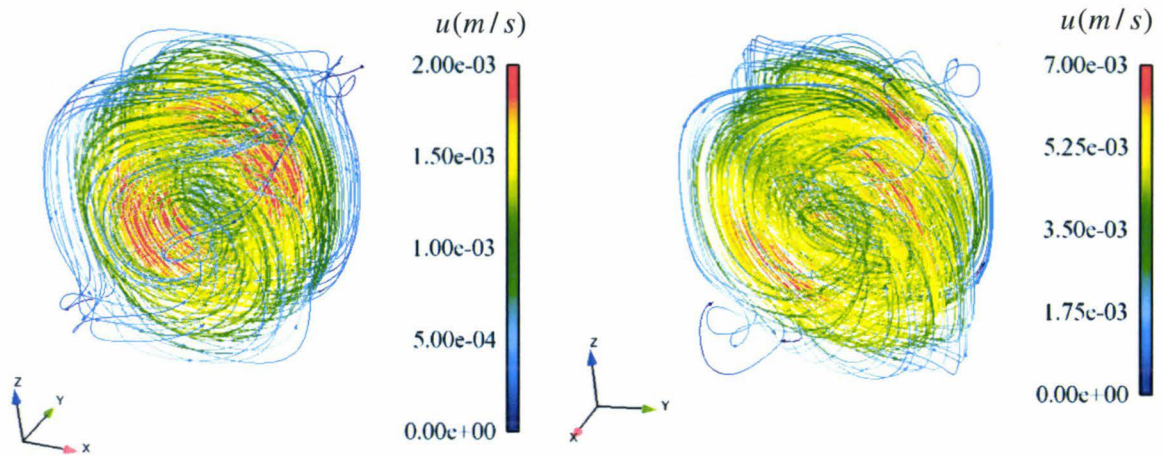


Figure A.4.8. Flow streamlines at  $Ra = 10^4$  (left) and  $Ra = 4 \times 10^4$  (right), structure S1 with a  $109^3$  nodes grid.

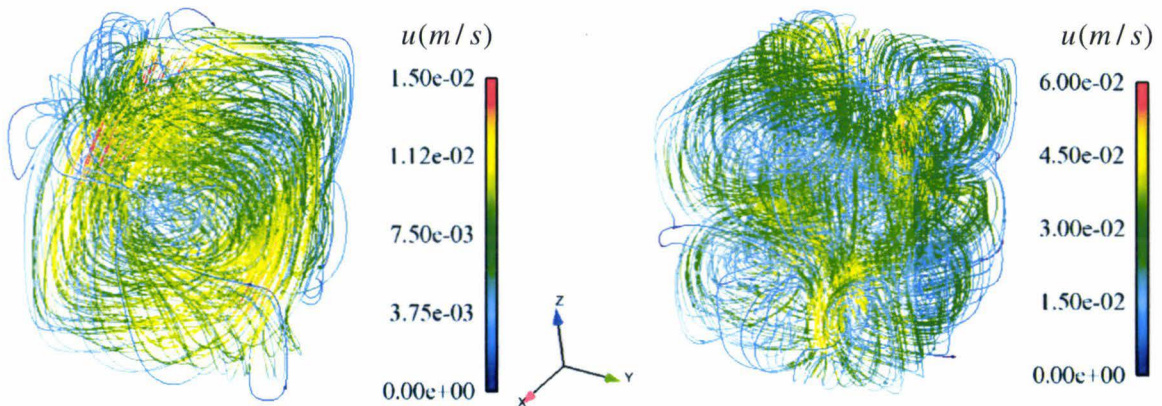


Figure A.4.9. Flow streamlines at  $Ra = 10^5$ , structure S3 (left) and  $Ra = 10^6$ , structure VR (right) with a  $109^3$  nodes grid.

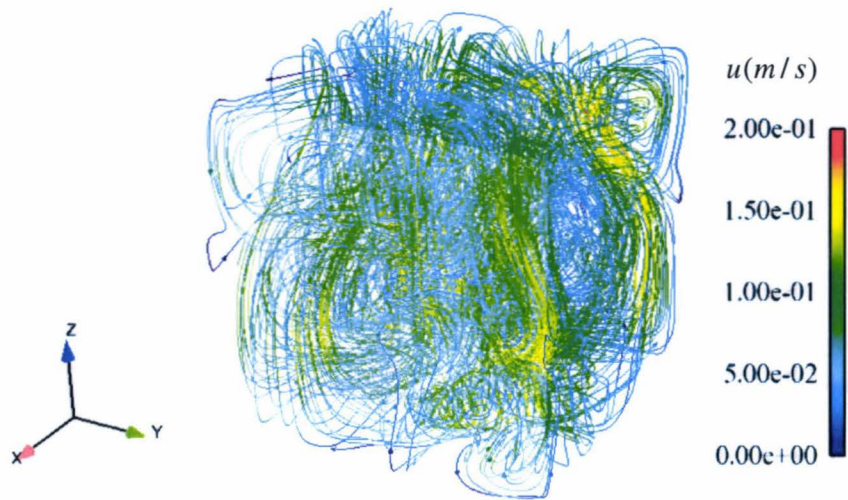


Figure A.4.10. Flow streamlines at  $Ra = 10^7$  with a  $109^3$  nodes grid.

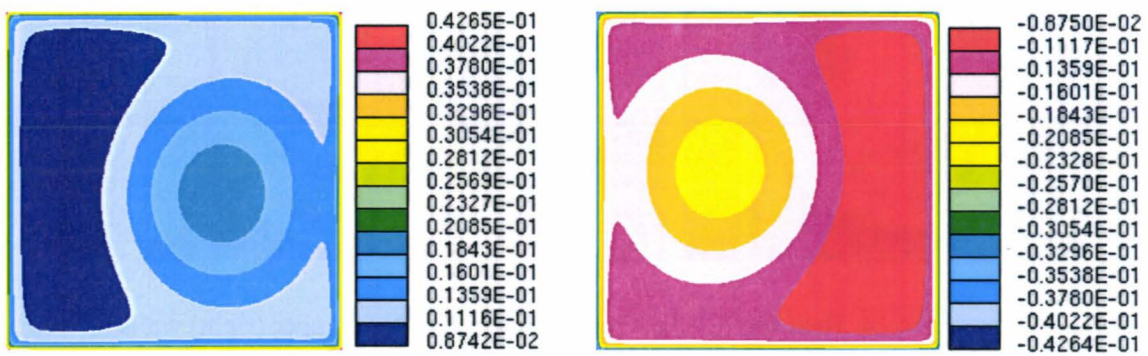


Figure A.4.11. Heat flux [ $W / m^2$ ] on the lower (left) and upper (right) walls at  $Ra = 10^4$  with a  $109^3$  nodes grid, structure S1.

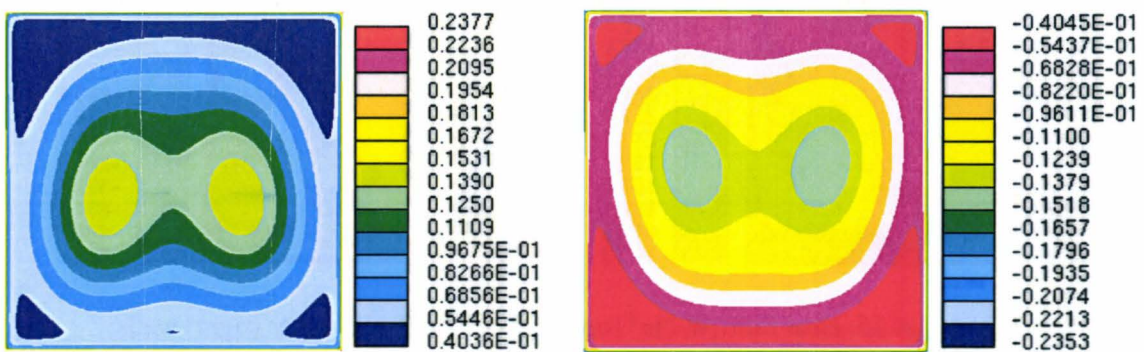


Figure A.4.12. Heat flux [ $W / m^2$ ] on the lower (left) and upper (right) walls at  $Ra = 4 \times 10^4$  with a  $109^3$  nodes grid, structure S1.

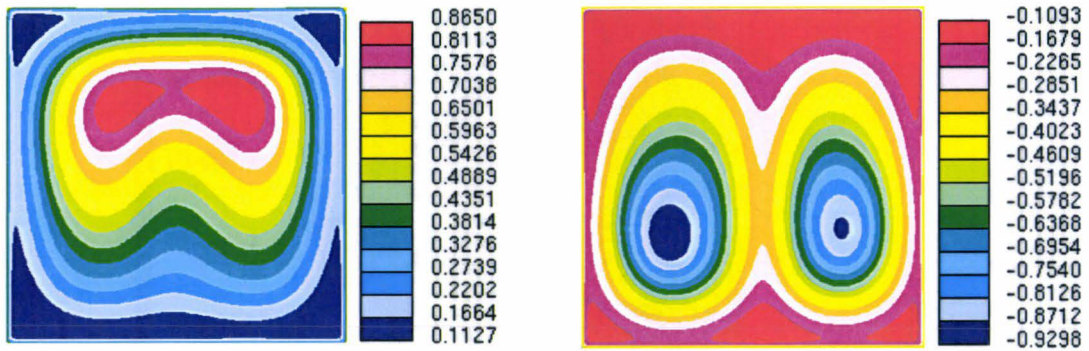


Figure A.4.13. Heat flux  $[W / m^2]$  on the lower (left) and upper (right) walls at  $Ra = 10^5$  with a  $109^3$  nodes grid, structure S3.

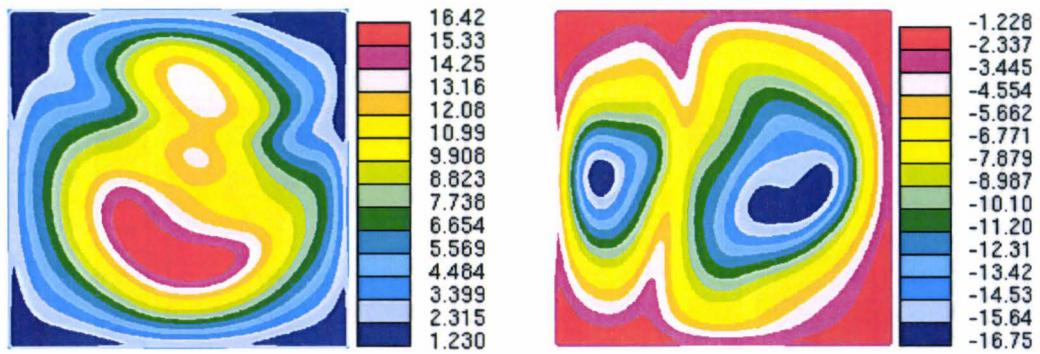


Figure A.4.14. Heat flux  $[W / m^2]$  on the lower (left) and upper (right) walls at  $Ra = 10^6$  with a  $109^3$  nodes grid, structure VR.

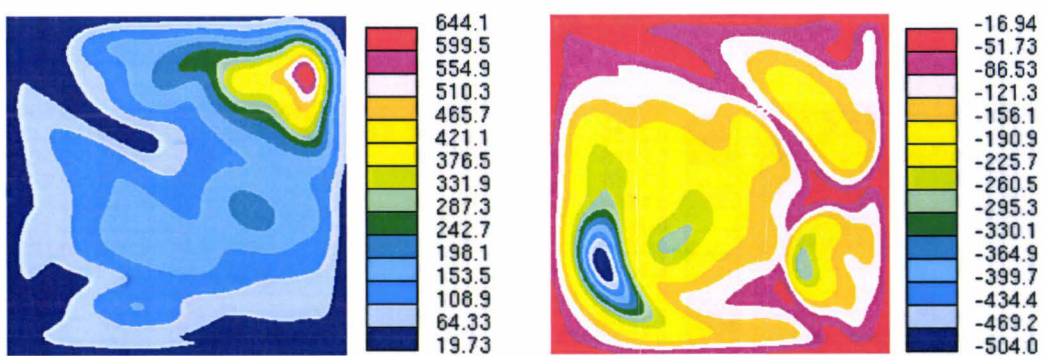


Figure A.4.15. Heat flux  $[W / m^2]$  on the lower (left) and upper (right) walls at  $Ra = 10^7$  with a  $109^3$  nodes grid.

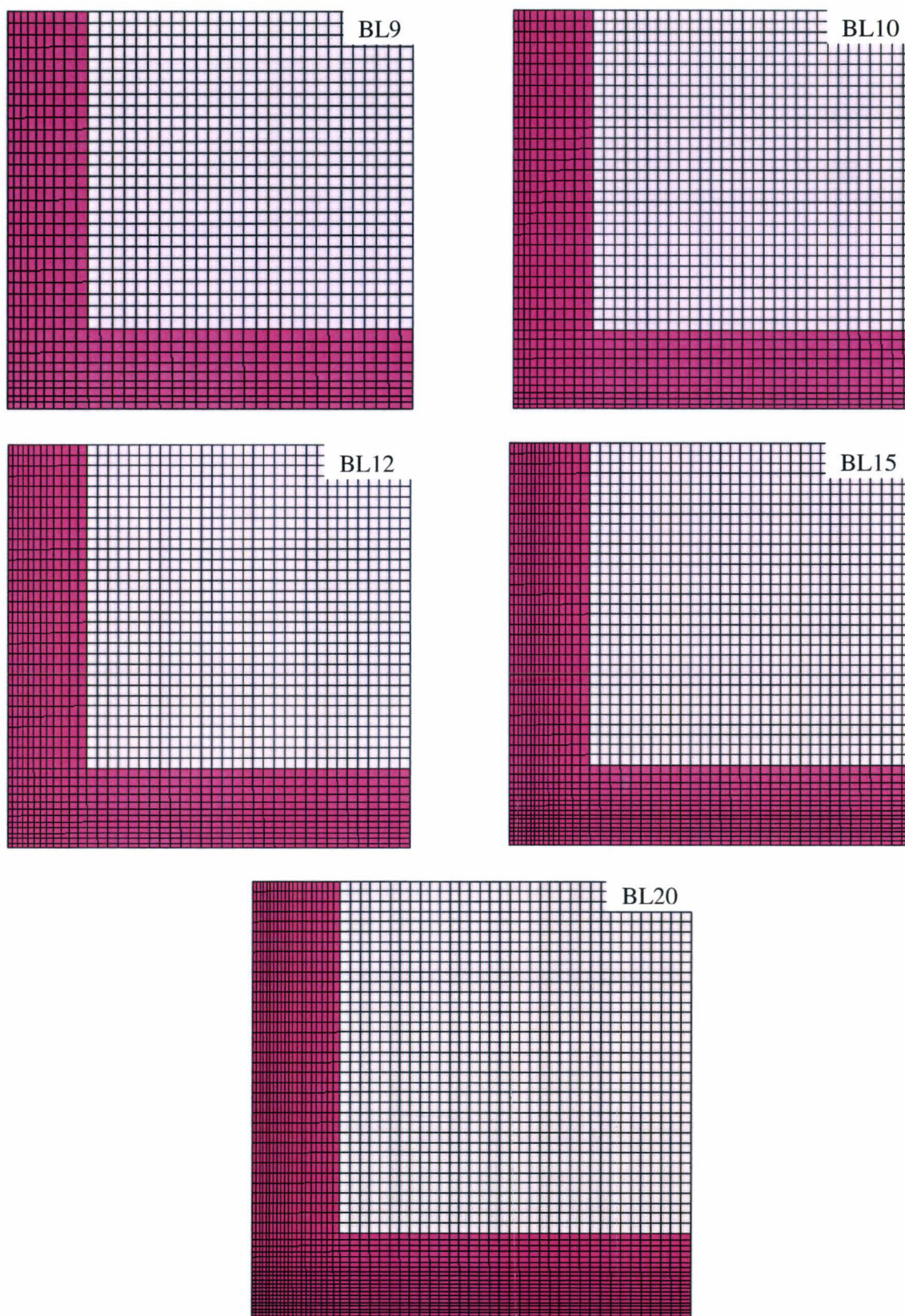


Figure A.4.16. Section of the grids generated for the investigation of mesh independency; only a quarter of the fluid volume is represented.

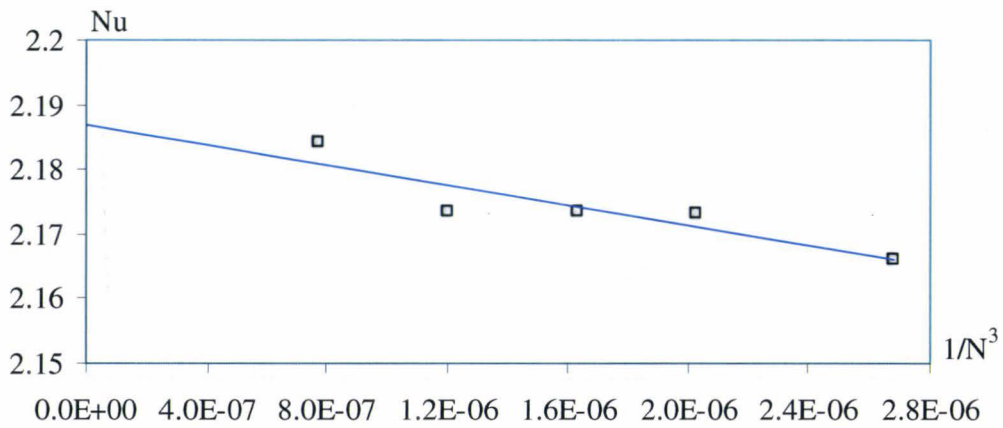


Figure A.4.17. Extrapolation of the averaged Nusselt number on a horizontal wall in the Richardson chart,  $Ra = 4 \times 10^4$ , structure S1.

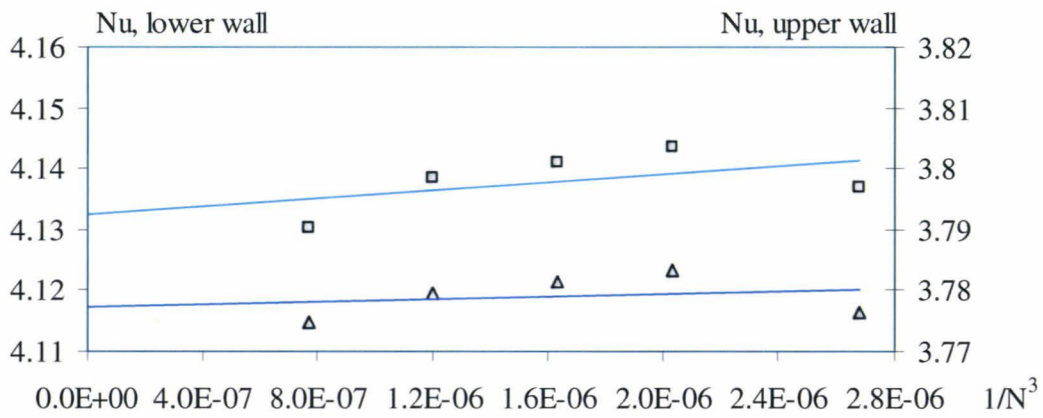


Figure A.4.18. Extrapolation of the averaged Nusselt number on the lower wall ( $\square$ ) and on the upper wall ( $\triangle$ ) in the Richardson chart,  $Ra = 10^5$ , structure S3.

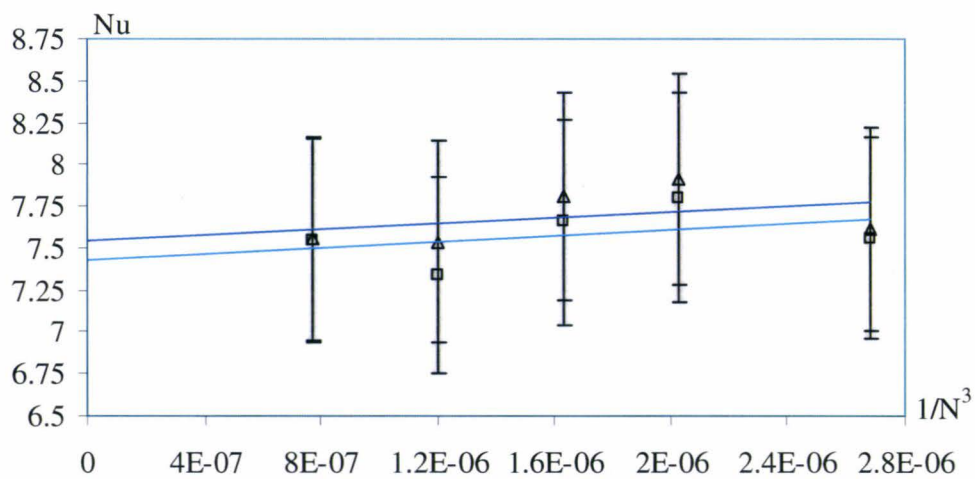


Figure A.4.19. Extrapolation of the averaged Nusselt number on the lower wall ( $\square$ ) and on the upper wall ( $\triangle$ ) in the Richardson chart,  $Ra = 10^6$ , structure CR.

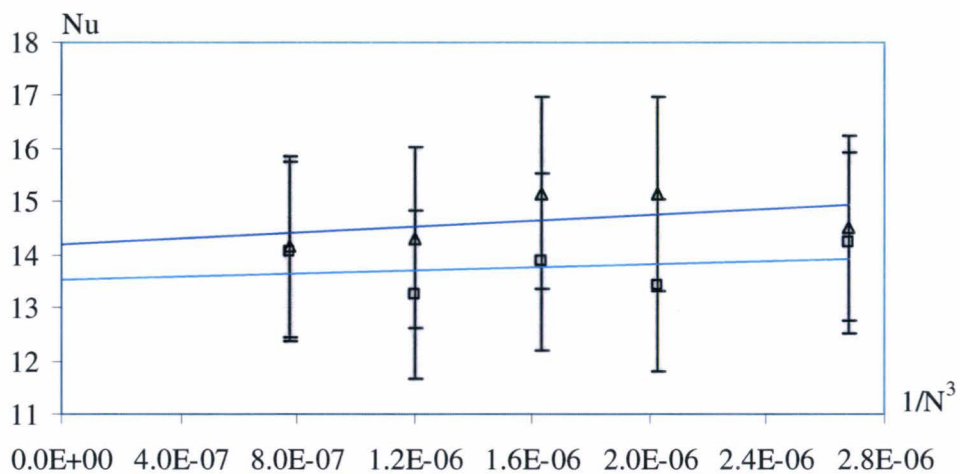


Figure A.4.20. Extrapolation of the averaged Nusselt number on the lower wall (□) and on the upper wall (△) in the Richardson chart,  $Ra = 10^7$ .

## A.5. Forced convective flows

### A.5.1. Electronic fans considered

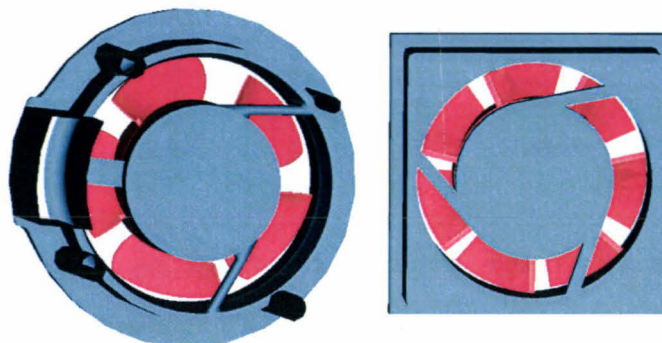


Figure A.5.1. Back view of the axial fans of the sound amplifier (left) and TV-tuner (right).

	Sound amplifier fan		TV-tuner fan	
Number of blades	5		7	
Fan casing diameter (mm)	38		37	
Hub-to-tip diameter ratio	0.667		0.694	
Operating voltage (V DC)	8.3	13.6	4	5
Range of rotational speed in the fan test-rig (rpm)	4600-5050	6850-7600	3450-3700	5500-5900

Table A.5.1. Characteristics of the axial fans situated in the sound amplifier and TV-tuner of actual Mercedes-Benz cars.

### A.5.2. Turbulence modeling and mesh refinement study

Grid	Number of cells		Resolution of the fan near-wall region, $y \leq 2 \times 10^{-4} m$		
	Fan region	Elsewhere	Number of cell layers	Growth rate	Range of $y^+$ values
T2	$2.13 \times 10^6$	$3.84 \times 10^6$	2	1.1	$[10^{-4}; 23]$
NW3	$5.44 \times 10^5$	$1.81 \times 10^6$	3	1.1	$[10^{-4}; 13]$
NW6	$1.33 \times 10^6$	$1.81 \times 10^6$	6	1.1	$[10^{-3}; 12]$
NW9	$1.87 \times 10^6$	$1.81 \times 10^6$	9	1.1	$[10^{-3}; 10]$

Table A.5.2. Grid refinement for the MRF computations; fan of the sound amplifier in the test-rig.

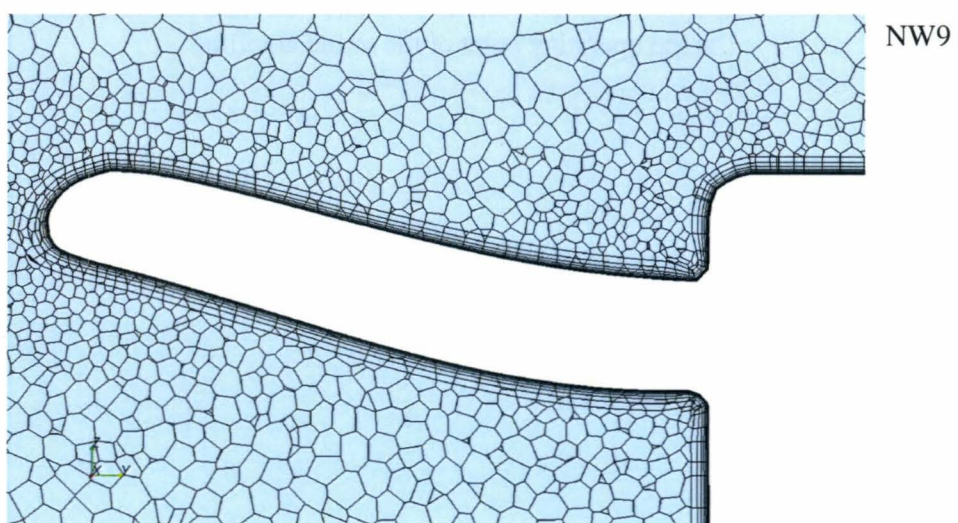
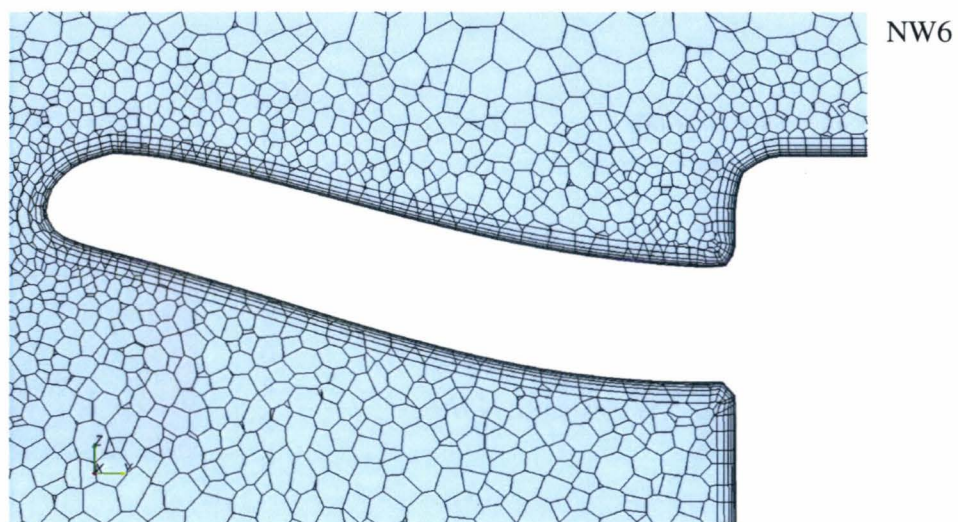
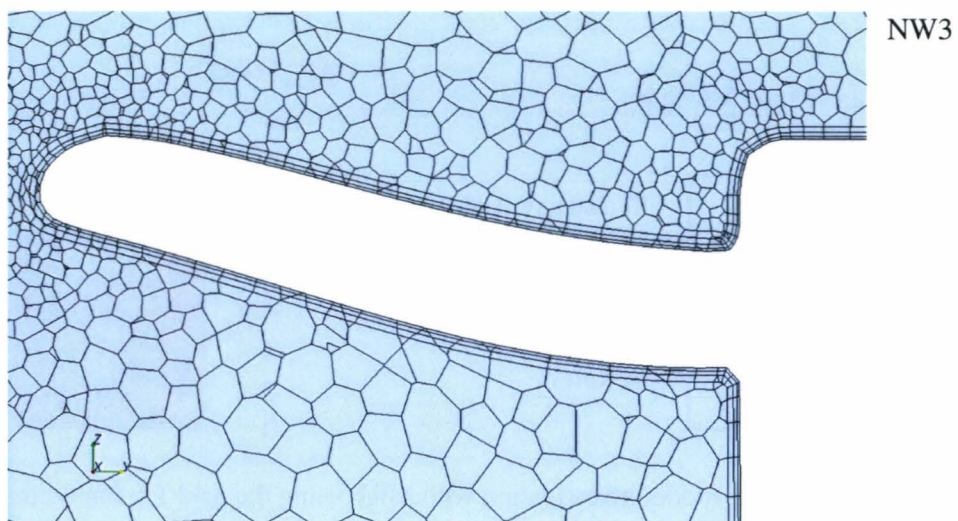


Figure A.5.2. Grids generated for the mesh refinement study; detail view of a fan blade.

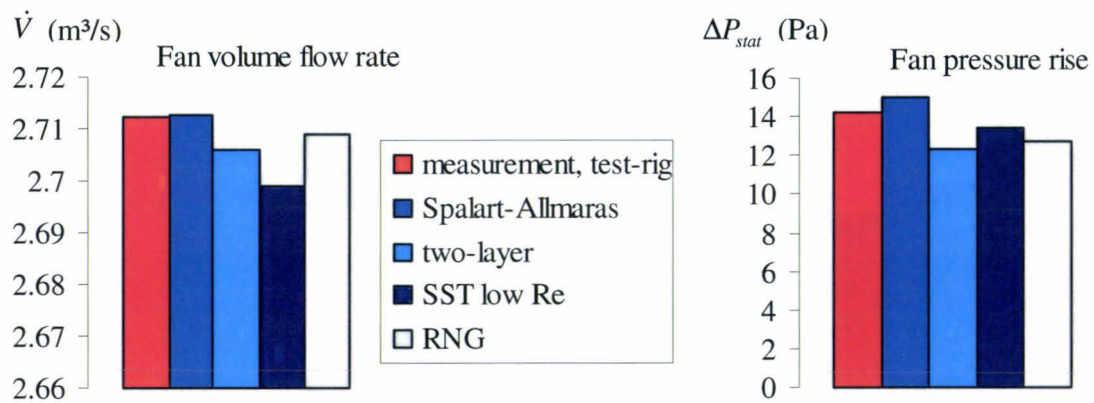


Figure A.5.3. Turbulence model investigation with MRF using the grid T2; fan volume flow rate (left) and pressure rise (right) at the operating point of the sound amplifier.

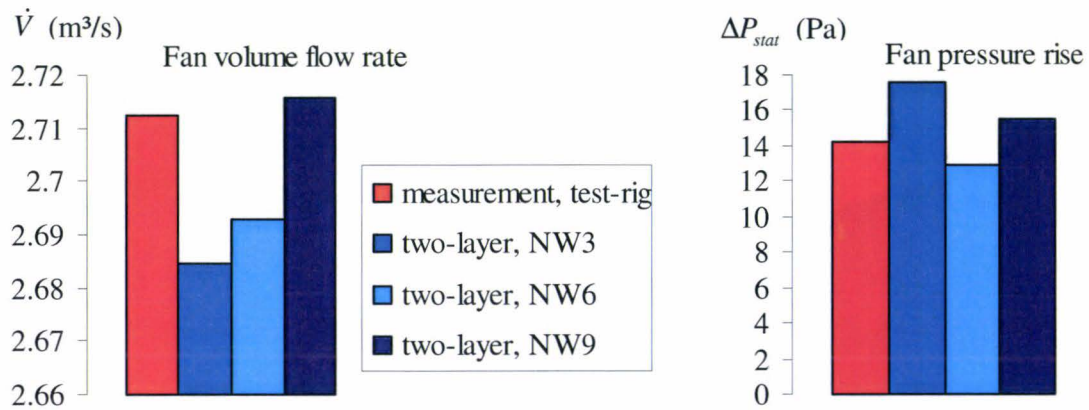


Figure A.5.4. Mesh refinement study with MRF using the standard high-Re  $k-\epsilon$  model with the two-layer approach.; fan volume flow rate (left) and pressure rise (right) at the operating point of the sound amplifier.

## A.6. Outlet grills, TV-tuner

### A.6.1. Geometric parameters

	Upper wall	Lower wall	Sidewall	Interference shield
Grill area $A_g (m^2)$	$1.80 \times 10^{-2}$	$5.21 \times 10^{-3}$	$1.20 \times 10^{-3}$	$6.33 \times 10^{-3}$
Total orifice area $A_o (m^2)$	$2.30 \times 10^{-3}$	$9.82 \times 10^{-4}$	$3.04 \times 10^{-4}$	$1.27 \times 10^{-3}$
Orifice diameter $d_o (m)$	$4.00 \times 10^{-3}$	$2.50 \times 10^{-3}$	$3.00 \times 10^{-3}$	$2.00 \times 10^{-3}$
Orifice angular offset	45°	90°	45°	45°
Orifice centre distance $p_o (m)$	$9.00 \times 10^{-2}$	$5.00 \times 10^{-3}$	$5.00 \times 10^{-3}$	$1.00 \times 10^{-3}$
Grill plate thickness $L (m)$	$5.00 \times 10^{-4}$	$5.00 \times 10^{-4}$	$5.00 \times 10^{-4}$	$5.00 \times 10^{-4}$
Free area ratio $A_o / A_g (%)$	8.25	18.8	25.3	20.1

Table A.6.1. Geometric parameters of the outlet grills of the TV-tuner.

	TV-tuner fan	
Operating voltage (V DC)	4	5
Range of rotational speed in the TV-tuner (rpm)	3850-3870	5050-5080

Table A.6.2. Fan rotational speed measured in TV-tuner with a photoelectric tachometer.

	Perforated plate
Grill area $A_g (m^2)$	$4.34 \times 10^{-2}$
Total orifice area $A_o (m^2)$	$4.47 \times 10^{-3}$
Orifice diameter $d_o (m)$	$8.00 \times 10^{-3}$
Orifice angular offset	45°
Orifice centre distance $p_o (m)$	$2.14 \times 10^{-2}$
Grill plate thickness $L (m)$	$2.00 \times 10^{-3}$
Free area ratio $A_o / A_g (%)$	10.3

Table A.6.3. Geometrical parameters of the perforated plate computed in the test-rig model.

### A.6.2. Grill modeling

Grid	Number of cells		Resolution of the perforated plate near-wall region, $y \leq 1 \times 10^{-3} m$		
	Perforated plate region	Elsewhere	Number of cell layers	Growth rate	Range of $y^+$ values
NW2	$1.85 \times 10^5$	$9.60 \times 10^5$	2	1.05	$[10^{-1}; 48]$
NW3	$1.73 \times 10^6$	$9.60 \times 10^5$	3	1.05	$[10^{-1}; 20]$
NW5	$3.78 \times 10^6$	$9.60 \times 10^5$	5	1.05	$[10^{-2}; 18]$

Table A.6.4. Grid refinement for the computation of the flow through perforated plate; perforated plate in the test-rig model.

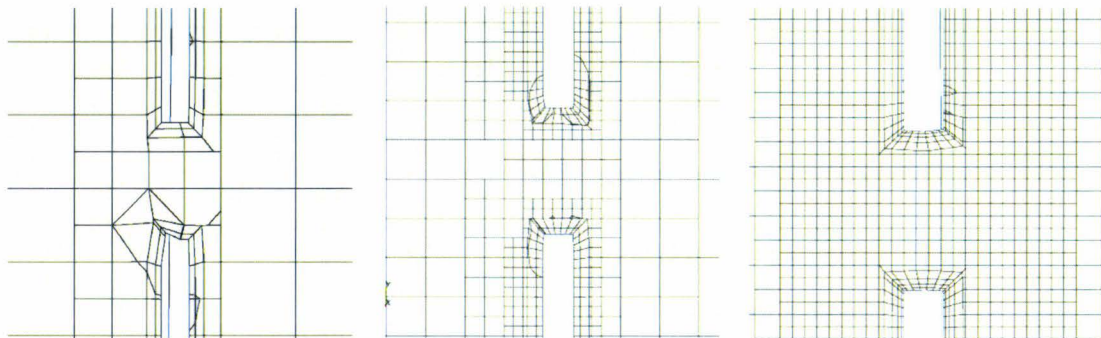


Figure A.6.1. Mesh resolution in the orifice region; NW2 (left), NW3 (middle), NW5 (right).

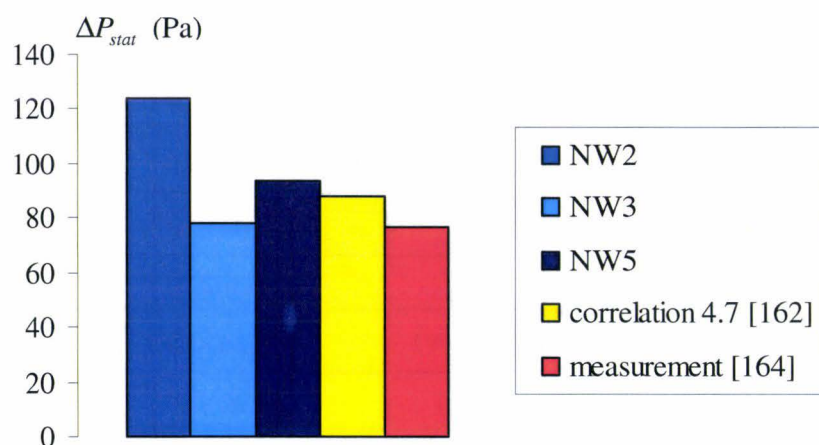


Figure A.6.2. Static pressure drop of the perforated plate in the test-rig with an inlet velocity  $u_i = 1$  m/s; mesh refinement study.

Grid	Present study		Correlation 4.7 [162]		Measurements [164]	
	$\Delta p_{stat}$ (Pa)	$k$ (-)	$\Delta p_{stat}$ (Pa)	$k$ (-)	$\Delta p_{stat}$ (Pa)	$k$ (-)
NW2	$1.23 \times 10^2$	2.22	$8.76 \times 10^1$	1.57	$7.70 \times 10^1$ $\pm 0.77$	1.38 $\pm 0.03$
NW3	$7.78 \times 10^1$	1.39				
NW5	$9.34 \times 10^1$	1.67				

Table A.6.5. Mesh refinement study; static pressure drop and pressure loss coefficient of the perforated plate in the test-rig with an inlet velocity  $u_i = 1$  m/s.

Inlet velocity (m/s)	Present study		Correlation 4.7 [162]		Measurements [164]	
	$\Delta p_{stat}$ (Pa)	$k$ (-)	$\Delta p_{stat}$ (Pa)	$k$ (-)	$\Delta p_{stat}$ (Pa)	$k$ (-)
0.25	5.67	1.63	5.47	1.57	$2.86 \pm 0.03$	$0.82 \pm 0.02$
0.5	$2.34 \times 10^1$	1.68	$2.19 \times 10^1$	1.57	$1.47 \times 10^1 \pm 0.15$	$1.05 \pm 0.02$
1	$9.34 \times 10^1$	1.67	$8.76 \times 10^1$	1.57	$7.70 \times 10^1 \pm 0.77$	$1.38 \pm 0.03$
3	$8.36 \times 10^2$	1.66	$7.89 \times 10^2$	1.57	$7.59 \times 10^2 \pm 7.59$	$1.51 \pm 0.03$

Table A.6.6. Static pressure drop and pressure loss coefficient of the perforated plate in the test-rig for different inlet velocities.

### A.6.3. TV-tuner, outlet grills

Region	Number of cells	Resolution of the near-wall region, $y \leq 2 \times 10^{-4}$ m		
		Number of cell layers	Growth rate	$y^+$ values
Fan	$1.31 \times 10^6$	6	1.1	$[10^{-2}; 4.8]$
Outlet grills	$4.27 \times 10^6$	5	1.05	$[10^{-3}; 4.7]$
Populated upper PCB	$4.67 \times 10^5$	2 (PCB), 4 (ICs)	1.3	$[10^{-4}; 10]$
Populated lower PCB	$5.74 \times 10^5$	2 (PCB), 4 (ICs)	1.3	$[10^{-4}; 7.2]$
Shield grill housing	$8.29 \times 10^5$	4	1.05	$[10^{-3}; 5.4]$
TV-tuner case	$2.85 \times 10^6$	2	1.3	$[10^{-4}; 7.4]$
Environment	$4.14 \times 10^5$	1	1.3	$[10^{-4}; 3.6]$

Table A.6.7. Grid generated for the computation of forced convective flow in the TV-tuner, solving each orifice.

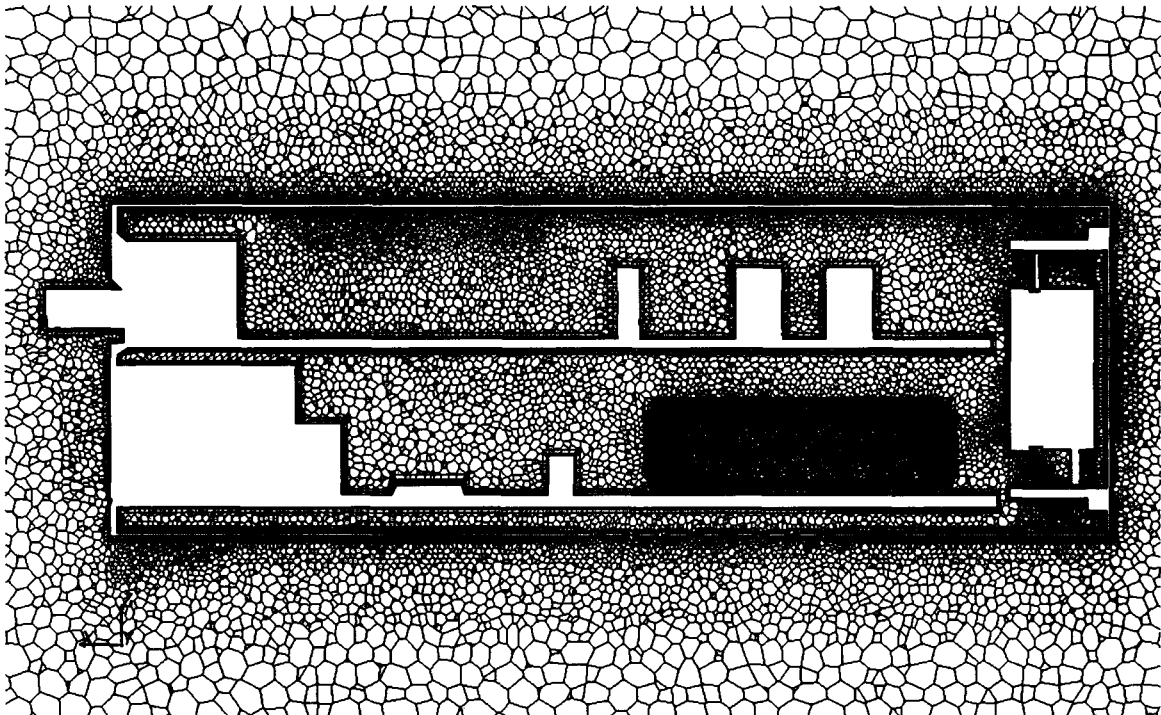


Figure A.6.3. Mesh section in the fan mid-section plane ( $x; z$ ).

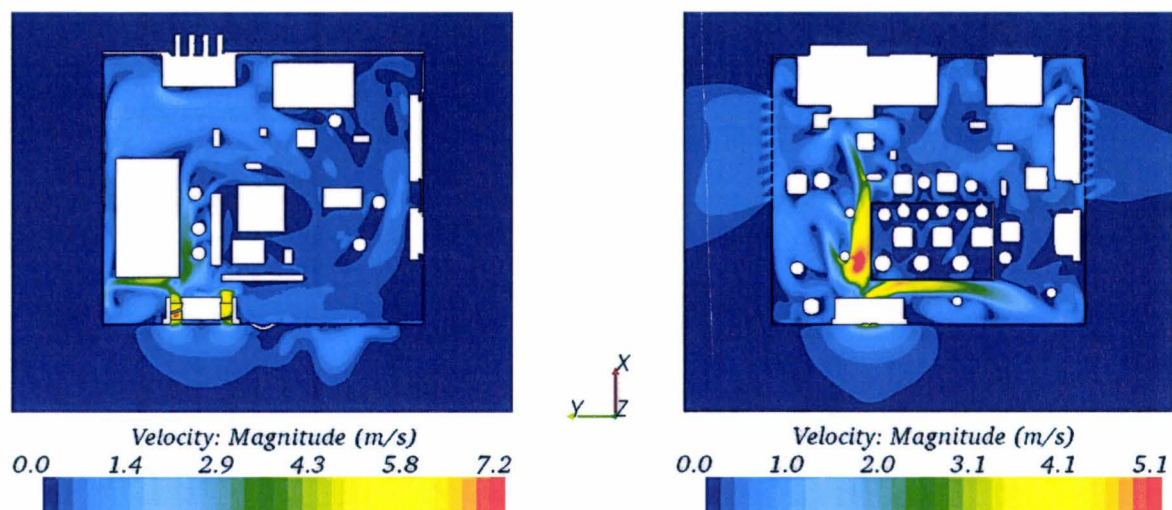


Figure A.6.4. Velocity magnitude in the plane  $(x; y)$  located  $10^{-3}$  m over the upper (left) and lower (right) PCBs for  $\omega = 5065$  rpm.

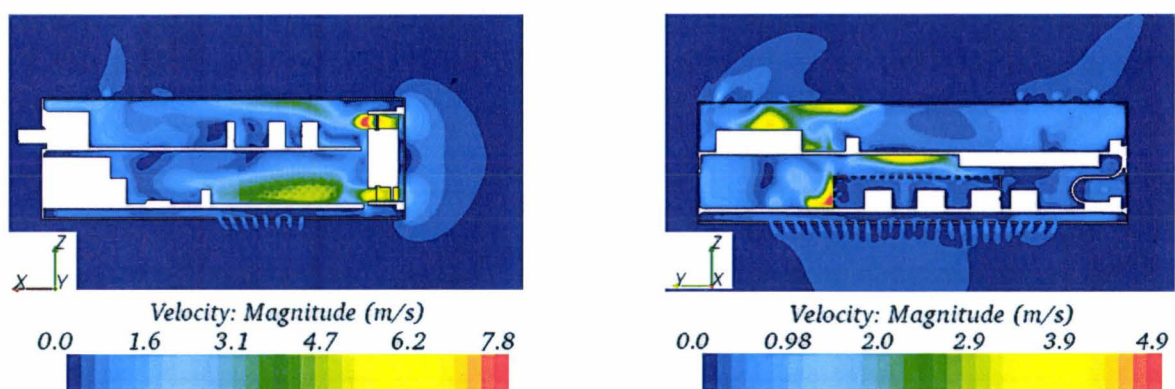


Figure A.6.5. Velocity magnitude in the fan mid-section plane  $(x; z)$  (left) and in the section plane  $(y; z)$  located  $4 \times 10^{-2}$  m downstream from the fan outlet (right) for  $\omega = 5065$  rpm.

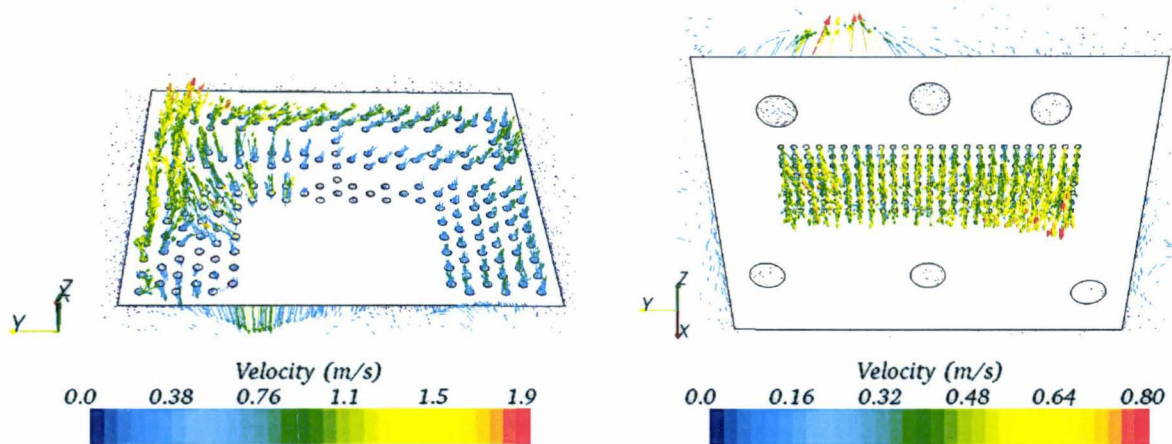


Figure A.6.6. Velocity vectors in the section plane coincident with the outlet grill on the upper wall (left) and lower wall (right) for  $\omega = 5065$  rpm.

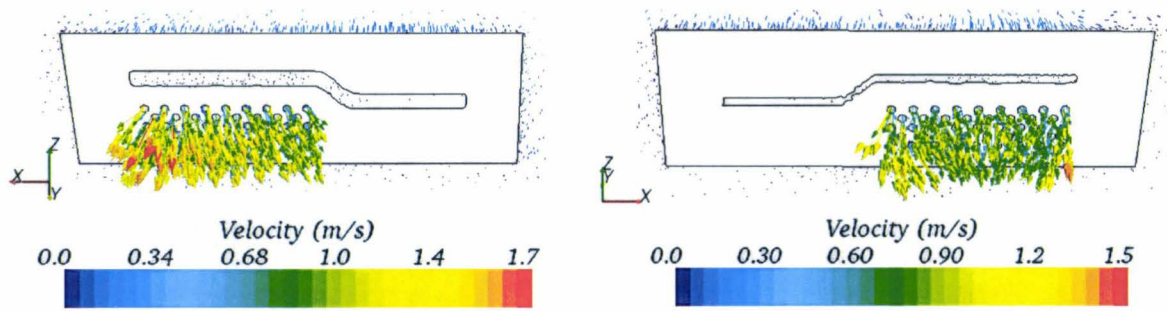


Figure A.6.7. Velocity vectors in the section plane coincident with the outlet grill on the sidewall 1 (left) and on the sidewall 2 (right) for  $\omega = 5065$  rpm.

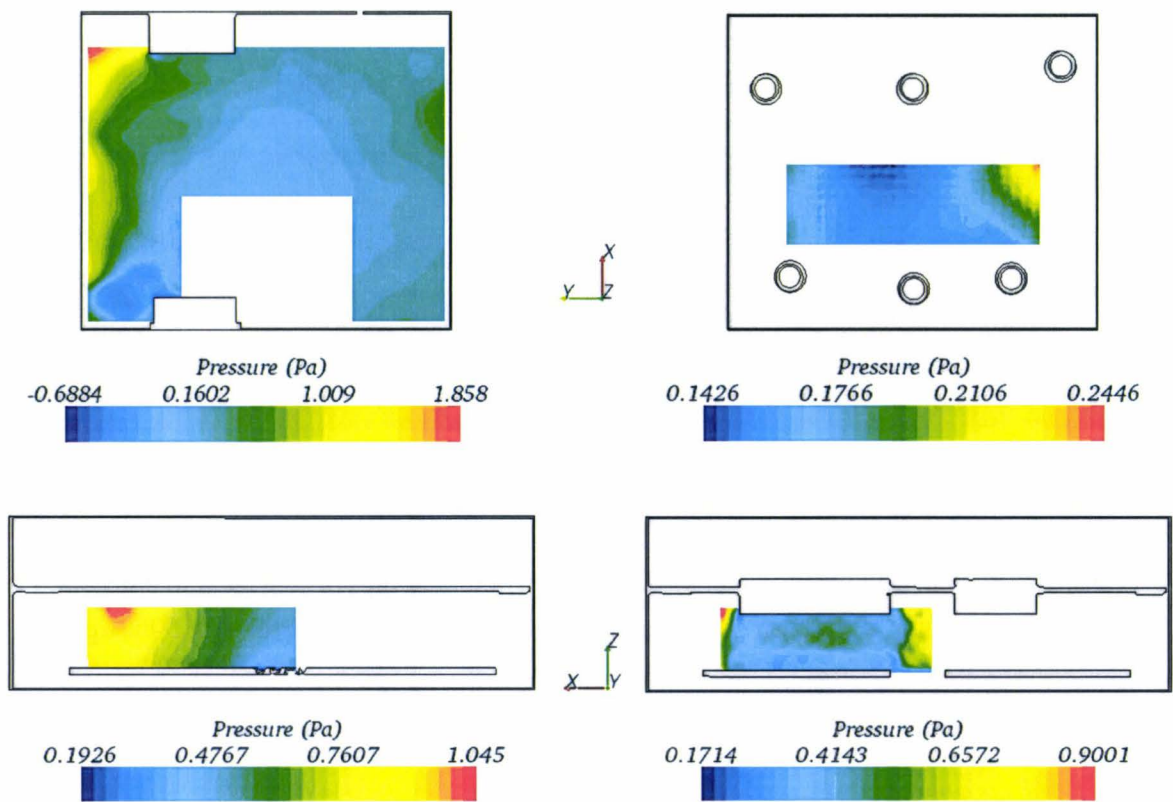


Figure A.6.8. Static pressure distribution in the section planes  $P_3$  (left) and  $P_4$  (right); results of the detailed model of the grills with orifices for  $\omega = 3860$  rpm.

**A.6.4. Upper grill of the TV-tuner in the test-rig**

Region	Number of cells	Resolution of the near-wall region, $y \leq 2 \times 10^{-4} m$		
		Number of cell layers	Growth rate	$y^+$ values
Upper grill	$4.51 \times 10^6$	5	1.05	$[10^{-4}; 2.1]$
Elsewhere	$2.42 \times 10^6$	2	1.01	$[10^{-4}; 3.1]$

Table A.6.8. Grid generated for the computation of the flow through upper grill of the TV-tuner in the test-rig model.

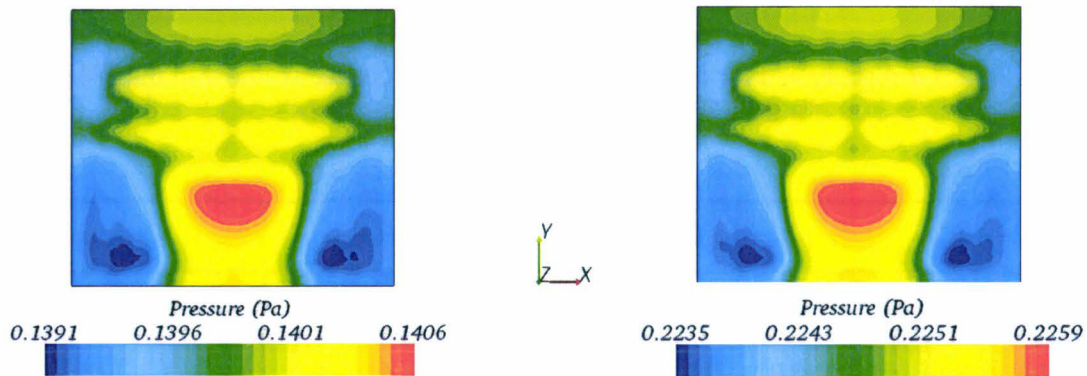


Figure A.6.9. Static pressure distribution in a section plane situated  $10^{-2} m$  upstream of the upper grill with an inlet velocity  $u_i = 2.297 \times 10^{-2} m/s$  (left) and  $u_i = 2.969 \times 10^{-2} m/s$  (right).

Inlet velocity $u_i$ ( $m/s$ )	Mass flux $\dot{M}$ ( $kg/m^2s$ )	RMS of the static pressure drop $\Delta p_{stat,RMS}$ ( $Pa$ )	Standard deviation $\sigma_p$ ( $Pa$ )
$2.297 \times 10^{-2}$	$4.29 \times 10^{-2}$	0.1397	$2.437 \times 10^{-3}$
$2.969 \times 10^{-2}$	$5.55 \times 10^{-2}$	0.2246	$2.762 \times 10^{-3}$

Table A.6.9. Mean static pressure drop and standard deviation of the static pressure of the upper grill of the TV-tuner in the test-rig for different inlet velocities.

$\dot{M}$ ( $kg/m^2s$ )	$\Delta \bar{p}_{stat}$ ( $Pa$ )	$\alpha$ (-)	$\beta$ ( $m/s$ )	$I_{ij}$ ( $kg/m^4$ )	$V_{ij}$ ( $kg/m^3s$ )
$4.29 \times 10^{-2}$	0.1397	$7.62 \times 10^1$	$5.42 \times 10^{-1}$	$I_{ij} \cdot \bar{u}_i = 1.84 \times 10^5 \bar{u}_i$	$V_{ij} \cdot \bar{u}_i = 1.31 \times 10^3 \bar{u}_i$
$5.55 \times 10^{-2}$	0.2246				

Table A.6.10. Porous coefficients and tensors of the upper grill of the TV-tuner in the test-rig.

### A.6.5. TV-tuner, 2D and 3D porous elements

Region	Number of cells	Resolution of the near-wall region, $y \leq 2 \times 10^{-4} m$		
		Number of cell layers	Growth rate	$y^+$ values
Fan	$1.44 \times 10^6$	6	1.1	$[10^{-2}; 6.0]$
Porous baffle	$1.78 \times 10^6$	5	1.05	$[10^{-2}; 1.3]$
TV-tuner	$4.41 \times 10^6$	4 (ICs), 2 elsewhere	1.3	$[10^{-4}; 14.4]$
Environment	$6.19 \times 10^5$	1	1.3	$[10^{-4}; 6.3]$

Table A.6.11. Grid generated for the computation of forced convective flow in the TV-tuner for the 2D and 3D porous resistance models.

	$\alpha$ (-)	$\beta$ (m/s)	$I_{ij}$ (kg/m <sup>4</sup> )	$V_{ij}$ (kg/m <sup>3</sup> s)
Grill, upper wall	$7.62 \times 10^1$	$5.42 \times 10^{-1}$	$I_{ij} \cdot \bar{u}_i = 1.84 \times 10^5 \bar{u}_i$	$V_{ij} \cdot \bar{u}_i = 1.31 \times 10^3 \bar{u}_i$
Grill, lower wall	$2.32 \times 10^1$	$6.90 \times 10^{-1}$	$I_{ij} \cdot \bar{u}_i = 5.58 \times 10^4 \bar{u}_i$	$V_{ij} \cdot \bar{u}_i = 5.50 \times 10^2 \bar{u}_i$
Grill, sidewall 1	$1.07 \times 10^1$	$3.21 \times 10^{-1}$	$I_{ij} \cdot \bar{u}_i = 2.58 \times 10^4 \bar{u}_i$	$V_{ij} \cdot \bar{u}_i = 7.70 \times 10^2 \bar{u}_i$
Grill, sidewall 2	$1.09 \times 10^1$	$3.30 \times 10^{-1}$	$I_{ij} \cdot \bar{u}_i = 2.63 \times 10^4 \bar{u}_i$	$V_{ij} \cdot \bar{u}_i = 8.00 \times 10^2 \bar{u}_i$

Table A.6.12. Inertial and viscous coefficients for the 2D and 3D porous resistance models.

	Mass flux (kg/m <sup>2</sup> s)	Ratio of mass flow rate (%)	$\Delta p_{stat,RMS}$ (Pa)	$\sigma_p$ (Pa)
Fan	4.17	100	-	-
Grill, upper wall	$4.64 \times 10^{-1}$	44.1	0.7386	0.4642
Grill, lower wall	$4.54 \times 10^{-1}$	18.4	0.3849	0.05322
Grill, sidewall 1	1.03	12.9	1.541	0.3551
Grill, sidewall 2	$8.28 \times 10^{-1}$	10.4	1.055	0.2542
Leakage, front wall	$8.21 \times 10^{-1}$	13.8	-	-
Single hole, back wall	$7.64 \times 10^{-1}$	0.397	-	-

Table A.6.13. Mass flux and RMS of the static pressure drop through the different outlet areas of the TV-tuner modelled with 2D porous elements for  $\omega = 5065$  rpm.

	Mass flux ( $kg / m^2 s$ )	Ratio of mass flow rate (%)	$\Delta p_{stat,RMS}$ (Pa)	$\sigma_p$ (Pa)
Fan	4.19	100	-	-
Grill, upper wall	$5.27 \times 10^{-1}$	49.5	0.3548	0.4648
Grill, lower wall	$4.86 \times 10^{-1}$	19.5	0.2090	0.0413
Grill, sidewall 1	$7.69 \times 10^{-1}$	9.55	1.447	0.3691
Grill, sidewall 2	$6.86 \times 10^{-1}$	8.53	1.068	0.2066
Leakage, front wall	$7.60 \times 10^{-1}$	12.6	-	-
Single hole, back wall	$6.08 \times 10^{-1}$	0.312	-	-

Table A.6.14. Mass flux and RMS of the static pressure drop through the different outlet areas of the TV-tuner modelled with 3D porous elements for  $\omega = 5065$  rpm.

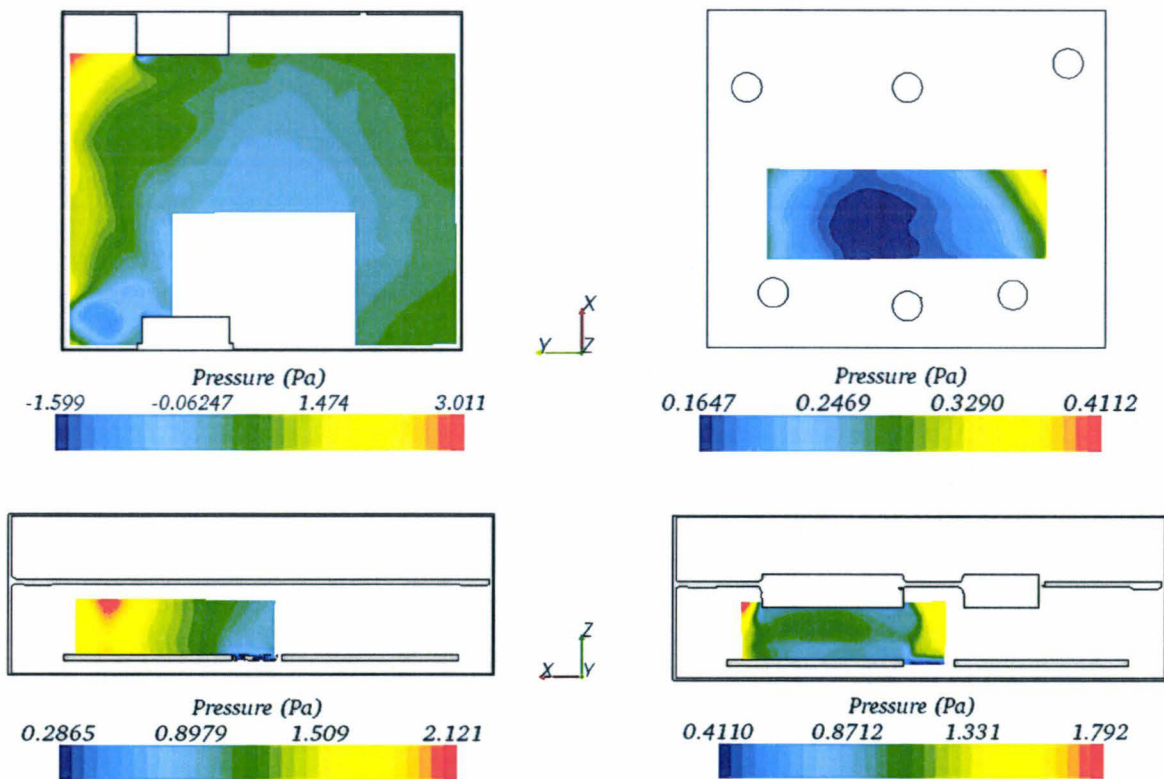


Figure A.6.10. Static pressure distribution in the section planes  $P_1$  (top left),  $P_2$  (top right),  $P_3$  (bottom left) and  $P_4$  (bottom right); results of the 3D porous model for  $\omega = 5065$  rpm.

---

## A.7. Battery in the spare-wheel cavity

### A.7.1. Experimental set-up and results

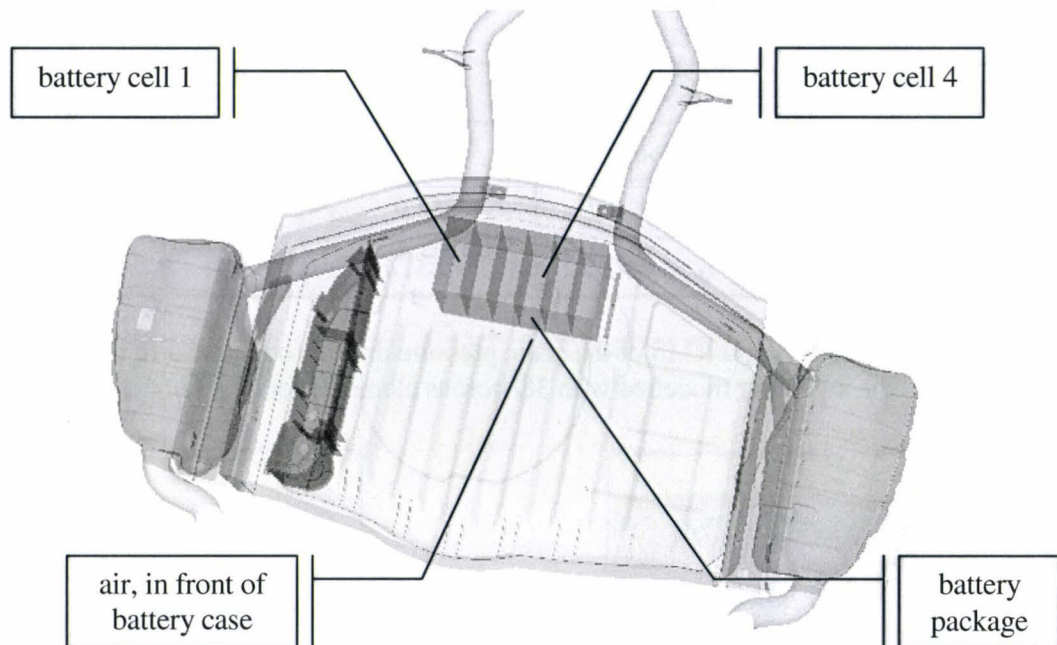


Figure A.7.1. Position of the thermocouples in the spare-wheel cavity; view from above.

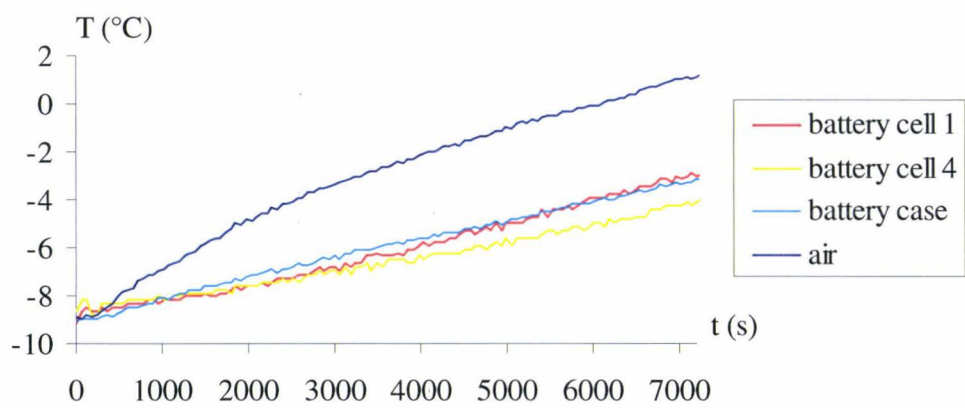


Figure A.7.2. Solid temperatures of the battery cells 1 and 4; solid temperature of the battery package and corresponding air temperature; case of winter.

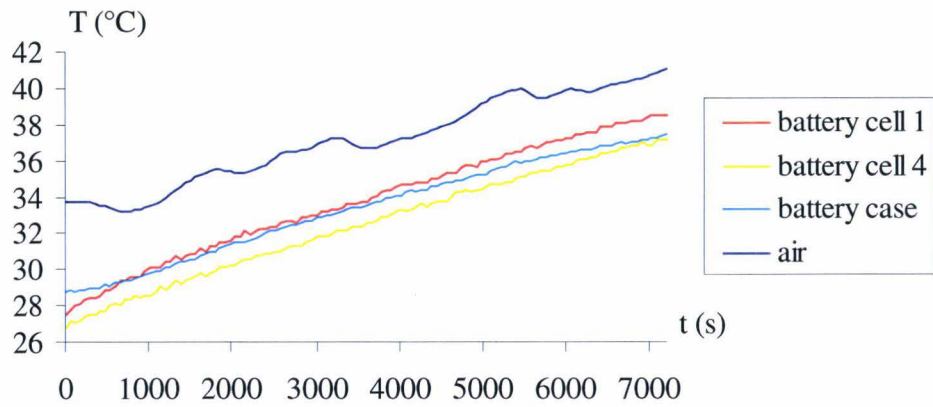


Figure A.7.3. Solid temperatures of the battery cells 1 and 4; solid temperature of the battery package and corresponding air temperature; case of summer.

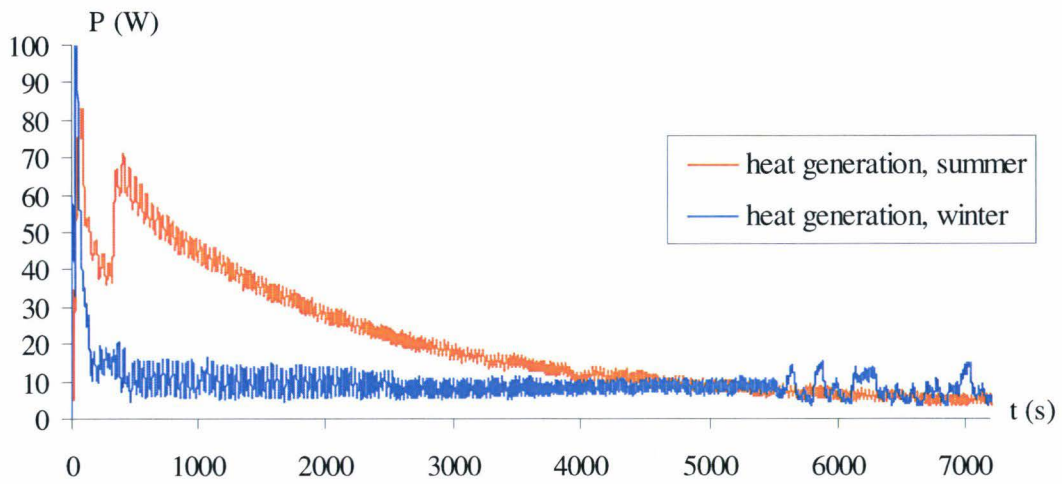


Figure A.7.4. Transient heat generated by the battery for both cases of winter and summer.

## A.7.2. Numerical model

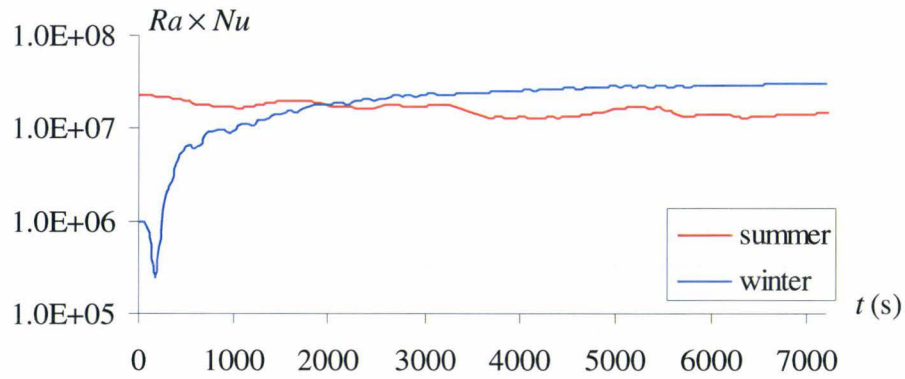


Figure A.7.5. Product of the Rayleigh and Nusselt numbers (equation A.7.1) with time for both cases of winter and summer.

$$Ra \times Nu = \frac{g\beta H^4}{\nu\alpha} \frac{T_{air} - T_{case}}{\Delta x} \quad (A.7.1)$$

Region	Number of cells	Boundary layer			
		Thickness (m)	Cell layers	Growth rate	$y^+$ values
Battery	$5.95 \times 10^6$	$6 \times 10^{-3}$	12	1.23	$[10^{-3}; 10^{-1}]$
Elsewhere					$[10^{-4}; 10^{-1}]$

Table A.7.1. Grid generated for the computation of the flow in the spare-wheel cavity with STAR-CD.

**A.7.3. Validation of the numerical model**

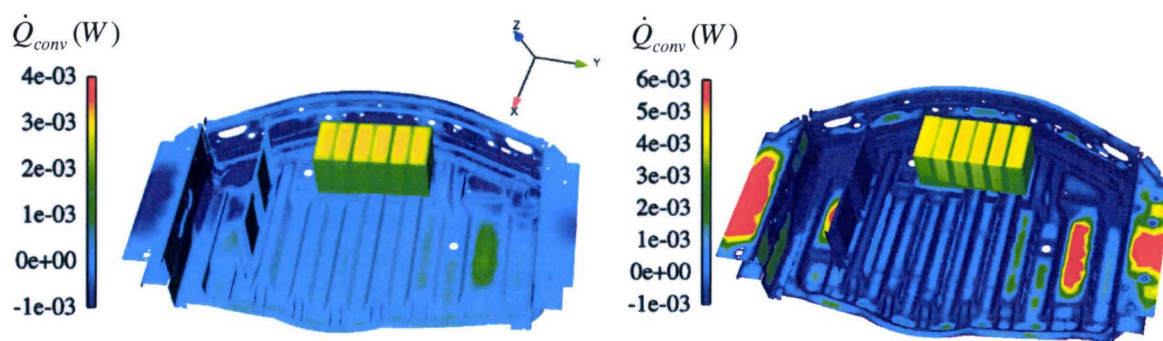


Figure A.7.6. Distribution of convective net heat rate of the battery in the spare-wheel cavity after 1800 s (left) and 7200 s (right) of simulation time; case of winter.

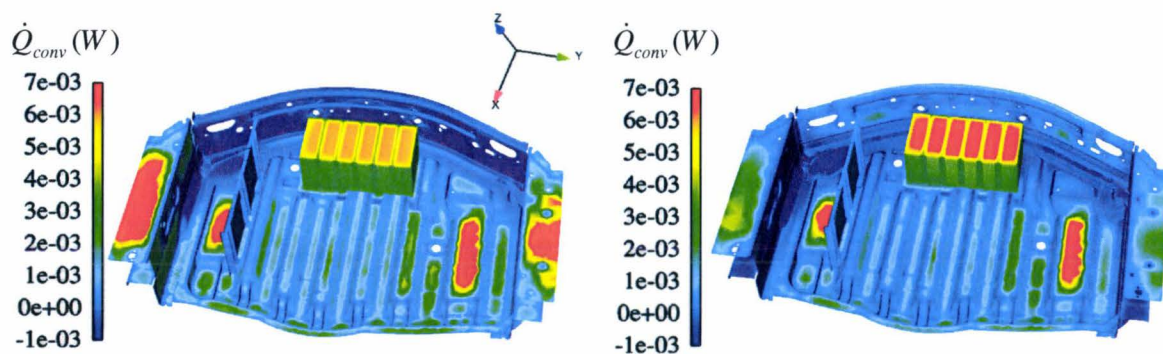


Figure A.7.7. Distribution of convective net heat rate of the battery in the spare-wheel cavity after 1800 s (left) and 7200 s (right) of simulation time; case of summer.

$t$ (s)	$n_i$ (mol), discharge of the battery			
	$Pb + PbO_2$	$+ 2 H_2SO_4$	$\rightarrow 2 PbSO_4$	$+ 2 H_2O$
0	87	57	0	0
3	72.7	28.5	28.5	28.5

$t$ (s)	$n_i$ (mol), charge of the battery			
	$2 PbSO_4$	$+ 2 H_2O$	$\rightarrow Pb + PbO_2$	$+ 2 H_2SO_4$
4	28.5	28.5	72.7	28.5
7200	12.8	12.8	80.6	44.3

Table A.7.2. Variation of the mole of each chemical component of the battery with time; case of summer.

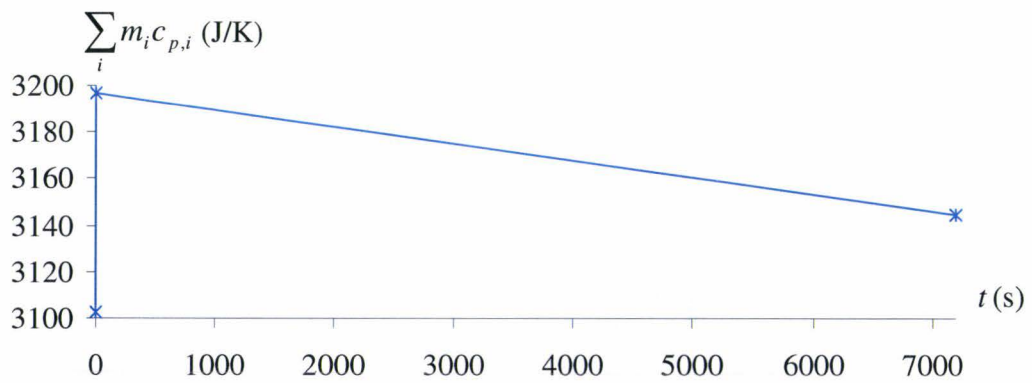


Figure A.7.8. Variation with time of the sum of the molar heat capacity of each chemical component per battery cell; case of summer.

#### A.7.4. Validation of the coupling strategy

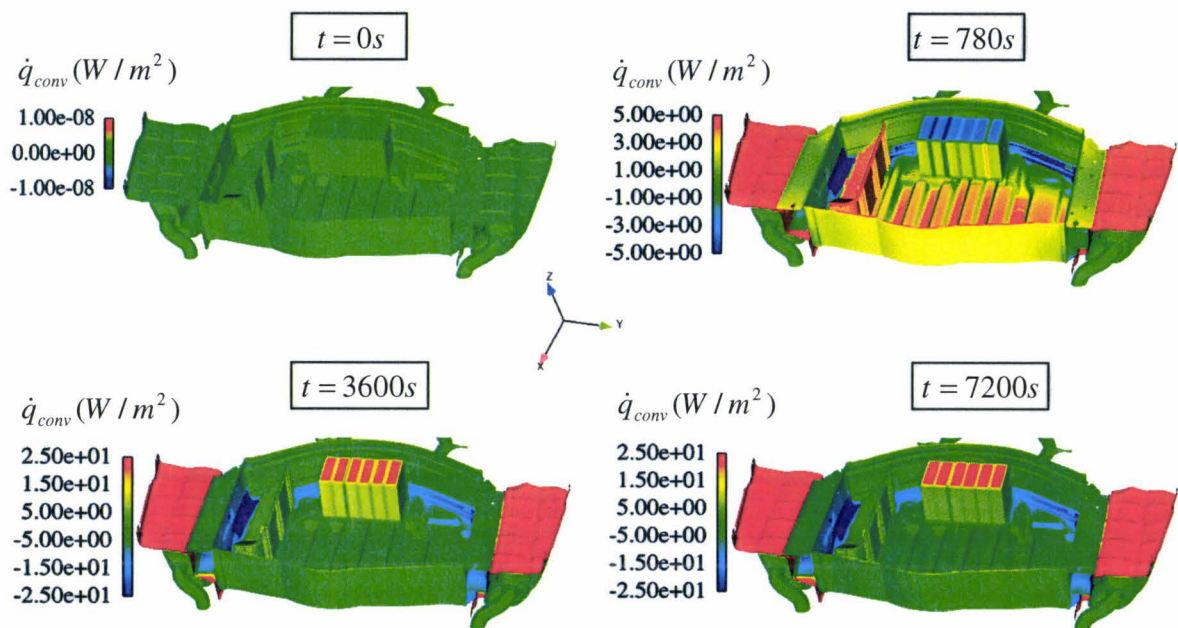


Figure A.7.9. Distribution of convective net heat flux in the spare-wheel cavity at different time-steps; results of the initial transient analysis with RadTherm.

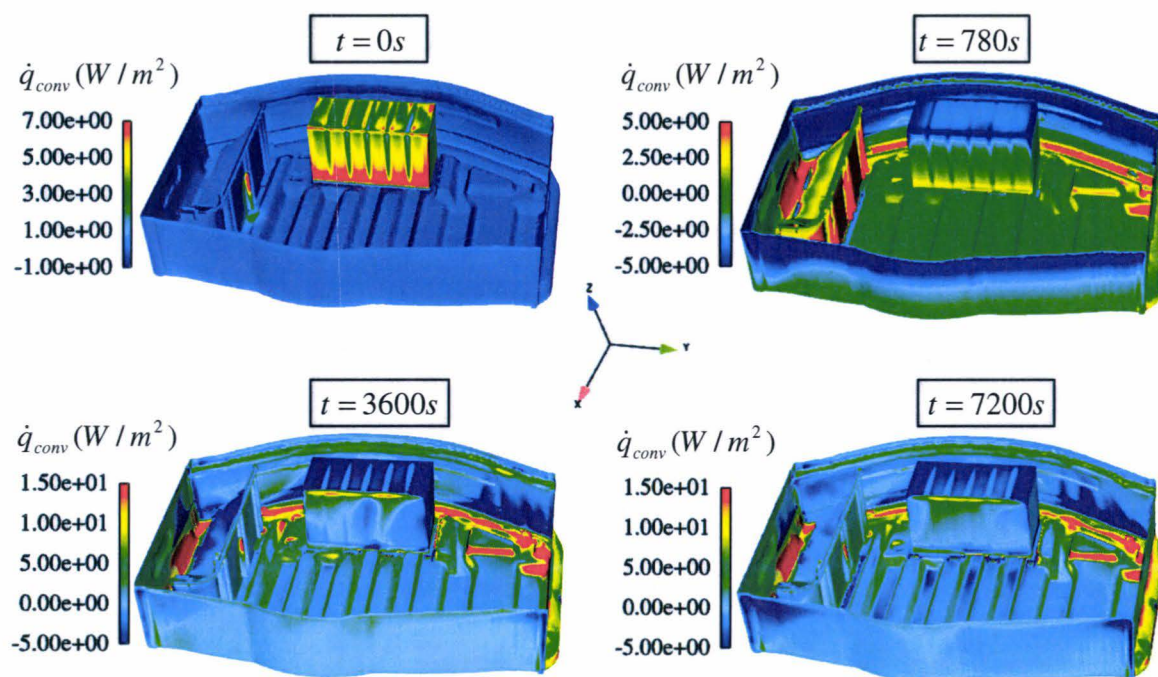


Figure A.7.10. Distribution of convective net heat flux in the spare-wheel cavity at different time-steps resulting from a steady-state computation with STAR-CD.

### A.7.5. Critical use case of summer

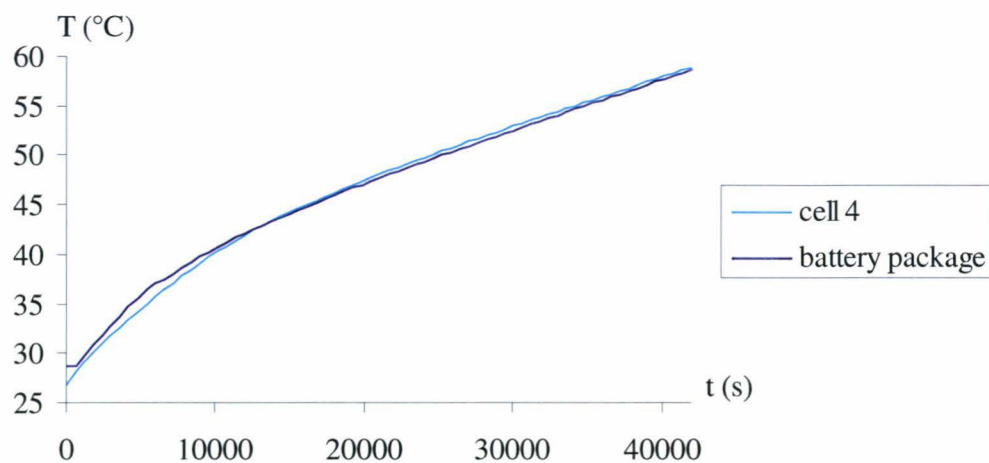


Figure A.7.11. Battery operating time period by idle predicted by a thermal analysis for the case of summer; temperature of the battery package (blue) and cell 4 (green).

---

## A.8. Sound amplifier in a cavity under the passenger's feet

### A.8.1. Measurements of the thermal resistances and capacitances from the power ICs in the main heat path

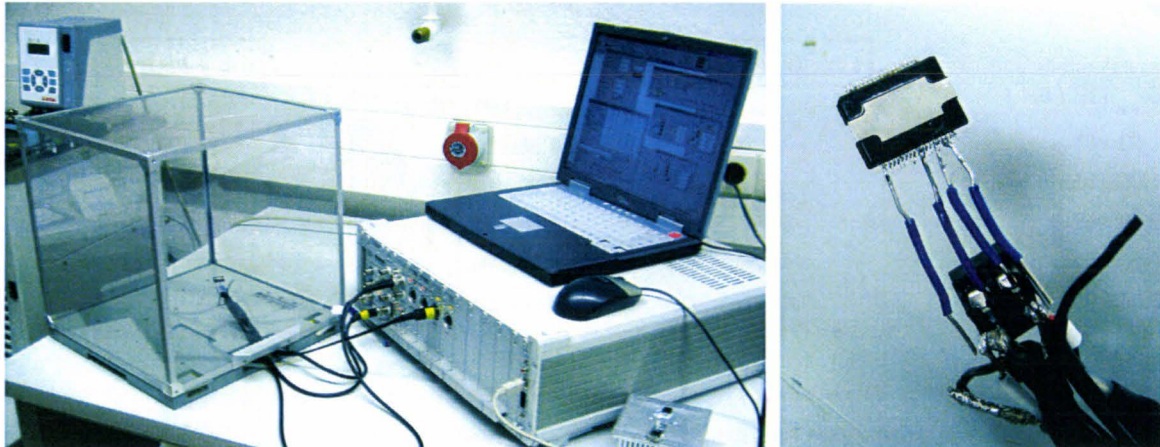


Figure A.8.1. Experimental test-rig (left) and first measurement with the power IC cooled only by natural convection (right).

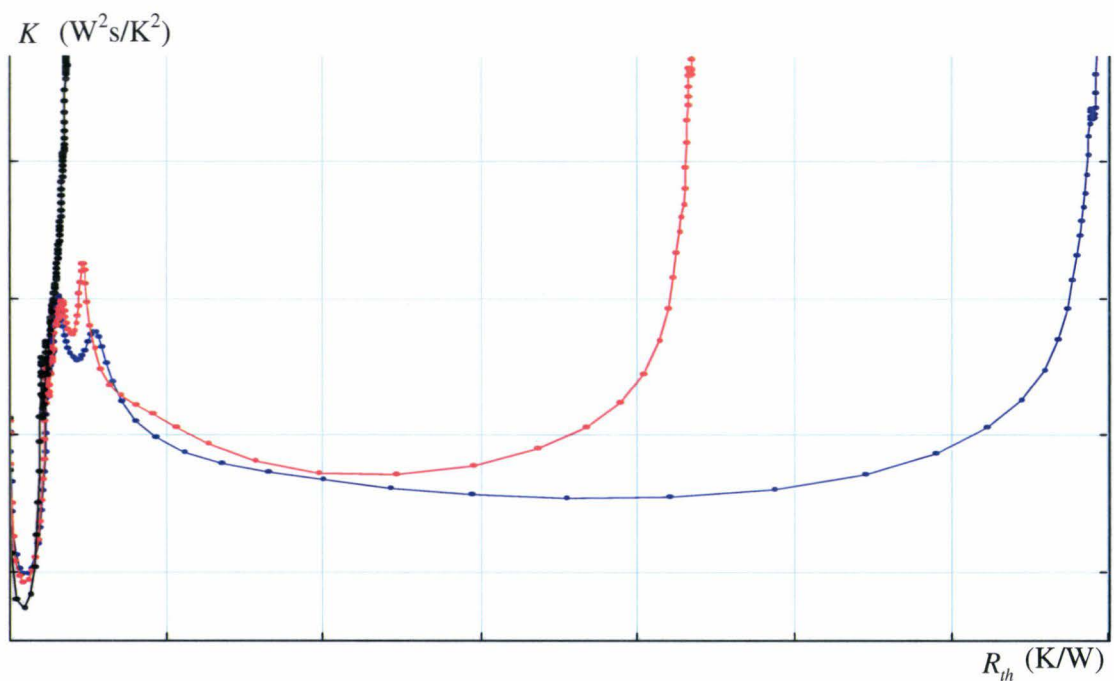


Figure A.8.2. Differential structure function; system 1 (blue), system 2 (red) and system 3 (black).

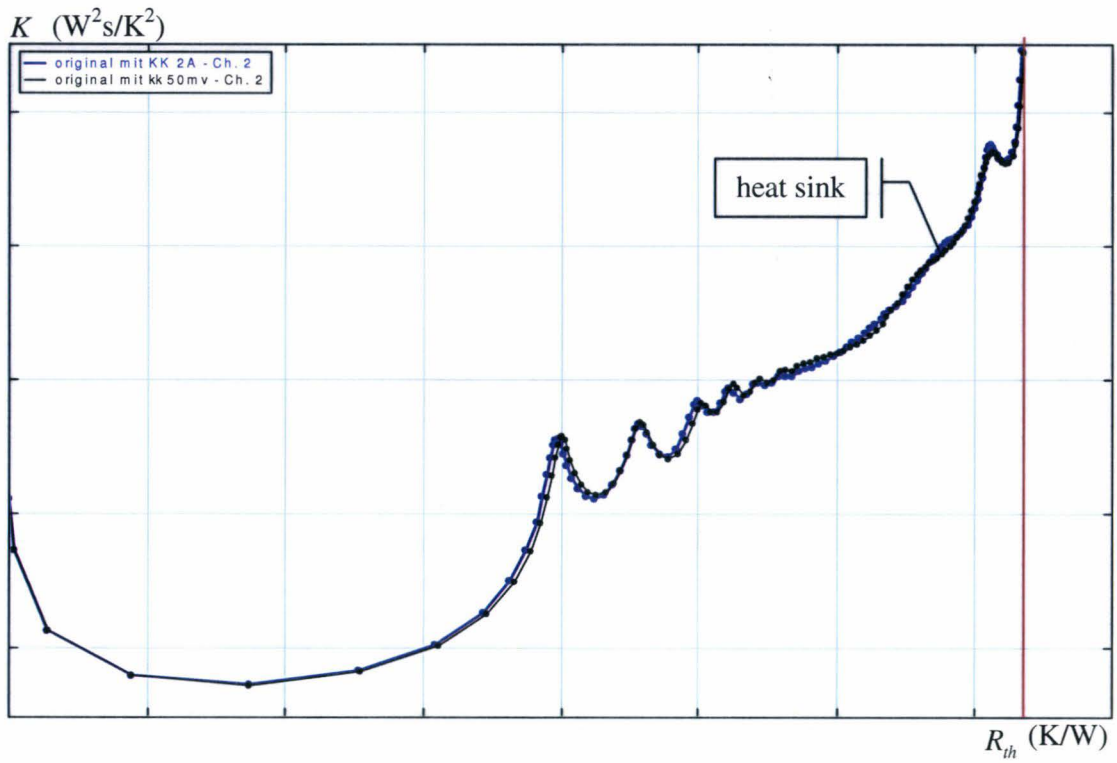


Figure A.8.3. Differential structure function, zoomed.

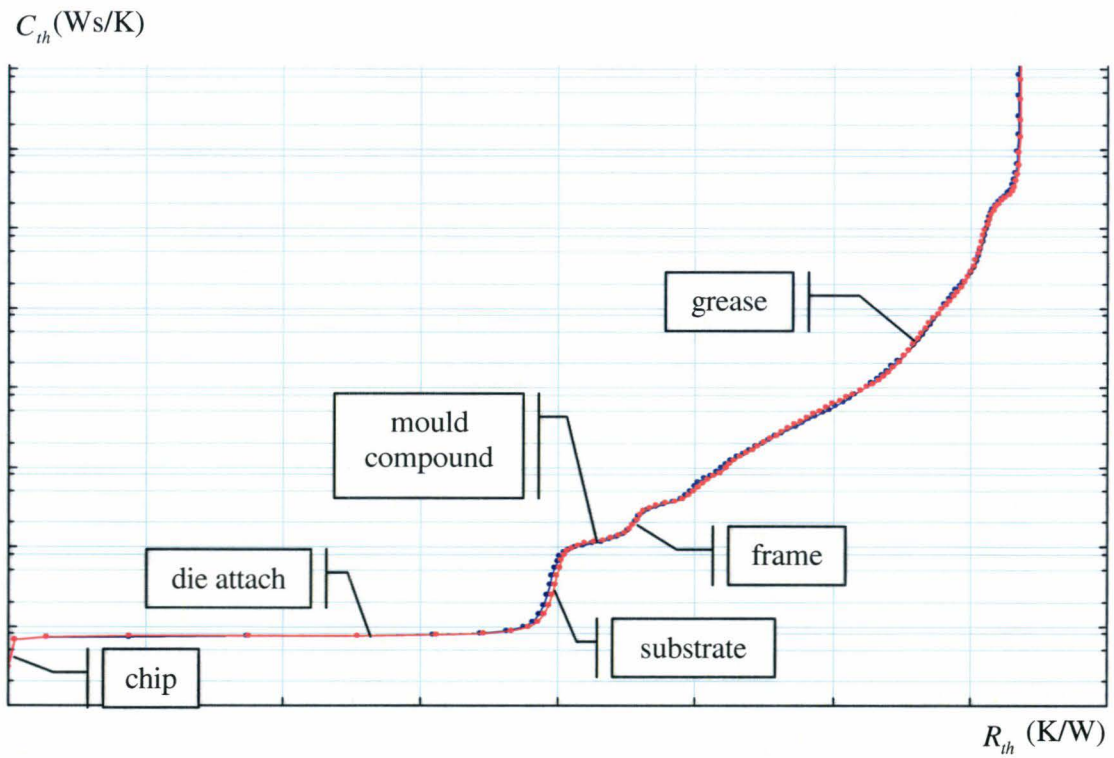


Figure A.8.4. Cumulative structure function.

### A.8.2. Experimental set-up in the vehicle and results

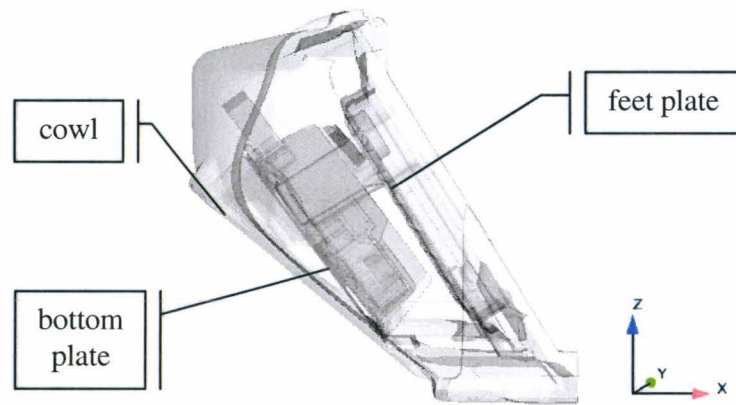


Figure A.8.5. Position of the thermocouples in the cavity of the sound amplifier; lateral view.

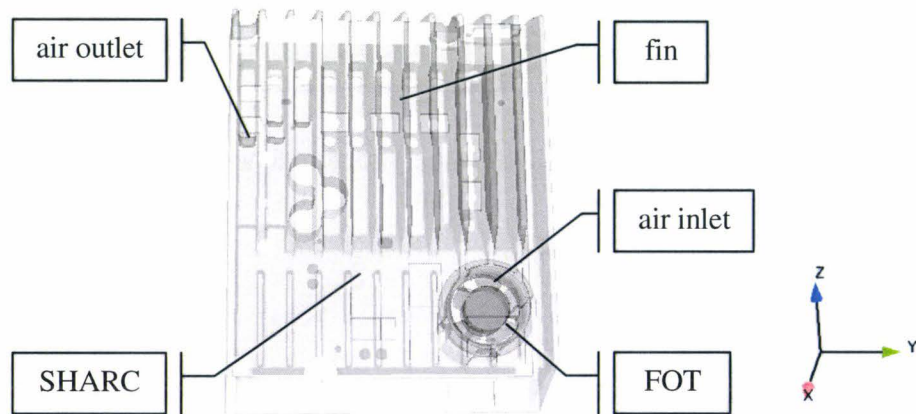


Figure A.8.6. Position of the thermocouples in the sound amplifier; front view.

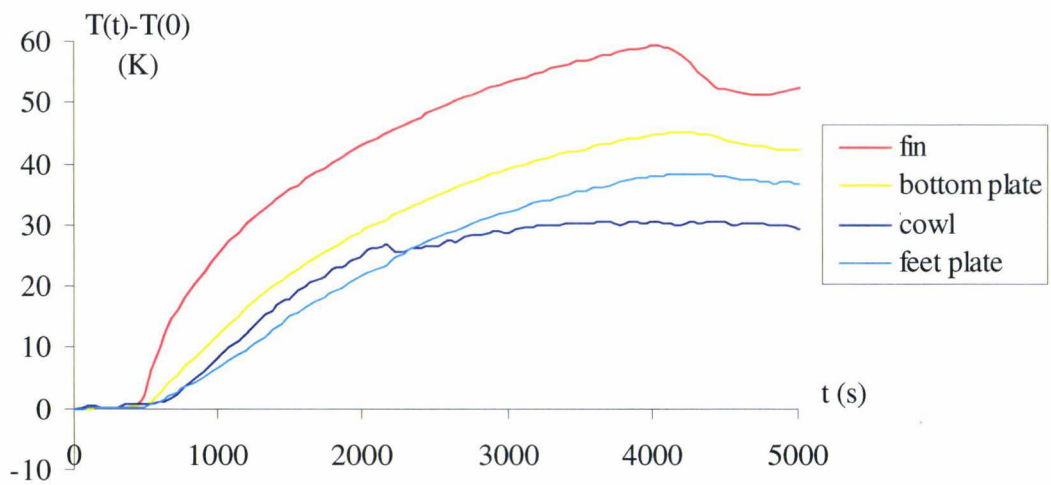


Figure A.8.7. Relative temperatures of the fin and bottom plate of the sound amplifier; cowl and feet plate of the cavity.

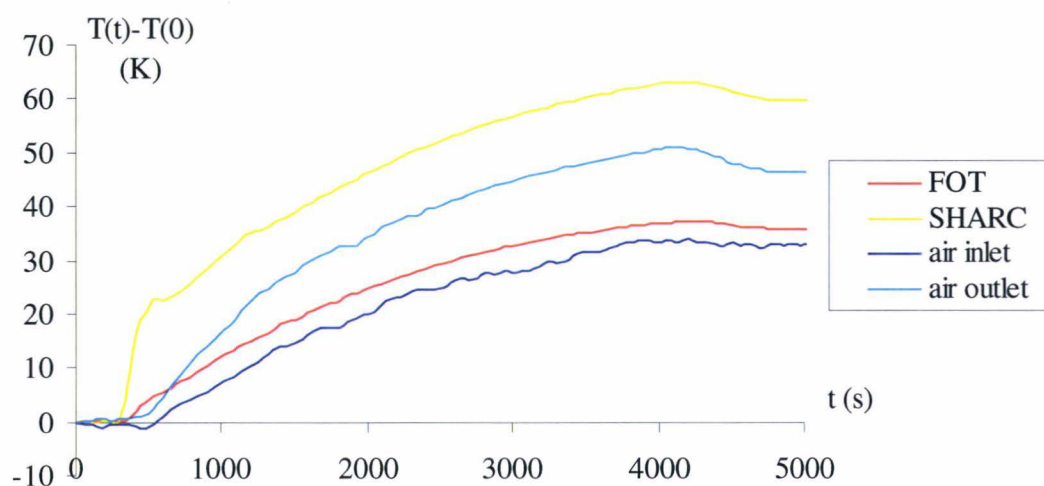


Figure A.8.8. Relative temperatures of the FOT and of the SHARC processor; inlet and outlet air temperatures.

### A.8.3. Numerical model

Geometrical parameters	Fin base	Fin tip
Fin height $L$ (m)	$0.035 \leq L \leq 0.051$	
Fin spacing $S$ (m)	0.0087	0.011
Fin thickness $T$ (m)	0.0063	0.0037
Fin width $W$ (m)	0.136	0.115
Thickness of the air layer between the fin base and the upper wall $H$ (m)	$0.058 \leq H \leq 0.068$	-

Table A.8.1. Geometrical parameters of the fins of the heat sink assembled in the cavity.

Region	Number of cells	Near-wall region			
		Thickness ( $m$ )	Cell layers	Growth rate	$y^+$ values
Heat sink	$5.27 \times 10^6$	$y \leq 1 \times 10^{-3} m$	3	1.5	$[10^{-3}; 3 \times 10^{-1}]$
Elsewhere		$y \leq 1 \times 10^{-2} m$	9		$[10^{-4}; 1.5]$

Table A.8.2. Grid generated for the computation of the flow in the cavity of the sound amplifier with STAR-CD; fan switched off.

Region	Number of cells	Near-wall region			
		Thickness (m)	Cell layers	Growth rate	$y^+$ values
Fan	$3.52 \times 10^6$	$y \leq 1.25 \times 10^{-2}$ m	2	1	$[10^{-4}; 6.2]$
Interior sound amplifier	$9.50 \times 10^5$	$y \leq 1 \times 10^{-3}$ m	3	1.5	$[10^{-3}; 9.1]$
Heat sink	$6.51 \times 10^6$	$y \leq 1 \times 10^{-3}$ m	3	1.5	$[10^{-4}; 4.9]$
Cavity	$8.29 \times 10^5$	$y \leq 1 \times 10^{-2}$ m	9	1.5	$[10^{-4}; 1.5]$
Cockpit	$1.53 \times 10^5$	$y \leq 1.5 \times 10^{-2}$ m	3	1	$[10^{-2}; 9.7]$

Table A.8.3. Grid generated for the computation of the flow in the cavity of the sound amplifier with STAR-CD; fan switched on.

Total time	Solid time increment	Coupling time-step
0	0	1
30	30	2
60	30	3
90	30	4
120	30	5
150	30	6
180	30	7
210	30	8
240	30	9
270	30	10
300	30	11
330	30	12
341.46	11.46	13
349.53	8.07	
360	10.46	
390	30	14

Total time	Solid time increment	Coupling time-step
420	30	15
450	30	16
480	30	17
510	30	18
540	30	

Table A.8.4. Solid time-steps used for the computation of solid conduction.

**A.8.4. Validation of the numerical model**

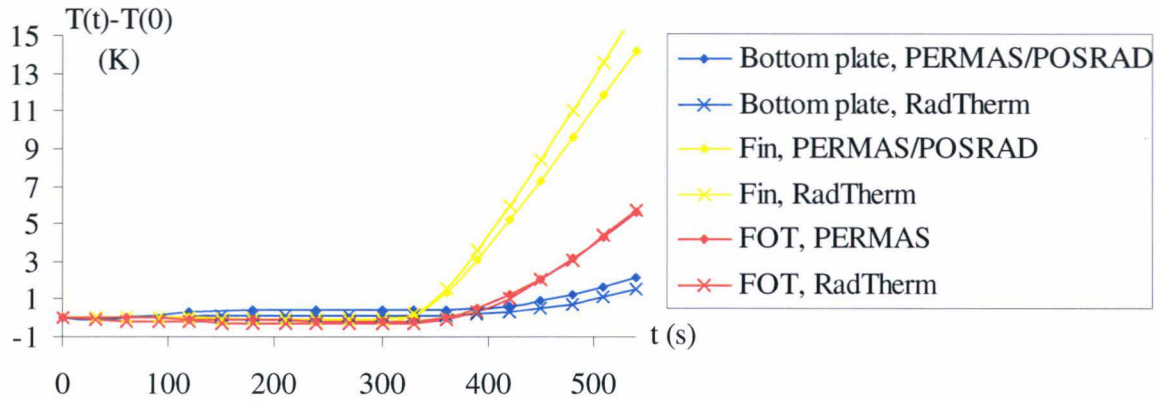


Figure A.8.9. Relative temperature of the FOT (red), fin (yellow) and bottom plate (blue). Computation with PERMAS/POSRAD (dotted line) and with RadTherm (crossed line).

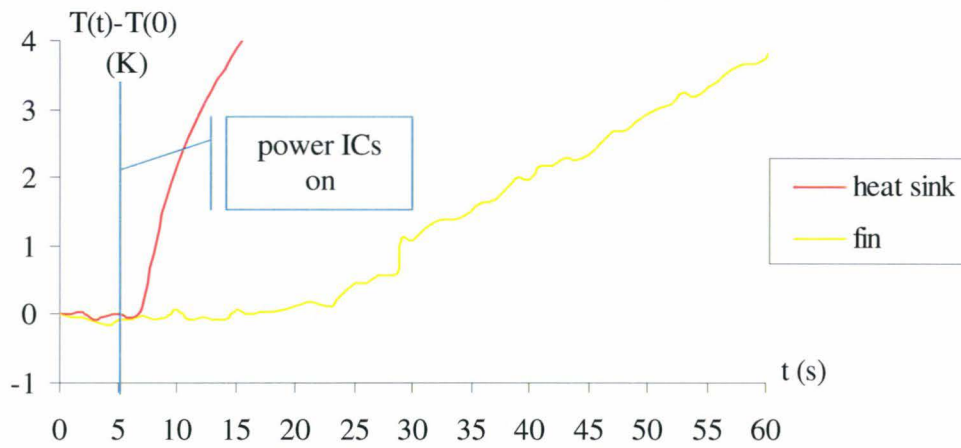


Figure A.8.10. Relative temperature of the heat sink above a power IC (red) and of the fin (yellow). Measurements of the heat sink temperature with a thermographic camera.

Bibliothèque Universitaire de Valenciennes



00900619